Characterisation of solution-processable organic light emitting diodes

GARETH CHRISTOPHER GRIFFITHS

Characterisation of solution-processable organic light emitting diodes

Gareth Christopher Griffiths

A thesis submitted in partial fulfilment of the requirements for the degree of Doctor of Philosophy

Organic Electroactive Materials Group

Department of Physics

University of Durham

August 2014

Characterisation of solution-processable organic light emitting diodes

Gareth Christopher Griffiths

Abstract

A range of new materials for organic light emitting diodes (OLEDs) synthesised in the Department of Chemistry at Durham University have been characterised and electroluminescent devices containing these materials have been optimised.

High triplet oxadiazole based electron transport materials were tested in devices blended with the host material poly(9-vinylcarbazole) (PVK). The materials exhibit comparable performance to standard OXD-7 in electrophosphorescent devices, while emission from exciplex devices indicate the new materials have higher LUMO energies than OXD-7.

Single layer devices containing new sky-blue iridium(III) emitters were optimised. The improved solubility of these emitters over FIrpic, the standard sky-blue emitter, resulted in improved device efficiency and brightness due to reduced aggregation, concentration quenching and self absorption in film, and higher radiative yield. Derivatives of these new emitters, with emission shifted towards a deeper blue, were characterised. Increased trapping by the PVK host led to a reduction in the device efficiency for these materials.

Two series of iridium(III) emitters with emission tuned from green to red by systematically substituted electron withdrawing or donating groups were characterised. Photophysical properties of these emitters, including the solvatochromic shift of photoluminescence spectra, correlate with theoretical values of the molecular dipole moment, thus linking changes in chemical structure with device performance.

Finally, white electroluminescence was demonstrated from single copolymers exhibiting broadened blue-green intramolecular charge transfer emission due to the interaction of fluorene (F) and dibenzothiophene-S,S-dioxide (S) units. Single layer and multilayer devices were optimised, and white emission with good spectral coverage and CIE coordinates of (0.35, 0.39) was achieved with the F/S copolymer. The emission colour varies significantly with emissive layer thickness and applied voltage. Addition of a thermally evaporated electron transport layer resulted in improvement in both device efficiency and colour stability.

Contents

List of Figures

List of Tables

List of Publications

Work included in this thesis has contributed to the following publications:

1. *Highly Efficient, Solution-Processed, Single-Layer, Electrophosphorescent Diodes and the Effect of Molecular Dipole Moment.* Hameed A. Al-Attar, Gareth C. Griffiths, Tom N. Moore, Mustafa Tavasli, Mark A. Fox, Martin R. Bryce & Andrew P. Monkman, *Advanced Functional Materials* **21** (2011), 2376 - 2382

2. *Colour tuning from green to red by substituent effects in phosphorescent tris-cyclometalated iridium(III) complexes of carbazole-based ligands: synthetic, photophysical, computational and high efficiency OLED studies.* Mustafa Tavasli, Tom N. Moore, Yonghao Zheng, Martin R. Bryce, Mark A. Fox, Gareth C. Griffiths, Vygintas Jankus, Hameed A. Al-Attar & Andrew P. Monkman, *Journal of Materials Chemistry* **22** (2012), 6419 - 6428

3. *Cyclometalated Ir(III) Complexes for High-Efficiency Solution-Processable Blue PhOLEDs.* Valery N. Kozhevnikov, Yonghao Zheng, Matthew Clough, Hameed A. Al-Attar, Gareth C. Griffiths, Khalid Abdullah, Steponas Raisys, Vygintas Jankus, Martin R. Bryce & Andrew P. Monkman, *Chemistry of Materials* **25** (2013), 2352 - 2358

Work on some of the materials presented is ongoing and further manuscripts will be submitted for publication in due course. Additionally, work not included in this thesis has contributed to the following publications:

1. *Ultrahigh Efficiency Fluorescent Single and Bi-Layer Organic Light Emitting Diodes: The Key Role of Triplet Fusion.* Chien-Jung Chiang, Alpay Kimyonok, Marc K. Etherington, Gareth C. Griffiths, Vygintas Jankus, Figen Turksoy & Andy P. Monkman, *Advanced Functional Materials* **23** (2013), 739 - 746

Declaration

All material contained in this thesis is original and is the result of my own work except where explicit reference is made to the work of others.

This thesis has not been submitted in whole or in part for the award of a degree at this or any other university.

Gareth Griffiths

Durham, August 2014

Acknowledgements

I would like to thank Prof. Andy Monkman for his supervision and guidance, as well as giving me the opportunity to perform this research. I would also like to thank Dr. Hameed Al-Attar and all the members of the Organic Electroactive Materials group past and present for their helpful discussions, advice and assistance with equipment. I am also grateful to Prof. Martin Bryce and his group in the Department of Chemistry for synthesising and supplying the new materials tested during the course of this project. Thanks must also go to the EPSRC for funding.

I would also like to thank my friends, members past and present of Durham University Hill Orchestra, Durham University Palatinate Orchestra, Collingwood College MCR and Durham University Anglo-Japanese Society for making the past few years memorable and enjoyable. Finally, I would like to thank my family for all the help and support they have provided over the years.

1 Introduction

Organic Light Emitting Diodes (OLEDs) have in recent years found many commercial applications in the electronic display industry. Mobile phones and digital media players with active matrix OLED screens are now common and large-area television screens are now on sale. Prototype devices boasting improved performance, larger area, thinner profile, sometimes with flexible active areas, are regularly showcased at technology exhibitions around the world.

Artificial lighting is another major area of interest for the development of organic light emitting diodes, as a possible replacement for the incandescent light bulbs and fluorescent tubes in widespread use today. Incandescent bulbs are inefficient, losing much of the energy supplied to heat and other non-visible radiation. The emission spectrum of fluorescent tubes or LED lighting may be poor compared to natural light or incandescent light bulbs, and the corresponding colour rendering index may suffer as a result. They can also contain materials harmful to health or the environment such as mercury. The simplicity of colour tuning for a more natural white light emission and the large area of solution processable devices, combined with potentially very high efficiencies and low driving voltages make organic light emitting diodes a promising candidate for use in lighting applications.

Additionally, there is much interest in the related field of organic photovoltaics, where similar materials, physical principles and device architectures may be employed to obtain a flexible, large area renewable energy source that is efficient, affordable and simple to manufacture.

This chapter provides an overview of the history of OLED devices, from early reports of organic electroluminescence in the mid-20th century, to the development of efficient thin film devices in the 1990s and their present and future commercial applications in the field of electronic displays and solid state lighting. An outline of the structure and scope of this thesis is then provided.

1.1 History of organic electroluminescence

Observations of electroluminescence from organic materials have been reported since the mid-1950s, when André Bernanose and co-workers at the Université de Nancy in France applied intense alternating electric fields, with potentials of up to 2000 V, to films of acridine derivatives [1, 2]. In 1963, Martin Pope and colleagues at New York University observed direct current electroluminescence above 400 V from 10 - 20 μm single crystals of anthracene [3]. Helfrich and Schneider, working at the Canadian National Research Council, demonstrated carrier injection into anthracene single crystals from liquid electrodes resulting in light emission attributed to the recombination of electrons and holes [4]. As high voltages were required, electroluminescence from these thick organic single crystals had few practical applications.

Electroluminescence from polymer films was reported in 1983 by Roger Partridge of the National Physical Laboratory in the United Kingdom [5–8], who observed blue electroluminescence from a device consisting of a film of poly(vinyl carbazole) up to 2.2 μm thick. Although light could be observed from these devices at relatively low operating voltages, commercial development was limited by low device efficiencies and by the stability of the low work function materials used as the cathode. Low operating

voltages were also reported in 1982 by Vincett and co-workers at ICI and the University of Durham [9], who observed electroluminescence from 0.6 μm vacuum deposited anthracene films which was visible at 30 V under normal lighting conditions and 12 V in darkness.

In 1987, Ching W. Tang and Steven Van Slyke of Eastman Kodak developed a bilayer structure device consisting of a hole-transporting layer of organic diamine and light-emitting electron-transporting layer of 8-hydroxyquinoline aluminium (Alq_3) deposited by thermal evaporation [10]. The device exhibited a comparatively high external quantum efficiency of 1% and high brightness of above 1000 cd m^{-2} at a driving voltage of less than 10 V, and was considered to be viable for practical use in display applications. Interest in electroluminescent polymer devices was renewed in 1990 by Jeremy Burroughes *et al.* at the Cavendish Laboratory in Cambridge, who reported green electroluminescence from a 100 nm single film of poly(*p*-phenylene vinylene) (PPV), formed after spin-coating of a precursor polymer [11]. The ease of solution processing and simple device structure demonstrated that electroluminescent polymer devices could be developed for large area display applications.

Since then, much research has been undertaken into device architecture, materials design and fabrication techniques. For example, the important development of phosphorescent organometallic dopants facilitates light emission from triplet states such that the internal quantum efficiency of doped devices approaches 100% [12]. The performance, stability and lifetime of organic electroluminescent devices has improved to the extent that they are now finding many commercial uses from display applications to solid state lighting.

1.2 Applications of OLED devices

The interest in OLED technology is driven by the promise of better performance, higher efficiency and simpler manufacturing procedures when compared to competing technologies such as liquid crystal displays (LCD) or inorganic light emitting diodes. For example, OLED displays require no backlight to function, reducing the need for polarisers or colour filters that block a significant portion of emitted light and reducing the drain on battery life of mobile devices. A thin device profile, limited only by the thickness of the substrate and encapsulation increases the suitability for mobile applications further. Devices using OLED technologies also potentially have a better contrast ratio, lower turn-on voltages, full viewing angle, faster response times and a larger range of colours than other display technologies [13, 14].

Roll-up or wearable displays may be possible by using flexible substrates, for example poly(ethylene terephthalate) (PET) [15]. Quick, cheap and easily scalable manufacturing of such devices can also be achieved, by using a procedure based on inkjet printing [16, 17] which would not require high vacuum levels for thin film deposition.

The vast range of materials available through chemical synthesis influences the properties of both device performance and the manufacturing procedure. Specific materials can take advantage of solubility or stability which aids processing and device lifetime, and the mobility of charge carriers or the band gap of the material can be modified to improve efficiency or tune the colour of light emitted.

As a result, in the past decade many commercial devices incorporating OLED displays have been released to the consumer market. They are most commonly found

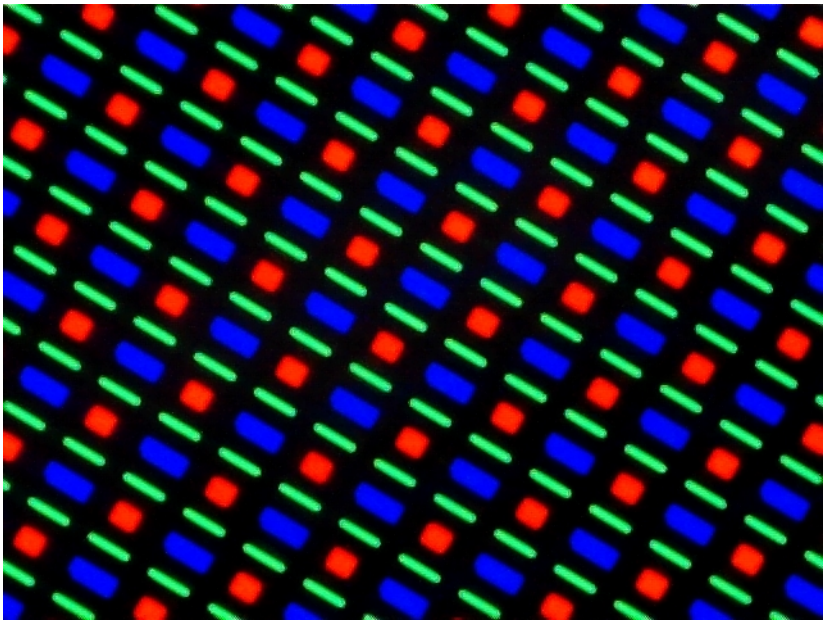

Figure 1.1: Photograph of the Active-Matrix OLED display of a Samsung Galaxy S3 smart phone taken using a Veho VMS-004 USB Microscope at *ca.* 400x magnification showing the PenTile RGBG subpixel matrix. The screen is displaying a plain white background.

in mobile devices with screen sizes of 140 mm (approximately 5.5") or less, ranging from smart phones (for example the Samsung HD Super AMOLED display pictured in Figure 1.1) to cameras, digital media players and mobile gaming consoles. Tablet computers with larger AMOLED displays measuring 20 cm (approximately 8") have also been released.

Ultrathin, large area television screens have been developed by manufacturers and are now widely available in stores, with 55" curved OLED televisions produced by both LG and Samsung on the market. Examples of OLED televisions showcased at recent editions of the Consumer Electronics Show (CES) in Las Vegas are shown in Figure 1.2, including a flexible prototype from LG (left) that can bend from a flat screen to a curved screen. Prototypes of truly flexible phones and displays have also been demonstrated at trade fairs.

Figure 1.2: Left: photograph of a flexible OLED television prototype produced by LG [18] displayed at CES 2014. Right: photograph of a curved OLED television showcased by Samsung at CES 2013 [19].

1.2.1 Organic solid-state lighting

Artificial lighting accounts for approximately 20% of the total electricity consumption in the developed world [20], and in recent years the replacement of traditional incandescent light bulbs with compact fluorescent lamps (CFLs) and inorganic LED lighting has aimed to increase energy efficiency and save money. Incandescent bulbs have power efficiencies of approximately 15 lm W^{-1} and are very inefficient, converting only 5% of the energy supplied into visible light [21, 22]. The vast majority of energy supplied to incandescent bulbs is lost as heat.

Incandescent bulbs have by now largely been replaced by more energy efficient lighting with longer operating lifetimes such as fluorescent tubes, CFLs and inorganic LED solid state lighting. Fluorescent lighting is around 20 - 25% efficient and typically 60 - 100 lm W^{-1}, while white LED lighting can perform better still at approximately 50% efficiency and in excess of 100 lm W^{-1} [22]. White OLEDs with efficient light outcoupling have been demonstrated in laboratory conditions with efficiencies comparable to that of fluorescent tube lighting [23].

The quality of a lighting source is quantified by its Colour Rendering Index (CRI), which measures how natural the colour of a range of standard colour samples appear compared to a defined standard lighting source [24]. Incandescent bulbs have a CRI of 100, while fluorescent lighting contains phosphors exhibiting sharp, narrow peaks in the emission spectrum, leading to poorer quality light sources with a CRI typically around 80. A typical white inorganic LED consisting of a blue LED exciting a yellow phosphor has a CRI of around 75 [24], although higher CRIs of 90 or more can be obtained by using a mixture of phosphors [25].

The colour of light emitted by organic materials is broad and can be easily tuned by control of the chemical structure during synthesis. OLED lighting can mix several of these emitters together resulting in a broad, continuous spectrum and high CRI values above 80 - 90. In addition, the colour of light emitted can be tuned to provide 'cooler' or 'warmer' lighting depending on the market.

OLED lighting has other advantages over current lighting. Fluorescent tubes and CFLs contain small amounts of mercury which is harmful to the environment if disposed of improperly. LED lighting is more suited to point sources, while diffuse large area lighting sources can be realised with organic materials. This has the added advantage of OLED lighting not needing a luminaire, which causes significant losses in light output from fluorescent tube lighting. OLED lighting also creates opportunities for more innovation in lighting design with the possibility of creating ultrathin, transparent and flexible light sources.

Currently there are no widespread commercial OLED lighting products on the market, although demonstration models are available and prototype designs such as those

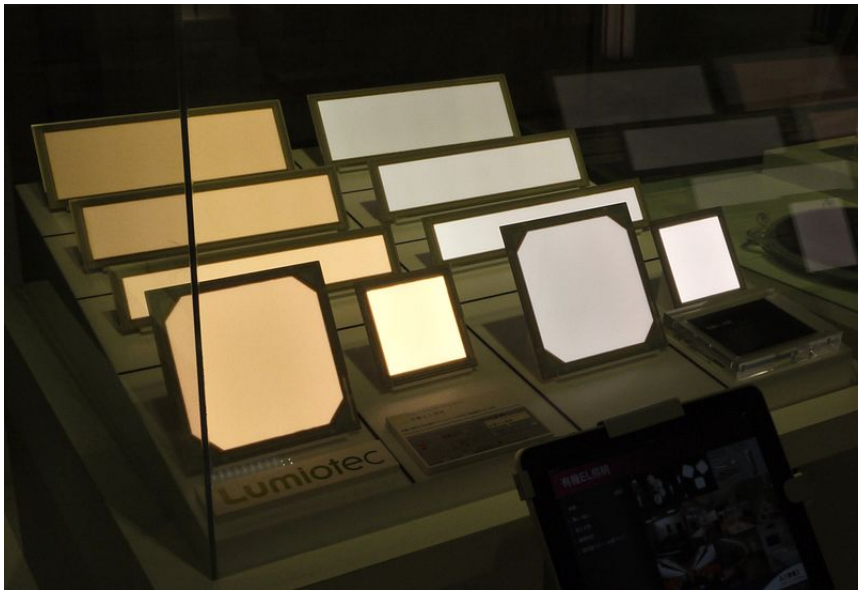

Figure 1.3: Photograph of a selection of OLED lighting demonstration panels produced by Lumiotec [26].

in Figure 1.3 are regularly showcased at industry fairs. For example, both LG and Konica Minolta have recently showcased flexible lighting panels, the latter having a radius of curvature of 10 mm.

1.3 Scope of this thesis

This thesis presents work undertaken in the Organic Electroactive Materials research group in the Department of Physics, University of Durham between 2009 and 2014. In collaboration with researchers in the Department of Chemistry, a range of new materials including electron transport materials, iridium emitters and single white emitting polymers have been characterised and electroluminescent devices containing these materials have been optimised.

The relevant background theory to the field of electroluminescent organic materials is presented in chapter 2, while chapter 3 describes the experimental procedures utilised

during the course of this thesis from the fabrication and characterisation of OLED devices to techniques for photophysical characterisation of thin films and solutions.

Chapters 4 and 5 deal with the optimisation of blue solution-processable OLED devices and the characterisation of new materials including oxadiazole materials for electron transport and both sky blue and deep blue iridium emitters. In chapter 4, device testing of high triplet electron transport materials is presented, followed by the optimisation of simple single layer OLED devices which contain new sky blue emitting iridium(III) complexes where the ligands incorporate large branched aryl ring substituents. Chapter 5 follows on from this work, characterising a range of new sky blue and deep blue iridium(III) emitters with simpler alkyl, mesityl or carbazole substituted ligands, along with further optimisation of the device structure.

Chapter 6 follows on from initial characterisation of a series of iridium(III) complexes investigated as part of the MPhys research project carried out prior to this work [27], where substituent effects are used to achieve colour tuning from green to red and the effect of the transition dipole moment is investigated.

Finally, chapter 7 describes the characterisation and optimisation of single copolymers incorporating fluorene (F) and dibenzothiophene-S,S-dioxide (S) units in multilayer devices for white light emission, with different polymers varying the relative proportions of red, green or blue emitter and determining the effect of the S unit on the colour of emission and the device performance.

The main conclusions of the work are summarised in chapter 8.

References

[1] A. Bernanose, M. Comte & P. Vouaux, *Journal de Chimie Physique et de Physico-Chimie Biologique* **50** (1953), 64 - 68

[2] A. Bernanose & P. Vouaux, *Journal de Chimie Physique et de Physico-Chimie Biologique* **50** (1953), 261 - 263

[3] M. Pope, H. P. Kallmann & P. Magnante, *Journal of Chemical Physics* **38** (1963), 2042 - 2043

[4] W. Helfrich & W. G. Schneider, *Physical Review Letters* **14** (1965), 229 - 231

[5] R. H. Partridge, *Polymer* **24** (1983), 733 - 738

[6] R. H. Partridge, *Polymer* **24** (1983), 739 - 747

[7] R. H. Partridge, *Polymer* **24** (1983), 748 - 754

[8] R. H. Partridge, *Polymer* **24** (1983), 755 - 762

[9] P. S. Vincett, W. A. Barlow, R. A. Hann & G. G. Roberts, *Thin Solid Films* **94** (1982), 171 - 183

[10] C. W. Tang & S. A. Van Slyke, *Applied Physics Letters* **51** (1987), 913 - 915

[11] J. H. Burroughes, D. D. C. Bradley, A. R. Brown, R. N. Marks, K. Mackay, R. H. Friend, P. L. Burns & A. B. Holmes, *Nature* **347** (1990), 539 - 541

[12] M. A. Baldo, D. F. O'Brien, Y. You, A. Shoustikov, S. Sibley, M. E. Thompson & S. R. Forrest, *Nature* **395** (1998), 151 - 154

[13] R. J. Visser, *Philips Journal of Research* **51** (1998), 467 - 477

[14] J. N. Bardsley, *IEEE Journal of Selected Topics in Quantum Electronics* **10** (2004), 3 - 9

[15] G. Gustafsson, Y. Cao, G. M. Treacy, F. Klavetter, N. Colaneri & A. J. Heeger, *Nature* **357** (1992), 477 - 479

[16] T. R. Hebner, C. C. Wu, D. Marcy, M. H. Lu & J. C. Sturm, *Applied Physics Letters* **72** (1998), 519 - 521

[17] J. Bharathan & Y. Yang, *Applied Physics Letters* **72** (1998), 2660 - 2662

[18] Chris F, uploaded to flickr.com/photos/114264438@N03/12518650925/ under the Creative Commmons CC BY 2.0 licence, 14 February 2014

[19] samsungtomorrow, uploaded to flickr.com/photos/samsungtomorrow/8363846374/ under the CC BY-NC-SA 2.0 licence, 9 January 2013

[20] B. W. D'Andrade & S. R. Forrest, *Advanced Materials* **16** (2004), 1585 - 1595

[21] K. T. Kamtekar, A. P. Monkman & M. R. Bryce, *Advanced Materials* **22** (2010), 572 - 582

[22] C. J. Humphreys, *MRS Bulletin* **33** (2008), 459 - 470

[23] S. Reineke, F. Lindner, G. Schwartz, N. Seidler, K. Walzer, B. Lüssem & K. Leo, *Nature* **459** (2009), 234 - 238

[24] Y.-L. Chang & Z.-H. Lu, *Journal of Display Technology* **9** (2013), 459 - 468

[25] S. Pimputkar, J. S. Speck, S. P. DenBaars & S. Nakamura, *Nature Photonics* **3** (2009), 180 - 182

[26] User:STRONGlk7, uploaded to commons.wikimedia.org/wiki/File:OEL_right.JPG under the Creative Commons CC BY-SA 3.0 licence, 7 November 2012

[27] G. C. Griffiths, *Characterisation and Optimisation of Electrophosphorescent OLED Devices*, MPhys thesis, Durham University (2009)

2 Theory

The electronic and photophysical properties of organic molecules are important in understanding the processes involved in the operation of organic light emitting diodes. This chapter introduces the concepts of bonding and conjugation in carbon based molecules, from which the electrical and optical properties of these materials arise. The nature of excited states formed after either optical or electrical excitation and the transitions they may make within the electronic structure of the material are described. Physical processes important to the functioning of electroluminescent devices are discussed including mechanisms for energy transfer between molecules as well as mechanisms for charge injection into active device layers and charge transport within these layers. Finally, processes leading to quenching of the excited state that result in non-radiative decay, and therefore a reduction in device efficiency, are outlined.

2.1 Bonding and conjugation

The basis of organic molecules is carbon, with atoms that can form four covalent bonds with other atoms. Through organic synthesis, a vast range of different molecules with widely varying properties can be realised. As well as small molecules, long polymer chains can be formed through repeated bonding between monomer units. The electronic and optical properties of organic molecules originate in the bonding properties of the carbon backbone, in particular the interaction of multiple atomic orbitals resulting in delocalisation of electron density. In this way, the properties of organic molecules can be optimised through modification of their chemical structure.

2.1.1 Atomic orbitals and hybridisation

Electrons are fermions with half integer spin, whose quantum state is described by a complex wavefunction. The wavefunction depends on four quantum numbers, n, l, m_l and m_s and as a result of the Pauli Exclusion Principle, no two fermions in a system may share the same two quantum numbers. Electrons in atoms therefore progressively fill up atomic orbitals starting from the lowest energy orbitals.

Atomic orbitals are denoted in spectroscopic notation by nl, where the principal quantum number n describes the energy level of the orbital. The angular momentum quantum number l can take values from 0 to $n-1$. Orbitals with $l=0$ are denoted s in spectroscopic notation, and subsequent values of l from $l=1$ are denoted p, d, f and so on. For example, the lowest energy atomic orbitals are the 1s orbitals, followed by the 2s and 2p orbitals. There are three degenerate 2p orbitals corresponding to the three possible values of m_l, which can take integer values from $-l$ to $+l$. Finally, each atomic orbital can accommodate two electrons, as the spin angular momentum m_s takes two values of $1/2$ and $-1/2$ for fermions.

Figure 2.1 shows a representation of the s atomic orbital and three degenerate p

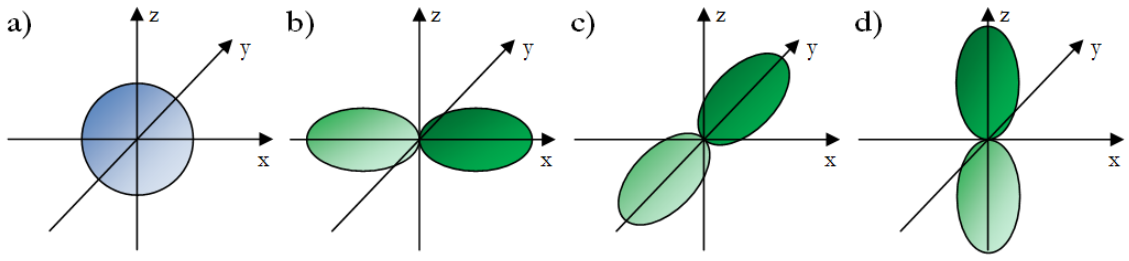

Figure 2.1: Schematic of s and p atomic orbitals, where the atom is located at the origin of the coordinate system. The s orbital is shown in a), while the degenerate p_x, p_y and p_z orbitals are represented in b), c) and d) respectively.

atomic orbitals, oriented along the x, y and z axes of a Cartesian coordinate system with the atom located at the origin.

A carbon atom has six electrons and the corresponding electronic configuration of the atom is therefore $1s^2 2s^2 2p^2$. There is one 1s and one 2s orbital, as well as three 2p orbitals (with two occupied by a single electron) oriented perpendicular to each other in directions that can be labelled as x, y and z. Depending on the arrangement of bonding between a carbon atom and the surrounding atoms, there may be mixing, or hybridisation, between the 2s atomic orbital and the 2p orbitals on the carbon atom to form a number of hybridised atomic orbitals [1].

For example in methane (CH_4), which consists of one carbon atom covalently bonded to four hydrogen atoms, the 2s orbital on the carbon atom mixes with all three 2p orbitals to form four sp^3 hybrid orbitals which have equal energy and are equally spaced around the molecule. These hybrid orbitals, each occupied by one electron, are what form the sigma (σ) bonds with the hydrogen atoms. The bonds are all of the same length and strength, and the molecule exhibits a tetrahedral shape with bonds separated by an angle of 109.5° as shown in Figure 2.2 a).

Ethene (C_2H_4), also known as ethylene, is the simplest example of sp^2 hybridisation in carbon atoms. The bonding of ethene is shown in Figure 2.2 b). In this case, the 2s orbital on the carbon atom mixes with two of the 2p orbitals, forming three sp^2 hybrid orbitals and leaving the remaining p orbital intact. The sp^2 hybrid orbitals are oriented in a plane with an angle of 120° between them and form single σ bonds by overlap with orbitals on other atoms. The remaining p orbital has electron density above and below this plane, and can overlap with a corresponding out of plane p orbital on a

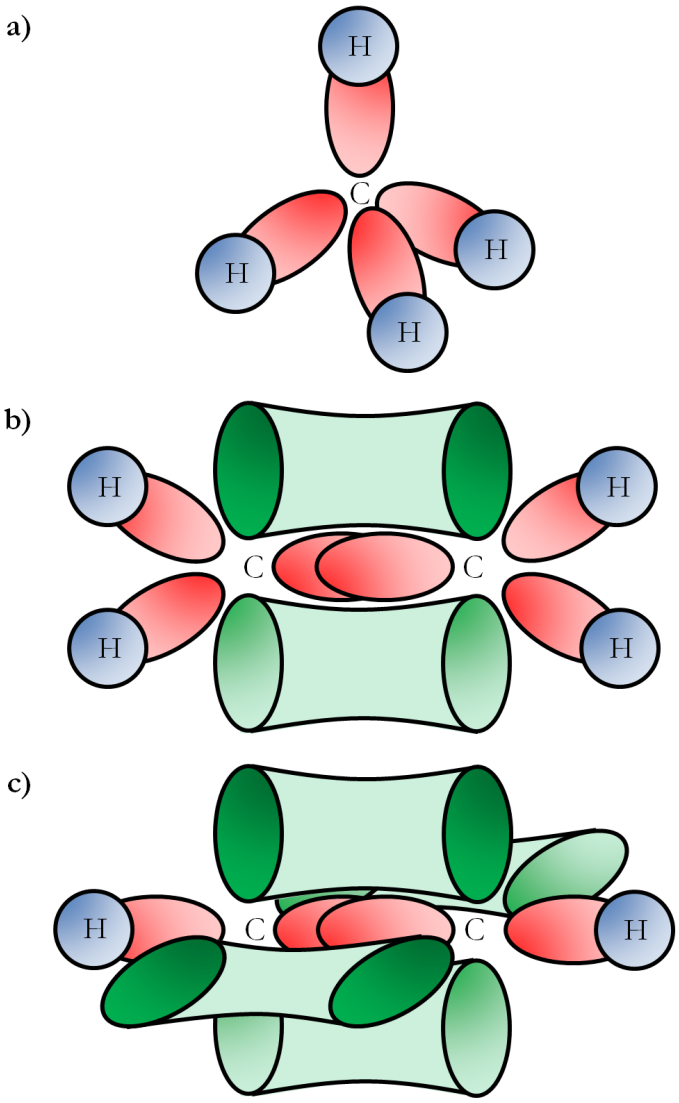

Figure 2.2: A simplified diagram of the atomic and molecular orbitals involved in bonding for a) methane, b) ethene and c) ethyne. Hybridised orbitals are shown in red, while p orbitals are shown in green. For methane, four sp^3 orbitals are formed in a tetrahedral configuration. In ethene, sp^2 hybrid orbitals in a trigonal planar arrangement form σ bonds with other atoms while the p orbitals form a π bond between carbon atoms with electron density above and below the plane. In ethyne, the sp hybrid orbitals are arranged linearly. Two π bonds between the carbon atoms are formed by overlap of p orbitals, which complete the carbon-carbon triple bond.

neighbouring carbon atom to form a pi (π) bond. The combination of one σ bond and one π bond forms a double bond between the carbon atoms.

Additionally, in systems such as ethyne (C_2H_2) (also known as acetylene), atomic orbitals are sp hybridised. In this case, shown in Figure 2.2 c), the carbon 2s orbital hybridises with just one 2p orbital to form two sp hybrid orbitals in a linear configuration, which form σ bonds with other atoms. The remaining 2p orbitals are unaffected and form two π bonds, completing the triple carbon-carbon bond.

2.1.2 Conjugation

When two atomic orbitals overlap to form a bond between atoms, two molecular orbitals are formed [1]. The example of two s orbitals forming a σ bond is shown in figure 2.3. The overlap of the s orbitals forms both a σ orbital, through in-phase addition of the individual atomic orbitals, and a higher energy σ^* anti-bonding orbital formed through out-of-phase addition of the atomic orbitals. This contains a nodal plane where there is no electron density between atoms.

Similarly, bonding π orbitals and anti-bonding π^* orbitals are formed from the overlap of p orbitals. Conjugation, or the interaction of adjacent p atomic orbitals resulting in the delocalisation of electrons across part of the molecule, is the basis of electrical conduction in organic molecules. The structure of organic materials synthesised for use in OLEDs is usually conjugated over part of the molecule, for example along a number of monomer units of a polymer or a ligand in an organometallic dopant.

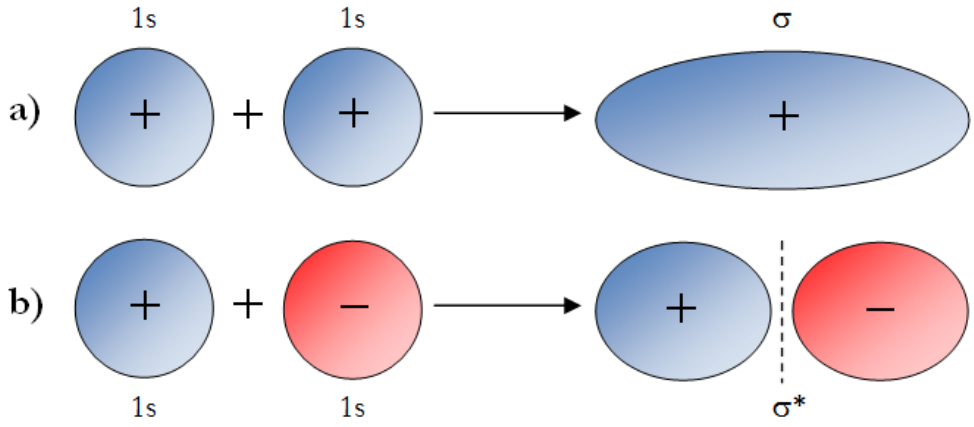

Figure 2.3: Representation of the formation of bonding and antibonding σ and σ^* molecular orbitals by the overlap of s orbitals. In phase addition (a) results in formation of a bonding σ molecular orbital, while out of phase addition (b) results in formation of a higher energy σ^* antibonding molecular orbital.

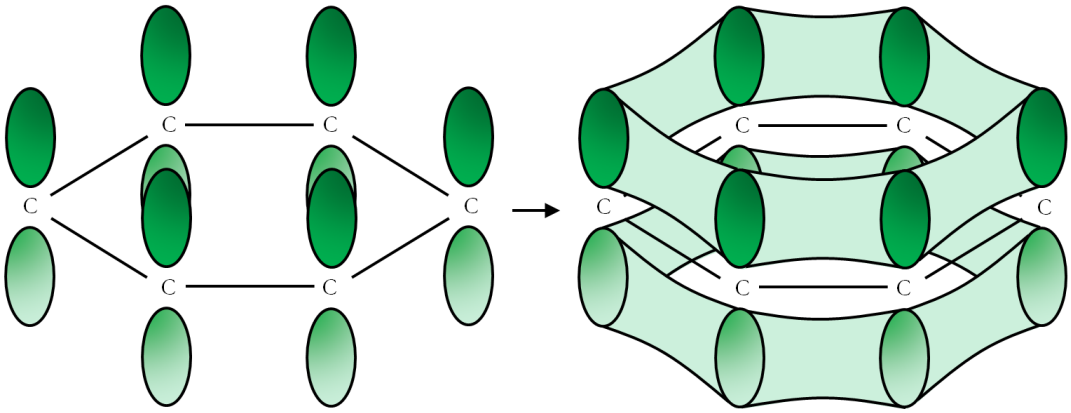

Figure 2.4: Representation of the formation of delocalised π molecular orbitals in a benzene ring, an example of a conjugated system. Bonds to hydrogen atoms are not shown, while σ bonds between carbon atoms are represented as a straight line. Conjugation leads to overlap of the six out of plane p orbitals (left) to form regions of delocalised electron density above and below the plane of the molecule (right).

The form of bonding that describes the carbon backbone in conjugated systems is sp^2 hybridisation. Conjugation is most commonly achieved by alternating single and double carbon-carbon bonds in a chain of carbon atoms, but other atoms with available p orbitals such as nitrogen or oxygen can contribute to conjugation as well.

Figure 2.4 shows benzene (C_6H_6), an example of a conjugated system. Overlap of sp^2 hybrid orbitals forms the σ bonds between carbon atoms in the benzene ring, while the neighbouring out of plane p orbitals overlap and form a region of delocalised electron density above and below the plane of the molecule. Due to the continuous overlap of p orbitals around the ring, all of the carbon-carbon bonds exhibit equal bond lengths of 139.5 pm, which is between those expected for single (154.1 pm) or double (133.7 pm) bonds [1].

In a polymer, conjugation may be broken by defects in the polymer structure or twisting of the polymer backbone that disrupt the overlap of adjacent p orbitals. A long polymer chain will consist of several distinct areas of conjugation, each acting

as a chromophore, instead of being conjugated over the entire molecule. The average conjugation length due to defects varies from polymer to polymer, for example the average conjugation length of poly(p-phenylene vinylene) (PPV) is approximately six to eight monomer units, [2, 3] and a Gaussian distribution of conjugation lengths in a polymer sample is often assumed [4].

Two important molecular orbitals formed by this series of overlaps between p orbitals are the Highest Occupied Molecular Orbital (HOMO) and the Lowest Unoccupied Molecular Orbital (LUMO), often termed the frontier orbitals. In a simplified analogy with inorganic semiconductors, the HOMO is comparable to the valence band and the LUMO is comparable to the conduction band, although in reality localised states and distortions of the molecular structure caused by the presence of free charges complicate organic systems further.

An electron from the HOMO may be excited to the LUMO, while the absence of an electron in the HOMO can also be treated as a mobile charge carrier, in this case as positively charged holes. Excitations can also be introduced electrically via injection of charges into the HOMO or LUMO from electrodes.

The gap in energy between HOMO and LUMO characterises the energy (and therefore the wavelength) of light emitted by a molecule, although in reality molecular vibrations and structural relaxations result in a broad emission profile as opposed to the transition occurring at one single energy. Modification of the chemical structure by a wide variety of chemical synthesis and substitution methods can alter the energy levels of an organic molecule. The colour of light emitted can therefore be tuned, and other desirable properties such as carrier mobility or solubility may be altered as well.

2.2 Excited states

Excited states can be formed in organic materials by photoexcitation (such as absorption of a photon) or by electrical excitation due to the attraction of free charge carriers injected on application of an electric field. This section describes some of the different types of excited state that can be formed as well as how the spin state of the excitation can affect the probability of a radiative transition and place limitations on the efficiency of electroluminescent devices.

2.2.1 Excitons and excited states

The exciton is a bound quasi-particle consisting of an electron in the LUMO and hole in the HOMO coupled by their Coulomb interaction. In materials with a low dielectric constant where there is little electric field screening, such as organic semiconductors, the exciton may be tightly bound. Excitons of this type are called molecular or Frenkel excitons. The excited state is localised to a single chromophore, with a small separation between the electron and hole of the order of 0.5 nm [3].

In contrast, in materials with higher dielectric constants such as inorganic semiconductors, the electric field screening reduces the Coulomb interaction between electron and hole, and the exciton becomes more weakly bound. These are called Wannier-Mott excitons and have lower binding energies than Frenkel excitons, with the radius of separation being of the order of 4 - 10 nm [3].

Excitons formed in organic materials are commonly either molecular Frenkel excitons or charge transfer excitons. Charge transfer excitons are intermediate in separation between Frenkel and Wannier-Mott excitons, with the electron and hole located

on orbitals on spatially separate parts of the molecule or two neighbouring molecules. Experiments to determine the exciton binding energy in organic semiconductors result in a binding energy of the order of 0.5 - 1 eV [5].

Bimolecular excited states can be formed due to an interaction between one molecule in its excited state and a second molecule in the ground state forming an excited state complex. If both molecules are chemically the same, the state is referred to as an excimer. When the two molecules are chemically different the term exciplex is used [6, 7]. These species only exist in the excited state, while the ground state is dissociative. Exciplexes may have charge transfer character if donor and acceptor type molecules are involved. Excimers and exciplexes can be formed by photoexcitation and may as a result be observable in photoluminescence spectra.

Electromers [8, 9] and electroplexes [10, 11] may be formed under electrical excitation, so can be observed in electroluminescence spectra but not in photoluminescence spectra. In these cases there is greater charge separation in the excited state, with one charge carrier located on a donor molecule and the other charge carrier situated on a second molecule.

In the same manner as excimers and exciplexes, electromer refers to the case where both molecules are the same whereas electroplex refers to the case where both molecules are different. These excited states are often at a lower energy due to the greater charge separation than the molecular exciton, so the resultant emission is observed at a longer wavelength.

Finally, polymers can aggregate with interactions between chains, causing the ground state wavefunction to be delocalised over more than one molecule or poly-

mer chain as well as the excited state. These are known as aggregate states [12] and are similar to dimer states. Aggregate states may be identifiable in absorption spectra, distinguishing them from excimer states.

2.2.2 Polarons

The presence of extra charges on the backbone of a polymer or molecule leads to distortion of the molecular structure caused by strong coupling of electrons and phonons, as well as a field of polarisation surrounding the charge [13]. The charge and its associated lattice distortions can be considered to be a quasi-particle called a polaron.

Polarons can be formed by both free electrons and free holes, and geminate polaron pairs can be formed by correlated electron and hole polarons. Additionally, bipolarons can be formed by two like charges coupled by molecular distortions [13].

Distortion of the molecular structure affects the energy levels of the molecule, and therefore polaron states may occupy different energy levels situated between the HOMO or LUMO levels of a material. Polarons can be generated in devices directly through charge injection at an electrode under an applied bias or by introduction of charged chemical dopants.

They may also be generated from optically excited excitons on application of an electric field or excitation sufficient to dissociate the exciton into its free charges. Transitions involving polaron states can often be observed in optical spectra of the material in question.

2.2.3 Singlet and triplet states

When an excited state is formed in an organic material by charge recombination, it can be either singlet or triplet in nature, where the terms refer to the spin multiplicities of the excited states. There are four different ways in which the spins of two spin-half fermions can be combined. Three of these have a total spin of 1, hence the term triplet state, while the fourth has a total spin of 0, hence the term singlet state.

A particle with half integer spin may be either in the spin-up or spin-down state, which can be represented as $|\uparrow\rangle$ and $|\downarrow\rangle$ respectively. When two of these particles combine, there are two possible states describing the two particle system for when the two spins are aligned in the same direction, namely $|\uparrow\uparrow\rangle$ and $|\downarrow\downarrow\rangle$. In addition to these two states, there are two possible states to account for when the two spins are aligned in opposite directions. These are $\frac{1}{\sqrt{2}}(|\uparrow\downarrow\rangle + |\downarrow\uparrow\rangle)$ for when the spins are precessing in phase, and $\frac{1}{\sqrt{2}}(|\uparrow\downarrow\rangle - |\downarrow\uparrow\rangle)$ for when the spins are precessing out of phase.

When the total spin of each of these states is determined, it is found that the $|\uparrow\uparrow\rangle$, $|\downarrow\downarrow\rangle$ and $\frac{1}{\sqrt{2}}(|\uparrow\downarrow\rangle + |\downarrow\uparrow\rangle)$ states have a total spin of 1. As there are three such states, they are called triplet states. The remaining state of $\frac{1}{\sqrt{2}}(|\uparrow\downarrow\rangle - |\downarrow\uparrow\rangle)$ has a total spin of 0 and is therefore a singlet state.

In the case of charge recombination, there is statistically an equal chance of forming each of these states when an excited state is formed, so it is expected that triplets and singlets are formed in a 3:1 ratio. However only the singlet state undergoes radiative decay readily, as the decay from a triplet state is spin forbidden, being a transition from a state with a total spin of one to the ground state which has a total spin of

zero. It would therefore be expected that 75% of the excited states formed within the organic layer are triplets and are wasted, not producing useful light emission.

Phosphorescence (described further in section 2.3.4) refers to emission observed from triplet states. By using phosphorescent dopants, as will be explained later in section 2.4.3, the triplet excited states can be utilised more efficiently with internal quantum efficiencies of such devices approaching 100%. Other processes such as triplet-triplet fusion (section 2.7.1) can result in formation of singlet states and delayed fluorescence [14]. Thermally activated delayed fluorescence (TADF), due to the thermally activated up-conversion from triplet state to singlet state, is also a promising method of achieving 100% triplet harvesting [15].

2.3 Photophysical transitions

A number of photophysical transitions and processes, both radiative and non-radiative, may occur between the different states in an organic system. This section provides a brief overview of the most important transitions, which may be summarised on a Jablonski diagram [3,16]. A simple example of a Jablonski diagram is shown in Figure 2.5, where solid horizontal lines denote the electronic states of the system.

2.3.1 Selection rules

The transition from triplet to singlet states described in the previous section is forbidden. The selection rules governing which transitions are allowed or forbidden arise from Fermi's Golden Rule [17]

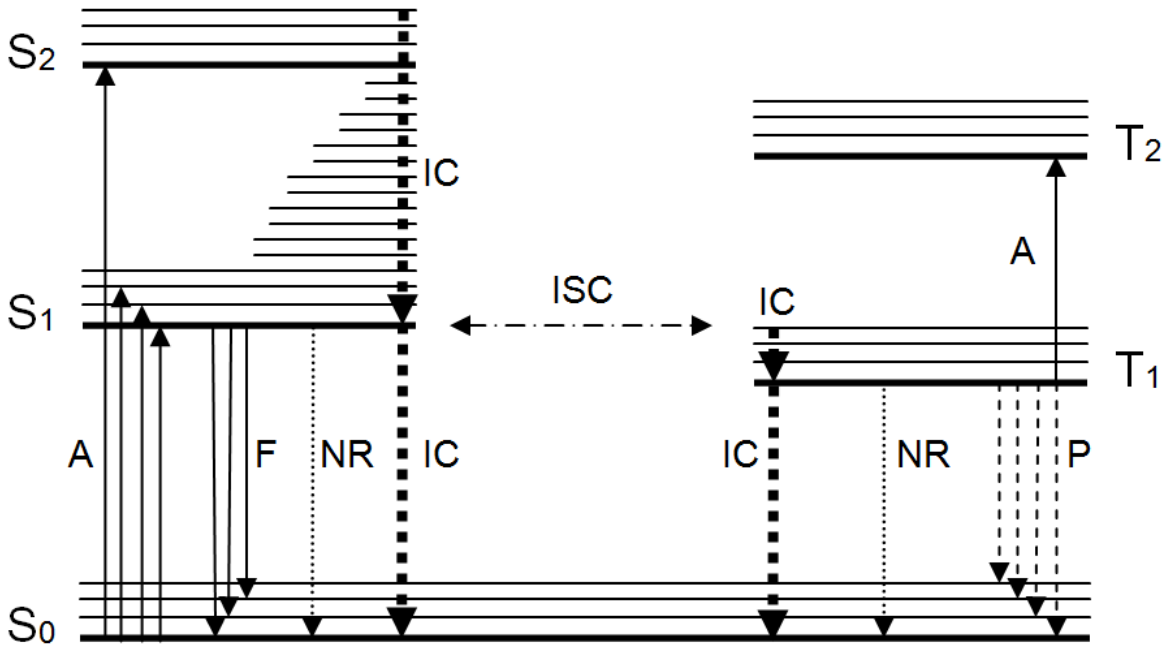

Figure 2.5: A typical Jablonski diagram showing the photophysical processes that may occur in organic molecules. S and T denote Singlet and Triplet states respectively, while 0, 1 and 2 represent ground state, first excited state and second excited state. Processes labelled are: A - Absorption, F - Fluorescence, P - Phosphorescence, ISC - inter-system crossing, IC - internal conversion and NR - other non-radiative decay processes. Heavy horizontal lines represent the energy levels while the lighter horizontal lines denote vibrational modes.

$$W_{i\to f} = \left(\frac{2\pi}{\hbar}\right) |\langle f| H' |i\rangle|^2 \rho \tag{2.1}$$

which describes the rate of transition $W_{i\to f}$ between two different energy states $|i\rangle$ and $|f\rangle$. In the above equation ρ is the density of states, and H' is a Hamiltonian operator that acts as a perturbation on the system. In the case of an optical transition such as absorption this perturbation can be described by $e\mathbf{E}.\mathbf{r}$, the transition dipole moment operator. Considering the quantum mechanical properties of the two states $|i\rangle$ and $|f\rangle$ leads to a number of conditions, or selection rules, affecting the probability of a transition between the two states.

Spin: The matrix element $\langle f| H' |i\rangle$ is non-zero when both states have the same total spin, and hence in this case the transition is allowed. Transitions between states of different spin (such as singlet and triplet states) are consequently forbidden.

Angular momentum: In a transition where, for example, a photon is emitted or absorbed, the angular momentum of the electronic state must change correspondingly to ensure that the total angular momentum of the system is conserved.

Parity: Orbitals which have the same phase after an inversion operation are described as having even parity (or g, gerade) while those which change phase are described as uneven (or u, ungerade). The matrix element is zero for transitions involving electronic states with orbitals of the same parity. Therefore $g \rightarrow u$ and $u \rightarrow g$ transitions are allowed, while $g \rightarrow g$ and $u \rightarrow u$ are forbidden.

Symmetry: The symmetry types of the electronic states and of the transition dipole moment according to symmetry group theory determine whether the matrix element of the transition is zero. In general, if the direct product of the integrand of the matrix element contains the totally symmetric representation of the point group of the molecule, then the matrix element is non-zero and the transition is allowed [18].

These selection rules determine whether a transition is forbidden and allowed, and hence explain why, for example, emission from the transition between triplet and singlet states is not readily observed for non-phosphorescent materials.

2.3.2 Absorption

A photon of sufficient energy has a probability to excite an electron from the ground state to a vibrational level of an excited singlet state. The energy of the photon

absorbed will depend on the energy gap between ground and excited states. Electrons excited into the higher vibrational modes can then relax into the lowest vibrational mode of that excited state by internal conversion, which is a non-radiative process where the energy lost in relaxation is transferred, for example, to phonons.

A beam of light passed through a sample of material will decrease in intensity according to the Beer-Lambert law [19], equation 2.2, which relates the intensity I to the distance passed through the sample l, its concentration c and the molar absorption coefficient of the material ϵ. The initial intensity of the beam incident on the sample is denoted by I_0.

$$I = I_0 \cdot 10^{-\epsilon c l} \tag{2.2}$$

This is often rearranged to form the expression for the absorbance or optical density of a material A as shown in equation 2.3, which is the quantity commonly obtained in measurements of absorption spectra.

$$A = -\log_{10} \frac{I}{I_0} = \epsilon c l \tag{2.3}$$

While absorption from ground state to a triplet excited state is not possible due to the change in spin involved, triplet-triplet absorption may occur which involves the excitation of an electron from a triplet excited state to a higher energy triplet state.

2.3.3 Fluorescence

Fluorescence occurs when an electron in the lowest vibrational mode of the first excited singlet state decays radiatively with the emission of a photon whose energy depends

on the energy difference between excited and ground states. The transition is allowed according to quantum mechanical selection rules and thus occurs promptly on a short timescale of the order of picoseconds to nanoseconds [3]. The decay may be to one of the vibrational modes of the ground state, resulting in the vibrational broadening of the fluorescence spectrum. As some energy has been dissipated by relaxation and production of vibrations, the emission occurs at a lower energy and higher wavelength than the original absorption spectrum.

The difference between the absorption peak and the emission peak is known as the Stokes shift, and is a measure of the degree to which the structure of the molecule relaxes upon decay of the excited state. A small Stokes shift indicates a rigid molecule whose structure undergoes small distortions when excited, while a large shift indicates a major change in the configuration of the molecular structure in order to minimise the energy of the excited state, though this may be complicated by exciton migration.

Non-radiative decay routes to the ground state are also possible. These include internal conversion, where the excitation energy is lost to vibrations of the molecular bonds, as well as quenching caused by energy transfer to defects and dopants among other processes.

2.3.4 Phosphorescence

Phosphorescence refers to emission of light from the transition between the triplet excited state and singlet ground state. Due to the spin-forbidden nature of singlet-triplet transitions as described in section 2.2.3, triplet states have a long lifetime compared to the singlet state, needing for example interactions with phonons or spin orbit coupling

to conserve spin. The lifetime of singlet states is of the order of nanoseconds or less, while for triplet states the lifetime can range from the order of milliseconds to seconds for some polymer systems [20]. As a result, phosphorescence is not easily observed in photoluminescence spectra.

Triplet states may not be formed directly by absorption of a photon, but excited states may undergo a non-radiative transition from a singlet state to a degenerate triplet state in a process called inter-system crossing. The probability of both inter-system crossing and radiative emission from a triplet excited state is increased where there is strong spin-orbit coupling. This interaction between an electron's spin and orbital angular momentum results in the mixing of singlet and triplet character of excited states, facilitating transitions between the singlet and triplet manifold. The spin-orbit interaction is stronger in systems which contain heavier atoms and is exploited in electroluminescent devices by the use of phosphorescent dopants with lifetimes of the order of microseconds [20], as described in section 2.4.3.

In order to observe phosphorescence in photoluminescence spectra, samples must usually be cooled to low temperatures which minimises the probability that the triplet excited state migrates to a site where it may be quenched during its long lifetime. Ensuring that the sample is free of oxygen is also necessary, such as degassing of solutions or effective encapsulation of films. Room temperature phosphorescence may be observed if the material is sufficiently isolated. The first excited triplet state is lower in energy than the singlet in most organic materials, so the phosphorescence emission spectrum will be seen at a longer wavelength than the fluorescence.

2.4 Electroluminescent devices and phosphorescent dopants

There are a wide range of possible device architectures and materials that can be used in the fabrication of organic electroluminescent devices. This section describes the basic structure and operation of organic electroluminescent devices, as well as commonly used materials including those for electrodes and substrate, and the factors involved in their selection. Phosphorescent dopants are a widely used method of utilising the triplet state and their properties and use in electrophosphorescent devices are outlined.

2.4.1 Device structure and materials

The basic structure of an OLED device consists of an organic emissive layer situated between an anode and a cathode. When an electric field is applied to a luminescent organic material, electrons will be injected into the LUMO at the cathode and holes are injected into the HOMO at the anode. These charge carriers will move away from the electrodes into the bulk of the material due to the applied electric field. Carrier transport and injection will be discussed further in section 2.6. Recombination of the charge carriers occurs, resulting in the formation of excitons or other excited states. These can decay radiatively with the emission of a photon whose energy is dependent on the energy gap between excited state and ground state.

Spin coating and thermal evaporation are the two most widely used methods of depositing thin films of organic materials. Thermal evaporation is usually used for deposition of small molecules, as well as deposition of cathode materials. Complex multilayered device architectures can be realised through sequential deposition of different materials. Each layer can be functionalised for a particular purpose, with materials

chosen for carrier blocking and transport properties in addition to those chosen for their emission characteristics. Evaporated devices can therefore be optimised for effective transport and confinement of charges resulting in high efficiency devices. However high molecular weight molecules and polymers tend to decompose when heated and as a result are not suitable for deposition by thermal evaporation.

Spin coating is more commonly used for deposition of polymer films due to the ease of solution processing and the ability to produce large area films, although small molecules often form films with poor morphology on spin coating [21]. Formation of multilayer structures is difficult as application of a new layer tends to dissolve the previous layer. As a result, a single layer consisting of a blend of host and dopant materials is often used. Simple multilayer solution processable devices have been realised by use of orthogonal solvents [22] or varying solubility of different molecular weight materials [23].

Most electrophosphorescent devices fabricated in the course of this study use poly(n-vinyl carbazole) (PVK) as a host polymer. PVK has been shown to be a good host for triplet emitters, although it has been shown that the presence of triplet trap species may limit its suitability as a host for blue emitters [24]. As PVK has poor electron transporting properties, adding electron transporting materials such as 1,3,5-tris(1-phenyl-1H-benzimidazol-2-yl)benzene (TPBI) [25] as an electron injection layer, or 1,3-bis[(4-tert-butylphenyl)-1,3,4-oxadiazolyl]phenylene (PBD) or 1,3-bis(5-(4-tert-butylphenyl)-1,3,4-oxadiazol-2-yl)benzene (OXD-7) as dopants to the polymer layer [26] dramatically improves device efficiency. The chemical structures of these materials are shown in Figure 2.6.

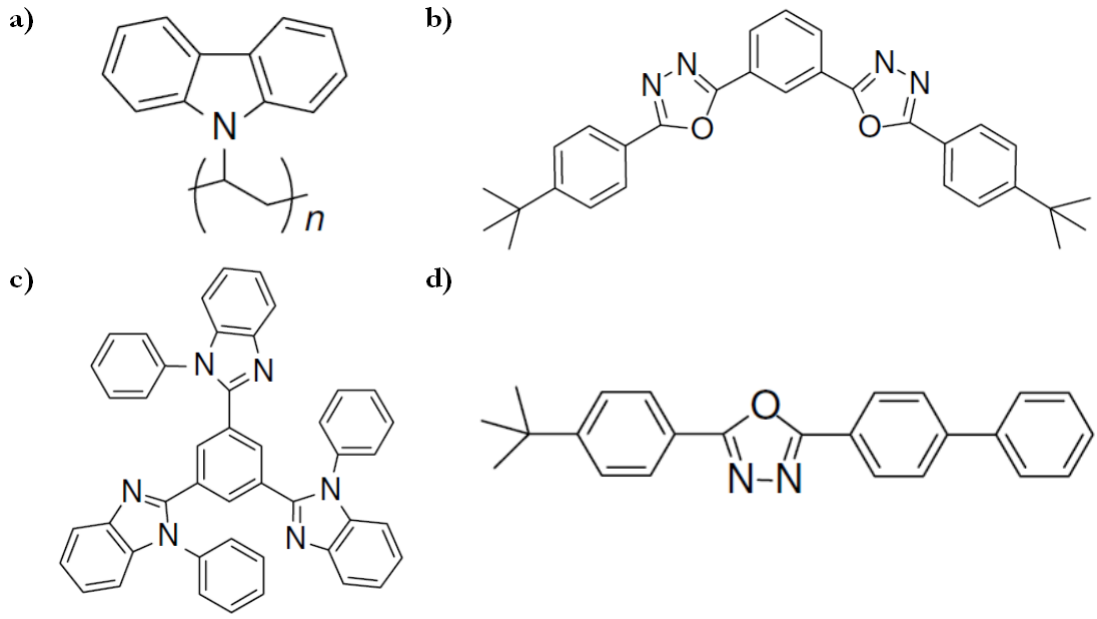

Figure 2.6: Chemical structures of a) PVK, the host polymer used in most devices in this work; as well as b) OXD-7, c) TPBI and d) PBD, which are widely used as electron transport materials [27].

The choice of materials used for electrodes depends on the device architecture as well as the energy levels of the organic materials used. The anode, in addition to being transparent to allow the passage of light, has to have a high work function to closely match the HOMO of the organic layer and aid the injection of holes. The cathode must have a low work function to match the LUMO of the organic layer and aid the injection of electrons.

Indium tin oxide (ITO) is commonly used as the transparent anode, due to its high transmittance of light in the visible spectrum and low resistivity. However, the surface of ITO films can be rough leading to inhomogeneities in organic layers and in current flow. Additionally, ITO films are brittle leading to poor mechanical stability of flexible OLED devices, and sources of indium are becoming increasingly expensive. Therefore, alternative anode materials are being developed. These include, among

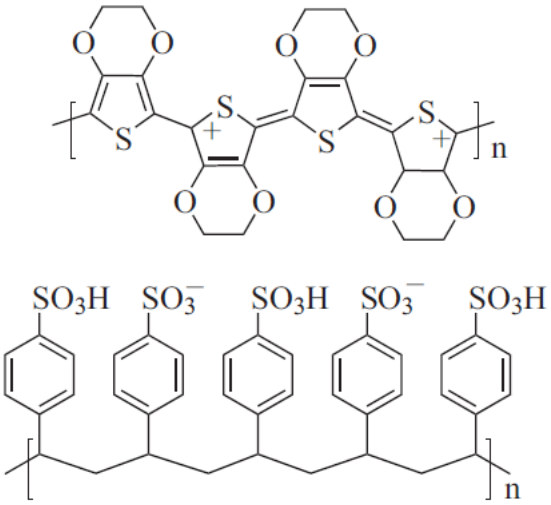

Figure 2.7: The chemical structures of poly(3,4-ethylenedioxythiophene) (PEDOT, top) and poly(styrenesulphonate) (PSS, bottom). PEDOT:PSS is commonly used as a hole injection layer [28].

other proposals, transparent conductive oxides such as aluminium doped zinc oxide or fluorine doped tin oxide, metal nanowires, carbon nanotubes and graphene [29, 30].

A layer of poly(3,4-ethylenedioxythiophene) and poly(styrenesulphonate) (or PEDOT:PSS) is commonly used as a solution processable hole injection layer in OLEDs. The structure of PEDOT:PSS is shown in Figure 2.7. The HOMO energy level of this material (between 4.9 to 5.2 eV [31, 32]) lies between that of the polymer (5.9 eV for PVK [32]) and the work function of ITO (4.5 - 4.75 eV, [33]), reducing the potential barrier for hole injection and improving the hole injection efficiency of the anode.

Low work function metals such as calcium and barium are often used for the cathode. These materials oxidise easily on exposure to air and therefore a capping layer of aluminium is often used in addition to encapsulation of the device to avoid degradation. Other materials that are often used as part of the cathode include thin layers (*ca.* 1 nm) of lithium fluoride or caesium fluoride.

2.4.2 Device microcavity effects

In a standard OLED device, the presence of a reflective metallic cathode adjacent to the organic layer can cause microcavity effects that affect the outcoupling of light from the device.

The effective wavelength of light within a medium is reduced by a factor of n, the refractive index of the medium. For example, PVK has a refractive index of 1.67, while that of ITO is 1.8 - 2.0 and the substrate around 1.51 - 1.85, depending on the type of glass used [34]. Considering the profile of the electromagnetic wave in the device, if the emitter is a sufficient distance from the metal cathode that a node of the emitted wave occurs at the organic-metal interface, there may be internal reflection of the wave at that interface.

The light emitted within the device may therefore be coupled into different modes, with some radiation being trapped and waveguided through the substrate or organic layers, or along the interface between the organic layer and metal cathode, as well as being outcoupled as useful light emission.

The internally reflected waveguided light can cause interference within the device layers, distorting the outcoupled emission spectrum of the device as the distance between the emitter and the reflective electrode changes. This effect can also lead to a shift in the colour and intensity of the emission spectrum as a function of the viewing angle [35].

The relative proportion of light coupled into each mode also depends on the distance between the emitter and the metal cathode. This results in maximum and minimum

values of the fraction of outcoupled light, and consequently the external quantum efficiency, as a function of the distance between the emitter and the reflective electrode [36].

Varying the thickness of non-emissive layers such as charge transport layers can be used as a strategy to alter the distance between the emitter and the reflective electrode. Modelling software can be used to predict how factors such as layer thicknesses affect both the electroluminescence spectra and the outcoupling efficiency of OLED devices [23, 35, 36].

2.4.3 Phosphorescent dopants

In order to overcome the 25% limit on internal quantum efficiency that the ratio of singlet to triplet states suggests, phosphorescent dopants can be added to the organic layer to utilise decay from both singlet and triplet states.

These are commonly organometallic complexes, consisting of a heavy metal atom surrounded by organic ligands. The platinum complex platinum octaethyl porphyrin (PtOEP) was one of the first phosphorescent materials investigated, having been doped into both an Alq_3 host [37] and a polymer host [38]. A wide range of organometallic complexes of heavy metals such as ruthenium, platinum, osmium and europium have been investigated, and iridium complexes have received the focus of much research in recent years [20].

There is strong spin-orbit coupling in these complexes due to the presence of the heavy metal atom. This interaction facilitates inter-system crossing between the singlet and triplet states, resulting in the formation of excited states that possess mixed singlet

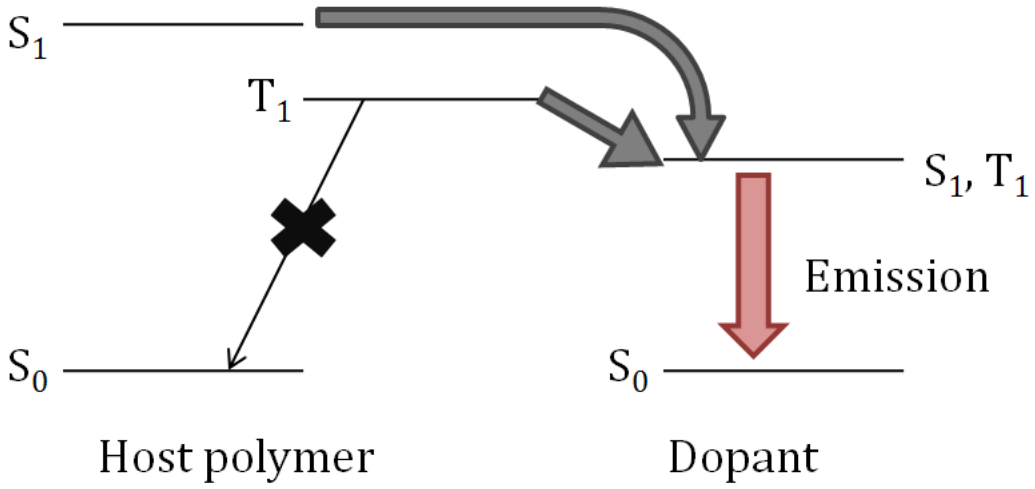

Figure 2.8: A representation of the energy levels of a phosphorescent material doped into a host polymer. Decay from the triplet level of the polymer is spin forbidden but excited states transfer to the dopant molecule, where due to strong inter-system crossing, singlet and triplet character is mixed.

and triplet character. As a result the triplet lifetime of the material is greatly reduced to the order of microseconds [39, 40].

As a result, phosphorescence is readily observable from these materials. When singlet and triplet excitons are formed in the host, transfer of both types of excited state to the phosphorescent dopant may occur and, in theory, all excitons formed will decay radiatively leading to internal quantum efficiencies approaching 100%. This 'harvesting' of both singlet and triplet excited states by a phosphorescent dopant is shown in Figure 2.8. Alternatively, the iridium dopant may act as a charge trap with exciton formation on the dopant molecule as opposed to energy transfer from the host.

As well as excited state formation by transitions from organic π to π^* orbitals, excited states in organometallic complexes can also be formed by transfer of a charge carrier between the heavy metal atom and the ligand. These result in metal to ligand

charge transfer states (MLCT) and ligand to metal charge transfer states (LMCT). Strong MLCT states may enhance the effect of spin-orbit coupling, improving inter-system crossing and the mixing of singlet and triplet character in the complex, hence improving the efficiency of emission. In particular, relativistic effects in heavier 5d metals such as iridium stabilise the MLCT states, thus increasing the effect that spin-orbit coupling has on mixing the singlet and triplet state [41].

The majority of excitons will be formed on the host molecule and then transferred to the dopant as indicated by the grey arrows in Figure 2.8. Mechanisms of energy transfer between organic molecules are discussed in the next section.

2.5 Energy transfer mechanisms in organic molecules

The transfer of energy between molecules is important in understanding the migration and transfer of excited states between host and dopant molecules within an organic film. One simple example of this process is self absorption, where an emitted photon can be re-absorbed forming another excited state if there is sufficient overlap between the absorption and emission spectra of the molecule.

Two other prominent mechanisms by which energy transfer can occur are Förster Resonant Energy Transfer (FRET) and Dexter electron transfer. Both of these phenomena are radiationless but have different physical origins and operate over different length scales, thus for some situations Förster transfer will dominate and for others the primary process will be Dexter transfer.

2.5.1 Förster resonant energy transfer

Förster Resonant Energy Transfer (FRET) is one method of radiationless energy transfer from a donor to an acceptor molecule, the theory of which was first described by Theodor Förster [42]. The mechanism of the interaction depends on resonance between the electric fields originating from the transition dipole moments of the donor and acceptor, leading to the transfer of energy and therefore the excited state to the acceptor. The donor and acceptor molecules must be in close proximity, with a separation typically of the order of ten nanometres or less [27].

At a separation distance r between a donor in an excited state and an acceptor in the ground state, the rate of Förster energy transfer k_T is given by equation 2.4 [42], where τ_D is the donor fluorescence lifetime and R_0 is the Förster radius.

$$k_T = \frac{1}{\tau_D}\left(\frac{R_0}{r}\right)^6 \tag{2.4}$$

The Förster radius is defined as the separation between donor and acceptor at which the efficiency of the process is 50%, i.e. half the energy from the donor is transferred to the acceptor by the Förster transfer process. Expressing the rate of Förster transfer k_T as a fraction of the total decay rate $\tau_D^{-1} + k_T$ of the donor (the sum of the donor fluorescence decay rate and the rate of non-radiative Förster transfer) gives the efficiency of Förster transfer as shown in equation 2.5.

$$E = \frac{k_T}{\tau_D^{-1} + k_T} = \frac{1}{1 + (r/R_0)^6} \tag{2.5}$$

With the expression for the rate of energy transfer in equation 2.4 substituted into equation 2.5 for k_T, it can be seen that when $r = R_0$ the efficiency of Förster transfer equals 1/2. The Förster radius can be calculated using equation 2.6 [16], where ϕ_D is the fluorescence quantum yield of the donor molecule, n is the refractive index of the material and N_A is the Avogadro number.

$$R_0^6 = \frac{9000\phi_D(\ln 10)\kappa^2}{128\pi^5 n^4 N_A} \int_0^\infty F_D(\lambda)\alpha_A(\lambda)\lambda^4 \, \mathrm{d}\lambda \tag{2.6}$$

The integral term in equation 2.6 describes the spectral overlap between the normalised emission spectrum of the donor molecule $F_D(\lambda)$ and the molar absorption coefficient of the acceptor molecule $\alpha_A(\lambda)$. The alignment of the transition dipole of the donor relative to that of the acceptor molecule is denoted by κ^2, which is obtained through equation 2.7 [42].

In this expression θ_T is the angle between the transition dipole moments of the donor and acceptor, θ_D is the angle between the donor dipole and the vector connecting donor and acceptor, and θ_A is the angle between the acceptor dipole and the donor-acceptor vector.

$$\kappa^2 = (\cos\theta_T - 3\cos\theta_D \cos\theta_A)^2 \tag{2.7}$$

The value of this orientation factor is usually taken to be 2/3, which is the average value of the relative orientation for random dipole orientations where dipoles are not fixed and are free to rotate. Otherwise, κ^2 can take a value between zero and four [43], where zero describes two dipoles oriented perpendicular to each other and four describes the parallel alignment of dipoles.

2.5.2 Dexter electron transfer

At even closer proximity between acceptor and donor molecules, such that there is an overlap between the wavefunctions of the acceptor and donor, the transfer of an excitation may occur through an electron exchange mechanism [44]. The rate of Dexter transfer, k_{ET}, depends on the spectral overlap integral J, the separation between donor and acceptor R_{DA} and the average of the van der Waals radii of the donor and acceptor L as shown in equation 2.8 [44, 45].

$$k_{ET} \propto J \exp\left(-\frac{2R_{DA}}{L}\right) \tag{2.8}$$

This process occurs at a shorter range than Förster transfer, occurring at a donor-acceptor separation of the order of 10 Ångströms [27]. The basic mechanism of the process is a direct exchange of electrons, where the excited electron in the donor LUMO is transferred to the LUMO of the acceptor, while an electron in the HOMO of the acceptor is transferred to that of the donor molecule, therefore transferring the excited state from one molecule to the other.

Dexter transfer allows the transfer of both singlet and triplet states from donor to acceptor. In contrast, as the ground state of the molecule must be a singlet state, Förster transfer is more prominent for singlet states than triplet.

2.6 Charge injection and transport models in devices

During device operation, electrons and holes must be injected from the electrodes into the organic layers. They must subsequently travel through the organic layers to the

recombination zone where exciton formation can take place. This section introduces a number of proposed mechanisms which describe the injection of charge carriers into an organic semiconductor as well as their motion through the semiconductor layer. For carrier injection the two main processes are Fowler-Nordheim tunnelling and thermionic emission, while bulk transport mechanisms include space charge limited conduction and variable range hopping between localised states.

These are not, however, the only mechanisms that have been proposed to explain charge injection and transport in devices, and articles summarising these processes have been published [46]. Although many of these models were originally developed to describe the behaviour of inorganic semiconductors or insulators and their interfaces with metals, they have been widely used to describe the injection and transport processes of polymer light-emitting diodes [47–49].

2.6.1 Carrier injection

The injection of charge carriers from an electrode into an organic semiconductor layer is governed by the potential barrier formed by the mismatch between the work function of the electrode and the energy levels of the organic material. There are two main mechanisms that describe the injection of charges at an electrode, firstly Fowler-Nordheim tunnelling or field emission through the potential barrier, and secondly thermionic emission over the potential barrier.

The process of field emission was described by Fowler and Nordheim in 1928 [50]. The potential barrier at the interface between the semiconductor and the electrode can be modelled as triangular in shape, neglecting the image force effect that results in a

lowering of the potential barrier. At low temperatures the charge carriers can tunnel through the barrier from the Fermi level of the metal electrode into the semiconductor. The current density J due to field emission is then given by [51]

$$J = \frac{A^* T^2}{\phi_B} \left(\frac{qF}{\alpha k_B T} \right)^2 \exp\left(-\frac{2\alpha \phi_B^{3/2}}{3qF} \right), \tag{2.9}$$

where

$$A^* = \frac{4\pi m_e k_B^2 q}{h^3} \tag{2.10}$$

is the Richardson constant, T is temperature, F is the applied electric field, ϕ_B is the height of the potential barrier, and α is a constant equal to $4\pi\sqrt{2m^*}/h$.

Grouping together constant terms in equation 2.9, the current density can be expressed as

$$J \propto F^2 \exp\left(-\frac{\kappa}{F} \right) \tag{2.11}$$

where $\kappa = 2\alpha\phi_B^{3/2}/3q$ is a constant.

Therefore, it can be seen that a plot of $\ln(J/F^2)$ against $1/F$ will result in a straight line in the injection limited current region if Fowler-Nordheim tunnelling is the dominant injection mechanism.

Thermionic emission of a charge carrier over the potential barrier may also contribute to charge injection. If charge carriers have sufficient energy, then under bias there may be a net current J across the barrier due to Schottky emission. This process

may be described by the Richardson law [51]

$$J = A^* T^2 \exp\left(-\frac{\phi_B}{k_B T}\right). \tag{2.12}$$

This law may be refined by considering the Schottky effect, where the presence of a charge carrier in the semiconductor close to the contact induces an opposite charge on the metal side of the contact temporarily. This leads to an attractive image force resulting in a field assisted lowering of the potential barrier by an amount $\Delta\phi_B$ [51], where

$$\Delta\phi_B = \left(\frac{q^3}{4\pi\epsilon\epsilon_0}\right)^{1/2} F^{1/2} = \beta_S F^{1/2}. \tag{2.13}$$

The combined Richardson-Schottky law [52, 53] then describes the current density due to thermionic emission at a potential barrier taking into account image force effects.

$$J = A^* T^2 \exp\left(-\frac{\phi_B}{k_B T}\right) \exp\left(\frac{\beta_S F^{1/2}}{k_B T}\right). \tag{2.14}$$

Carrier injection due to the Schottky effect should therefore result in a linear relationship between $\ln J$ and $F^{1/2}$.

For small potential barriers, the contacts can be considered to be Ohmic in nature and carrier injection does not limit the current-voltage behaviour of devices. However for larger potential barriers greater than approximately 0.3 to 0.4 eV, the current-voltage characteristics of the device may be limited by carrier injection [47]. In particular, the interface between PEDOT:PSS (with a work function ranging from around 4.9 to 5.2 eV) [31, 32] and a polymer such as PVK (with a HOMO level of around 5.9

eV [32]) has a relatively high potential barrier for hole injection which may lead to injection limited J-V properties.

The above models apply to generic metal-semiconductor contacts. Alternative charge injection models have been proposed which aim to better describe charge injection into disordered systems such as organic materials, which include models based on hopping mechanisms [54] and diffusion transport [55].

2.6.2 Carrier transport

Transport of charge carriers in organic semiconductor films may be due to both motion through the conduction band (for example mobility of electrons in the LUMO) or by hopping between localised states in the band gap. Disorder in organic materials results in localised states and traps which have an impact on the transport of carriers as well as the formation of excitons.

When the applied voltage is sufficiently low, the bulk transport conduction is Ohmic according to the equation

$$J = qn\mu\frac{V}{d} \tag{2.15}$$

where μ is the carrier mobility, n the carrier density at equilibrium and d the thickness of the organic layer [56].

At higher voltages the current will be due to space charge limited conduction (SCLC) of charge carriers in the conduction band. In the absence of traps SCLC

current may be described by Child's law (also known as the Mott-Gurney law) [57]

$$J = \frac{9}{8}\epsilon_0\epsilon_r\mu\frac{V^2}{d^3} \tag{2.16}$$

where ϵ_r is the relative permittivity of the material.

The theory can be extended by considering the presence of trap states in the material. As traps are filled by space charges the quasi-Fermi level is shifted towards (in the case of electron transport) the LUMO. This increases the effective mobility of the charge carriers, dependent on the depth and density of trap states [47, 58]. Assuming an exponential trap distribution, the modified current density is given by [59]

$$J \propto \frac{V^{m+1}}{d^{2m+1}} \tag{2.17}$$

where $m = E_t/k_BT$, E_t being an energy characterising the distribution of trap states.

In the case where only shallow traps are present, the ratio of free to trapped charge is a constant independent of the applied voltage. The space charge limited current is accordingly modified to [60]

$$J = \frac{9}{8}\theta\epsilon_0\epsilon_r\mu\frac{V^2}{d^3} \tag{2.18}$$

where θ is the ratio of free to trapped charge. For deep traps, θ will be voltage dependent.

A further mechanism of charge transport is the Poole-Frenkel effect, where charge carriers trapped in localised states may undergo field assisted emission from that trap

state. Trap states may be modelled as a Coulombic potential well with lowering of the potential barrier in an applied field by an amount [51]

$$\Delta\phi_T = \left(\frac{q^3}{\pi\epsilon\epsilon_0}\right)^{1/2} F^{1/2} = \beta_{PF} F^{1/2}, \tag{2.19}$$

which is similar to the lowering of the potential barrier at a metal contact due to the image force effect. The current density is thus modified according to

$$J = J_0 \exp\left(\frac{\beta_{PF} F^{1/2}}{k_B T}\right) \tag{2.20}$$

where J_0 is the current density at low fields [52, 53]. The current density properties of the Poole-Frenkel mechanism will therefore be similar to that of Schottky emission, resulting in a linear relationship between $\ln J$ and $F^{1/2}$, but can be distinguished from Schottky emission by the gradient of the linear plot which for the Poole-Frenkel effect should be double that of Schottky emission.

Variable Range Hopping is a mechanism of charge transport between localised states in the band gap of disordered semiconductors. More significant at lower temperatures, charges may hop to states closer in energy to the localised state rather than directly to the nearest neighbour, to which charge hopping may be less energetically favourable. The conductivity is temperature dependent and is given by [61–63]

$$\sigma = \sigma_0 \exp\left(-\frac{T_{1/4}}{T}\right)^{1/4} \tag{2.21}$$

where $T_{1/4}$ is a characteristic temperature which depends on the density of states at

the Fermi level and the spatial extent of localised states. The above is for 3D hopping, as the exponent depends on the dimensionality of the system.

Coulombic interactions between charge carriers lead to a Coulomb gap in the density of states at the Fermi level. This results in a modified temperature dependence of the conductivity at low temperatures given by [62, 63]

$$\sigma = \sigma_0 \exp\left(-\frac{T_{1/2}}{T}\right)^{1/2}. \tag{2.22}$$

In non-ideal organic films, surface states may be caused by defects at the interface between the film and the electrode. These states may have an effect on the charge transport characteristics of devices in addition to those mechanisms outlined above.

2.7 Quenching mechanisms in phosphorescent organic light emitting diodes

While using phosphorescent dopants in organic light emitting diodes dramatically increases device efficiency due to the added contribution of triplet excitons towards electroluminescence, a prominent roll-off in device efficiency is often observed at higher current density. Mechanisms that have been proposed as contributors to this marked decrease in efficiency include triplet-triplet annihilation, triplet-polaron quenching and dissociation of excitons due to the electric field.

The effect of these mechanisms on device efficiency is enhanced due to the fact that triplet excitons have a longer lifetime than singlet and therefore the probability of an exciton undergoing a quenching process is increased. Each of these processes also

has a greater probability of occurring with increased current density or electric field experienced within the device, thus accounting for the efficiency roll off observed in phosphorescent organic light emitting diodes under these circumstances.

The relative impact each process has on efficiency roll-off is still uncertain. Triplet-triplet annihilation has been proposed as the predominant method of quenching in phosphorescent organic light emitting diodes [64], although other investigations have identified triplet-polaron quenching [65] or exciton dissociation [66] as the primary cause of efficiency roll-off.

2.7.1 Triplet-triplet annihilation

Triplet-Triplet Annihilation (TTA) is a bi-molecular interaction that takes place between two triplet excitons. Migration of triplet states due to Dexter transfer leads to collisions between two such excited states, leading to nine possible spin states that can result from such a collision. These form a singlet, triplet and quintuplet set due to the multiplicities of each spin state [67], as shown below in equation 2.23.

$$T_1 + T_1 \rightarrow \begin{cases} S_n + S_0 & (1/9) \\ T_n + T_0 & (3/9) \\ T_1 + T_1 & (5/9) \end{cases} \tag{2.23}$$

Firstly, accounting for one out of the nine possible spin states, a collision between two triplet excitons can result in the formation of an excited singlet state and a singlet in the ground state, and thus one of the two initial excited states in question is quenched. The subsequent excited singlet state can then decay radiatively leading to a phenomenon called delayed fluorescence, which is fluorescence that occurs on a longer

timescale than the prompt decay of singlet excitons, with a lifetime on the order of magnitude of the triplet lifetime.

The second possibility is formation of a triplet excited state and a triplet ground state, thus also quenching one of the initial excited states. This outcome accounts for three out of the nine possible resulting spin states. The final outcome is the possibility of forming quintet, or quintuplet, states which have a multiplicity of five. However formation of these states is usually energetically unattainable, so this route would have less of an impact on phosphorescence quenching and instead results in reformation of the two initial triplet states.

The rate of interaction depends on the square of the concentration of triplet excitons, which increases with increasing current density in a device. Therefore this quenching of excited states is one of the mechanisms by which the efficiency of organic light emitting devices can roll off at higher current density. As a result, aggregation of phosphors is an issue for device efficiency, even in vacuum deposited films.

Similar bi-molecular interactions between excited states can contribute to quenching of device efficiency. These include singlet-triplet annihilation and singlet-singlet annihilation [68]. Singlet-triplet annihilation is the quenching of singlet states by triplet states. The result of the annihilation of an excited singlet and an excited triplet state is a higher excited triplet state and a singlet ground state.

$$S_1 + T_1 \rightarrow T_n + S_0 \tag{2.24}$$

Additionally, annihilation between two singlet excitons is possible and results in

the formation of a higher singlet excited state and a singlet ground state.

$$S_1 + S_1 \rightarrow S_n + S_0 \tag{2.25}$$

These interactions involve formation of one excited state and one ground state from two initial excited states, resulting in the quenching of an excited state. Due to the short lifetimes of singlet excitons these processes only become a factor when the concentration of singlet excitons is sufficiently large that they are able to interact before they decay, usually only under high intensity pulsed excitation.

2.7.2 Triplet-polaron quenching

Triplet-Polaron Quenching (TPQ) involves a transfer of energy, primarily due to Förster energy transfer, from an excited triplet state to a polaron A, a region of an organic molecule carrying a charge [69].

$$T_1 + A^{+,-} \rightarrow S_0 + (A^{+,-})^* \tag{2.26}$$

The rate of this quenching mechanism is proportional to the density of triplet excitons, and assuming that triplet excitons are found predominantly on phosphorescent dopant molecules, the rate of triplet-polaron quenching will increase slower than that of triplet-triplet annihilation as the dopant molecule concentration is increased. Doping of electron transport materials to improve charge balance and therefore reduce the concentration of hole polarons has been investigated as a method of reducing triplet-polaron quenching [70].

2.7.3 Exciton dissociation

During device operation an electric field is applied across the emissive layer of the device. The presence of an electric field increases the rate of thermally assisted dissociation of charge pairs [66] and thus the quenching of excited states. As a field dependent process, the effect of quenching increases as the voltage applied across the device is increased. Triplet states are more tightly bound and therefore require a higher voltage for dissociation.

Although some studies have proposed field induced exciton dissociation as a major method of quenching in phosphorescent devices with iridium dopants at high electric field [66], others have concluded that the process is not as relevant and that TTA and TPQ are the predominant mechanisms [69].

References

[1] J. Clayden, N. Greeves & S. Warren, *Organic Chemistry* Second edition (2012), Oxford University Press

[2] L. Rothberg, in G. Hadziioannou & G. G. Malliaras (eds.), *Semiconducting Polymers - Chemistry, Physics and Engineering* Second edition (2007), Wiley-VCH

[3] M. Pope & C. E. Swenberg, *Electronic Processes in Organic Crystals and Polymers* Second Edition (1999), Oxford University Press

[4] M. L. Shand, R. R. Chance, M. LePostollec & M. Schott, *Physical Review B* **25** (1982), 4431 - 4436

[5] M. Knupfer, *Applied Physics A* **77** (2003), 623 - 626

[6] S. A. Jenekhe & J. A. Osaheni, *Science* **265** (1994), 765 - 768

[7] S. A. Chen, T. H. Jen & H. H. Lu, *Journal of the Chinese Chemical Society* **57** (2010), 439 - 458

[8] J. Kalinowski, G. Giro, M. Cocchi, V. Fattori & P. Di Marco, *Applied Physics Letters* **76** (2000), 2352 - 2354

[9] Y. Z. Lee, X. Chen, M. C. Chen, S. A. Chen, J. H. Hsu & W. Fann, *Applied Physics Letters* **79** (2001), 308 - 310

[10] T. Granlund, L. A. A. Pettersson, M. R. Anderson & O. Inganäs, *Journal of Applied Physics* **81** (1997), 8097 - 8104

[11] G. Giro, M. Cocchi, J. Kalinowski, P. Di Marco & V. Fattori, *Chemical Physics Letters* **318** (2000), 137 - 141

[12] T. Q. Nguyen, V. Doan & B. J. Schwartz, *Journal of Chemical Physics* **110** (1999), 4068 - 4078

[13] J. L. Brédas & G. B. Street, *Accounts of Chemical Research* **18** (1985), 309 - 315

[14] C.-J. Chiang, A. Kimyonok, M. K. Etherington, G. C. Griffiths, V. Jankus, F. Turksoy & A. P. Monkman, *Advanced Functional Materials* **23** (2013), 739 - 746

[15] F. B. Dias, K. N. Bourdakos, V. Jankus, K. C. Moss, K. T. Kamtekar, V. Bhalla, J. Santos, M. R. Bryce & A. P. Monkman, *Advanced Materials* **25** (2013), 3707 - 3714

[16] J. R. Lakowicz, *Principles of Fluorescence Spectroscopy* Third Edition (2006), Springer

[17] B. H. Bransden & C. J. Joachain, *Physics of Atoms and Molecules* Second Edition (2003), Pearson

[18] D. C. Harris & M. D. Bertolucci, *Symmetry and Spectroscopy* (1978), Oxford University Press

[19] R. J. Anderson, D. J. Bendell & P. W. Groundwater, *Organic Spectroscopic Analysis* (2004), Royal Society of Chemistry

[20] H. Yersin (ed.), *Highly Efficient OLEDs with Phosphorescent Materials* (2008), Wiley-VCH

[21] L. Duan, L. Hou, T.-W. Lee, J. Qiao, D. Zhang, G. Dong, L. Wang & Y. Qiu, *Journal of Materials Chemistry* **20** (2010), 6392 - 6407

[22] S. Sax, N. Rugen-Penkalla, A. Neuhold, S. Schuh, E. Zojer, E. J. W. List & K. Müllen, *Advanced Materials* **22** (2010), 2087 - 2091

[23] H. A. Al-Attar & A. P. Monkman, *Journal of Applied Physics* **109** (2011), 074516 - 074521

[24] V. Jankus & A. P. Monkman, *Advanced Functional Materials* **21** (2011), 3350 - 3356

[25] E. A. Plummer, A. van Dijken, J. W. Hofstraat, L. De Cola & K. Brunner, *Advanced Functional Materials* **15** (2005), 281 - 289

[26] X. H. Yang, F. Jaiser, S. Klinger & D. Neher, *Applied Physics Letters* **88** (2006), 021107 - 021109

[27] D. F. Perepichka, H. Meng & M. M. Ling, in Z. R. Li & H. Meng, *Organic Light-Emitting Materials and Devices* (2006), CRC Press

[28] Images from C.-L. Ho, W.-Y. Wong, G.-J. Zhou, B. Yao, Z. Xie & L. Wang, *Advanced Functional Materials* **17** (2007), 2925 - 2936

[29] K. Ellmer, *Nature Photonics* **6** (2012), 809 - 817

[30] T.-H. Han, Y. Lee, M.-R. Choi, S.-H. Woo, S.-H. Bae, B. H. Hong, J.-H. Ahn & T.-W. Lee, *Nature Photonics* **6** (2012), 105 - 110

[31] T. M. Brown, J. S. Kim, R. H. Friend, F. Cacialli, R. Daik & W. J. Feast, *Applied Physics Letters* **75** (1999), 1679 - 1681

[32] A. van Dijken, J. J. A. M. Bastiaansen, N. M. M. Kiggen, B. M. W. Langeveld, C. Rothe, A. Monkman, I. Bach, P. Stössel & K. Brunner, *Journal of the American Chemical Society* **126** (2004), 7718 - 7727

[33] K. Sugiyama, H. Ishii, Y. Ouchi & K. Seki, *Journal of Applied Physics* **87** (2000), 295 - 298

[34] M.-H. Lu & J. C. Sturm, *Journal of Applied Physics* **91** (2002), 595 - 604

[35] C.-L. Lin, H.-C. Chang, K.-C. Tien & C.-C. Wu, *Applied Physics Letters* **90** (2007), 071111 - 071113

[36] C.-L. Lin, T.-Y. Cho, C.-H. Chang & C.-C. Wu, *Applied Physics Letters* **88** (2006), 081114 - 081116

[37] M. A. Baldo, D. F. O'Brien, Y. You, A. Shoustikov, S. Sibley, M. E. Thompson & S. R. Forrest, *Nature* **395** (1998), 151 - 154

[38] V. Cleave, G. Yahioglu, P. Le Barny, R. H. Friend & N. Tessler, *Advanced Materials* **11** (1999), 285 - 288

[39] D. F. O'Brien, M. A. Baldo, M. E. Thompson & S. R. Forrest, *Applied Physics Letters* **74** (1999), 442 - 444

[40] M. A. Baldo, S. Lamansky, P. E. Burrows, M. E. Thompson & S. R. Forrest, *Applied Physics Letters* **75** (1999), 4 - 6

[41] A. R. G. Smith, P. L. Burn & B. J. Powell, *ChemPhysChem* **12** (2011), 2429 - 2438

[42] T. Förster, *Discussions of the Faraday Society* **27** (1959), 7 - 17

[43] B. P. Lyons, K. S. Wong & A. P. Monkman, *Journal of Chemical Physics* **118** (2003), 4707 - 4711

[44] D. L. Dexter, *Journal of Chemical Physics* **21** (1953), 836 - 850

[45] M. Inokuti & F. Hirayama, *Journal of Chemical Physics* **43** (1965), 1978 - 1989

[46] D. Braun, *Journal of Polymer Science Part B: Polymer Physics* **41** (2003), 2622 - 2629

[47] H. A. Al-Attar & A. P. Monkman, *Advanced Functional Materials* **16** (2006), 2231 - 2242

[48] M. Ben Khalifa, D. Vaufrey, A. Bouazizi, J. Tardy & H. Maaref, *Materials Science and Engineering* **C 21** (2002), 277 - 282

[49] S. Karg, M. Meier & W. Riess, *Journal of Applied Physics* **82** (1997), 1951 - 1960

[50] R. H. Fowler & L. Nordheim, *Proceedings of the Royal Society A* **119** (1928), 173 - 181

[51] K. C. Kao & W. Hwang, *Electrical Transport in Solids* (1981), Pergamon Press

[52] S. M. Sze, *Physics of Semiconductor Devices* (1969), Wiley

[53] J. G. Simmons, in L. I. Maissel & R. Glang, *Handbook of Thin-Film Technology* (1970), McGraw-Hill

[54] V. I. Arkhipov, E. V. Emelianova, Y. H. Tak & H. Bässler, *Journal of Applied Physics* **84** (1998), 848 - 856

[55] L. Li, G. Mellor & H. Kosina, *Applied Physics Letters* **91** (2007), 172111 - 172113

[56] P. W. M. Blom, M. J. M. de Jong & J. J. M. Vleggaar, *Applied Physics Letters* **68** (1996), 3308 - 3310

[57] M. A. Lampert, *Current Injection in Solids* (1970), Academic Press

[58] P. E. Burrows, Z. Shen, V. Bulovic, D. M. McCarty, S. R. Forrest, J. A. Cronin & M. E. Thompson, *Journal of Applied Physics* **79** (1996), 7991 - 8006

[59] P. Mark & W. Helfrich, *Journal of Applied Physics* **33** (1962), 205 - 215

[60] M. A. Lampert, *Physical Review* **103** (1956), 1648 - 1656

[61] N. F. Mott & E. A. Davis, *Electronic processes in non-crystalline materials* (1979), Oxford University Press

[62] N. F. Mott, *Conduction in non-crystalline materials* (1987), Oxford University Press

[63] A. L. Efros & B. I. Shklovskii, *Electronic properties of doped semiconductors* (1984), Springer

[64] M. A. Baldo, C. Adachi & S. R. Forrest, *Physical Review B* **62** (2000), 10967 - 10977

[65] D. Song, S. Zhao, Y. Luo & H. Aziz, *Applied Physics Letters* **97** (2010), 243304 - 243306

[66] J. Kalinowski, W. Stampor, J. Mężyk, M. Cocchi, D. Virgili, V. Fattori & P. Di Marco, *Physical Review B* **66** (2002), 235321 - 235335

[67] Y. Y. Cheng, T. Khoury, R. G. C. R. Clady, M. J. Y. Tayebjee, N. J. Ekins-Daukes, M. J. Crossley & T. W. Schmidy, *Physical Chemistry Chemical Physics* **12** (2010), 66 - 71

[68] S. M. King, D. Dai, C. Rothe & A. P Monkman, *Physical Review B*, **76** (2007), 085204 - 085210

[69] S. Reineke, K. Walzer & K. Leo, *Physical Review B* **75** (2007), 125328 - 125340

[70] F. X. Zang, T. C. Sum, A. C. H. Huan, T. L. Li, W. L. Li & F. Zhu, *Applied Physics Letters* **93** (2008), 023309 - 023311

3 Experimental details

This chapter describes the experimental methods utilised during the course of this thesis. Experimental techniques used for fabrication and characterisation of OLED devices are discussed, followed by a description of the equipment used for photophysical characterisation of materials including absorption, emission and quantum yield measurements. Finally, the theory behind ellipsometry and the experimental procedure for measurement of thin film thickness are both outlined.

3.1 Device fabrication

Electrophosphorescent OLEDs were fabricated using a simple solution processable method. Firstly, glass substrates coated with Indium Tin Oxide (ITO) were patterned and cleaned. Thin films of PEDOT:PSS and polymer emissive layers were subsequently spin coated, followed by thermal deposition of a metal cathode and encapsulation of the device. Device fabrication was carried out in a nitrogen filled glove box in a class 5000 clean room, except for devices with a Ba/Al cathode where the spin coating of polymer layers was performed in air before being transferred to the glove box for cathode evaporation.

3.1.1 Photolithography

Sheets of glass measuring 72 x 72 mm coated with 150 nm ITO (15 $\Omega/\square$) were purchased from VisionTek. Photolithography was used to pattern the ITO such that each device would ultimately consist of four identical pixels. S1813 G2 photoresist (Rohm and

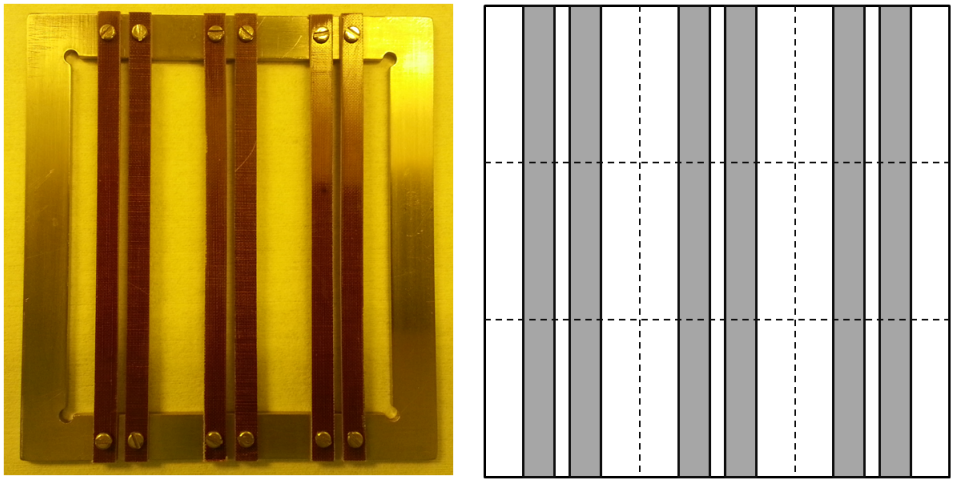

Figure 3.1: Left: photograph of the mask used for photolithography. Right: Diagram of patterned 72 x 72 mm ITO substrate, where the unshaded area is where ITO has been removed from the substrate. Dashed lines indicate where the glass is cut to obtain nine identical 24 x 24 mm device substrates.

Haas) was spin coated (section 3.1.4) on to the ITO coated glass at 500 rpm for five seconds followed by 3700 rpm for 30 seconds, and subsequently baked on a hotplate at 95° C for five minutes.

A mask (Figure 3.1, left) was placed over the substrate and exposed to ultraviolet light (Spectroline EN-180L/F lamp) for 30 seconds. The exposure of photoresist to ultraviolet light leads to breaking of bonds in the photoresist molecule, reducing the molecular weight of the exposed photoresist and leading to increased solubility in a developer solution. The substrates were immersed in developer solution (one part Microposit 351 Developer, two parts deionised water) then rinsed, dried and baked on a hotplate at 95° C for fifteen minutes.

After ensuring that all photoresist was removed from the edges of the glass, thus removing the possibility of a conductive bridge of ITO between pixels, the substrate was placed in a mixture of hydrochloric acid and nitric acid (20:1) for five minutes.

This removed the ITO coating that was not covered by the remaining photoresist. The substrate was rinsed and dried before the remaining photoresist was washed off with acetone revealing the patterned ITO as shown on the right hand side of Figure 3.1.

The sheet of glass was cut into nine squares of 24 x 24 mm, with two 5 mm stripes of ITO separated by 2 mm down the centre of each square. Combined with shadow masking of the cathode during thermal evaporation, four identical and individually addressable 5 x 4 mm pixels could be obtained.

3.1.2 Preparation of solutions

Solutions were prepared by measuring out an amount of material into a clean glass vial using a Mettler AE240 balance with a readability of 0.1 mg. An appropriate amount of solvent was added using Eppendorf calibrated pipettes of capacity 1000 μL or 100 μL. Solvents used included toluene and chlorobenzene (Romil Super Purity Solvent).

The solutions were left on a hotplate for at least an hour to mix at a temperature of 30 - 50° C with magnetic stirring. Blends of materials were made as required, and details of materials and concentrations used will be given in the relevant chapters.

3.1.3 Cleaning of substrates

It is important that the ITO substrates used for devices are cleaned thoroughly and are free from any contaminants, dirt or other particles. Any contaminant on the substrate would disrupt the homogeneity of any subsequent spin coated organic layer and lead to non-uniform current flow though the device and localised heating of the organic layer. This can affect the efficiency of the device, and also cause it to break down completely.

After cutting into 24 x 24 mm squares, substrates were wiped with acetone and isopropanol (IPA) with a clean room wipe to remove any markings and other material left by the glass cutter. Substrates were placed in a Coplin jar with grooves to hold them vertical and separate from each other. The jar was filled with acetone and placed in an ultrasonic bath for five minutes. The process was repeated with IPA and finally acetone again.

Substrates were dried with nitrogen and were placed in a UV-Ozone cleaner (Jelight Model 42-220) for five minutes. This cleaned any organic residue on the substrates and also had the effect of lowering the work function of ITO, thus providing better energy level matching between the anode and the HOMO of the organic layer and improving the efficiency of hole injection [1].

3.1.4 Spin coating

Thin films of organic material were spin coated using a Laurell WS-400B-6NPP/LITE programmable spin coater. Spin coating is a simple and low cost procedure that can deposit thin films with large area and uniform thickness. Materials can be processed in solution and high molecular weight materials such as polymers can be used as well as materials that may decompose under thermal evaporation.

Four stages to the spin coating process have been identified [2]. The first is deposition, where an excess of the solution is applied, covering the substrate to be coated. This is followed by the spin up stage, where the substrate starts rotating and accelerates to the final spin speed. The solution flows to the edge of the substrate due to radial forces and is thrown off the substrate when the forces exceed the surface tension

of the liquid. Surface tension leads to formation of an edge bead, an area of increased layer thickness at the edges of the substrate.

The third stage is the spin off stage, where the substrate is rotating at a constant speed and remaining solvent continues to move to the edges in a series of wave fronts. A thin, uniform layer of material is left behind on the substrate. The final stage is the evaporation of the solvent, which occurs throughout the entire process, overlapping with other stages. This process continues thinning of the film for the remainder of the spin time, while any remaining solvent at the end can be removed by baking the substrate on a hot plate after spin coating. Baking of the spin coated film in the glove box is also used for thermal annealing or promoting cross linking of polymer chains.

A number of factors affect the thickness of films prepared by spin coating. These include parameters of the spin programme such as spin time, spin speed and the acceleration to the final spin speed. Figure 3.2 shows the effect of these parameters on the thicknesses of PVK films. The films were spin coated on Si/SiO_2 substrates and their thicknesses were measured with an ellipsometer, which will be discussed in section 3.4. Ambient conditions such as temperature of the solution and substrate, and the air flow around the spin coater also affect film thickness. Although for each batch of films spun the conditions should not vary greatly, there will always be some variation between the thicknesses of films spun from the same solution at the same spin programme.

The effect of spin speed is shown in Figure 3.2 a). Six films were spun from a 17 mg/ml solution of PVK in chlorobenzene for 60 seconds under identical conditions with variation in spin speed from 1000 rpm to 3500 rpm. As the spin speed increases, the thickness of the film decreases from 81 nm at 1000 rpm to 56 nm at 2000 rpm.

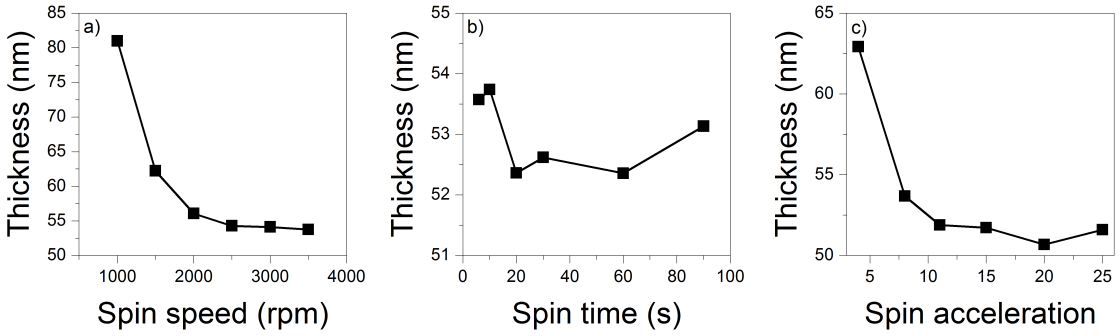

Figure 3.2: Effect of spin speed, time and acceleration on the thickness of spin coated films of PVK. Increasing spin speed (a) reduces film thickness, but has little effect above approximately 2500 rpm. The duration of spin coating (b) also has little effect, as the variation of thickness is within the range expected for identical conditions. Faster acceleration (c) also has the effect of reducing film thickness, although again the effect is reduced above a certain value.

Above 2500 rpm, increasing spin speed has little effect on film thickness with consistent thicknesses of 53 - 54 nm being obtained. An empirical relationship that film thickness is inversely proportional to the square root of spin speed has been reported [3]. This model does not fit the data shown particularly well, though at higher spin speeds the longer time taken to accelerate to the final speed may be the deciding factor in this case.

Figure 3.2 b) shows the change in film thickness as the spin time is increased from six seconds to 90 seconds. As before, films were spun from a 17 mg/ml solution of PVK in chlorobenzene, but at a constant speed of 2500 rpm. During the spinning process the acceleration of the substrate reached the final speed after approximately five seconds had elapsed, while interference fringes observed during redistribution of the solution were not observed after approximately six seconds. Therefore, across the range of spin times, the variation of all the film thicknesses are within the range that would be expected if the films were spun under identical conditions.

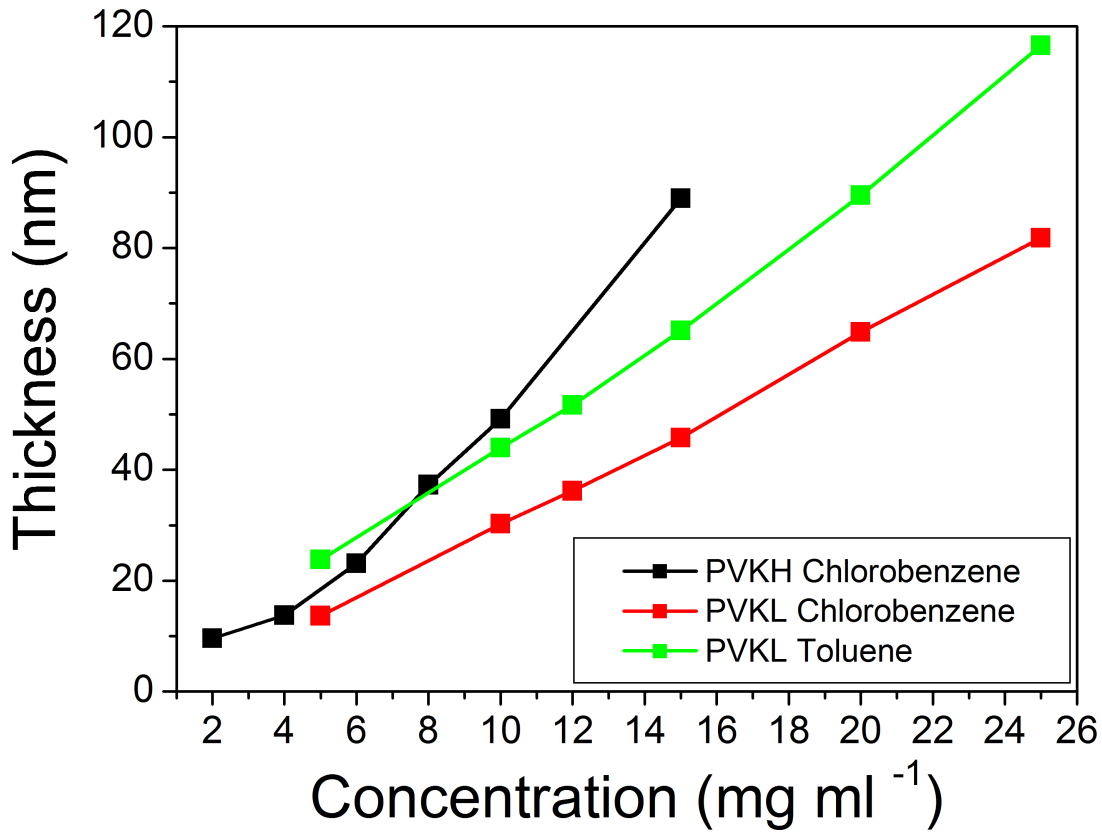

Figure 3.3: Effect of molecular weight, solvent and concentration on the thickness of spin coated films of PVK. High molecular weight PVK (PVKH) spins thicker films than a similar solution of low molecular weight PVK (PVKL), while using toluene as the solvent instead of chlorobenzene also has the effect of increasing film thickness.

The final parameter that can be determined by the spin coater programme is the acceleration, the effect of which is shown in Figure 3.2 c). All films were spun from a 17 mg/ml solution of PVK in chlorobenzene at 2500 rpm for 60 s. The acceleration settings tested ranged from 4 to 25, where the lowest setting reached 2500 rpm in approximately eight seconds while the highest setting reached the same speed in approximately three seconds. For comparison, the acceleration setting used for the spin speed and spin time tests was 11, near the middle of this range. Thinner films are obtained at faster accelerations, although there is not much difference between the highest settings.

The solution that is used to coat a substrate has a major effect on film thickness in

addition to spin conditions and programme parameters. Figure 3.3 shows the variation of film thickness of three different solutions as the concentration of PVK is increased. The three solutions used illustrate the effect of solvent used, in this case toluene and chlorobenzene, as well as the molecular weight of the PVK used.

Increasing the concentration of the solution increases its viscosity and results in larger film thickness. At higher concentrations, the film thickness increases linearly with concentration. High molecular weight PVK (PVKH, MW 1,100,000 from Sigma Aldrich) spins thicker films than a similar solution of low molecular weight PVK (PVKL, MW 90,000 from Acros Organics), while using toluene as the solvent instead of chlorobenzene also has the effect of increasing film thickness.

For the purposes of this thesis, solutions were dispensed onto the substrate from a syringe using a 0.45 μm pore filter, and baked on a hotplate after spin coating to remove any residual solvent. A layer of PEDOT:PSS (Clevios HIL) was deposited from an aqueous solution and spun at 2500 rpm for 60 seconds and baked for three minutes at 200° C. Polymer layers were subsequently spin coated at 2500 rpm for 60 seconds and baked for ten minutes at 120° C. Full details of the polymer films used for specific devices - such as their composition, thickness and solvent used - will be given in the relevant chapters.

3.1.5 Thermal evaporation

Thermal evaporation can be used to deposit further organic layers as well as the metal cathode. Two evaporation systems were used during the course of this project: an Edwards metal evaporator for metal cathode evaporation only or a Kurt J. Lesker

Figure 3.4: Photograph of the Edwards metal evaporator used to deposit the cathode. The evaporation bell jar can be seen in the right hand side of the glove box, while the control unit is outside the glove box on the far right.

Spectros II deposition system capable of depositing small molecule organic films as well as metal films.

Edwards metal evaporator: The Edwards metal evaporation system, shown in Figure 3.4, was used to deposit a metal cathode consisting of a 4 nm thick layer of barium and a 100 nm capping layer of aluminium.

The main components of the thermal evaporation system are shown in Figure 3.5. The materials to be deposited are placed in Molybdenum source boats (S27.005Mo, purchased from Testbourne Ltd.) at the bottom of the bell jar, which is located in a nitrogen filled glove box. A sample holder incorporating a shadow mask (shown in Figure 3.6, left) is located above the source boats along with a mechanically operated shutter to control the exposure of the samples to evaporated material. The combination of shadow masking of the cathode and the patterning of the ITO anode results in four

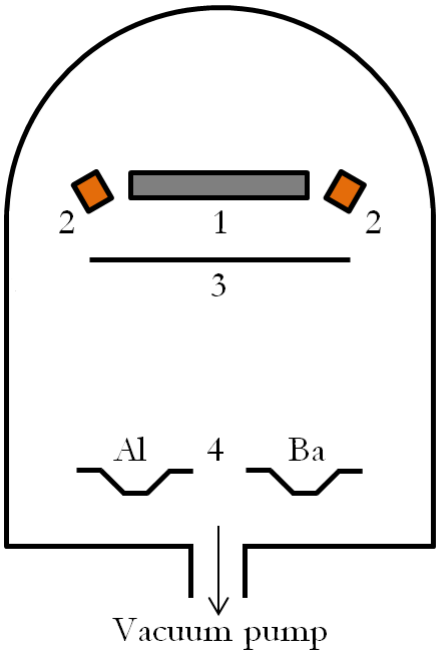

Figure 3.5: Diagram of the components of the Edwards vacuum evaporation system. Key: 1 - Sample holder and shadow mask. 2 - Crystal sensors for film thickness monitoring. 3 - Shutter. 4 - Evaporation source boats.

individually addressable pixels as shown on the right hand side of Figure 3.6.

Two quartz crystal film thickness monitors (Inficon) are located to either side of the sample holder. As material is deposited on the surface of the crystal monitor, the resonant frequency of crystal oscillation changes. This change can be used to measure the thickness of the deposited film if the density and acoustic impedance of the material being deposited are known.

Once the samples were mounted and the source boats were loaded with the appropriate material, the bell jar was pumped down to a vacuum of *ca.* 10^{-6} mbar using a roughing pump (up to *ca.* 10^{-2} mbar) followed by a turbomolecular pump. The low pressure ensures that there are no contaminants present during the deposition process and that the mean free path of evaporated molecules is much longer than the distance

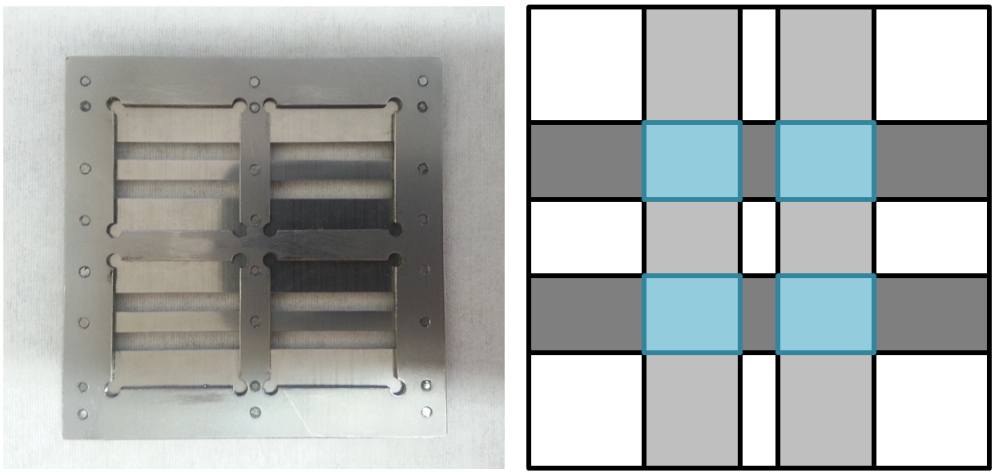

Figure 3.6: Left: photograph of the mask used during thermal evaporation of the cathode. Right: diagram of a device showing how shadow masking of the cathode (dark grey horizontal stripes) and patterning of the ITO anode (light grey vertical stripes) forms four active pixels.

between substrate and source, resulting in a straight line path through the shadow mask to the device.

Resistive heating of the source boat was used to evaporate the cathode materials. A current was passed through the source boat, slowly increasing to *ca.* 3 A for barium and 4.5 A for aluminium, heating both the boat and the source material. This causes the material to transform to the vapour state and move towards the substrate, condensing on the surface.

The rate of deposition of material was kept low, at around 0.1 nm per second. This promotes uniform film growth and protects against damage of existing layers by incident molecules with high kinetic energy.

Lesker evaporation system: The Kurt J. Lesker Spectros II thermal deposition system, shown in Figure 3.7, contains six evaporation sources used for organic materials and three metal evaporation sources in the evaporation chamber. The chamber is

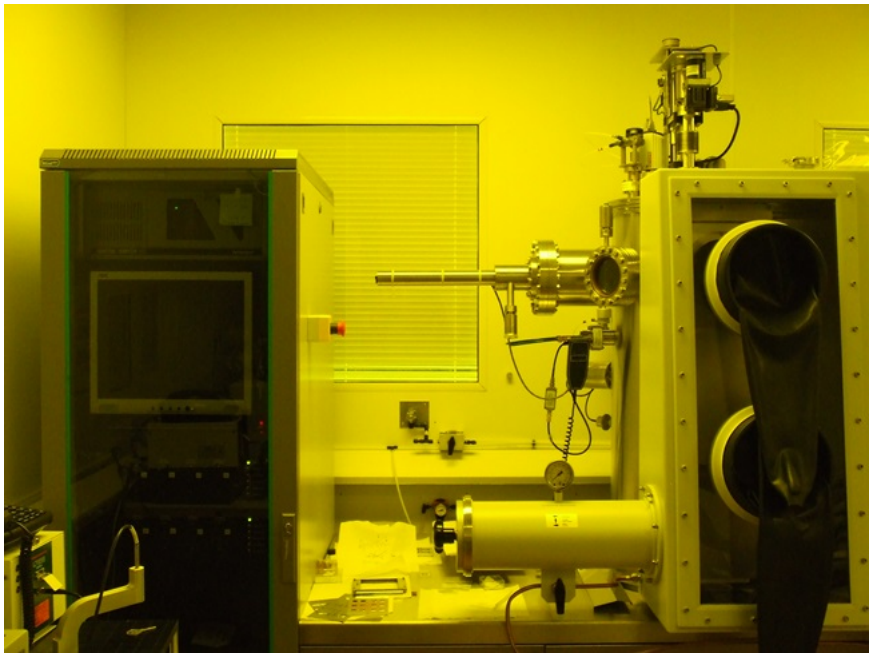

Figure 3.7: Photograph of the Kurt J. Lesker Spectros II evaporator used to deposit both small molecule organic layers and the metal cathode. The evaporation chamber is located behind the glove box to the right, while the controlling computer is on the left hand side.

pumped down to *ca.* 10^{-7} mbar with a turbomolecular vacuum pump. The deposition procedure can be run either manually or automatically using predetermined recipes.

The system allows for co-deposition of organic materials, i.e. simultaneous evaporation of two materials to obtain films consisting of both materials, for example the fabrication of films of dopant material in a small molecule host. There is one Film Thickness Monitor for each pairing of organic evaporation sources, as well as a fourth for the remaining metal evaporation sources [4].

A Linear Rack and Pinion (LRP) movable arm can be used to transfer substrates and masks between different shelves in the evaporation chamber. This allows for changing of the shadow mask without the need to break the vacuum.

Control of the vacuum, shutters, substrate stage rotation and evaporation sources

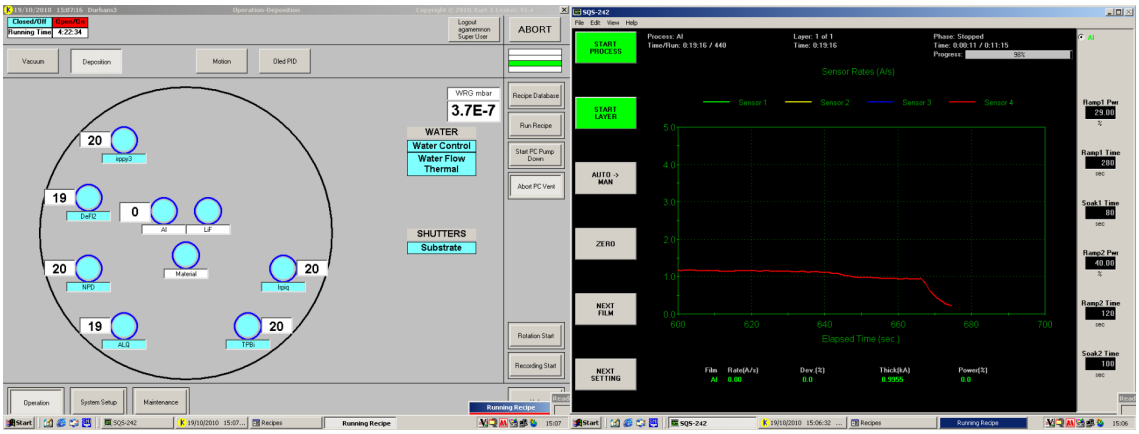

Figure 3.8: Screenshots of the software used to control the Lesker evaporation system, showing (left) deposition, vacuum and shutter controls and (right) monitoring of rate of deposition with the SQS-242 program.

are performed using the computer software shown in Figure 3.8, as well as the monitoring of material deposition rate and thickness.

3.1.6 Encapsulation

Effective encapsulation of the device is important to protect the emissive layer from oxygen or moisture that may quench emission or degrade the organic materials. After removing the devices from the evaporation chamber, UV curable epoxy glue (DELO KATIOBOND) was deposited onto the centre of the device. This was followed by a clean 14 x 14 mm glass cover slide such that the glue covered the entire emissive area of the device. Exposure to UV light (DELO Delolux 03 S) for three minutes hardened the epoxy glue, encapsulating the active area of the device.

3.2 Device characterisation

Devices were characterised in a calibrated Labsphere LMS-100 10 inch integrating sphere (Figure 3.9), which has an interior coating that reflects light emitted by a de-

Figure 3.9: Photograph of the Labsphere LMS-100 10 inch integrating sphere used for device characterisation.

vice diffusely such that the resulting measurement of the light source does not depend on the direction of light emission. A bias was applied to devices using an Agilent 6632B DC power supply, controlled with a home written NI LabVIEW programme. Figure 3.10 shows a screenshot of the user interface of this programme. The applied voltage was increased in steps of 0.5 V from 0 V to a maximum of 20 V, with a hold time of three seconds between steps. An Ocean Optics USB4000 fibre optic spectrometer measured the electroluminescence emission spectrum of the device. The device testing apparatus has been benchmarked with CDT, with good agreement between measurements performed across both institutions.

A number of measures of device efficiency were calculated by the LabVIEW programme, including external quantum efficiency, power efficiency (lm W^{-1}) and current efficiency (cd A^{-1}), which will be outlined in section 3.2.1. Other data collected in-

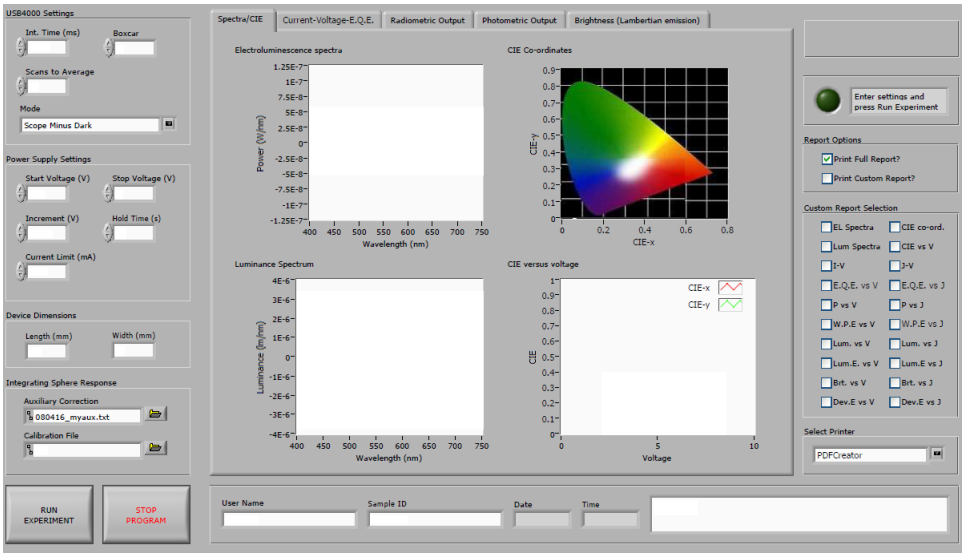

Figure 3.10: Screenshot of the home written LabVIEW programme used to record device performance.

cluded electroluminescence spectra and their CIE coordinates (discussed further in section 3.2.2), device brightness or luminance in cd m^{-2} as well as current-voltage data.

3.2.1 Measures of efficiency

There are a number of different measures of OLED device efficiency that are commonly reported in the literature, which have been reviewed by Forrest *et al.* [5]. A number of these quantities take into account the photopic response of the eye, which has its highest value at a wavelength of 555 nm and describes the wavelength sensitivity of an average human eye under normal levels of daylight (at lower levels of light, the scotopic response applies to the human eye, which peaks at a lower wavelength than the photopic response).

Internal and External Quantum Efficiency: The internal quantum efficiency (I.Q.E.) of an OLED device is simply a measure of how many photons are generated

in the emissive layer for each electron injected into the device. However photons may be reabsorbed or not outcoupled into the viewing direction (for example, by internal reflection), and are therefore not observed by a detector.

The external quantum efficiency (E.Q.E.) has a similar definition to the I.Q.E. in that it is a ratio of photons emitted (into the viewing direction, as light may also be waveguided towards the edge of the device) to electrons injected, although it only counts photons that are outcoupled from the device and observed by a detector. Measurements need to be corrected for detector efficiency as well as the response of the integrating sphere. The E.Q.E. does not depend on the response of the human eye. It has a maximum value of 1, or 100% if expressed as a percentage, and can be calculated using equation 3.1,

$$\eta_{\text{E.Q.E.}} = \frac{\int \lambda I_{\text{det}}(\lambda)\,\mathrm{d}\lambda}{I_{\text{OLED}} \int \lambda f(\lambda)\,\eta_{\text{det}}(\lambda)\,\mathrm{d}\lambda}, \tag{3.1}$$

where I_{OLED} is the current passing through the OLED device, $I_{\text{det}}(\lambda)$ is the measured photocurrent at the detector, $f(\lambda)$ is the amount of light emitted that is coupled into the detector and $\eta_{\text{det}}(\lambda)$ is the quantum efficiency of the detector.

A measurement of the E.Q.E. in an integrating sphere assumes that the OLED emission is Lambertian and requires a sunken device mount or the masking of substrate edges to prevent measurement of photons waveguided out through the edges of the substrate.

Luminous Power Efficiency: Also known as luminous efficacy, the power efficiency is the ratio of luminous flux emitted by the device to the power supplied to it,

measured in lm W^{-1}. The luminous efficacy is determined by equation 3.2,

$$\eta_{\text{power}} = \frac{\phi_0 \int g(\lambda) I_{\text{det}}(\lambda) \, d\lambda}{I_{\text{OLED}} V \int f(\lambda) R(\lambda) \, d\lambda}, \tag{3.2}$$

where ϕ_0 is the maximum luminous efficacy of 683 lm W^{-1} at 555 nm, the peak of the photopic response curve (as 1 W of radiation at 555 nm has a luminous flux of 683 lm, due to the definitions of the units involved). The calculation depends on the photopic response of the eye $g(\lambda)$ as well as the responsivity of the detector $R(\lambda)$. It is also possible to quote this as an efficiency based on the device performance as a fraction of 683 lm W^{-1}.

Wall Plug Efficiency: The wall plug efficiency is another measure of the power efficiency of the device, and is independent of the response of an observer. It is defined simply as $P_{\text{OLED}}/I_{\text{OLED}}V$, which is the ratio of the power of light emitted by the device to the power applied electrically to the device.

Luminance or Current Efficiency: The final measure of OLED efficiency is the current efficiency, given in units of cd A^{-1}. The candela, the SI base unit of luminous intensity, is defined in relation to the peak of the photopic response at 555 nm, taking into account the wavelength dependence of the eye. The current efficiency of the device describes how much brightness is achieved from the device compared to the current passing through it, and is defined as

$$\eta_{\text{current}} = \frac{AL}{I_{\text{OLED}}}, \tag{3.3}$$

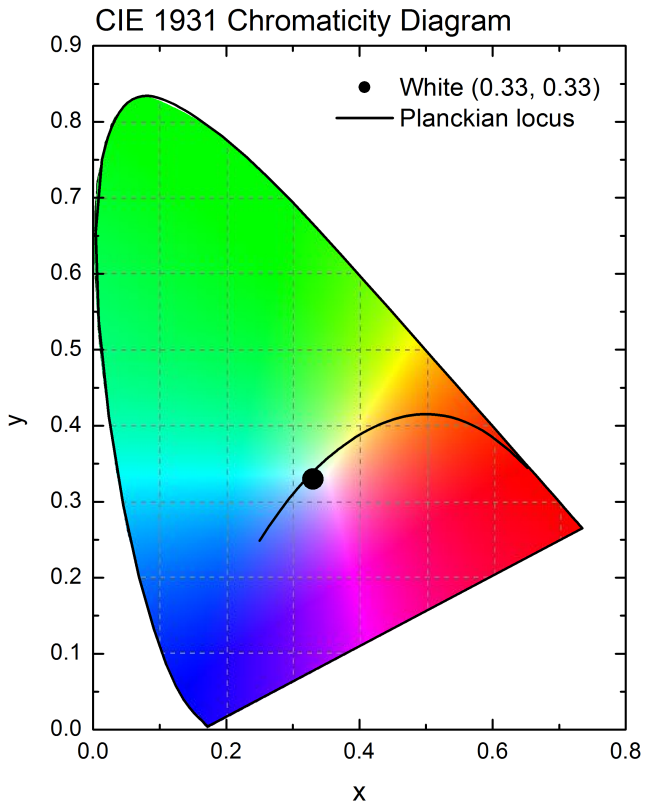

Figure 3.11: The CIE 1931 chromaticity diagram. Monochromatic light forms the outer boundary of the diagram. The equal energy 'white' point is defined as (0.33, 0.33). The central curve is the Planckian locus, describing light emitted as black body radiation at various temperatures.

where A is the active area of the device and L is the brightness or luminance of the device in cd m^{-2}.

3.2.2 CIE coordinates

One of the methods of quantifying the colour of light emitted by OLED devices is the CIE 1931 colour space. Figure 3.11 shows the CIE 1931 chromaticity diagram, which contains colours that are perceptible by the human eye. A colour may be represented as an (x, y) coordinate, and a given coordinate can be achieved by combinations of different colours. The outer boundary of the diagram describes monochromatic radiation, from blue in the lower left, through green at the top towards red in the lower right. The Planckian locus describes black body radiation at a range of colour temperatures, while the equal energy white point is located at (0.33, 0.33).

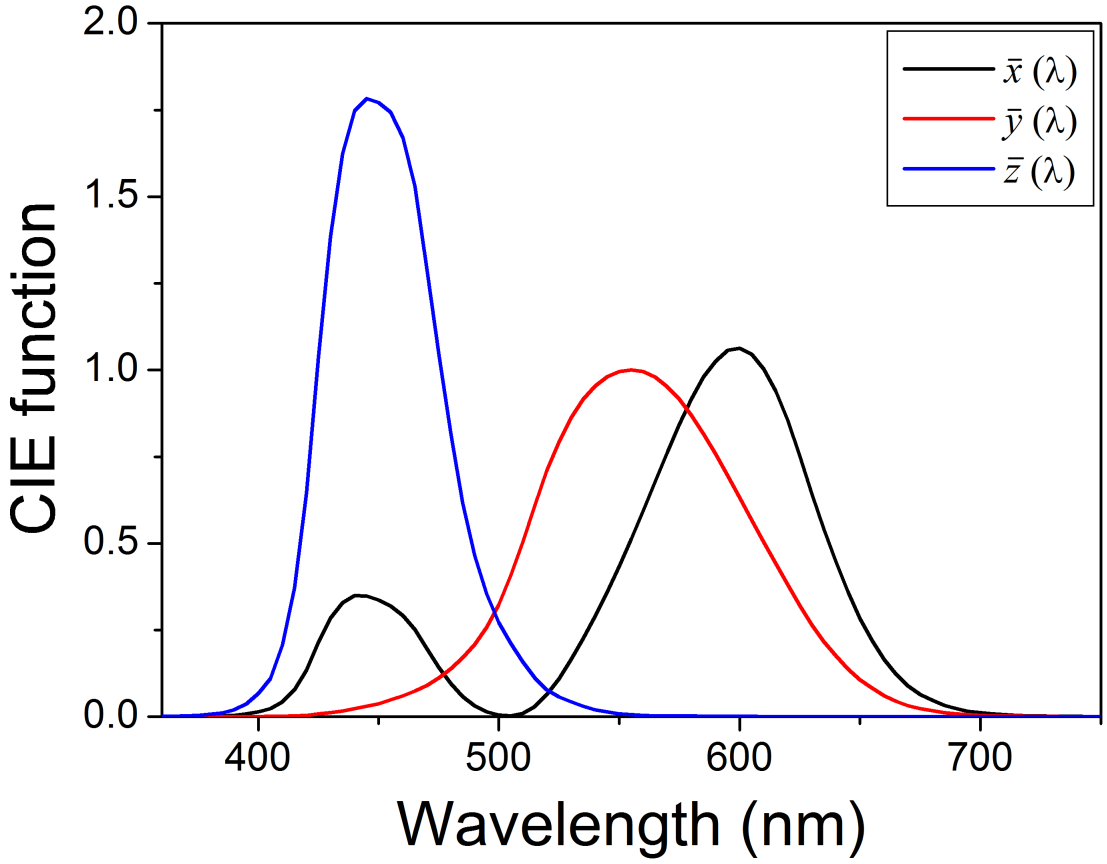

Figure 3.12: Graph of the three CIE colour matching functions characterising the chromatic response of a standard observer.

Three colour matching functions $\overline{x}(\lambda)$, $\overline{y}(\lambda)$ and $\overline{z}(\lambda)$ are used to characterise the chromatic response of a standard colorimetric observer, which are plotted in Figure 3.12. These functions are based on a series of experiments and aim to describe the average r, g and b response of the human eye at a 2° field of view [6, 7]. The products of the emission spectrum and each colour matching function are integrated with respect to wavelength as shown in equation 3.4. These give the three tristimulus values X, Y and Z.

$$
\begin{aligned}
X &= \int_0^\infty I(\lambda)\,\overline{x}(\lambda)\,\mathrm{d}\lambda \\
Y &= \int_0^\infty I(\lambda)\,\overline{y}(\lambda)\,\mathrm{d}\lambda \\
Z &= \int_0^\infty I(\lambda)\,\overline{z}(\lambda)\,\mathrm{d}\lambda
\end{aligned}
\tag{3.4}
$$

The CIE coordinates x and y are then calculated from X, Y and Z using equation 3.5. Only these two values are needed to characterise chromaticity, as the z value can be easily determined from x and y. It is also common to include Y, a measure of the luminance of the colour, forming the xyY derived colour space. This can be used to distinguish between two colours that may have the same chromaticity but differ in brightness.

$$
\begin{aligned}
x &= \frac{X}{X+Y+Z} \\
y &= \frac{Y}{X+Y+Z} \\
z &= \frac{Z}{X+Y+Z} \quad = 1-x-y
\end{aligned}
\tag{3.5}
$$

The equal energy white point shown on Figure 3.11 is defined as (0.33, 0.33). The colour of white OLEDs for lighting purposes however may lie around the Planckian locus, which describes the light emitted by a black body with varying temperature. Flexibility in organic synthesis can tune the colour of OLED devices to result in a range of effective colour temperatures, which is advantageous as there is a demand for a range of 'warm' and 'cool' lighting depending on the market [8].

3.3 Photophysical characterisation

The following section describes some of the commercial spectrometer equipment and methods used to characterise the photophysical properties of organic materials, including absorption and photoluminescence spectra, as well as two methods used to determine the quantum yield of materials.

3.3.1 Absorption measurements

Absorption spectra of solutions and thin films were measured using the Shimadzu UV-3600 UV-VIS-NIR Spectrophotometer as shown in Figure 3.13, controlled with UVProbe software. Samples in solution were measured using 10 mm path length cuvettes, of either optical glass or quartz, obtained from Starna Scientific. Thin film samples were prepared by spin coating on 10 mm diameter quartz substrates. Cuvettes and substrates were cleaned in dilute nitric acid solution followed by further cleaning in acetone and isopropanol.

A schematic of the spectrophotometer is shown in Figure 3.14. The light sources are a D2 deuterium lamp for ultraviolet light from 185 nm and above, and a WI halogen lamp for visible and near-infrared light up to 3300 nm [9]. The wavelength at which the light source switches from one lamp to the other can be changed, with the factory default setting at 310 nm. Along with a double monochromator, a resolution of 0.1 nm can be achieved for the light source. A beam splitter consisting of a chopper mirror splits the light source into two beams, one of which passes through the sample being measured and the other passing through a blank reference sample. This consists of a clean substrate if measuring absorption of a thin film, or a cuvette containing the

Figure 3.13: Photograph of the Shimadzu UV-3600 UV-VIS-NIR spectrophotometer used to measure absorption spectra.

solvent used if measuring absorption of a solution. A photomultiplier tube detects transmitted light in the UV-visible region, while an InGaAs photodiode and a PbS photoconductive cell are used for near-infrared light.

Before any measurements are taken, a baseline scan and auto zero are performed to ensure that there is no absorption measured when there is no sample present. The absorption of the sample, and the extinction coefficients of solutions, can be determined from the change of intensity of the transmitted beam according to equation 2.3. The reference beam passing through a blank sample is used to correct for absorption due to the substrate, solvent or cuvette used.

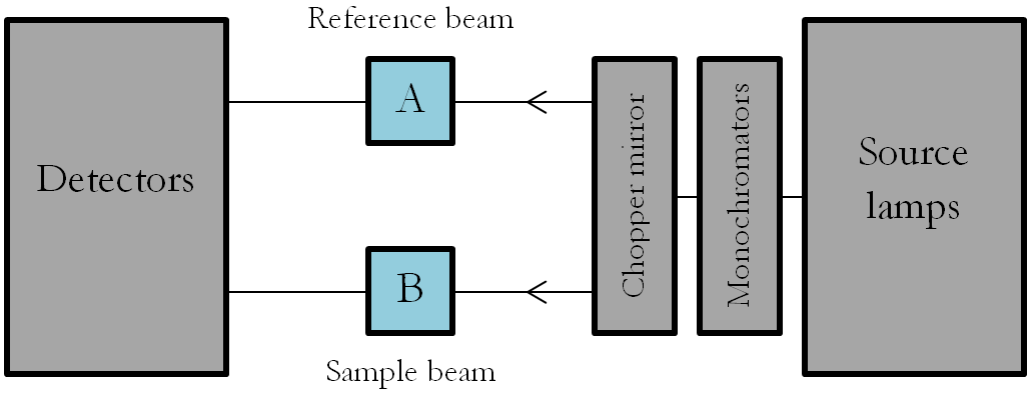

Figure 3.14: Schematic of the Shimadzu UV-3600 UV-VIS-NIR spectrophotometer used to measure absorption spectra. The sample holder for a blank substrate or solvent cuvette is denoted by A, while B denotes the holder for the sample to be measured.

3.3.2 Photoluminescence measurements

The Jobin Yvon Horiba Spex Fluoromax 3 shown in Figure 3.15 along with Datamax software was used to measure photoluminescence spectra of materials. The equipment can measure both photoluminescence emission spectra and excitation profiles of materials can be measured in solution and in thin film. The equipment can also, with use of an integrating sphere, be used to measure photoluminescence quantum yields (PLQY) of materials as described in Section 3.3.3.

Figure 3.16 shows a simplified schematic of the optical layout of the Fluoromax 3. A 150W Xenon arc lamp is used as the light source [10]. The source beam is focused onto the entrance slit of a Czerny-Turner monochromator which uses a reflection grating to separate the source beam into different wavelengths. The monochromatic excitation beam is focused on the sample, and the resulting photoluminescence emission of the sample is collected at 90° to the excitation beam. A R928P photomultiplier tube in conjunction with an emission monochromator measures the intensity of the sample photoluminescence at a particular wavelength, while a reference silicon photodiode

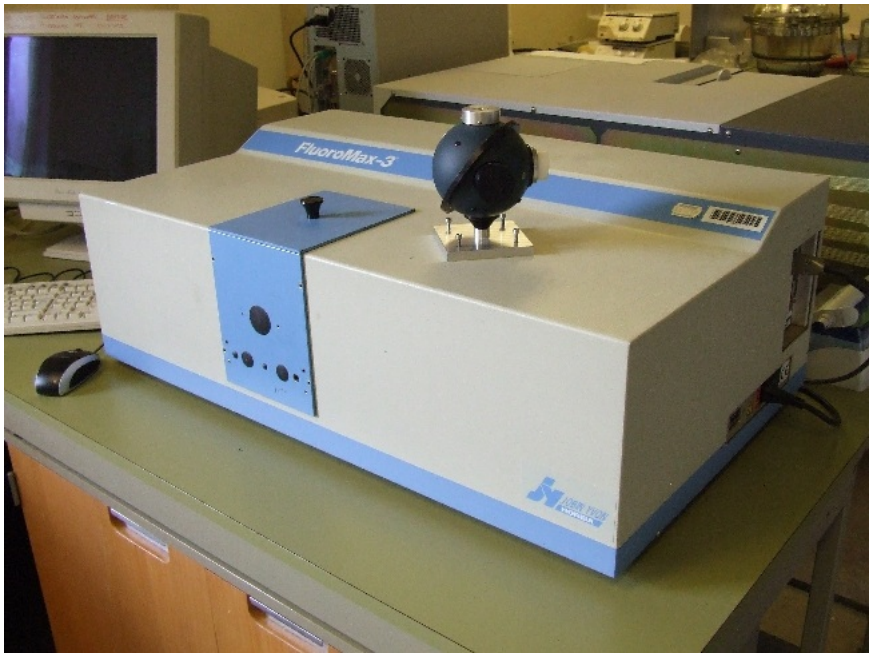

Figure 3.15: Photograph of the Jobin Yvon Horiba Fluoromax 3 used to measure photoluminescence spectra, along with the 10 cm integrating sphere for photoluminescence quantum yield measurements.

located between the excitation monochromator and the sample compartment corrects for the wavelength response of the light source. Slit widths for both monochromators can be varied manually to improve the intensity of the signal, although this is at the cost of reducing the resolution of the measurement.

By exciting the sample at a single excitation wavelength and varying the wavelength of the emission monochromator, the photoluminescence emission spectrum of a material may be obtained. Alternatively, an excitation spectrum may be measured by varying the wavelength of the excitation monochromator and collecting emission at a single wavelength, which can yield information about which of the transitions seen in the absorption spectrum are involved in the excitation of the sample. They are useful for choosing suitable excitation wavelengths to use in measurements of emission spectra for example when measuring iridium complexes where $\pi - \pi^*$ transitions may be the

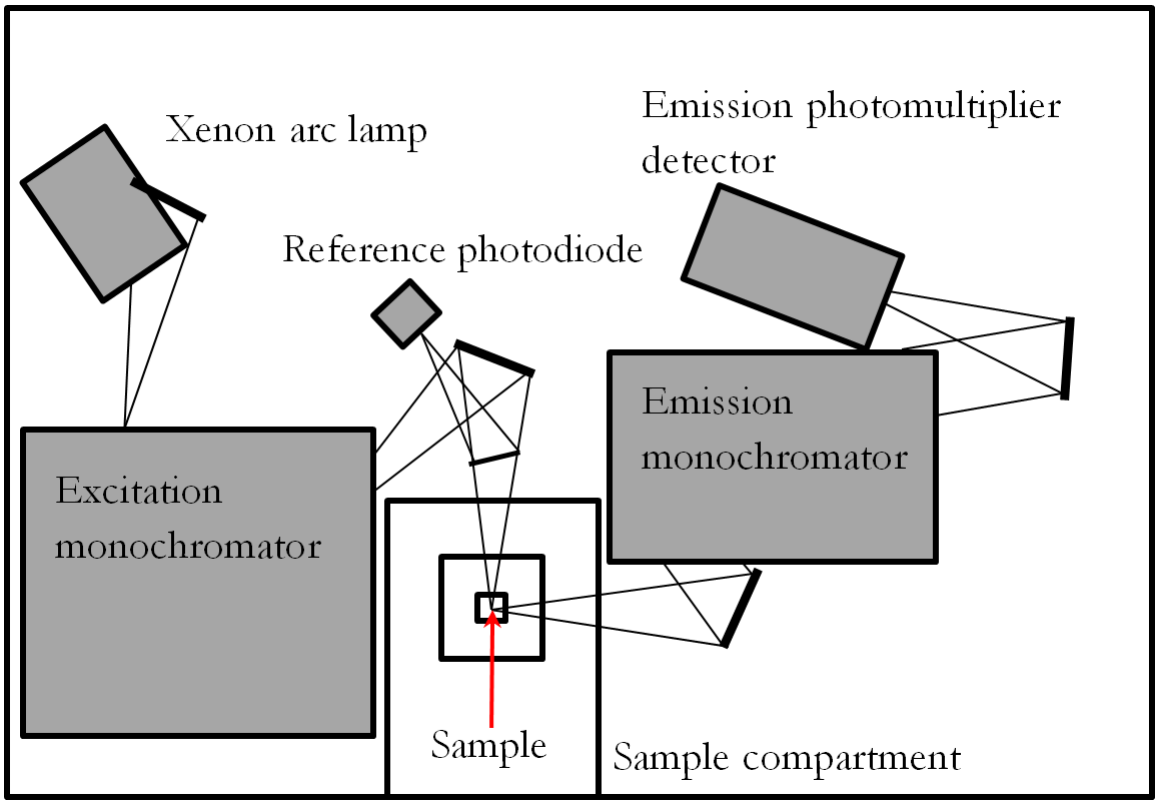

Figure 3.16: Simplified optical diagram of the Jobin Yvon Horiba Fluoromax 3 showing the approximate arrangements of the arc lamp, monochromators and detectors relative to the sample. Detailed components and optical paths of the monochromators are not shown, along with the lamp power supply and instrument controllers. Figure adapted from [10].

most prominent band in the absorption spectra but excitation is driven primarily by metal to ligand charge transfer (MLCT) transitions.

3.3.3 Quantum yield measurements

The photoluminescence quantum yield (PLQY) of a material can be defined as the ratio of the number of photons emitted to the number of photons absorbed by the material. It is a measure of how much light is emitted from a sample compared to the amount of light absorbed, and can be used with measurements of photoluminescence

lifetime to determine non-radiative decay rates as shown in equation 3.6,

$$\Phi_{PL} = \frac{k_r}{k_r + k_{nr}} = k_r \tau, \tag{3.6}$$

where Φ_{PL} is the quantum yield, τ is the lifetime of the excited state and k_r and k_{nr} are the radiative and non-radiative decay rates respectively.

Two methods of determining quantum yields were used, the first being a comparative method used for measuring the PLQY of solutions. The second is an absolute measurement involving an integrating sphere which was used primarily for measuring thin films, although the method can also be used to measure solutions. Both methods involved use of the Jobin Yvon Horiba Fluoromax 3 to measure emission of the sample as described above, and all spectra were multiplied by a calibration curve correcting for the spectral response of the Fluoromax (and integrating sphere, if used).

Comparative method: The comparative method requires use of a reference standard of known quantum yield to which the material being tested is compared. Common standards include 9,10-diphenylanthracene (DPA, $\Phi_{PL} = 0.95$ in dilute cyclohexane solution [11]), quinine sulphate ($\Phi_{PL} = 0.54$ in 0.1M H_2SO_4 [12]) and $Ir(ppy)_3$ ($\Phi_{PL} = 0.4$ in deaerated toluene solution [13]). Equation 3.7 is used to calculate the PLQY of the sample being measured [14], where I is the integrated intensity of emission, OD is the absorption of the sample at the excitation wavelength, and η is the refractive index of the solvent. The subscript $_{\text{ref}}$ denotes values for the reference material used.

$$\Phi = \Phi_{\text{ref}} \frac{\eta^2}{\eta_{\text{ref}}^2} \frac{OD_{\text{ref}}}{OD} \frac{I}{I_{\text{ref}}} \tag{3.7}$$

The concentration of the solution was kept low, with an OD of less than 0.1 at the excitation wavelength to prevent any self quenching or self absorption effects. In practice, many measurements were taken for a range of sample concentrations, with at least five data points taken to ensure accuracy. A plot of I against OD yields a straight line graph passing through the origin, and the gradient of this graph was taken as the term I/OD in equation 3.7.

Solutions were thoroughly degassed in a Schlenk cuvette by repeated freeze-thaw cycles to remove any oxygen that would quench emission. The solution was frozen by immersing the bulb of the Schlenk cuvette in liquid nitrogen, before the air in the Schlenk cuvette was evacuated using a vacuum pump and the stopper on the cuvette closed. The solution was allowed to thaw, bubbling away any oxygen in the solution. Repeated freezing, evacuation and thawing (typically three cycles) of the solution ensured that the solution was thoroughly deaerated.

Absolute method: The absolute method used to measure PLQYs of thin films requires a commercial fluorimeter and integrating sphere without the need for a reference or laser excitation or CCD detection [15]. As it is not always possible to encapsulate films, and the measurement must take place in air rather than a nitrogen glove box due to the equipment used, the quantum yield values may be affected by oxygen quenching of emission. Additionally, thicker films may experience self absorption or self quenching effects, further reducing the PLQY. Quantum yields are calculated using equation 3.8.

$$\Phi = \frac{\int E\left(\lambda\right) \mathrm{d}\lambda}{\int I_{\mathrm{blank}}\left(\lambda\right) \mathrm{d}\lambda - \int I_{\mathrm{sample}}\left(\lambda\right) \mathrm{d}\lambda} \tag{3.8}$$

The absorption of the sample can be determined from the difference between the integrated intensity of the excitation beam when a blank substrate is present $I_{\text{blank}}(\lambda)$ and when the sample is being excited $I_{\text{sample}}(\lambda)$. This can be used in conjunction with the integrated emission resulting from excitation of the sample $E(\lambda)$ to calculate the quantum yield of the film.

3.4 Ellipsometry

Thin film thickness measurements were obtained using a J. A. Woollam Variable Angle Spectroscopic Ellipsometer (VASE), shown in Figure 3.17. Ellipsometry is an indirect method of measuring optical constants such as the refractive index n, extinction coefficient k and thicknesses of thin films. A model using optical constants and film thicknesses as parameters must be fitted to the measured experimental data. The equipment consists of a xenon arc lamp and monochromator (HS-190) which generates a beam of light of a known polarisation state incident on the sample to be measured [16]. The beam reflects off the sample and passes through an iris into an analyser that measures two parameters, Ψ and Δ, that describe the elliptical polarisation state of the reflected beam [17]. A schematic of the general configuration of the Ellipsometer hardware is shown in Figure 3.18. Ellipsometry is very sensitive to the thickness of a thin film, and as it does not depend on the intensity of light reflected, it can be more accurate than reflectivity methods.

The resulting polarisation state of the beam can be described as having p- and s- components, where the p direction describes light where the electric field lies in the plane of incidence, and the s direction describes light where the electric field lies

Figure 3.17: Photograph of the J A Woollam VASE ellipsometer used for thin film thickness measurements.

perpendicular to the plane of incidence (from the German *Senkrecht*, meaning perpendicular). The parameters Ψ and Δ can be related to the complex reflectance ratio ρ of the reflection coefficients for s- and p- polarised light $\widetilde{R}_s$ and $\widetilde{R}_p$.

$$\rho = \frac{\widetilde{R}_p}{\widetilde{R}_s} = \tan(\Psi)\exp(i\Delta) \tag{3.9}$$

It can be shown by analysis of the Jones matrices of the system [17] that, for a rotating analyser ellipsometer, the intensity at the detector I_D can be expressed as a function of Δ, Ψ, the azimuthal angle of the analyser A and the azimuthal angle of the input polariser P to the plane of incidence as follows:

$$I_D \propto 1 + \frac{\tan^2\Psi - \tan^2 P}{\tan^2\Psi + \tan^2 P}\cos(2A) + \frac{2\tan\Psi\cos\Delta\tan P}{\tan^2\Psi + \tan^2 P}\sin(2A)\,. \tag{3.10}$$

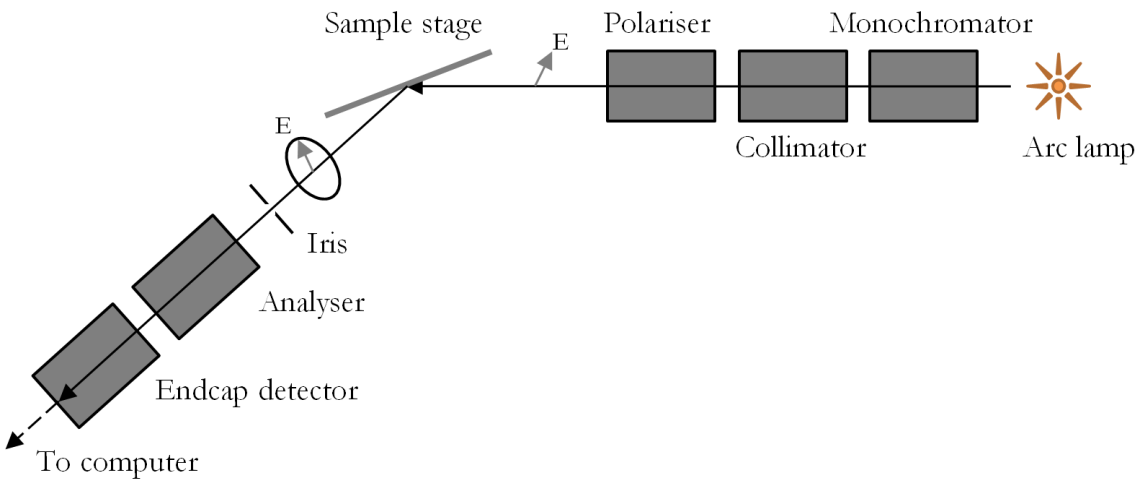

Figure 3.18: General configuration of ellipsometry hardware. A monochromatic, linearly polarised light source reflects off a sample. The resulting reflected beam is elliptically polarised and passes through an analyser that measures the resulting polarisation state.

This can be rewritten as

$$I_D \propto 1 + \alpha \cos(2A) + \beta \sin(2A) \tag{3.11}$$

where α and β are Fourier coefficients that can be obtained from a Fourier transform of the detector signal. This leads to equations 3.12 for Ψ and Δ in terms of α, β and P, which can all be obtained from the detector signal and system alignment.

$$\begin{aligned} \tan\Psi &= \sqrt{\frac{1+\alpha}{1-\alpha}}\,|\tan P| \\ \cos\Delta &= \frac{\beta}{\sqrt{1-\alpha^2}}\frac{\tan P}{|\tan P|} \end{aligned} \tag{3.12}$$

Samples were prepared on Si/SiO_2 wafers with a known SiO_2 layer thickness, which had been cleaned by the same procedure used for device substrates. The thin film to be investigated was spin coated onto the substrate from the same solution and under

the same conditions used for device fabrication.

The WVASE32 software is used to control the hardware, set experimental parameters and analyse the data. A screenshot of this software is shown in Figure 3.19. The experimental procedure begins by mounting a sample on the central sample stage, held in place by means of a vacuum. The sample stage is rotated and aligned using a Si quadrant detector to ensure that the incident beam is normal to the surface of the sample. A z-axis alignment is then performed to maximise the intensity of reflected light incident on the iris of the analyser unit. Calibration of the system is required once the hardware is initialised, in which case a calibration wafer is mounted and aligned first instead of the sample. Calibration is performed in order to redetermine certain operating values such as the analyser and polariser offset that may change slightly or be a random value on initialisation of the hardware. After calibration and alignment of the sample, a spectroscopic scan is performed where values of Ψ and Δ are measured in a wavelength range of 400 - 1000 nm in 10 nm steps, and two angles of incidence of 65° and 75°.

Once experimental data has been collected, a model is built consisting of the silicon and silicon dioxide layers, with known properties and thickness, and the unknown layer to be measured. This is modelled as a Cauchy layer where the refractive index n is described as a function of wavelength λ according to

$$n(\lambda) = A + \frac{B}{\lambda^2} + \frac{C}{\lambda^4}, \tag{3.13}$$

where A, B and C are constants used to parameterise the model. Expected values

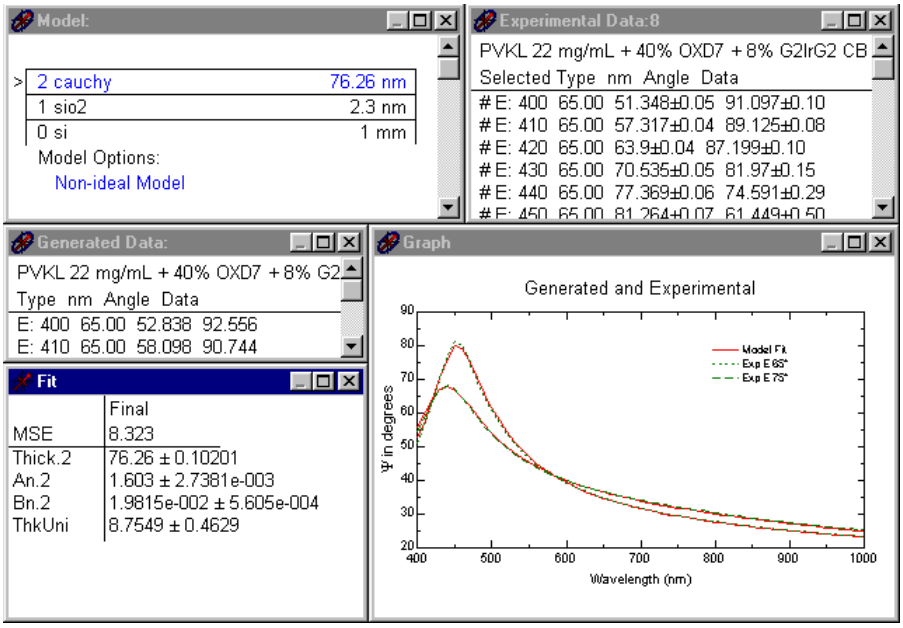

Figure 3.19: Screenshot of the WVASE32 program used to fit a model to the experimental data.

of Ψ and Δ can be calculated from the estimated values of n, k and thickness used by the model. A regression analysis is used to change the parameters of the model iteratively in order to minimise the mean square error (MSE) between the model and the experimental data. Once the process has yielded a minimum MSE, and the change in MSE is within a certain limit for each further iteration, the model fitting is complete and the film thickness and optical constants used to parameterise the model are optimised.

References

[1] K. Sugiyama, H. Ishii, Y. Ouchi & K. Seki, *Journal of Applied Physics* **87** (2000), 295 - 298

[2] D. E. Bornside, C. W. Macosko & L. E. Scriven, *Journal of Imaging Technology* **13** (1987), 122 - 130

[3] C. W. Extrand, *Polymer Engineering and Science* **34** (1994), 390 - 394

[4] Kurt J. Lesker Company Ltd., *Spectros II Deposition System Training Manual/Operating Instructions V1.0*

[5] S. R. Forrest, D. D. C. Bradley & M. E. Thompson, *Advanced Materials* **15** (2003), 1043 - 1048

[6] W. D. Wright, *Transactions of the Optical Society* **30** (1929), 141 - 164

[7] T. Smith & J. Guild, *Transactions of the Optical Society* **33** (1932), 73 - 134

[8] K. T. Kamtekar, A. P. Monkman & M. R. Bryce, *Advanced Materials* **22** (2010), 572 - 582

[9] Shimadzu Corporation, *Shimazdu UV-VIS-NIR Spectrophotometer Instruction Manual* (2004)

[10] Jobin Yvon Horiba, *Spex Fluoromax-3 Spectrofluorometer Hardware Manual* (1999)

[11] J. V. Morris, M. A. Mahaney & J. R. Huber, *Journal of Physical Chemistry*, **80** (1976), 969 - 974

[12] W. H. Melhuish, *Journal of Physical Chemistry* **65** (1961), 229 - 235

[13] K. A. King, P. J. Spellane & R. J. Watts, *Journal of the American Chemical Society*, **107** (1985), 1431 - 1432

[14] A. T. R. Williams, S. A. Winfield & J. N. Miller, *Analyst*, **108** (1983), 1067 - 1071

[15] L.-O. Pålsson & A. P. Monkman, *Advanced Materials*, **14** (2002), 757 - 758

[16] J. A. Woollam Co., Inc., *VASE Series Ellipsometers Hardware Manual* Rev 3.1 (1998)

[17] J. A. Woollam Co., Inc., *Guide to Using WVASE32 Software for VASE and M-44 Ellipsometers*

4 New high triplet electron transport materials and optimisation of single layer solution processable blue OLEDs

In this chapter, devices testing new high triplet electron transport materials synthesised in the Department of Chemistry at the University of Durham [1] are presented, as well as the optimisation of single layer solution processable blue OLED devices. The latter devices utilise new sky blue FIrpic derivative iridium emitters where the ligands incorporate branched aryl ring substituents. Additionally, literature reports of electron transport materials for polymer blend devices and sky blue dopants are reviewed, as well as reports of high efficiency sky blue solution processable OLED devices.

4.1 Review

In order to fabricate highly efficient organic light emitting diodes, the use of good electron transporting materials is important for balanced charge transport properties. In particular, as the hole mobility of PVK is higher than that of electrons, using PVK as a host requires additional electron transport materials for the fabrication of highly efficient devices.

Electron transport materials are often included in the device structure as a separate evaporated layer, which also acts as a hole blocking layer. For solution processable devices electron transport materials are often blended in with the host and dopant materials for ease of processing, although fabrication of multilayer devices with small

molecule solution processable electron transport layers has also been reported [2].

Two common commercially available electron transport materials used in polymer blends are 1,3-bis[(4-tert-butylphenyl)-1,3,4-oxadiazolyl]phenylene (PBD) or 1,3-bis(5-(4-tert-butylphenyl)-1,3,4-oxadiazol-2-yl)benzene (OXD-7). The structures of PBD and OXD-7 are shown in Figure 2.6.

Studies comparing the performance of PBD and OXD-7 in devices containing the commercially available sky blue emitter FIrpic (iridium(III) bis[4,6-(difluorophenyl)-pyridinato-N,C^2]picolinate) have been reported. Yang *et al.* [3] fabricated single layer devices with the emissive layer consisting of PVK + 40% OXD-7 or PBD + 10% FIrpic, and obtained higher brightness with OXD-7 as well as a higher device efficiency of 15 cd A^{-1} for OXD-7 compared to approximately 7 cd A^{-1} for PBD. Additionally a long lived component to the phosphorescence decay was observed with PBD.

This was attributed to the lower triplet energy of PBD (2.46 eV [4]) compared to OXD-7 (2.7 eV [5]) leading to triplet energy exchange between the electron transport materials and FIrpic (with a triplet energy of 2.6 eV). It was noted that the comparable triplet energies of OXD-7 and FIrpic would still lead to some triplet energy exchange, and that selecting high triplet energy electron transporting materials is important to avoid this triplet harvesting.

Lee *et al.* [6] also fabricated single layer devices consisting of PVK doped with FIrpic and either OXD-7 or PBD. They reported a device efficiency of 3.4 cd A^{-1} for OXD-7 compared to just 0.4 cd A^{-1} for PBD, confirming the findings of Yang *et al.* They also fabricated devices with a separate evaporated layer of either OXD-7 or PBD, and found that while the performance of multilayer OXD-7 devices was comparable with that of

the blended OXD-7 devices, the performance of multilayer PBD devices was improved by up to five times that of the blended PBD device by increasing the thickness of the PBD electron transport layer. This suggests that separating the PBD from the blue emitter reduces the energy transfer, improving efficiency.

As deep blue dopant emitters are developed, and as the triplet energy of OXD-7 is comparable to that of FIrpic, there is a corresponding need for high triplet electron transport materials to avoid energy transfer. Reviews of new electron transporting materials for OLED devices have been published in 2004 [7] and 2005 [8], with areas of research commonly focusing on oxadiazole or triazole derivatives. The first half of this chapter, section 4.2, describes the testing of a new range of high triplet energy oxadiazole derivatives synthesised at Durham.

The studies summarised above are not the highest efficiency devices reported for single layer PVK:OXD-7:FIrpic devices however, and it is clear that significant optimisation of device structure and emissive layer composition is necessary to achieve highly efficient OLED devices. Improving on their initial reported value of 15 cd A^{-1} for single layer OXD-7 devices above, Yang *et al.* attained a device efficiency of 18.2 cd A^{-1} by reducing the concentration of FIrpic to 5% and reducing the annealing time of the emissive layer [3]. Emissive layer thicknesses were not reported for these devices.

Other reports of highly efficient PVK:OXD-7:FIrpic single layer devices include a report by Wu *et al.* [9] of a 15.6 cd A^{-1} device with a 70 - 80 nm emissive layer with FIrpic doped at 10% and a Ba/Al cathode. Zacharias *et al.* [10] reported a device reaching 17 cd A^{-1} with a 75 nm emissive layer of PVK:OXD-7:FIrpic doped in the ratio 67:28:5 and a CsF/Al cathode. This could be increased to 19.2 cd A^{-1} with

inclusion of a cross linkable hole transport layer.

Mathai *et al.* [11] reported a device reaching 22 cd A^{-1} with a 75 nm emissive layer of PVK + 30% OXD-7 + 10% FIrpic and a CsF/Al cathode. Finally, Li *et al.* [12] reported a 20 cd A^{-1} by with a device structure consisting of a 75 nm layer of PVK:OXD-7:FIrpic in the ratio 100:40:10 and a CsF/Al cathode. This device was subsequently optimised to 26.5 cd A^{-1} by inclusion of a poly(ethylene glycol) dimethyl ether additive.

One final consideration in the fabrication of highly efficient solution processable sky blue OLED devices is the use of FIrpic as the standard commercially available material. Having been used primarily in devices fabricated by vacuum deposition, FIrpic has poor solubility in common organic solvents, which leads to aggregation in thin film and increased concentration quenching.

The second half of this chapter, as well as chapter 5, describes the characterisation of new sky blue iridium emitters with solubilising side chains in order to reduce this aggregation and improve device efficiency. In this chapter, simple single layer devices containing one of these new emitters are optimised, followed by a comparison of the first series of emitters.

4.2 New high triplet electron transport materials

This section reports the initial device testing of a new group of diaryloxadiazole compounds synthesised by Dr. Yonghao Zheng in the Department of Chemistry at the University of Durham. These materials have a twisted chemical structure with the intention of reducing conjugation thereby aiming to increase the triplet energy of the

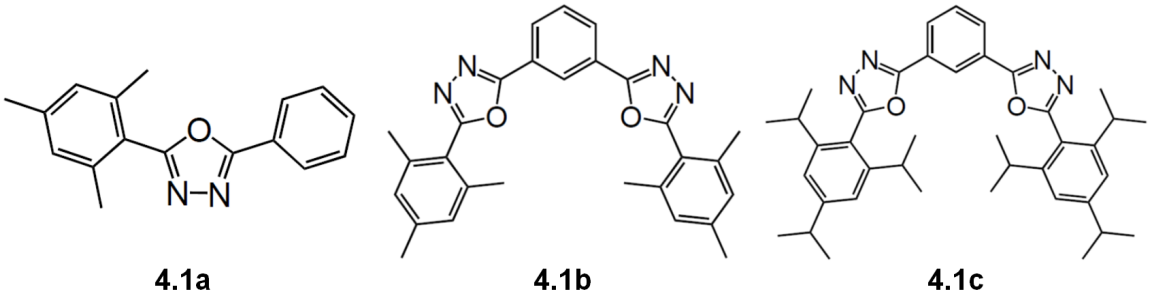

Figure 4.1: Chemical structures of the high triplet oxadiazole based electron transport materials tested in this section [1].

material. The materials were compared to commercially available OXD-7 both in multilayer blue OLED devices with FIrpic as a commercially available sky blue emitter, as well as in single layer devices containing a blend of only PVK and the electron transport material in order to observe the exciplex emission originating from these two materials.

4.2.1 Materials

The chemical structures of the new electron transporting materials tested in this section are shown in Figure 4.1, and their synthetic procedure is detailed in reference [1] as well as photophysical and theoretical studies.

In the initial photophysical and theoretical studies it was found that materials **4.1a-c** have higher LUMO levels than OXD-7 and correspondingly have a larger HOMO-LUMO gap. The principle of twisting the chemical structure in order to increase the triplet energy was demonstrated for similar materials, and it is therefore expected that the triplet level of these molecules should in turn be higher than that of OXD-7 [1].

4.2.2 Device results and discussion

The first set of devices tested the three electron transport materials **4.1a-c** against commercially available OXD-7 in electrophosphorescent devices with the standard iridium complex FIrpic as a sky blue emitter.

The devices were fabricated in a multilayer structure incorporating a 25 nm hole transporting layer of high molecular weight PVK with an emissive layer consisting of the electron transporting material doped into low molecular weight PVK at 30% and FIrpic doped at 2%. The emissive layer was spin coated from toluene solution, and due to the insolubility of the high molecular weight PVK in this solvent, well defined multilayer structures can be formed with this method [13]. The structure of the devices were therefore ITO // PEDOT:PSS // PVKH (20 nm) // PVKL:ET:FIrpic (100:30:2) (*ca.* 81 nm) // Ba (4 nm) // Al (100 nm).

Current density, brightness and efficiency data for this set of devices are shown in Figure 4.2. Both the efficiency and brightness of all devices are comparable despite the change in electron transport material. The variation between these devices is similar to the variation expected between different devices with identical structure and composition. It can be concluded that these new materials are as good as OXD-7 with very similar device performance, and the presumed higher triplet energy makes little difference for sky-blue dopant emitters.

The turn on voltages of all devices are similar, with 10 - 11 V required to attain a brightness of 10 cd m^{-2}. The lowest turn on voltage of 10 V was observed for OXD-7, and the increase in turn on voltage across the material set correlates with the increase

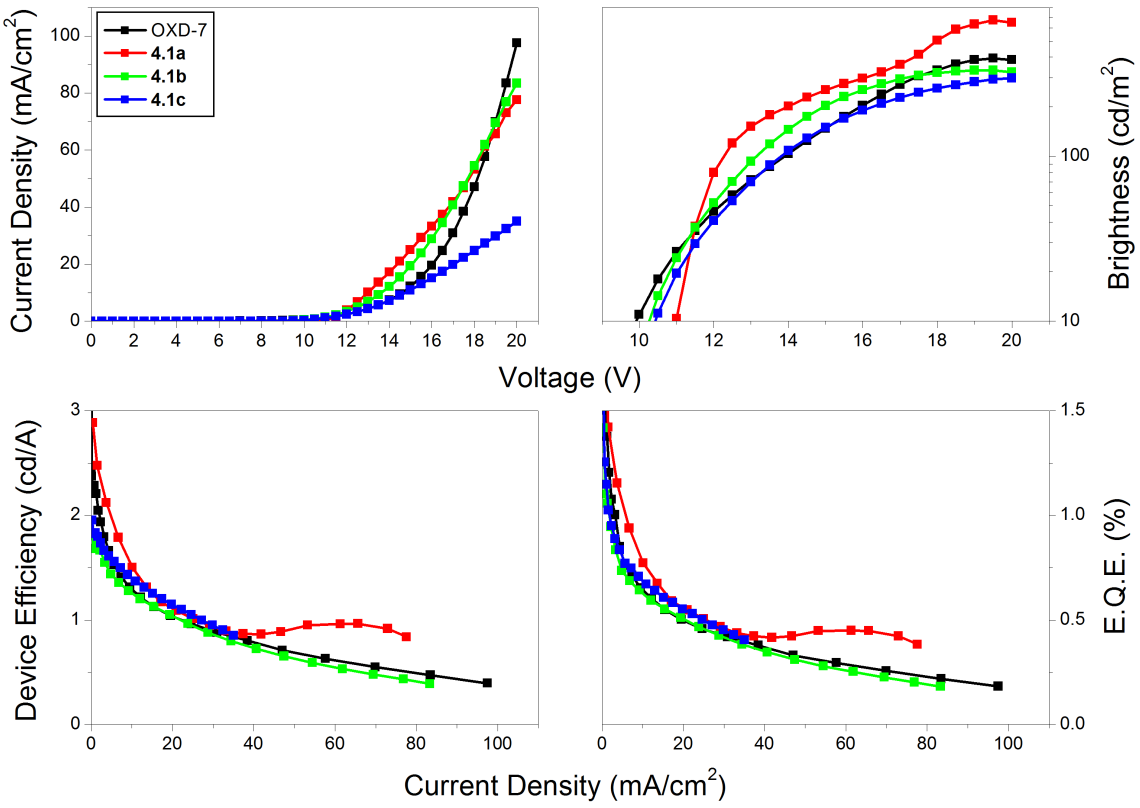

Figure 4.2: *J-V*, *L-V* and device efficiency data of multilayer devices consisting of PVK blended with each electron transport material and FIrpic. ITO // PEDOT:PSS // PVKH (20 nm) // PVKL:ET:FIrpic (100:30:2) (*ca.* 81 nm) // Ba (4 nm) // Al (100 nm).

in LUMO level of the material. This suggests that with the lowest LUMO level of all materials studied, OXD-7 is still a slightly better electron transport material for sky-blue dopant materials despite the comparable performance in efficiency and brightness.

Electroluminescence spectra of these devices are shown in Figure 4.3. The sky blue emission peaking at 472 nm observed for all devices is that of FIrpic and the change of electron transport material has little effect on the electroluminescence spectrum.

Secondly, single layer devices were fabricated without any dopant emitter in order to observe the PVK:ET exciplex emission. The device structure was ITO // PEDOT:PSS // PVKL:ET (100:30) (*ca.* 80 nm) // Ba (4 nm) // Al (100 nm). In terms of effi-

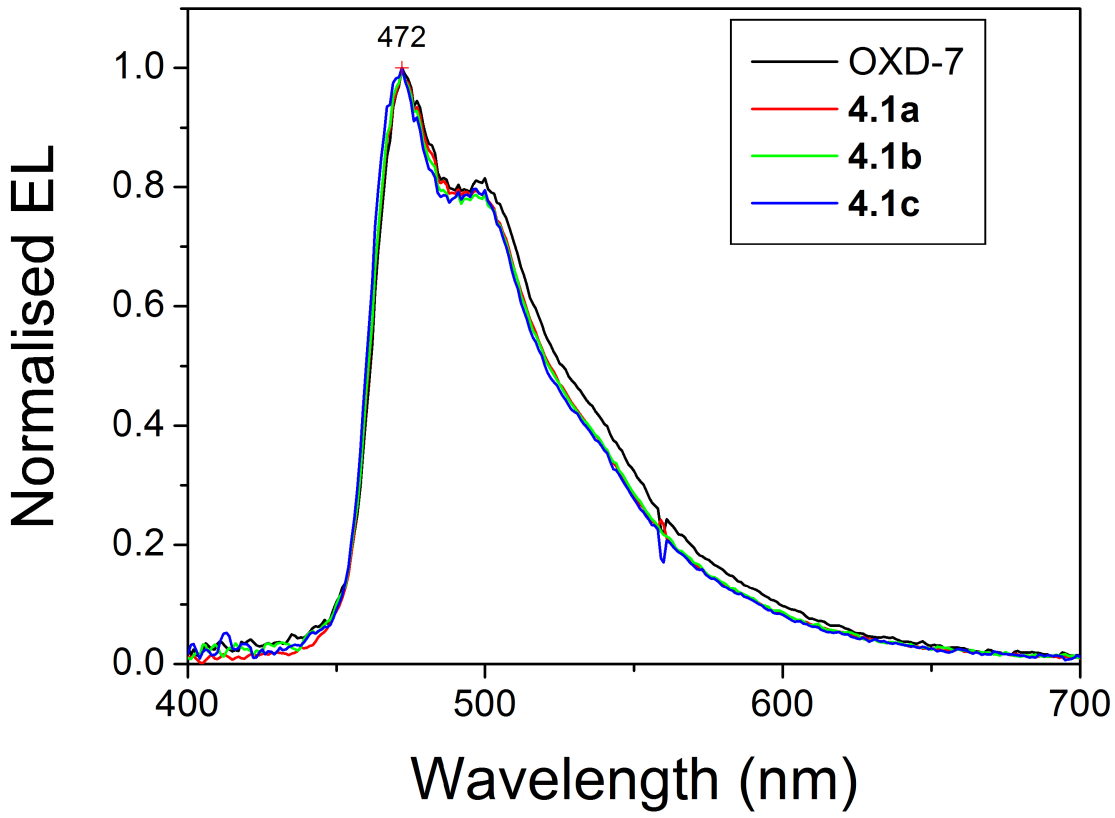

Figure 4.3: Normalised electroluminescence spectra of multilayer devices consisting of PVK blended with each electron transport material and FIrpic. All devices exhibit sky blue emission originating from FIrpic, and there is little effect of the change of electron transport material on device emission.

ciency and brightness, device performance (shown in Figure 4.4) was low as is expected from PVK devices with no dopant emitter. The highest efficiency and brightness was achieved using OXD-7, with a brightness of 80 cd m^{-2} and device efficiency of 0.35 cd A^{-1}, although the external quantum efficiency was comparable with other materials at just under 0.2%. Again, the turn on voltage was lowest for OXD-7 at 8 V, although the high turn on seen for the **4.1c** device here is likely to be mostly due to poor film quality rather than the material itself.

A hysteresis effect can be seen in the device efficiency and E.Q.E. plots of some of these devices, such as those of the **4.1b** device. This is caused by current heating

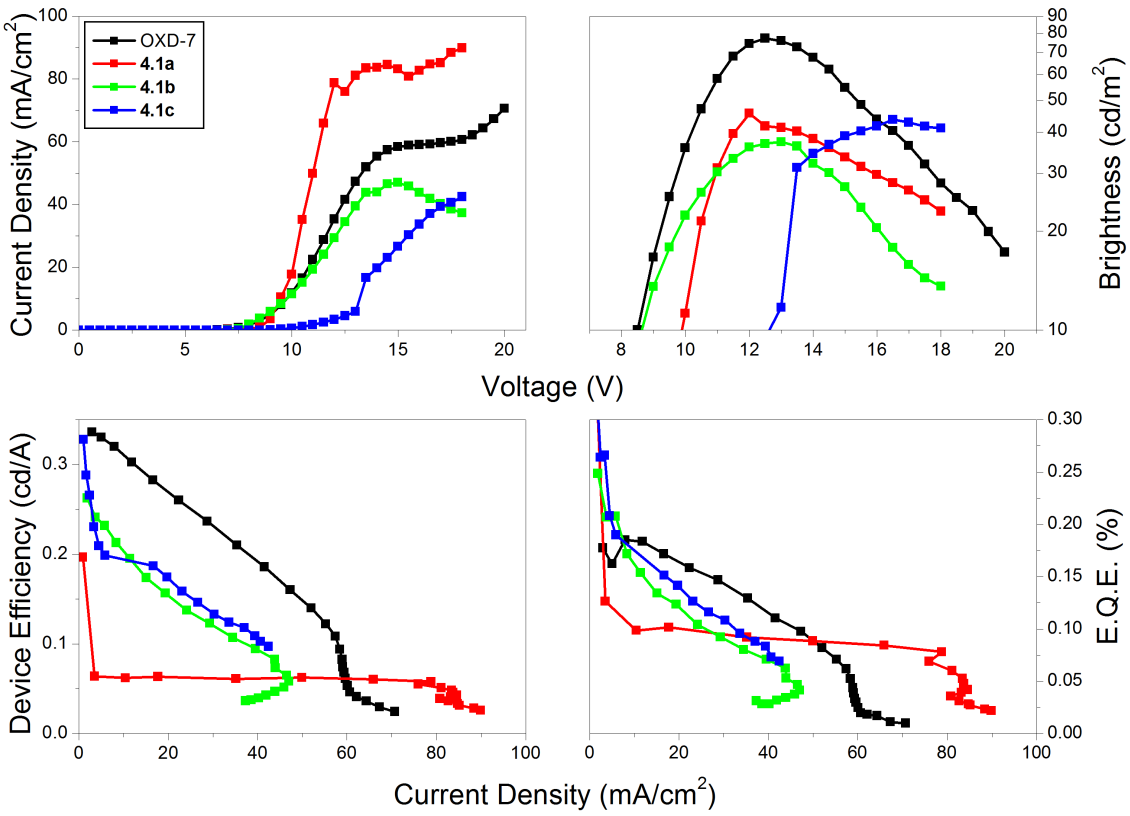

Figure 4.4: *J-V*, *L-V* and device efficiency data of single layer devices consisting of PVK blended with each electron transport material without any dopant emitter. Device structure ITO // PEDOT:PSS // PVKL:ET (100:30) (*ca.* 80 nm) // Ba (4 nm) // Al (100 nm).

degrading the polymer layer, leading to a decrease in current density at higher voltages, in conjunction with efficiency roll off.

Electroluminescence spectra of these devices are shown in Figure 4.5. The exciplex formed by PVK and OXD-7 is the most strongly redshifted, with a peak wavelength of 454 nm. The two materials **4.1b** and **4.1c** also exhibit emission from PVK:ET material exciplexes, but not as redshifted as OXD-7, peaking at 441 nm and 436 nm respectively. In contrast, the emission spectrum of the **4.1a** device peaks at 388 nm and is the same as the emission of a pure PVK device, with no exciplex formed between the host and **4.1a**.

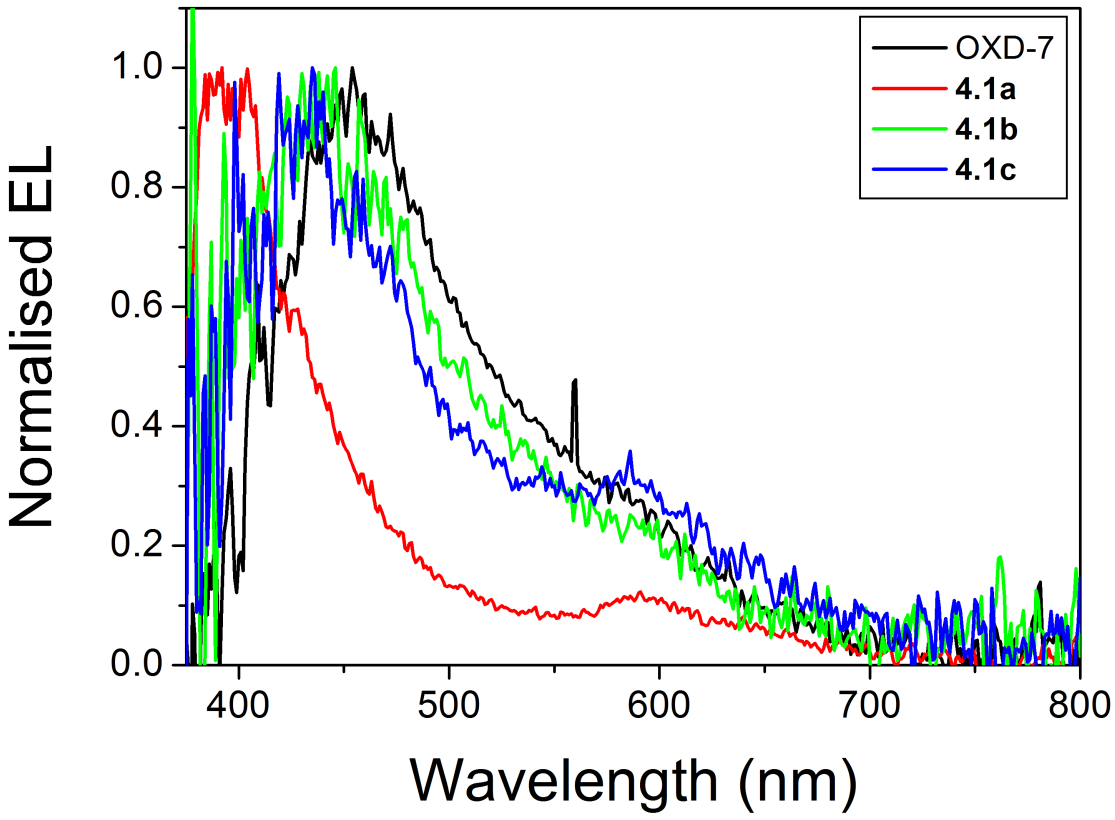

Figure 4.5: Normalised electroluminescence spectra of single layer devices consisting of PVK blended with each electron transport material, showing the exciplex emission observed from **4.1b-c** and OXD-7. The emission from the **4.1a** device is that of PVK.

A comparison between the electroluminescence of this device and a pure PVK device (structure ITO // PEDOT:PSS // PVK // Ba // Al) is shown in Figure 4.6, demonstrating that the emission of the PVK:**4.1a** device is the same as that of PVK.

Considering a model of exciplex emission consisting of an excited state on the LUMO of the electron transport material and the HOMO of the PVK host, these devices are consistent with the previous observation that the new materials **4.1a-c** have higher LUMO levels than OXD-7, and additionally suggest that the LUMO level of **4.1a** may be higher than that of PVK which indicates no loss of energy to exciplexes.

Although the triplet energies of these new materials are expected to be higher than

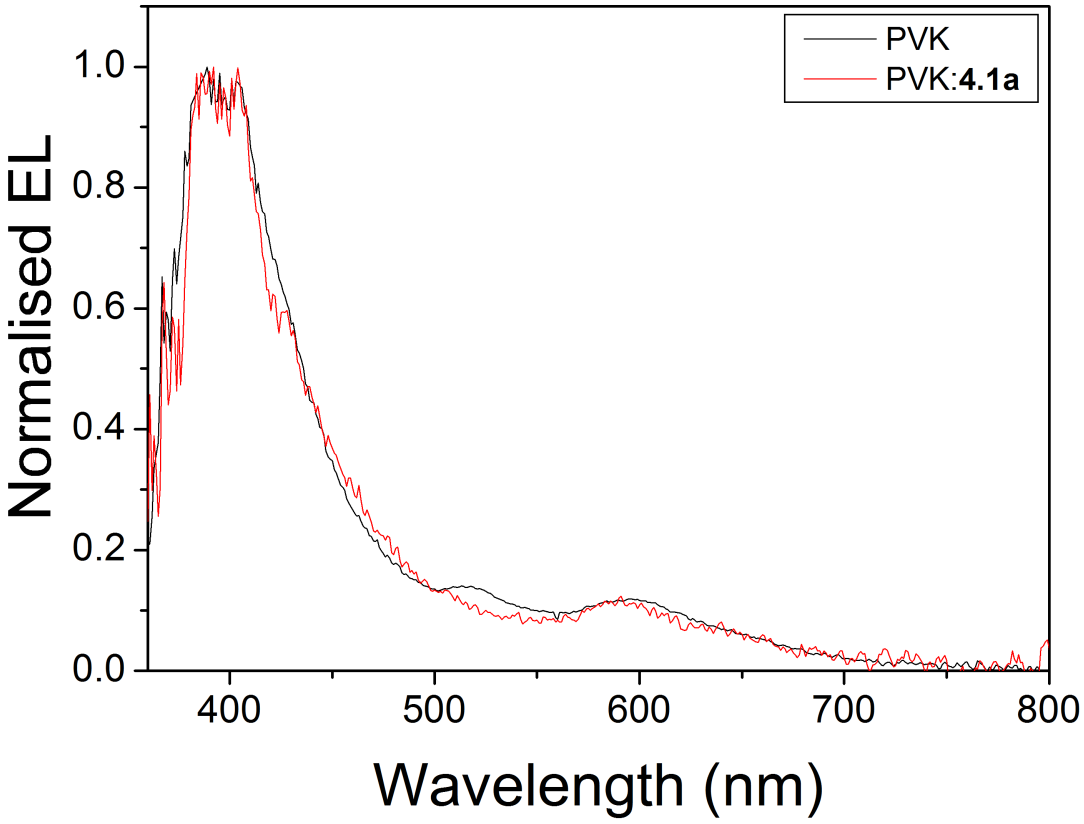

Figure 4.6: Comparison between the electroluminescence of the PVK:**4.1a** device and a pure PVK device (structure ITO // PEDOT:PSS // PVK // Ba // Al) demonstrating that the emission of PVK:**4.1a** is the same as that of PVK.

that of OXD-7, device performance across all the materials was comparable to OXD-7. Additionally, due to its lower LUMO level, OXD-7 is a better electron transporting material than the new materials tested. However with work ongoing towards high triplet hosts for deeper blue dopants, corresponding development of electron transport materials with high triplet energies is advantageous for deep blue OLED devices.

A number of attempts to determine the relative electron mobilities of the electron transport materials were carried out by fabricating electron only devices on a borosilicate glass substrate with the structure Al (100 nm) // PVK:ET // Ba (4 nm) // Al (100 nm). The PVK:ET layer was tested at varying thicknesses and electron transport

dopant concentrations. As aluminium replaces the ITO as the anode, the energy barrier becomes too large for hole injection to take place and the only current flow is that of electrons.

The devices fabricated were poor, exhibiting very high irreproducible and irregular current flow, often Ohmic in nature, before the devices broke down. Studies into the requirements for reliable electron transport devices have been carried out [14], and with thicker organic layers (beyond 300 nm) as well as substrates and bottom anodes with lower surface roughness, it is possible that good quality, repeatable electron only devices could have been fabricated. Due to the limited supply of materials, however, the development of successful single carrier devices for this set of electron transport materials was not possible.

4.3 Optimisation of single layer blue OLEDs

In this section, new sky blue iridium emitters with large bulky aryl ring side chains synthesised by researchers in the Department of Chemistry are introduced. Simple single layer devices using one of these emitters are optimised, with the emissive layer thickness, emitter concentration and electron transport concentration being varied. Finally, the series of new iridium emitters is compared with FIrpic. Due to both material supply and the results of the OXD material characterisation, commercially available OXD-7 purchased from Lumtec was used as the electron transport material in subsequent blue OLED devices.

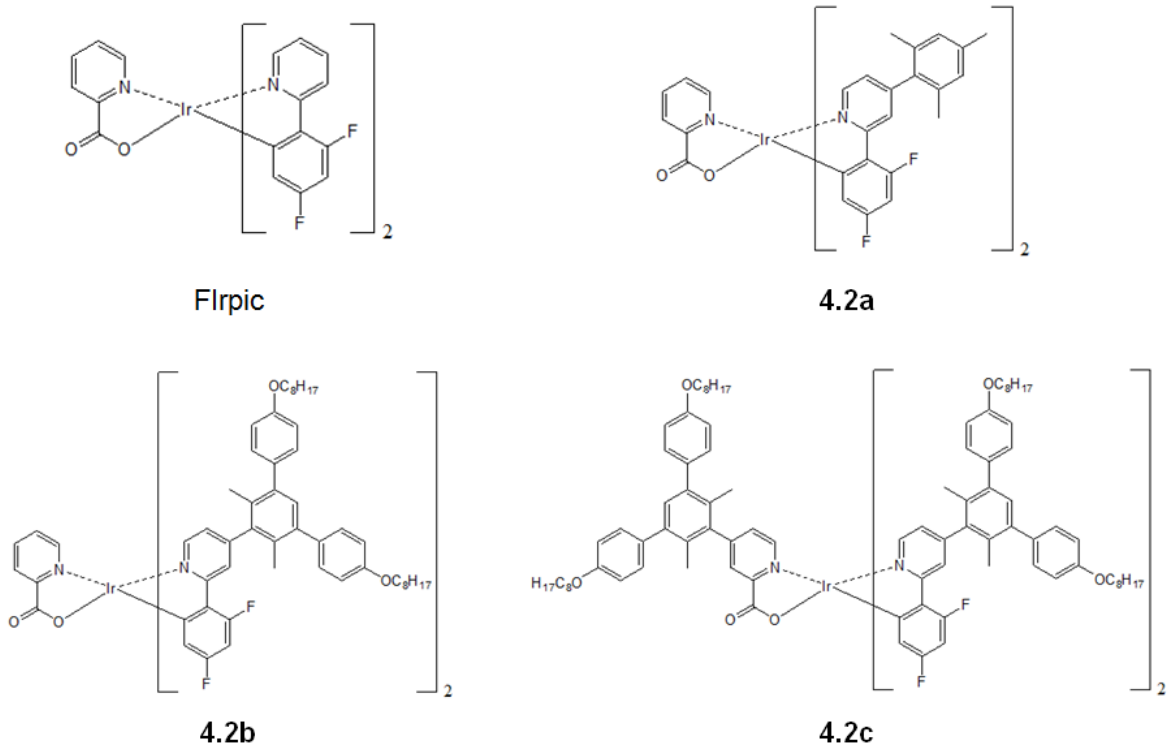

Figure 4.7: Chemical structures of the blue emitting iridium complexes **4.2a-c** characterised in this section as well as that of FIrpic. These aim to improve the solubility of FIrpic and, in the case of **4.2b-c**, shield the iridium core by functionalisation of the ligands with bulky aryl side chains.

4.3.1 Materials

Chemical structures of the three new sky blue iridium emitters characterised in this section are shown in Figure 4.7 as well as that of FIrpic. Complex **4.2a** has a mesityl group substituted on the ligand, which is expected to improve the solubility of the complex compared to FIrpic while retaining the sky blue emission.

Complexes **4.2b-c** both have a bulkier branched aryl ring side group substituted, with complex **4.2c** having the same side group located on the ancillary picolinate ligand. Similar dendrimer based ligands for iridium complexes have been reported [15–17]. In addition to the improvement in solubility, it is hoped that these ligands will add steric bulk and effectively shield one hemisphere of the iridium core [18] protecting it from

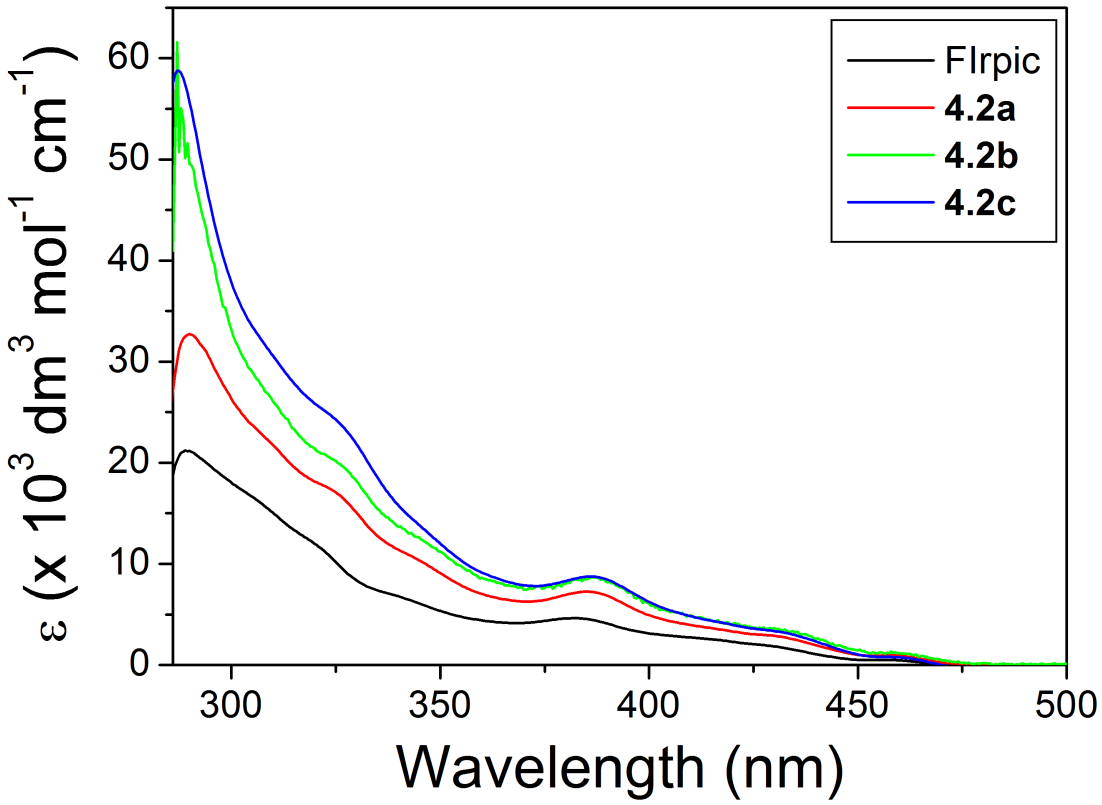

Figure 4.8: Extinction coefficient spectra of the three blue iridium emitters **4.2a-c** characterised in this section compared to FIrpic in dilute toluene solution.

energy transfer.

4.3.2 Absorption and photoluminescence spectra

Figure 4.8 shows the extinction coefficient (absorption) spectra of complexes **4.2a-c** and FIrpic in toluene solution. A general increase in the value of the absorption coefficient is seen as longer side chains are added to the molecule. Additionally, a slight redshift in features of approximately five nanometres is seen for the new emitters compared to FIrpic. The strong absorption observed below 350 nm is assigned to $\pi - \pi^*$ transitions centred on the ligand, while weaker metal to ligand charge transfer (MLCT) absorption bands are seen above 350 nm.

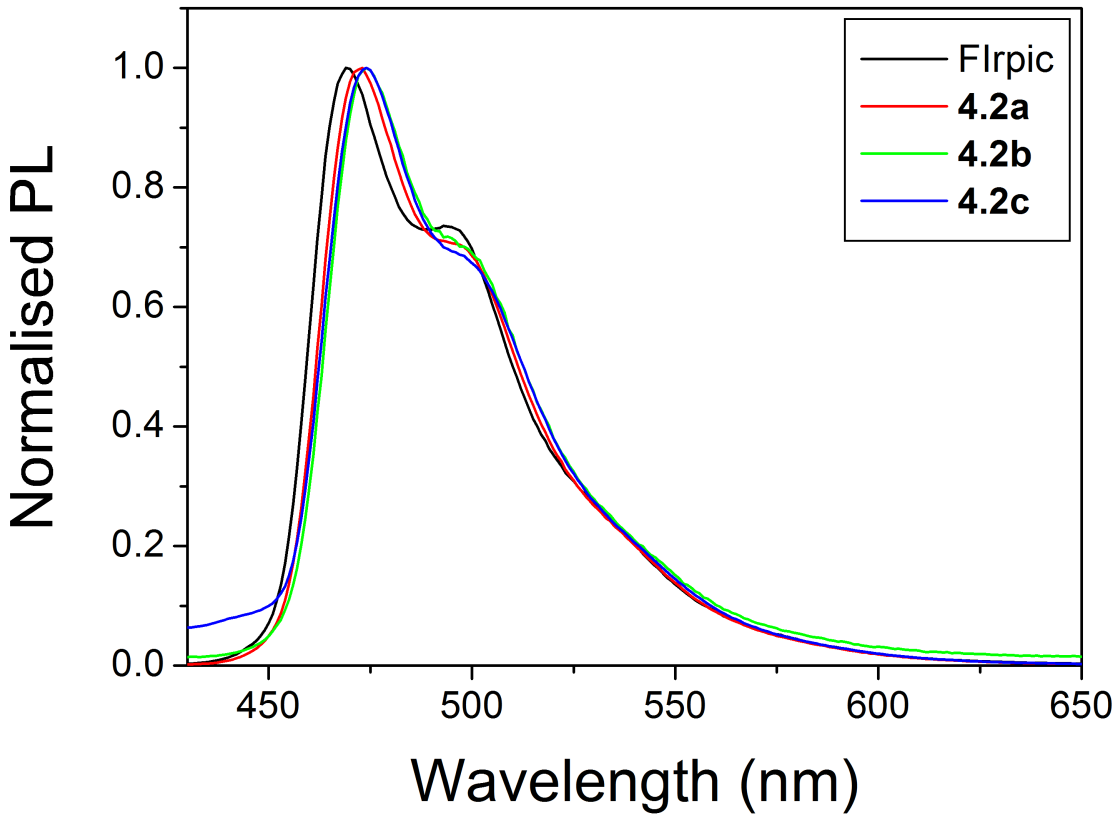

Figure 4.9: Normalised photoluminescence spectra of the three blue iridium emitters **4.2a-c** compared to FIrpic in dilute toluene solution. Excitation wavelength 400 nm.

Normalised photoluminescence spectra of complexes **4.2a-c** and FIrpic measured in dilute toluene solution are shown in Figure 4.9. The excitation wavelength was 400 nm. The emission of FIrpic peaks at 469 nm, while that of **4.2a** is redshifted to 473 nm. The emission of complexes **4.2b-c** are slightly redshifted further to 474 nm. In general the different substituent groups have no major effect on the emission.

4.3.3 Optimisation of emissive layer thickness

The first set of devices fabricated in the course of optimising single layer OLED devices involved varying the emissive layer thickness. By increasing the PVK concentration of the solution used to spin coat the emissive layer from 14 mg/ml to 18, 22 and 26 mg/ml

Device	Thickness [a] / nm	Turn-on [b] voltage / V	E.Q.E. [c] / %	Device [c] efficiency / cd A^{-1}	Brightness [c] / cd m^{-2}	Power [c] efficiency / lm W^{-1}
1	42.6	5.5	2.3	4.1	925	2.1
2	59.9	6.5	2.3	4.8	1003	2.2
3	74.2	6.5	4.2	8.8	1421	3.9
4	103.6	8.0	3.8	8.2	1026	3.1

Table 4.1: Summary of the performance of single layer **4.2c** devices with varying emissive layer thicknesses. Device structure ITO // PEDOT:PSS // PVK:OXD-7:Ir (100:40:8) // Ba (4 nm) // Al (79 nm).
[a]: Device thicknesses obtained by spin coating from PVK concentrations of 14, 18, 22 and 26 mg/ml chlorobenzene solution.
[b]: Voltage at which the device reaches a brightness of 10 cd m^{-2}.
[c]: Peak values for the device.

chlorobenzene solution, emissive layer thicknesses were increased and were measured to be 42.6 nm, 59.9 nm, 74.2 nm and 103.6 nm respectively. Due to the supply of materials available at the time of device fabrication, the iridium complex used in these devices, as well as subsequent devices, was **4.2c**.

Table 4.1 summarises the efficiency, brightness and turn-on voltage of these devices, while full *J*-*V*, *L*-*V* and device efficiency data are shown in Figure 4.10. It can be seen that, although peak brightnesses are similar for all devices, the highest brightness and highest device efficiencies are achieved for a 74 nm emissive layer thickness. This device attained a peak efficiency of 8.8 cd A^{-1} and 4.2% E.Q.E. and a peak brightness of 1,421 cd m^{-2}. As expected, a large increase in the turn on voltage is seen as the device thickness is increased.

Electroluminescence spectra of this set of devices are shown in Figure 4.11. The wavelength at which the emission peaks is the same for all emissive layer thicknesses tested at 477 nm. Increasing the thickness of the emissive layer, however, increases

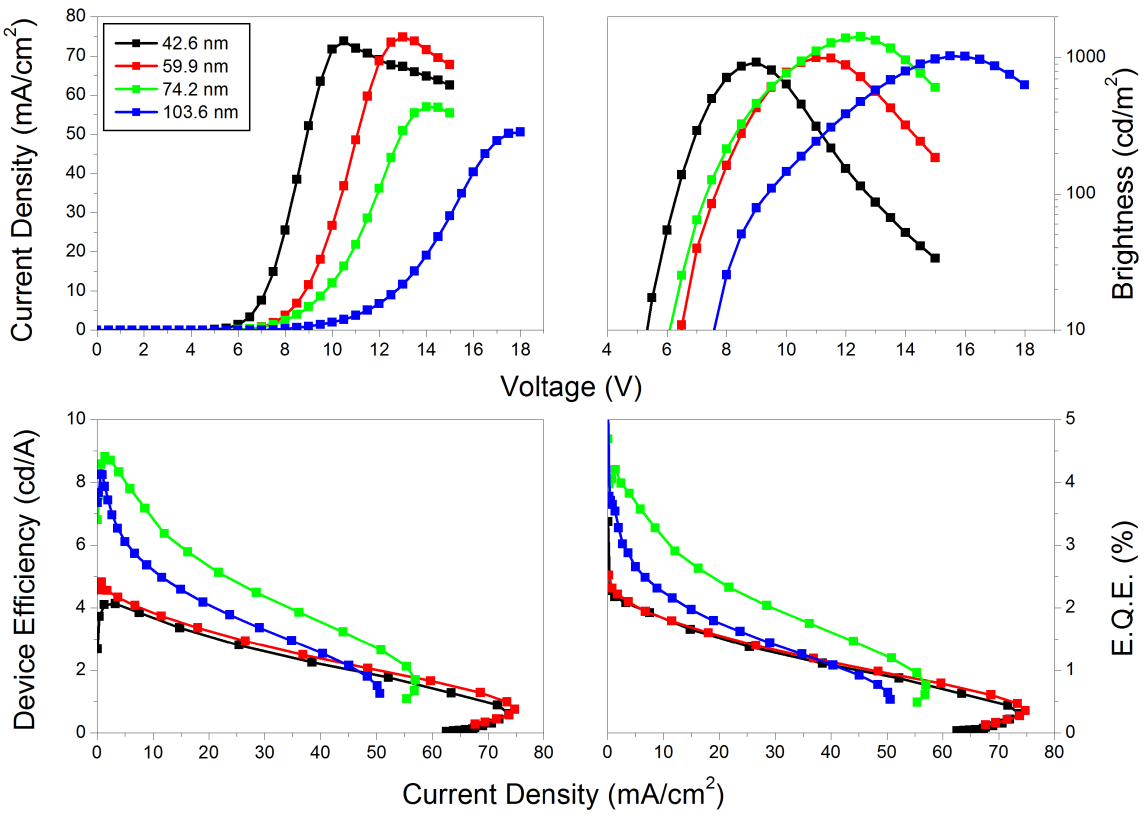

Figure 4.10: *J-V*, *L-V* and device efficiency data of single layer devices containing **4.2c** with varying layer thickness. Device structure ITO // PEDOT:PSS // PVK:OXD-7:Ir (100:40:8) // Ba (4 nm) // Al (79 nm). Increasing emissive layer thickness generally increases the turn on voltage, and the highest device efficiency was achieved with an emissive layer thickness of 74.2 nm.

the relative intensity of the emission shoulder above 500 nm. This may be due to the thicker emissive layer leading to increased self absorption, or a device microcavity effect.

As both the highest brightness and device efficiency were obtained for the 74.2 nm device, all devices in the following sections were fabricated aiming for an emissive layer thickness in this range.

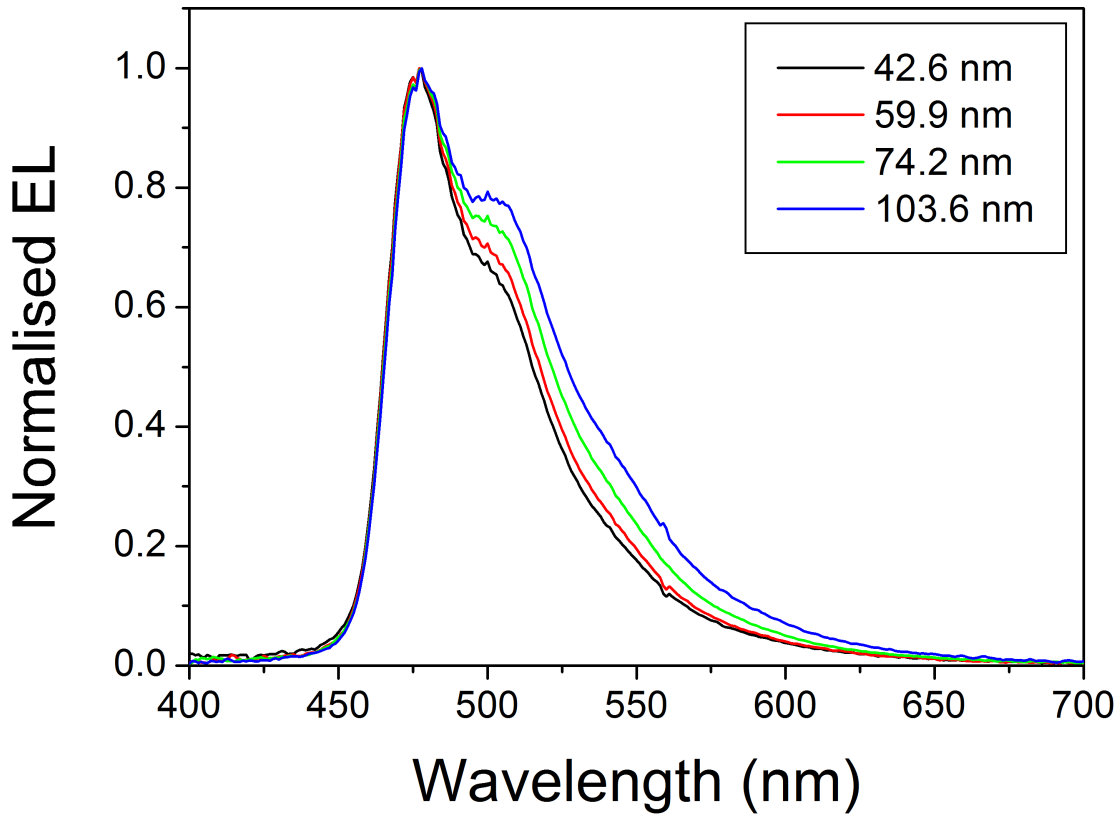

Figure 4.11: Normalised electroluminescence spectra of single layer devices containing **4.2c** with varying layer thickness. Device structure ITO // PEDOT:PSS // PVK:OXD-7:Ir (100:40:8) // Ba (4 nm) // Al (79 nm). Increasing layer thickness increases the relative intensity of the shoulder in the emission spectrum.

4.3.4 Optimisation of OXD-7 concentration

The following set of devices investigates the effect of varying the amount of OXD-7 doped in the emissive layer. Devices with the emissive layer composition PVK:OXD-7:Ir in the ratio 100:x:8, where x ranged from 20 to 80, were fabricated. Table 4.2 summarises the device brightness and efficiency, while full *J*-*V*, *L*-*V* and device efficiency data are shown in Figure 4.12.

The general trend for the devices, as the amount of OXD-7 in the emissive layer is increased, is an increase in the turn on voltage and a reduction in the overall current through the device.

OXD-7 concentration	Turn-on [a] voltage / V	E.Q.E. [b] / %	Device [b] efficiency / cd A^{-1}	Brightness [b] / cd m^{-2}	Power [b] efficiency / lm W^{-1}
20%	6.0	4.1	7.7	1946	3.6
30%	6.5	4.7	10.1	2214	4.2
40%	7.0	5.1	10.3	1571	3.9
50%	6.5	5.3	11.1	1869	4.9
60%	8.5	4.6	10.3	788	3.6
70%	9.0	4.5	10.2	673	3.3
80%	9.5	3.3	7.8	313	2.4

Table 4.2: Summary of the performance of single layer **4.2c** devices with varying concentrations of OXD-7. Device structure ITO // PEDOT:PSS // PVK:OXD-7:Ir (100:x:8) // Ba (4 nm) // Al (100 nm).
[a]: Voltage at which the device reaches a brightness of 10 cd m^{-2}.
[b]: Peak values for the device.

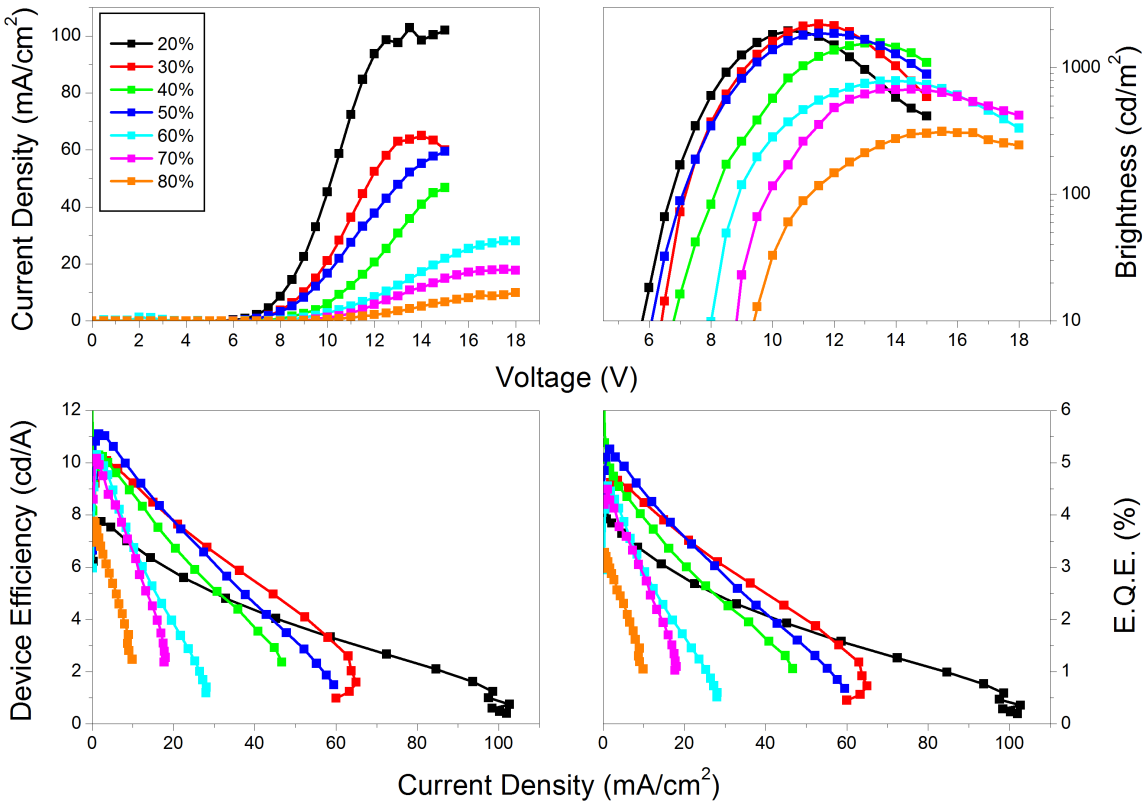

Figure 4.12: *J-V*, *L-V* and device efficiency data of single layer devices containing **4.2c** with varying concentrations of OXD-7. Device structure ITO // PEDOT:PSS // PVK:OXD-7:Ir (100:x:8) // Ba (4 nm) // Al (100 nm). Between 30% and 70% OXD-7 there is little variation in peak device efficiency but there is a significant increase in efficiency roll-off and decrease in brightness observed at concentrations of 60% and above.

Turn on voltages range from 6.0 V for 20% OXD-7 to 9.5 V for 80% OXD-7. However the variation in amount of OXD-7 included in the emissive layer leads in turn to an increase in the emissive layer thickness as the solution from which the layer is spin coated becomes more viscous. The thicknesses measured for the emissive layer ranged from 68 nm for 20% OXD-7 to 90 nm for 80% OXD-7. The thicknesses measured for the 30%, 40% and 50% OXD-7 dopant levels however were similar, ranging from 74 nm to 78 nm.

In order to account for this difference in thickness, Figure 4.13 shows the device

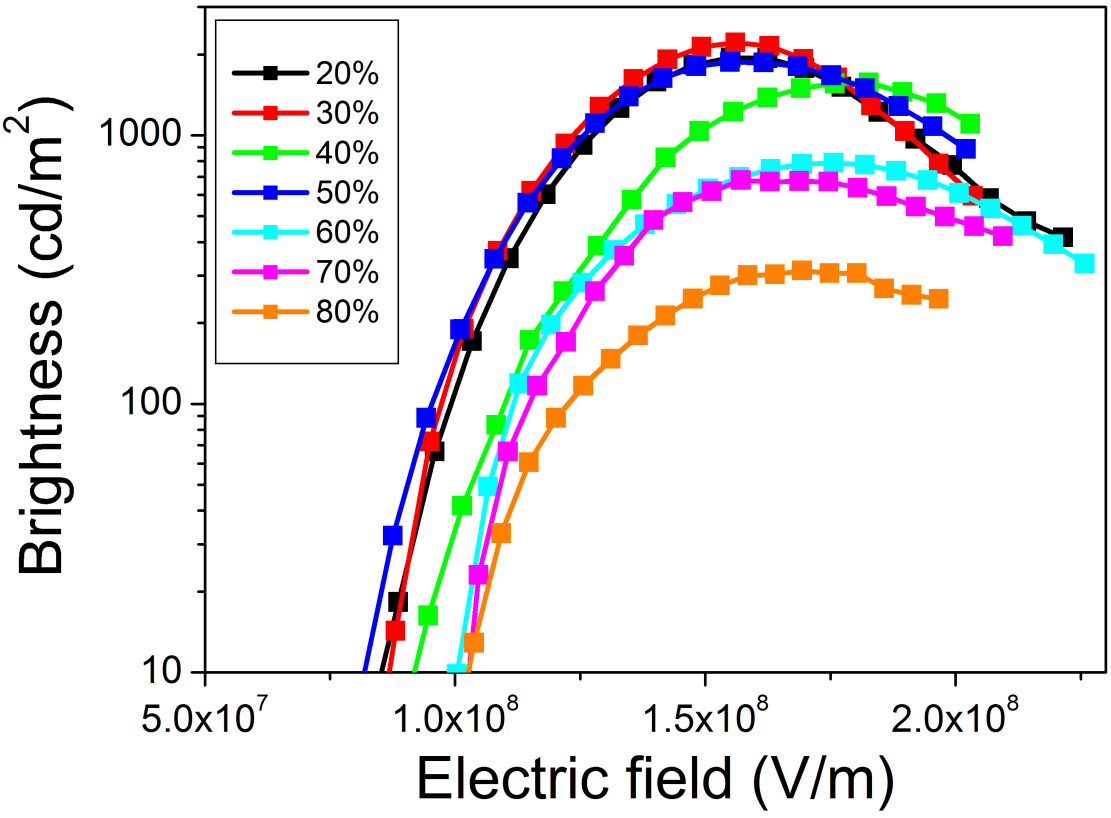

Figure 4.13: Plot of brightness against applied electric field for the same set of devices with varying OXD-7 concentration, accounting for the varying thickness of the device. There is a general trend towards a higher electric field needed to achieve 10 cd m^{-2} with higher OXD-7 concentration, but the turn on field for 50% OXD-7 was comparable to those of the lowest concentrations of 20% and 30%.

brightness plotted against applied electric field instead of applied voltage. Again, the general trend is for higher OXD-7 concentrations exhibiting a higher turn on field although the spread is somewhat reduced. The lowest turn on field was achieved with a concentration of 50% OXD-7, although this was comparable to that achieved with OXD-7 concentrations of 20% and 30%.

The peak device efficiency increases from 7.7 cd A^{-1} and 4.1% E.Q.E. for 20% OXD-7 to 10.1 cd A^{-1} and 4.7% E.Q.E. for 30% OXD-7. Maximum efficiencies for all devices from 30% OXD-7 to 70% OXD-7 are comparable to each other, although

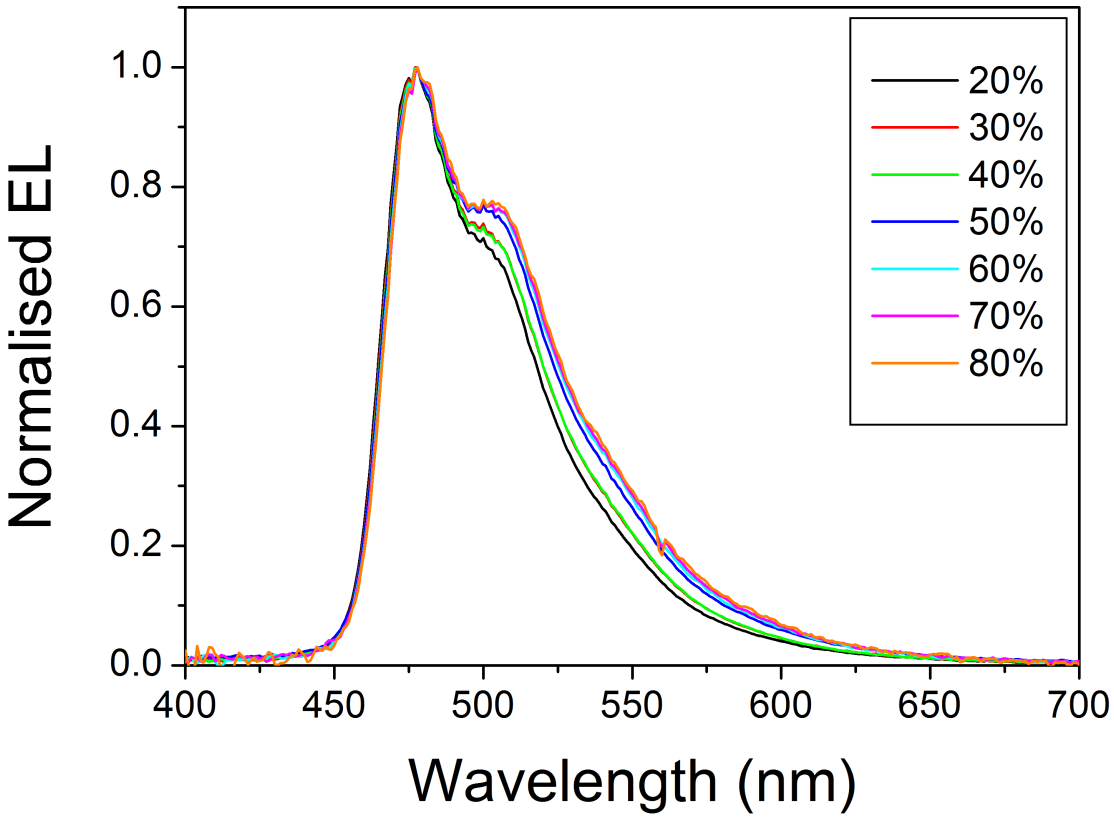

Figure 4.14: Normalised electroluminescence spectra of single layer devices containing **4.2c** with varying concentrations of OXD-7. Device structure ITO // PEDOT:PSS // PVK:OXD-7:Ir (100:x:8) // Ba (4 nm) // Al (100 nm). Increasing OXD-7 concentration increases the relative intensity of the shoulder in the emission spectrum, although this could also be due to an increase in the layer thickness.

there is more significant efficiency roll off at higher OXD-7 concentrations which is also reflected in the decrease in the maximum device brightness seen above 60% OXD-7 dopant levels.

Normalised electroluminescence spectra of these devices are shown in Figure 4.14. Increasing the amount of OXD-7 in the emissive layer also results in an increase in the relative intensity of the shoulder seen in the emission spectrum, although this may also be an effect of increased device thickness due to higher OXD-7 dopant levels resulting in slightly thicker emissive layers, similar to the effect seen in Figure 4.11.

4.3.5 Optimisation of iridium complex concentration

The following set of devices investigates the effect of varying the amount of iridium emitter doped in the emissive layer. Devices with the composition PVK:OXD-7:Ir in the ratio 100:50:x, where x ranged from 2 to 12, were fabricated. Table 4.3 summarises the device brightness and efficiency, while full *J-V*, *L-V* and device efficiency data are shown in Figure 4.15.

Ir concentration	Turn-on [a] voltage / V	E.Q.E. [b] / %	Device [b] efficiency / cd A^{-1}	Brightness [b] / cd m^{-2}	Power [b] efficiency / lm W^{-1}
2%	6.5	2.3	4.7	785	2.1
5%	7.5	3.8	8.2	1123	3.2
8%	6.5	4.4	9.6	2099	3.9
12%	6.5	4.9	11.3	1574	4.2

Table 4.3: Summary of the performance of single layer **4.2c** devices with varying concentration of iridium emitter. Device structure ITO // PEDOT:PSS // PVK:OXD-7:Ir (100:40:8) // Ba (4 nm) // Al (79 nm).
[a]: Voltage at which the device reaches a brightness of 10 cd m^{-2}.
[b]: Peak values for the device.

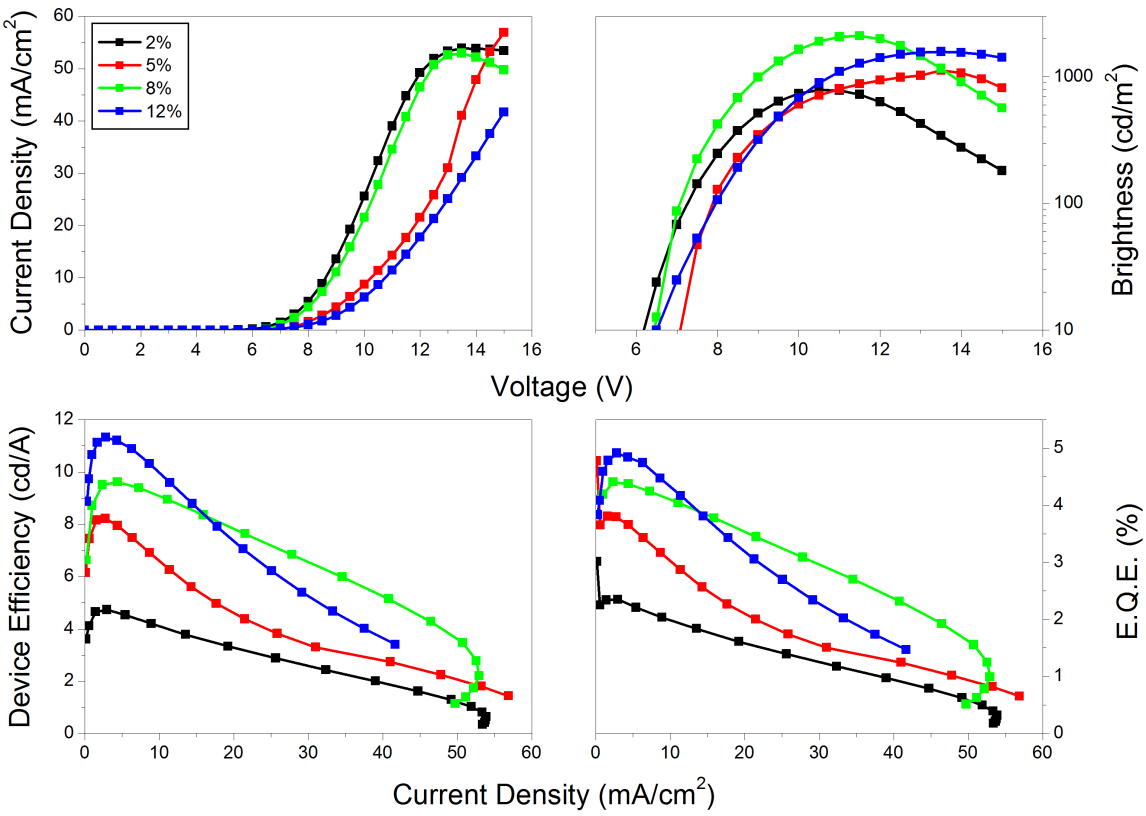

Figure 4.15: *J-V*, *L-V* and device efficiency data of single layer devices containing **4.2c** at varying concentrations. Device structure ITO // PEDOT:PSS // PVK:OXD-7:Ir (100:50:x) // Ba (4 nm) // Al (100 nm). The efficiency of devices increases as the emitter concentration increases, but at the highest concentration a larger efficiency roll-off is observed.

As the amount of iridium emitter in the emissive layer increases, there is a corresponding increase in the maximum efficiency of the device. This ranges from 4.7 cd A^{-1} and 2.3% E.Q.E. for a dopant level of 2% to the highest value across this set of devices, 11.3 cd A^{-1} and 4.9% E.Q.E. for a dopant level of 12%.

Although a dopant level of 12% resulted in the maximum efficiency obtained, a larger efficiency roll-off was observed, possibly due to the higher concentration of dopant molecules leading to increased triplet-triplet annihilation, resulting in the maximum brightness of 1,574 cd m^{-2} being lower than the 2,099 cd m^{-2} seen for the device doped with 8% iridium emitter.

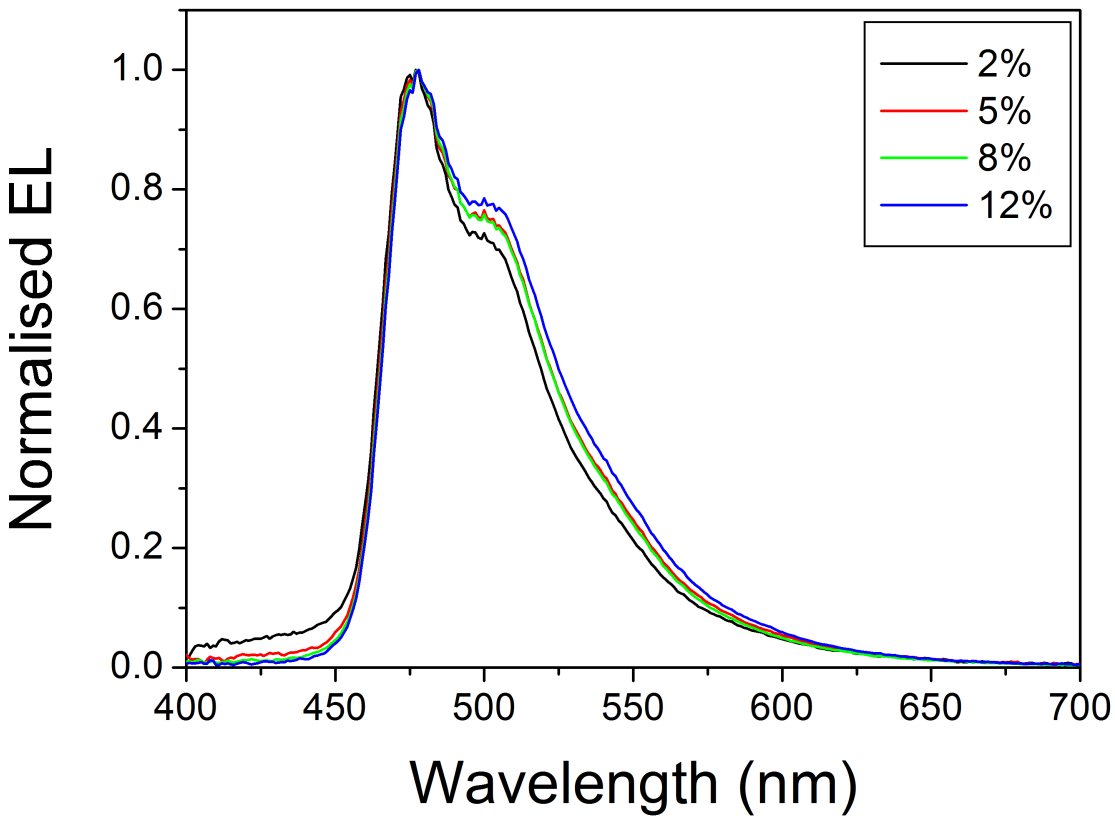

Figure 4.16: Normalised electroluminescence spectra of single layer devices containing **4.2c** at varying concentrations. Device structure ITO // PEDOT:PSS // PVK:OXD-7:Ir (100:50:x) // Ba (4 nm) // Al (100 nm). Increasing iridium emitter concentration again increases the relative intensity of the shoulder in the emission spectrum, although this could also be due to an increase in the layer thickness.

Normalised electroluminescence spectra for this set of devices are shown in Figure 4.16. Increasing the dopant concentration has little effect on the overall colour of emission, but there is once again an increase in the relative intensity of the shoulder as the dopant concentration is increased.

Again, increasing the concentration of dopant resulted in an increase in the thickness of the emissive layer. A thickness of 75 nm was measured for the lowest dopant level of 2%, while the thickness of the 12% device was as high as 86 nm. As the thicknesses of the 5% and 8% devices were similar to that of the 2% device at 77 and 76 nm

respectively, the high thickness of the 12% device could be due to other variations in the deposition conditions of the layer.

Finally, at the low dopant level of 2%, residual emission from the PVK host is observed with increased emission between 400 nm and 450 nm, as the dopant level is too low for complete energy transfer from the host to the emitter molecules.

The change in concentration of iridium dopant is also likely to change the electrical properties of the device, although in this set of devices there is no trend in one particular direction in the electrical properties as the dopant concentration increases. This adds a further variable to the optimum charge carrier balance in addition to the concentration of OXD-7, and thus the optimum OXD-7 doping level for one iridium emitter concentration may not be the same as that for a different emitter concentration.

4.3.6 Comparison of iridium complexes

The final set of devices fabricated with these materials used a choice of emissive layer composition based on the results of the optimisation tests detailed above. Comparing FIrpic with complexes **4.2a-c**, the device structure used was ITO // PEDOT:PSS // PVK:OXD-7:Ir (100:50:12) // Ba (4 nm) // Al (100 nm). Emissive layer thicknesses were measured to be broadly similar for all devices at 73.9 nm (FIrpic), 79.7 nm (**4.2a**), 78.6 nm (**4.2b**) and 78.9 nm (**4.2c**). Table 4.4 summarises the maximum brightness and efficiencies for these devices, while full *J-V*, *L-V* and device efficiency data are shown in Figure 4.17.

Complex	Turn-on [a] voltage / V	E.Q.E. [b] / %	Device [b] efficiency / cd A^{-1}	Brightness [b] / cd m^{-2}	Power [b] efficiency / lm W^{-1}
FIrpic	7.5	1.5	3.3	1071	1.1
4.2a	7.0	5.4	11.6	970	4.4
4.2b	7.0	5.3	11.7	1908	4.4
4.2c	7.0	5.0	10.9	1134	4.2

Table 4.4: Summary of the performance of single layer devices comparing complexes **4.2a-c** with FIrpic. Device structure ITO // PEDOT:PSS // PVK:OXD-7:Ir (100:50:12, 78 nm) // Ba (4 nm) // Al (60 nm).
[a]: Voltage at which the device reaches a brightness of 10 cd m^{-2}.
[b]: Peak values for the device.

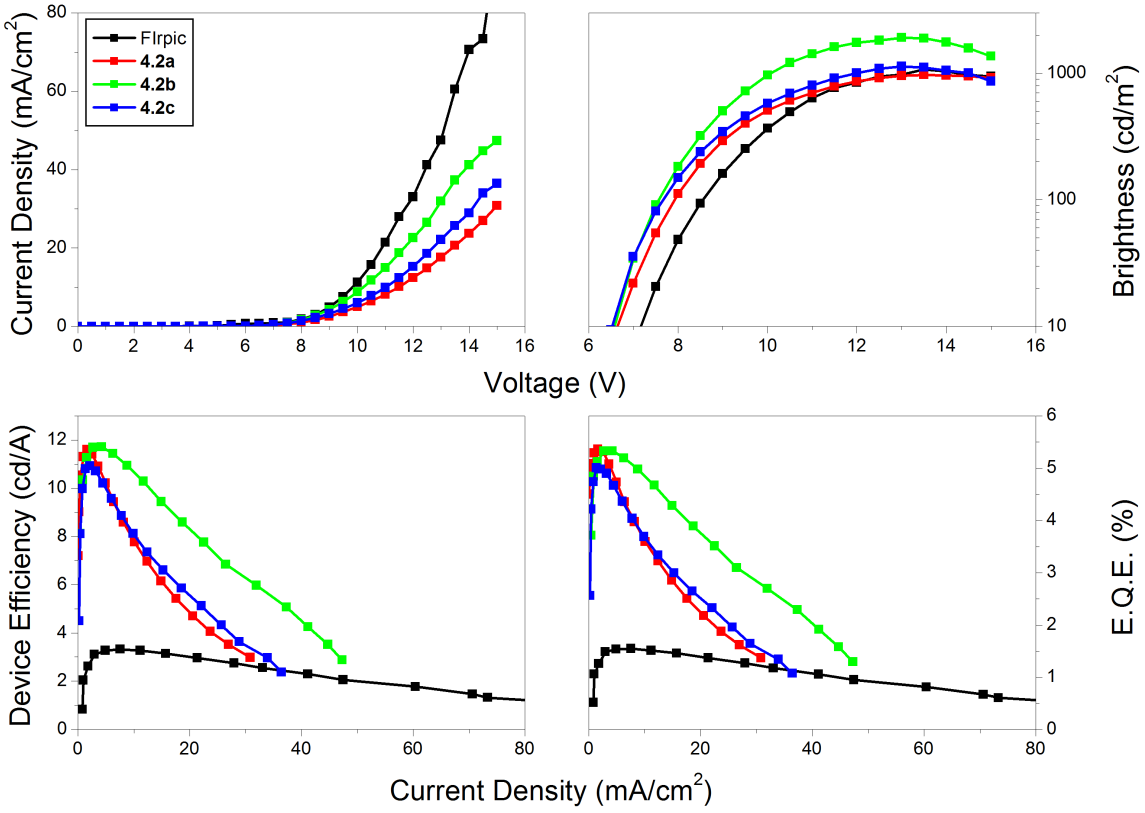

Figure 4.17: *J-V*, *L-V* and device efficiency data of single layer devices comparing complexes **4.2a-c** with FIrpic. Device structure ITO // PEDOT:PSS // PVK:OXD-7:Ir (100:50:12, 78 nm) // Ba (4 nm) // Al (60 nm). All new complexes exhibit comparable maximum efficiencies, significantly outperforming FIrpic. However less efficiency roll off is observed for complex **4.2c**.

The peak efficiency attained by the single layer FIrpic device was 3.3 cd A^{-1} and 1.5% E.Q.E. All the new complexes **4.1a-c** achieve higher maximum efficiencies than FIrpic, being comparable to each other at around 11 - 12 cd A^{-1} and 5.0 - 5.5% E.Q.E. However complex **4.2b** exhibits reduced efficiency roll-off at higher concentration densities which results in this complex having the highest brightness of 1,908 cd m^{-2}.

Figure 4.18 shows the normalised electroluminescence spectra of these devices. All complexes retain the sky blue emission of FIrpic, with only a slight redshift of around 4 nm observed when compared to the commercial standard. Additionally, the emission shoulder is slightly reduced in intensity for the new complexes, which can be explained by better solubility leading to less aggregation and therefore less self absorption.

In addition to the emission spectra not being altered compared to FIrpic, the device efficiency using the new complexes is significantly increased. Although complex **4.2b** exhibits reduced efficiency roll-off at higher current density compared to the other emitters, there is no significant improvement in the maximum device efficiency as a result of using complexes with the bulkier branched ligands.

Additionally, complexes **4.2b-c** are harder and more expensive to synthesise than **4.2a**. Therefore for further investigation **4.2a** and a second series of complexes with simpler alkyl substituent side chains were synthesised and their characterisation will be described in Chapter 5.

4.4 Conclusions

In this chapter, three new electron transport materials which are expected to have higher triplet energies than commercially available OXD-7 have been tested. Elec-

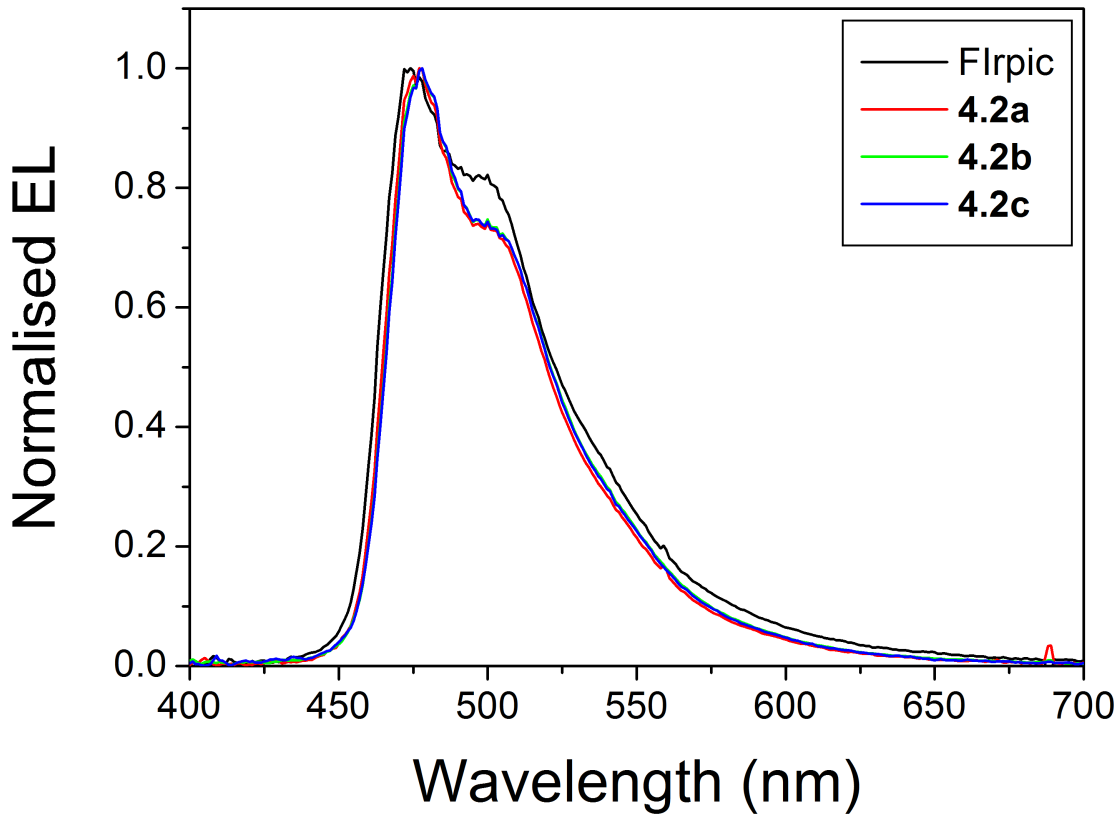

Figure 4.18: Normalised electroluminescence spectra of single layer devices comparing complexes **4.2a-c** with FIrpic. Device structure ITO // PEDOT:PSS // PVK:OXD-7:Ir (100:50:12, 78 nm) // Ba (4 nm) // Al (60 nm). Emission is slightly redshifted by 4 nm for **4.2a-c** and the shoulder in emission is reduced in intensity compared to FIrpic.

trophosphorescent devices employing FIrpic as a sky blue emitter exhibit similar maximum device efficiencies to each other, but the turn on voltage increases with the higher LUMO energy level of the electron transport materials, with OXD-7 having the lowest turn on voltage.

Devices without FIrpic show emission from an exciplex between the PVK host and the electron transporting material. The emission of OXD-7 was the most redshifted, again indicating that OXD-7 has the lowest LUMO of the series. The emission observed from the PVK:**4.1a** device was that of pure PVK, suggesting that the LUMO of this

electron transport material was higher than that of PVK. The fabrication of electron only devices was attempted, but limited supply of materials and quality of the substrate and anode surfaces meant that good quality, repeatable devices could not be made.

It is concluded that although all electron transport materials attain comparable efficiencies and brightnesses for sky blue electrophosphorescent devices, OXD-7 is still a slightly better electron transport material due to its lower LUMO energy. However with development ongoing into high triplet host materials suitable for deep blue emitting dopants, the corresponding development of high triplet electron transport materials is also necessary for highly efficient deep blue OLED devices.

Secondly, a series of blue iridium emitters based on FIrpic was characterised. These complexes retained the sky blue emission of FIrpic, while incorporating mesityl or bulky branched aryl ring side chains with the aim of improving solubility and increasing device efficiency. Simple single layer devices employing complex **4.2c** as the emitter were optimised for emissive layer thickness, OXD-7 concentration and iridium dopant concentration. Finally, this device architecture was used to compare the three new complexes with FIrpic. The new complexes were more than three times more efficient than FIrpic, with efficiencies of 11 - 12 cd A^{-1} and 5.0 - 5.5% E.Q.E. compared to 3.3 cd A^{-1} and 1.5% E.Q.E. for FIrpic, with reduced self absorption in electroluminescence spectra due to the improved solubility of the complexes.

However it is noted that even the highest efficiency devices reported here do not reach the best reported single layer FIrpic devices in the literature reviewed in section 4.1. This may indicate that further optimisation of the device architecture, such as PEDOT:PSS conductivity and thickness or the composition of the cathode may be

needed. It also reflects the difficulty in obtaining reproducible measurements across different laboratories.

With all the new sky blue iridium emitters **4.2a-c** having comparable maximum device efficiencies, and due to the comparative difficulty and expense incurred in the chemical synthesis of **4.2b-c** with bulky branched aryl ring side chains, work in the following chapter concentrates on complex **4.2a** and similar complexes with simpler alkyl chain substituents.

References

[1] Y. Zheng, *New Luminescent Organic and Organometallic Materials for OLED Applications*, PhD thesis, Durham University (2011)

[2] Z.-Y. Liu, S.-R. Tseng, Y.-C. Chao, C.-Y. Chen, H.-F. Meng, S.-F. Horng, Y.-H. Wu & S.-H. Chen, *Synthetic Metals* **161** (2011), 426 - 430

[3] X. H. Yang, F. Jaiser, S. Klinger & D. Neher, *Applied Physics Letters* **88** (2006), 021107 - 021109

[4] M. Suzuki, S. Tokito, F. Sato, T. Igarashi, K. Kondo, T. Koyama & T. Yamaguchi, *Applied Physics Letters* **86** (2005), 103507 - 103510

[5] S. Tokito, M. Suzuki, F. Sato, M. Kamachi & K. Shirane, *Organic Electronics* **4** (2003), 105 - 111

[6] D.-H. Lee, Z. Xun, H. Chae & S. M. Cho, *Synthetic Metals* **159** (2009), 1640 - 1643

[7] A. P. Kulkarni, C. J. Tonzola, A. Babel & S. A. Jenekhe, *Chemistry of Materials* **16** (2004), 4556 - 4573

[8] G. Hughes & M. R. Bryce, *Journal of Materials Chemistry* **15** (2005), 94 - 107

[9] H. Wu, J. Zou, F. Liu, L. Wang, A. Mikhailovsky, G. C. Bazan, W. Yang & Y. Cao, *Advanced Materials* **20**, 696 - 702

[10] P. Zacharias, M. C. Gather, M. Rojahn, O. Nuyken & K. Meerholz, *Angewandte Chemie International Edition* **46** (2007), 4388 - 4392

[11] M. K. Mathai, V.-E. Choong, S. A. Choulis, B. Krummacher & F. So, *Applied Physics Letters* **88** (2006), 243512 - 243514

[12] L. Li, J. Liu, Z. Yu & Q. Pei, *Applied Physics Letters* **98** (2011), 201110 - 201112

[13] H. A. Al-Attar & A. P. Monkman, *Journal of Applied Physics* **109** (2011), 074516 - 074521

[14] R. Steyleuthner, S. Bange & D. Neher, *Journal of Applied Physics* **105** (2009), 064509 - 064516

[15] J. P. J. Markham, S.-C. Lo, S. W. Magennis, P. L. Burn & I. D. W. Samuel, *Applied Physics Letters* **80** (2002), 2645 - 2647

[16] T. D. Anthopoulos, J. P. J. Markham, E. B. Namdas & I. D. W. Samuel, *Applied Physics Letters* **82** (2003), 4824 - 4826

[17] S.-C. Lo, G. J. Richards, J. P. J. Markham, E. B. Namdas, S. Sharma, P. L. Burn & I. D. W. Samuel, *Advanced Functional Materials* **15** (2005), 1451 - 1458

[18] S. M. King, H. A. Al-Attar, R. J. Evans, A. Congreve, A. Beeby & A. P. Monkman, *Advanced Functional Materials* **16** (2006), 1043 - 1050

5 Cyclometalated Ir(III) complexes for highly efficient solution processable blue PhOLEDs

Following on from the work presented in Chapter 4, in this chapter the optimised single layer device architecture is used to characterise a further series of new sky blue iridium emitters, this time either with simpler branched and straight alkyl chain substituents on the ligands, or using the same mesityl substituents as in complex **4.2a** but located on a different part of the ligand to investigate the optimal form and location of the solubilising substituent.

A further series of new cyano substituted or bipyridyl based derivative emitters were characterised, exhibiting progressively blueshifted emission compared to the sky blue parent emitters. Finally, a pair of complexes with carbazole based substituent moieties are tested.

Continued optimisation of the device structure in this chapter involves the fabrication of bilayer hybrid devices with an evaporated layer of 1,3,5-tris(1-phenyl-1H-benzimidazol-2-yl)benzene (TPBI) as an electron transport and hole blocking layer. This addition dramatically increases device efficiency and reduces the turn on voltage.

The work presented in Section 5.2 has contributed to the following publications:

1. *Cyclometalated Ir(III) Complexes for High-Efficiency Solution-Processable Blue PhOLEDs.* Valery N. Kozhevnikov, Yonghao Zheng, Matthew Clough, Hameed A. Al-Attar, Gareth C. Griffiths, Khalid Abdullah, Steponas Raisys, Vygintas Jankus, Martin R. Bryce & Andrew P. Monkman, *Chemistry of Materials* **25** (2013), 2352 - 2358

5.1 Review

Extensive research has focused on the fabrication of blue OLED devices and the characterisation of new blue iridium(III) emitters. The challenges that this research has tried to overcome include the synthesis of deep blue emitters and the fabrication of highly efficient devices.

There are many reports in the literature of new blue iridium emitters for OLED applications. Reviews such as references [1–3] summarise some of these new materials and their performance, along with progress towards other organometallic complexes or materials for deep blue devices and other applications.

Applications such as displays require deeper blue emitters than FIrpic, as a sky blue emitter with CIE coordinates of around (0.17, 0.38). The deep blue complex bis(4',6'-difluorophenylpyridinato)tetrakis(1-pyrazolyl)borate iridium(III) (FIr6) [4] has been used in vacuum deposited devices with external quantum efficiencies reaching 22.9% with CIE coordinates of (0.16, 0.29) [5].

In solution processable devices, an external quantum efficiency of 22.1% was reported using a cyano substituted FIrpic derivative (iridium(III) bis[5-cyano-4,6-(difluorophenyl)-pyridinato-N,C^2]picolinate) (FCNIrpic) in a solution processable small molecule host. The CIE coordinates for this device were (0.14, 0.19). Using PVK as a host in a comparable device reached an E.Q.E. of 12.1% [6]

As the above report shows, one obstacle for the fabrication of highly efficient deep blue OLED devices is the host material. PVK is commonly used as a host material for phosphorescent dopants of all colours and has been used as the host material in

devices reported in this thesis. However the performance of PVK devices with blue dopant emitters is not good compared to those doped with green emitters.

Although the triplet energy of PVK has been reported to be 2.88 eV, triplet trap species have been observed with the lowest energy triplet dimer states having an energy of 2.5 eV [7]. This will result in quenching of dopant excitons. As a result much research is being performed into the synthesis of high triplet host polymers for efficient deep blue OLED devices.

5.2 Improving efficiency by functionalisation of FIrpic with solubilising alkyl or mesityl groups

The following section details the characterisation of five blue emitting iridium complexes synthesised by researchers in the Department of Chemistry at the University of Durham. These complexes aim to improve the performance of FIrpic, a commercially available sky-blue emitter, by modifying the chemical structure of the ligands with solubilising alkyl or mesityl side groups while retaining the blue emission of the parent complex. These complexes are easier to synthesise than the complexes **4.2b-c** characterised in the previous chapter with large, branched side groups. The chemical structures of these materials are shown in Figure 5.1, and their synthesis and chemical characterisation is described in reference [8].

The materials **5.1a-c** have been functionalised with alkyl groups of varying lengths and branching. Complex **5.1a**, with a *t*-butyl group, has been reported previously [9]. The remaining complex **5.1d** has been functionalised with mesityl groups similar to

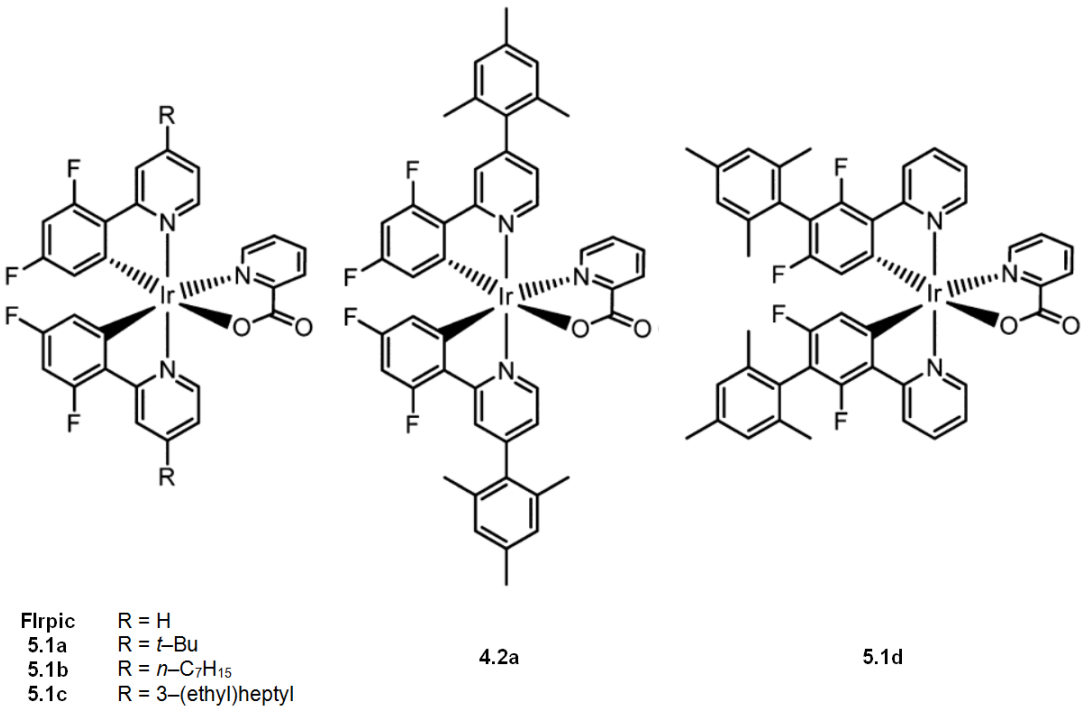

Figure 5.1: Chemical structures of the blue emitting iridium complexes characterised in section 5.2. These aim to improve the solubility of FIrpic by functionalisation of the ligands with alkyl or mesityl side groups [8].

4.2a, but at different locations on the ligand to determine the effect of the location of the solubilising group on the properties of the material. The ring in the mesityl group is twisted out of the plane of the ligand by the methyl groups, minimising conjugation over the substituent and retaining the sky blue emission.

All complexes have improved solubility, with concentrations of 25 mg/ml achievable in common organic solvents for all complexes, compared to FIrpic where the solubility may be 5 mg/ml or less [8].

5.2.1 Absorption and photoluminescence spectra

Figure 5.2 shows the extinction coefficient (absorption) spectra in toluene solution for the five complexes compared to commercially available FIrpic (purchased from

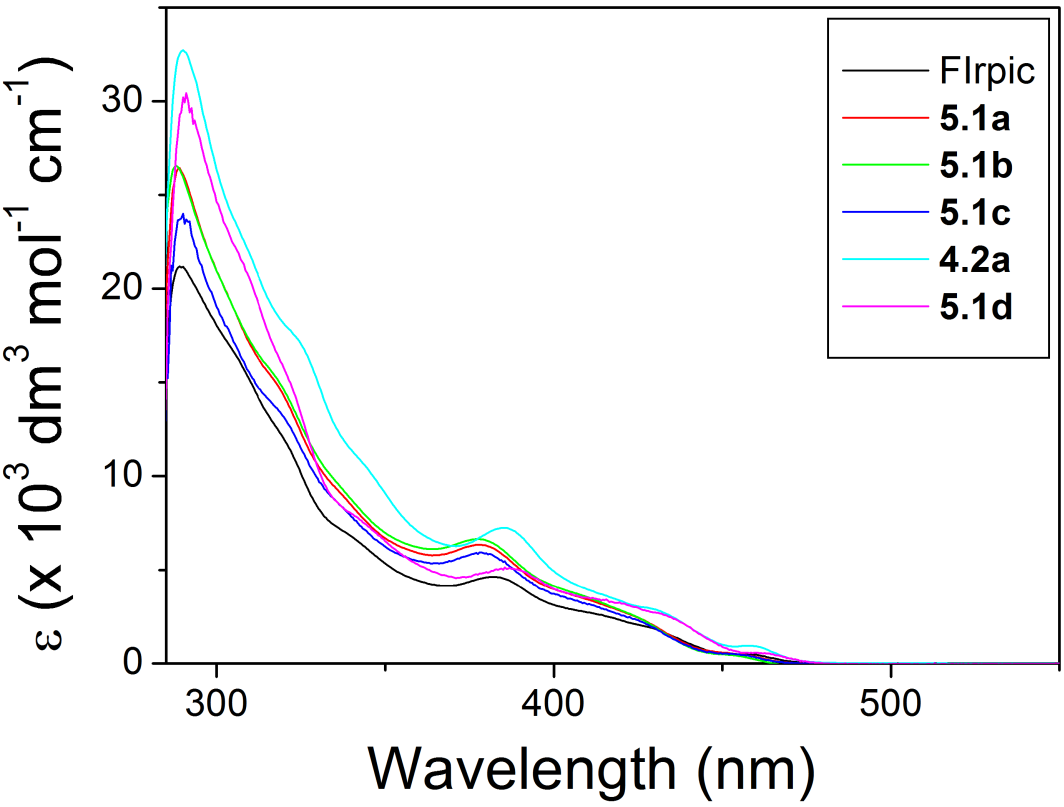

Figure 5.2: Extinction coefficient spectra of the five blue iridium emitters characterised in this section compared to FIrpic in toluene solution.

American Dye Source). The strong absorption seen below 350 nm is assigned to $\pi - \pi^*$ transitions centred on the ligand. Weaker absorption bands assigned to metal to ligand charge transfer (MLCT) states are observed between 350 and 400 nm. Functionalisation of FIrpic with alkyl groups (complexes **5.1a-c**) results in a small blueshift in these bands compared to those of FIrpic, while functionalisation with mesityl groups (complexes **4.2a**, **5.1d**) results in a small redshift.

The photoluminescence properties of the complexes are summarised in Table 5.1. A quantum yield of 0.54 was measured for FIrpic in degassed toluene solution with an excitation wavelength of 400 nm. This compares to literature reports of 0.5 - 0.6 in 'fluid solution' [11], 0.5 in chloroform [12], 0.62 in dichloromethane [13] and 0.68 in

Material	λ_{max,PL,sol^n} [a] / nm	$\lambda_{max,PL,film}$ [b] / nm	ϕ_{PL} [c]	$conc^n$ quenching [d] efficiency
FIrpic	469	470	0.54	0.33
5.1a	467	467	0.68	0.05
5.1b	465	467	0.66	-
5.1c	464	466	0.71	-
4.2a	473	474	0.92	0.04
5.1d	475	476	0.55	0.12

Table 5.1: Summary of the photoluminescence properties of the series of new complexes compared to FIrpic.
[a]: Measured in toluene solution.
[b]: Measured in PMMA film doped with 10% w/w Ir complex, excitation wavelength 400 nm.
[c]: PLQY ± 5%, using $Ir(ppy)_3$ ($\phi = 0.40$) [10] as a reference. Measured in degassed toluene solution with an excitation wavelength of 400 nm.
[d]: Calculated concentration quenching efficiency in doped zeonex film by Dr. Vygintas Jankus as detailed in reference [8].

acetonitrile [14]. The quantum yields measured for all complexes are similar to FIrpic, except for that of **4.2a** which is significantly higher at 0.92.

Table 5.1 also includes values of the concentration quenching efficiency for FIrpic, **5.1a**, **4.2a** and **5.1d** calculated by Dr. Vygintas Jankus. These values were based on measurements of the decay rate of the complexes doped at 0.01% and 12% in zeonex as detailed in reference [8]. They show that the concentration quenching is much reduced for **5.1a**, **4.2a** and **5.1d** compared to FIrpic.

Possible explanations for the variation in concentration quenching included, firstly, the increased solubility of the complex leading to improved dispersion in the polymer matrix, and secondly the presence of the mesityl side groups reducing the intermolecular interactions in the film. Concentration quenching efficiencies of 0.92 for FIrpic and 0.77 for **4.2a** measured in neat films indicated that improved solubility was the predominant cause of the reduction in concentration quenching efficiency [8].

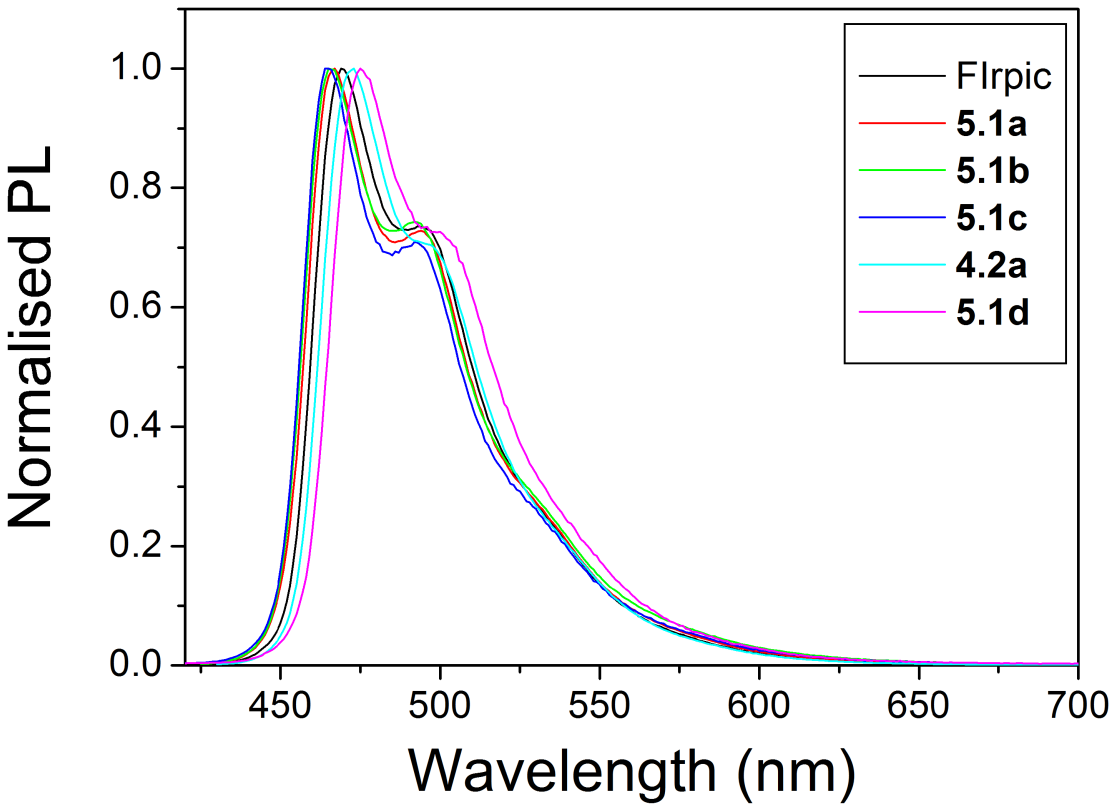

Figure 5.3: Normalised photoluminescence spectra of the series of new blue iridium emitters compared to FIrpic in toluene solution. Excitation wavelength 400 nm.

Normalised photoluminescence spectra in toluene solution are shown in Figure 5.3. The excitation wavelength was 400 nm. All the complexes retain the sky-blue emission of FIrpic ($\lambda_{max,PL}$ = 469 nm), with alkyl substituted complexes being slightly blueshifted and mesityl substituted complexes being slightly redshifted ($\lambda_{max,PL}$ = 475 nm for **5.1d**). In the mesityl substituted complexes, the *ortho*-methyl groups twist the mesityl groups out of plane with respect to the rest of the ligand [8]. This limits the effect the substitution has on the conjugation, ensuring that the emission is not redshifted significantly.

The photoluminescence spectra in thin film follow a similar pattern, as shown in Figure 5.4. The emission of the complexes doped at 10% w/w in PMMA film were

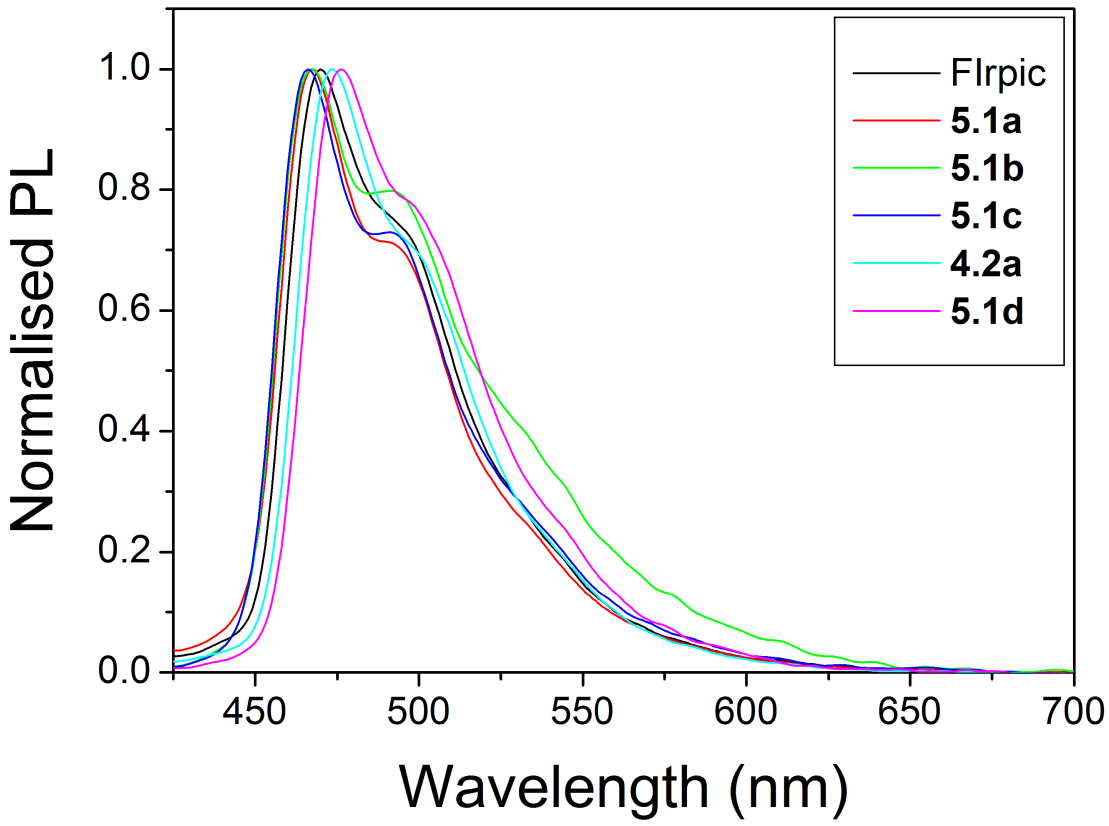

Figure 5.4: Normalised photoluminescence spectra of the series of new blue iridium emitters compared to FIrpic doped at 10% w/w in PMMA thin film, excitation wavelength 400 nm.

measured. The excitation wavelength was 400 nm. The peak emission wavelengths are redshifted by a maximum of 2 nm compared to the emission spectra in toluene solution.

5.2.2 Characterisation of single layer solution processable devices

Normalised electroluminescence spectra of devices with a simple single layer structure ITO // PEDOT:PSS (HIL 1.5) // PVK:OXD-7:Ir (100:50:12, 76 nm) // Ba (4 nm) // Al (100 nm) for FIrpic and this series of emitters are shown in Figure 5.5.

The electroluminescence spectra of complexes **5.1a**, **4.2a** and **5.1d** are all similar to that of FIrpic, while the spectra of both **5.1b** and **5.1c** show a broad band of emission

Device	$\lambda_{EL,max}$ / nm	Turn-on [a] voltage / V	E.Q.E. [b] / %	Device [b] efficiency / cd A^{-1}	Brightness [b] / cd m^{-2}	Power [b] efficiency / lm W^{-1}
FIrpic	474	7.0	1.9	3.9	1390	1.4
5.1a	472	7.0	3.8	7.1	1440	2.7
5.1b	472	7.0	4.3	10.1	1080	4.0
5.1c	472	9.0	5.2	8.9	470	3.1
4.2a	477	6.5	4.6	10.1	2290	3.6
5.1d	478	7.0	3.2	7.7	1560	2.7

Table 5.2: Summary of the performance of single layer devices comparing the blue iridium emitters **5.1a-d** with **4.2a** and commercially available FIrpic. Device structure ITO // PEDOT:PSS (HIL 1.5) // PVK:OXD-7:Ir (100:50:12, 76 nm) // Ba (4 nm) // Al (100 nm).
[a]: Voltage at which the device reaches a brightness of 10 cd m^{-2}.
[b]: Peak values for the device.

at longer wavelengths. This was possibly due to formation of an electroplex state. The broadened green shoulder is not observed in the photoluminescence emission spectra in either solution or thin film of these two complexes.

Two batches of four devices each were fabricated with this single layer architecture. The first batch compared FIrpic with the alkyl substituted complexes **5.1a**, **5.1b** and **5.1c**, while the second batch compared FIrpic with **5.1a**, **4.2a** and **5.1d**. The variation in device performance between batches is small, with the FIrpic control devices exhibiting comparable efficiencies across both sets of devices.

The efficiency and luminance data of the electrophosphorescent devices doped with FIrpic and this series of emitters are summarised in Table 5.2. Full *J-V*, *L-V* and device efficiency data are shown in Figure 5.6.

All complexes exhibit improved device efficiencies than the commercially available FIrpic, with the best performing devices containing complexes **5.1b** and **4.2a** (10.1 cd A^{-1}) being approximately two and a half times as efficient as the FIrpic devices

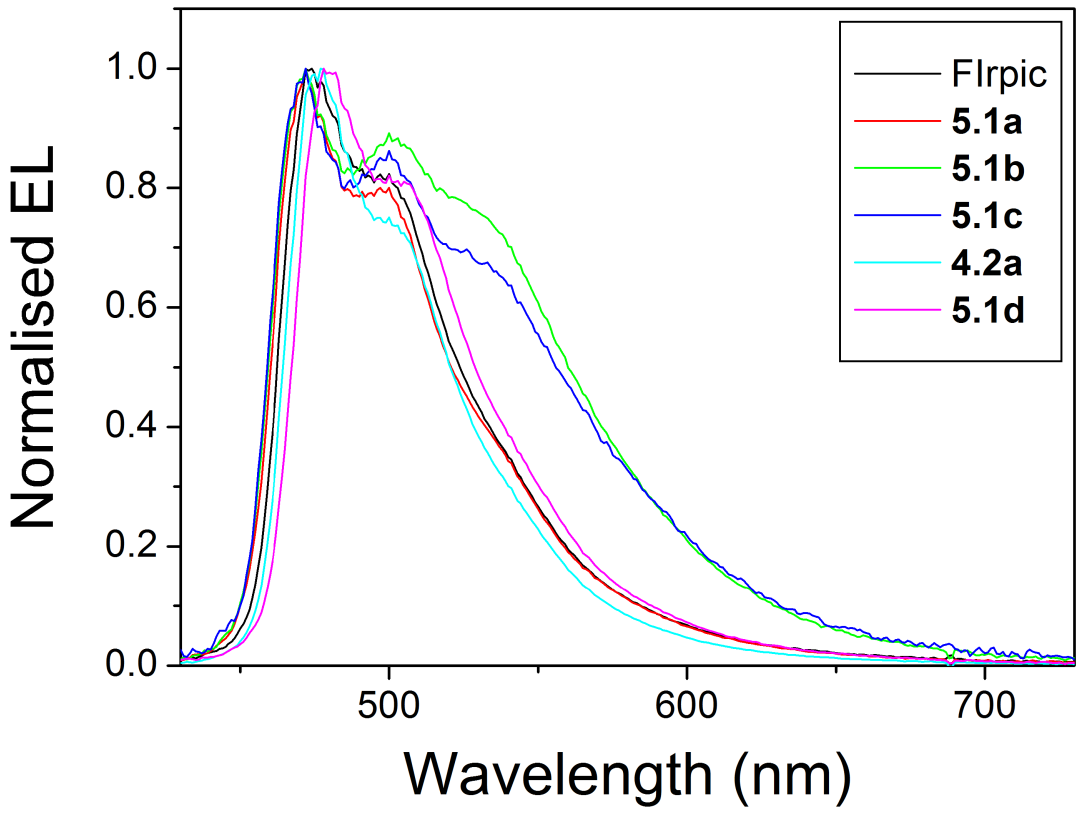

Figure 5.5: Normalised electroluminescence spectra of the blue iridium emitters **5.1a-d**, **4.2a** and FIrpic in single layer devices. The CIE coordinates at 12 V are as follows: FIrpic - (0.17, 0.38), **5.1a** - (0.17, 0.36), **5.1b** - (0.24, 0.43), **5.1c** - (0.24, 0.41), **4.2a** - (0.16, 0.38), **5.1d** - (0.18, 0.43).

(3.9 cd A^{-1}). However as the electroluminescence spectra of **5.1b** and **5.1c** are broadened towards green emission the efficiencies of these complexes would not be directly comparable with the other sky-blue dopants.

Turn-on voltages, defined here as the voltage needed for the device to attain a brightness of 10 cd m^{-2}, are similar for most of the complexes at 6.5 - 7 V in single layer devices. Complex **5.1c** is the exception, where the device had a higher turn on voltage of 9 V. The highest device brightness was obtained with **4.2a** at 2,290 cd m^{-2}, compared with 1,390 cd m^{-2} for FIrpic.

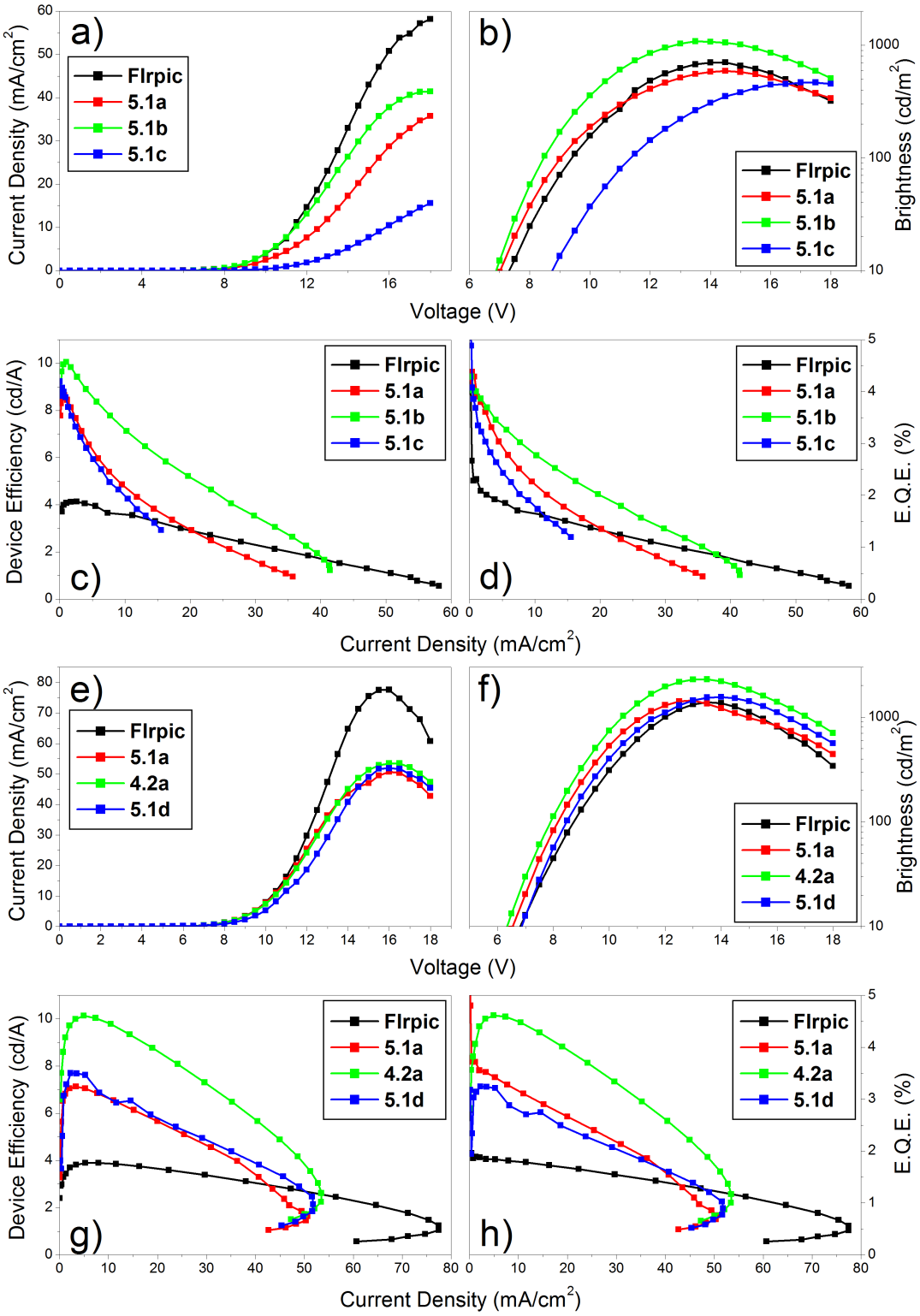

Figure 5.6: *J-V*, *L-V* and device efficiency data for single layer devices comparing (panels a - d) FIrpic and **5.1a-c** and (panels e - h) FIrpic and **5.1a**, **4.2a** and **5.1d**. Device structure ITO // PEDOT:PSS (HIL 1.5) // PVK:OXD-7:Ir (100:50:12, 76 nm) // Ba (4 nm) // Al (100 nm).

Subsequent optimisation of **4.2a** devices by co-workers resulted in single layer devices with an efficiency of 19.1 cd A^{-1} and 8.7% E.Q.E. and a brightness of 5,455 cd m^{-2} with the device structure ITO // PEDOT:PSS (HIL 1.5) (75 nm) // PVK:OXD-7:**4.2a** (100:37:8, 80 nm) // Ba (4 nm) // Al (100 nm).

Also, devices including a layer of 1,3,5-tris(1-phenyl-1H-benzimidazol-2-yl)benzene (TPBI) as an electron transporting layer achieved an efficiency of 23.7 cd A^{-1} and 10.4% E.Q.E. and a brightness of 4,600 cd m^{-2} with the device structure ITO // PEDOT:PSS (HIL 1.1) (32 nm) // PVK:**4.2a** (100:20, *ca.* 50 nm) // TPBI (32 nm) // LiF (0.7 nm) // Al (100 nm) [8]. This also resulted in a reduction of the turn-on voltage to 5 V.

Further investigation of **5.1b** was carried out as the broadened green shoulder observed in the initial devices (Figure 5.5) could be exploited for the fabrication of white light emitting devices. Initial results suggested that the green emission from this complex was concentration dependent, as shown in Figure 5.7, panel (a). Increasing the percentage doping concentration of the complex in PVK:OXD7 from 5% to 12% resulted in an increase in the intensity of emission seen above 500 nm.

Due to material availability, a second batch of the material was synthesised for further investigation. Devices using this second batch did not display the broadened emission at all, with dopant concentrations of as high as 20% in an identical device structure showing no significant change in the electroluminescence spectrum at all. The broadened emission was likely due to material purity and as it could not be reproduced in the second batch was not pursued further.

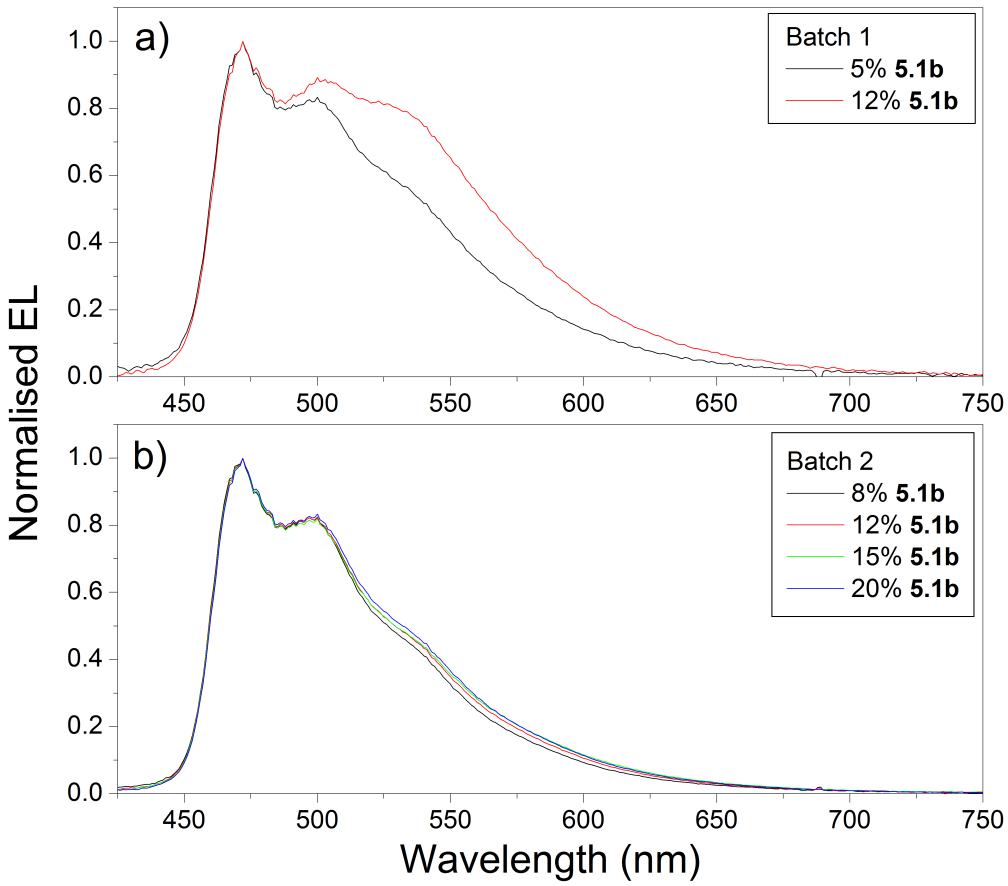

Figure 5.7: Normalised electroluminescence spectra of **5.1b** showing the concentration dependence of emission using two different batches of the same material in single layer devices. The second batch, shown in panel (b), does not exhibit the broad green shoulder that was observed in initial measurements of the first batch, shown in panel (a).

5.3 Characterisation of deep blue iridium complexes

Following the demonstration of highly efficient solution processable devices with the sky blue emitters described in section 5.2, a further series of iridium complexes was fabricated by researchers in the Department of Chemistry with the aim of progressively shifting emission towards a deeper blue colour. The chemical structures of these materials are shown in Figure 5.8.

Using **5.1a** (with a *t*-butyl side group) and **4.2a** (with the mesityl side group)

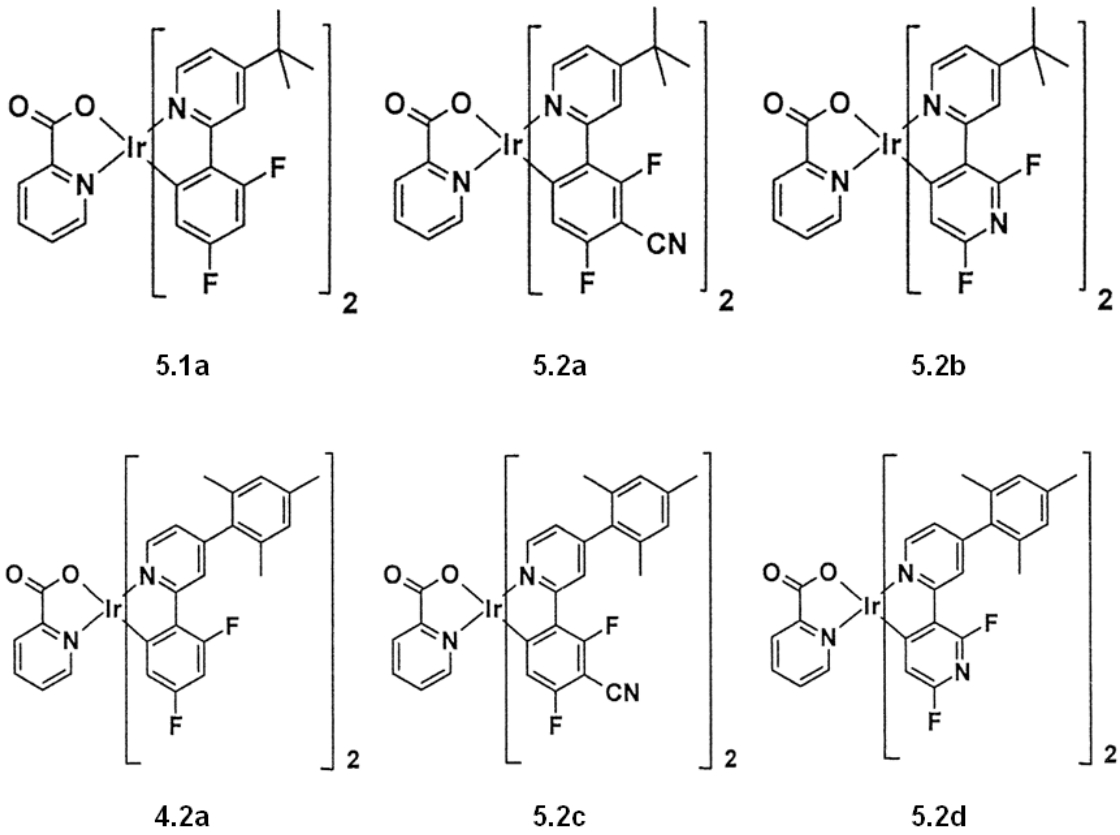

Figure 5.8: Chemical structures of the blue emitting iridium complexes characterised in section 5.3. These aim to further blueshift the emission of FIrpic derivatives **5.1a** and **4.2a** by substitution with either a cyano group (**5.2a,c**) or a bipyridyl ring (**5.2b,d**).

as parent complexes, blueshifting of emission was achieved by either substitution of a cyano group on the phenyl ring (**5.2a,c**) or replacement of the phenyl ring with a pyridyl ring (**5.2b,d**).

The cyano substituted complexes **5.2a,c** are analogues to FCNIrpic, mentioned in section 5.1. Complex **5.2b** is similar to the bipyridyl complex reported in reference [15], except the reported complex has an acetylacetonate ancillary ligand instead of the picolinate ligand in the complexes reported in this work. Similar complexes were also reported by Yang *et al.* [16] and Park *et al.* [17]. These reports demonstrate that this substitution does result in the expected blueshift in emission.

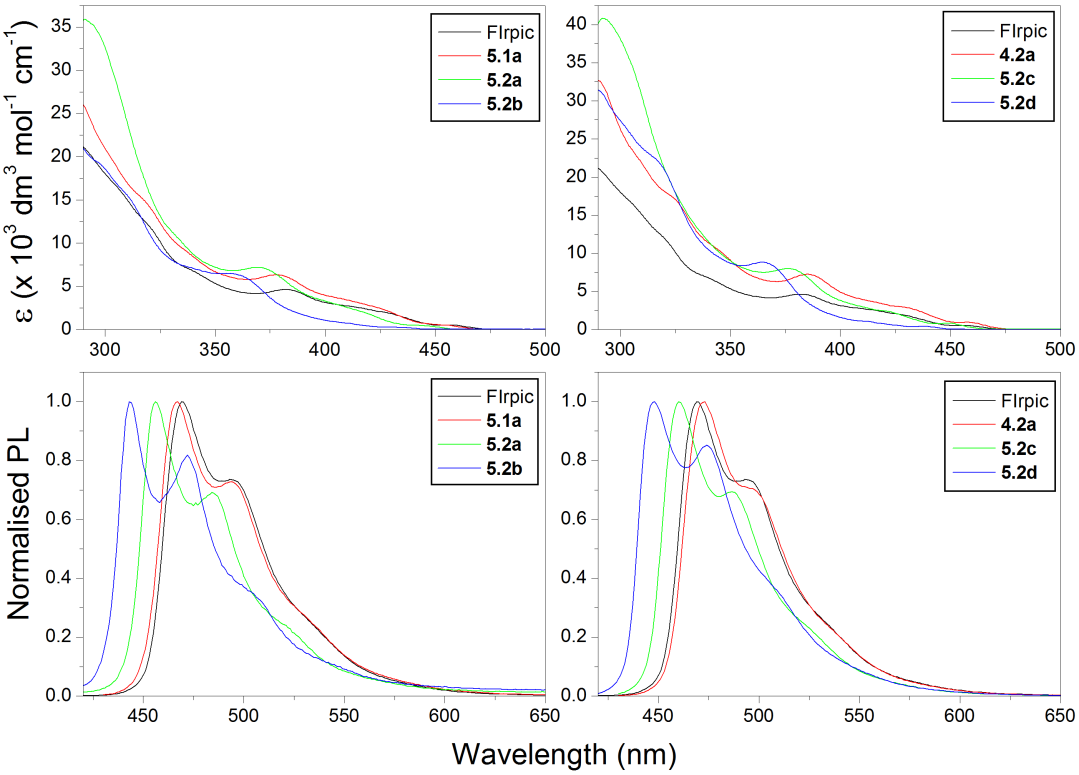

Figure 5.9: Extinction coefficient spectra (top) and normalised photoluminescence spectra (bottom) in toluene solution of (left) the blueshifted iridium emitters **5.2a-b** compared to the parent complex **5.1a** and FIrpic, and (right) **5.2c-d** compared to the parent complex **4.2a** and FIrpic. The excitation wavelength for PL measurements was 400 nm.

5.3.1 Absorption and photoluminescence spectra

Extinction coefficients of **5.2a-d** in 10^{-5} M toluene solution are shown in Figure 5.9 (top panels) compared to the parent complexes as well as FIrpic. Again, strong absorption below 350 nm is assigned to the $\pi - \pi^*$ transition with weaker MLCT absorption bands above 350 nm. The most prominent MLCT peaks for the *t*-butyl substituted complexes are progressively blueshifted from 378 nm for **4.2a** to 369 nm for **5.2a** and 357 nm for **5.2b**. Meanwhile, compared to **4.2a** the mesityl substituted complexes have their most prominent MLCT peaks progressively blueshifted from 385 nm to 377 nm for **5.2c** and 364 nm for **5.2d**.

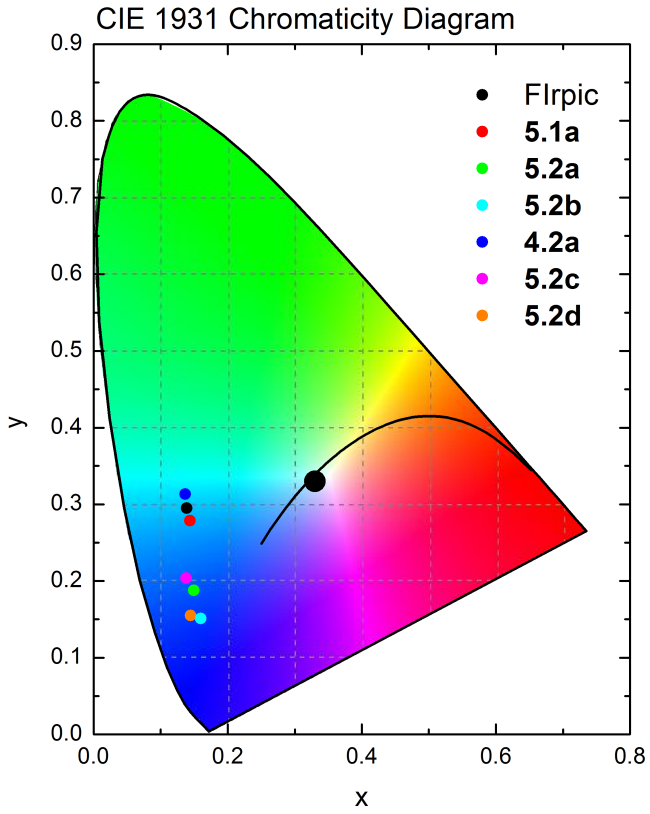

Figure 5.10: CIE chromaticity diagram showing the coordinates of photoluminescence emission of the complexes studied in this section. Coordinates are detailed in table 5.3.

Photoluminescence spectra of the same complexes in toluene solution are shown in the lower panels of Figure 5.9. For cyano substituted complexes **5.2a** and **5.2c**, the peak emission wavelength is blueshifted compared to their parent complexes from 467 nm to 456 nm (**5.2a**) and from 469 nm to 460 nm (**5.2c**). The bipyridyl complexes are blueshifted even further to 443 nm (**5.2b**) and 448 nm (**5.2d**). Additionally, the shoulder on the red side of the emission spectrum of FIrpic and the parent complexes becomes a more prominent peak as emission is blueshifted. These peaks can be seen at 472 nm for **5.2b** and 474 nm for **5.2d**.

5.3.2 Characterisation of electrophosphorescent devices

Due to the better performance of mesityl substituted **4.2a** over *t*-butyl substituted **5.1a** in devices as shown in Chapter 4, only the corresponding mesityl substituted

Material	$\lambda_{max,PL}$ [a] / nm	$\lambda_{max,EL}$ [b] / nm	CIE (PL) [a]	CIE (EL) [b,c]
FIrpic	469	472	(0.14, 0.29)	(0.18, 0.38)
5.1a	467	-	(0.14, 0.28)	-
5.2a	456	-	(0.15, 0.18)	-
5.2b	443	-	(0.16, 0.15)	-
4.2a	473	477	(0.14, 0.31)	(0.16, 0.38)
5.2c	460	467	(0.14, 0.20)	(0.16, 0.28)
5.2d	448	482	(0.14, 0.16)	(0.20, 0.31)

Table 5.3: Summary of peak wavelengths for photoluminescence emission in toluene solution (λ_{exc} = 400 nm) and electroluminescence in single layer devices for the complexes studied in this section. Due to the improved performance of **4.2a** over **5.1a** in single layer devices, complexes **5.2a-b** were not tested in devices. CIE coordinates were also calculated for each spectrum.
[a]: Measured in toluene solution.
[b]: Single layer devices, device structure detailed in section 5.3.2.
[c]: CIE coordinates for electroluminescence at peak brightness.

blueshifted complexes **5.2c-d** were tested in devices. Single layer and multilayer devices incorporating TPBI were fabricated comparing these complexes with their parent complex **4.2a**, with the single layer devices also comparing them to FIrpic.

The structure of devices tested was ITO // PEDOT:PSS (HIL 1.1) // PVK:OXD-7:Ir (100:50:12, 75 nm) // Ba (4 nm) // Al (80 nm) for single layer devices and ITO // PEDOT:PSS (HIL 1.5) // PVK:OXD-7:Ir (100:50:8) // TPBI (32 nm) // LiF (0.7 nm) // Al (100 nm) for bilayer devices. The device efficiency and brightness data are summarised in Table 5.4. Figure 5.11 shows the *J-V*, *L-V* and device efficiency data for both single layer and multilayer devices.

As the emission of the dopant complex is shifted towards the blue, both the efficiency and brightness (governed by the eye response curve) attained by the single layer devices are reduced. For single layer devices, the sky blue complex **4.2a** is the best performing emitter with a maximum device efficiency of 12.8 cd A^{-1} and 5.9% E.Q.E. and a peak

Material	Structure [a]	Turn-on [b] voltage / V	E.Q.E. [c] / %	Device [c] efficiency / cd A^{-1}	Brightness [c] / cd m^{-2}	Power [c] efficiency / lm W^{-1}
FIrpic	S	6.5	2.1	4.5	2460	1.6
4.2a	S	6.0	5.9	12.8	4169	5.1
5.2c	S	7.5	2.2	3.7	1392	1.3
5.2d	S	8.0	0.6	0.9	249	0.3
4.2a	M	7.0	10.2	22.4	1459	8.5
5.2c	M	7.0	7.3	13.0	385	5.8
5.2d	M	8.5	1.5	2.5	63	1.0

Table 5.4: Summary of the performance of single layer and multilayer devices comparing **5.2c-d**, **4.2a** and FIrpic in single and bilayer devices.
[a]: Device structure: S (single layer), M (multilayer) incorporating a 32 nm evaporated layer of TPBI.
[b]: Voltage at which the device reaches a brightness of 10 cd m^{-2}.
[c]: Peak values for the device.

brightness of 4,169 cd m^{-2}.

The cyano substituted emitter **5.2c** reaches a maximum device efficiency of 3.7 cd A^{-1} and 2.2% E.Q.E. and the brightness is reduced to 1,392 cd m^{-2}. This is comparable to the performance of FIrpic which reached a maximum efficiency of 4.5 cd A^{-1} and 2.1% E.Q.E. although the emission was not as deep blue as **5.2c**. Devices containing the bipyridyl emitter **5.2d** were the weakest, with an efficiency of just 0.9 cd A^{-1} and 0.6% E.Q.E. and a peak brightness of 249 cd m^2.

Multilayer devices with a 32 nm evaporated layer of TPBI as an electron transport are more efficient than the single layer devices, with the maximum current density measured in the device being reduced by more than ten times. This suggests that the better electron injection improves the balance of charge carriers, with fewer holes passing straight through the emissive layer without recombining, and the emission zone being moved away from the cathode preventing quenching at the interface.

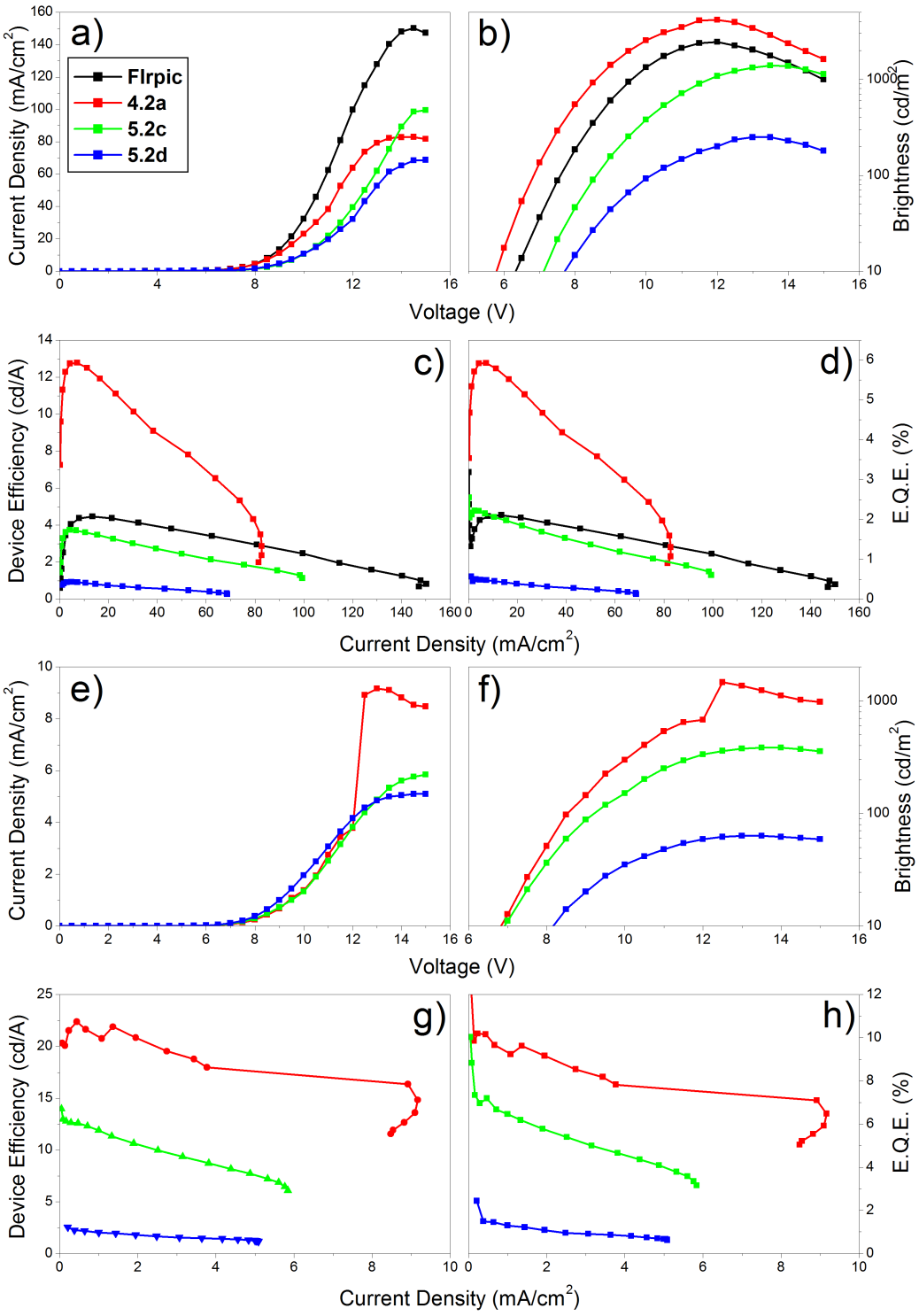

Figure 5.11: *J-V*, *L-V* and device efficiency data comparing **5.2c-d** and **4.2a** for (panels a - d) single layer devices (also compared to FIrpic) with structure ITO // PEDOT:PSS (HIL 1.1) // PVK:OXD-7:Ir (100:50:12, 75 nm) // Ba (4 nm) // Al (80 nm), and (panels e - h) bilayer devices with structure ITO // PEDOT:PSS (HIL 1.5) // PVK:OXD-7:Ir (100:50:8) // TPBI (32 nm) // LiF (0.7 nm) // Al (100 nm).

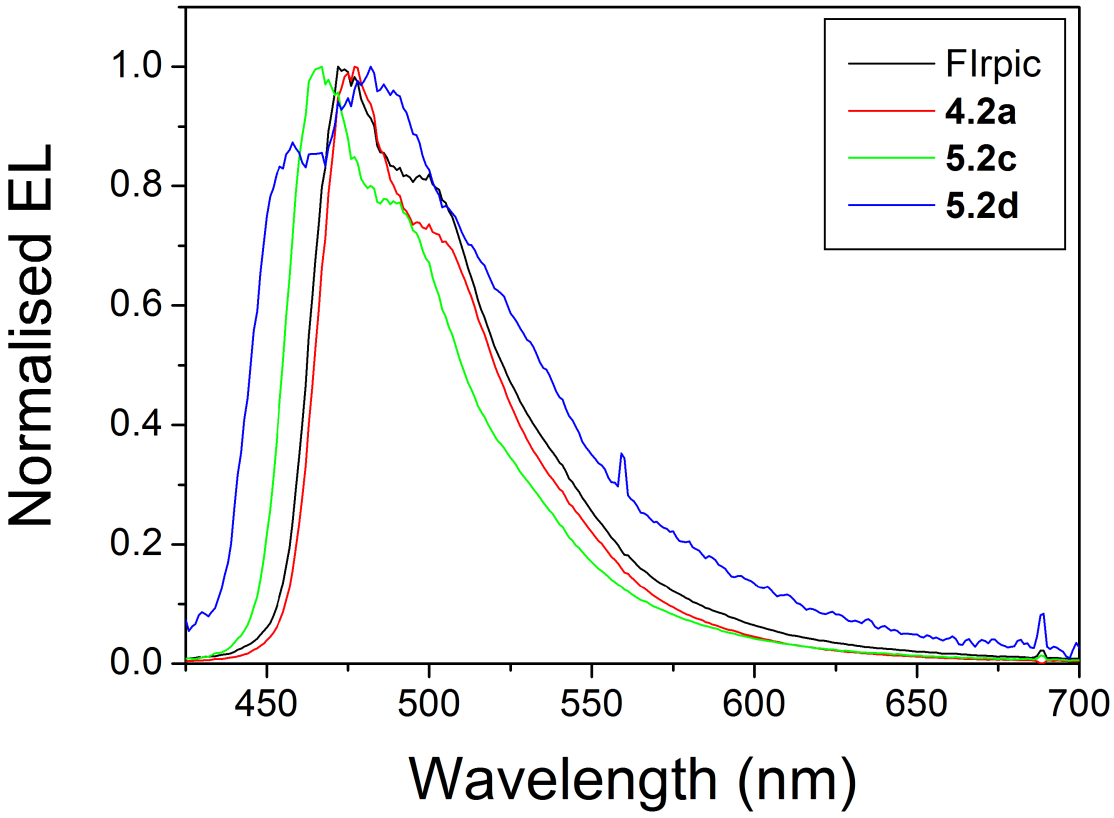

Figure 5.12: Normalised electroluminescence spectra of the series of blueshifted iridium emitters **5.2c-d** compared to the parent **4.2a** and FIrpic in single layer devices.

This results in an increase in efficiency from 12.8 cd A^{-1} and 5.9% E.Q.E. to 22.4 cd A^{-1} and 10.2% E.Q.E. for **4.2a** and similar increases in efficiency were observed for the other two complexes, although for all multilayer devices the peak brightness was lower than the corresponding single layer devices. However the multilayer devices show the same trend as the single layer devices that blueshifting the emission reduces the efficiency and brightness of the device. The reduction in efficiency with increasingly blueshifted complexes can be attributed to increased quenching by the PVK host as the energy of the blueshifted complex increases.

Figure 5.12 shows the electroluminescence spectra of the single layer devices. The peak emission wavelength for the cyano substituted **5.2c** is 467 nm, which corresponds

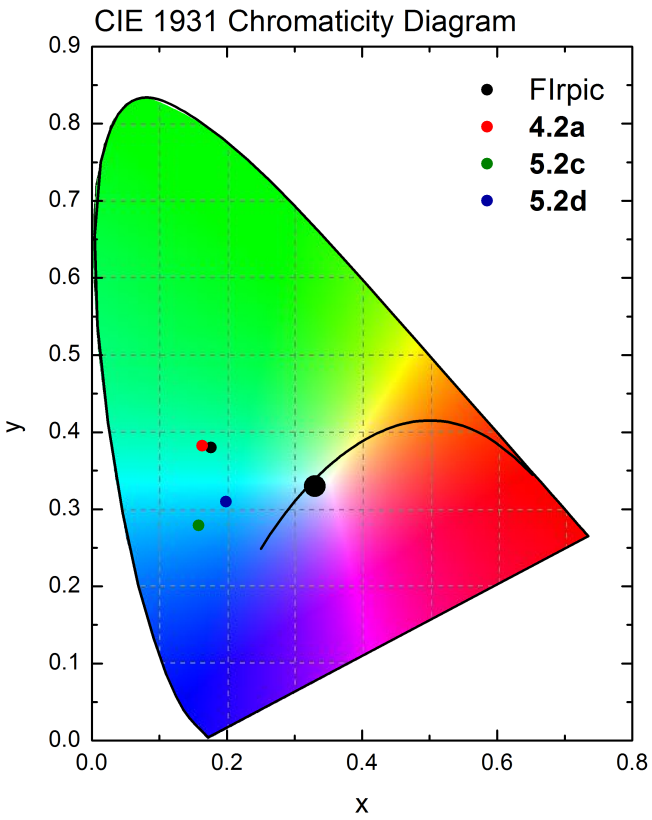

Figure 5.13: CIE chromaticity diagram showing the coordinates of electroluminescence emission for FIrpic, **4.2a** and **5.2c-d** in single layer devices.
Coordinates:
FIrpic: (0.18, 0.38)
4.2a: (0.16, 0.38)
5.2c: (0.16, 0.28)
5.2d: (0.20, 0.31)

to a blueshift of 7 nm compared to FIrpic and 10 nm compared to the parent **4.2a**. However, the spectrum of the bipyridyl complex **5.2d** is distorted towards the bluer region of the spectrum, possibly due to strong self absorption or a device microcavity effect. The peak in emission was observed at 482 nm which may correspond to the secondary peak observed in the photoluminescence spectrum. The emission spectra were the same for both single layer and bilayer devices.

Comparing the emission spectrum of **5.2d** with the extinction coefficient spectrum (shown in Figure 5.9) it can be seen that in the affected region of the emission spectrum between *ca.* 425 and 475 nm the extinction coefficient of the dopant complex is small, at less than 1 x 10^3 dm^3 mol^{-1} cm^{-1}, and there is little excitation of the dopant at these wavelengths. The Beer-Lambert law (equation 2.2) therefore suggests that the

reduction in the intensity of emission due to self absorption is small over the thickness of the emissive layer (*ca.* 75 nm) and that self absorption is not a significant effect in these devices. A microcavity effect may consequently be the main cause of the distorted emission spectrum for this complex.

The CIE coordinates of the single layer devices measured at peak brightness are shown in Figure 5.13, showing the similarity in colour between FIrpic (0.18, 0.38) and **4.2a** (0.16, 0.38), and the blueshift seen for **5.2c** (0.16, 0.28). However, devices containing complex **5.2d** are not blueshifted further, with coordinates of (0.20, 0.31) due to the distortion of the emission spectrum.

5.4 Functionalisation of FIrpic with carbazole based moieties

This section reports the characterisation of two iridium complexes synthesised by Dr. Yonghao Zheng in the Department of Chemistry. The structures of these materials **5.3a** and **5.3b** are shown in Figure 5.14. In these complexes the ligands are functionalised with 2,7-dihexyloxycarbazole moieties, which are strongly electron donating. They are also expected to improve the solubility of the complexes, leading to reduced aggregation in thin films. Complex **5.3a** exhibits a HOMO level of -5.45 eV, which is 0.2 eV higher than that of FIrpic and suggests better hole injection [18].

While complex **5.3a** is expected to retain the sky-blue emission colour of FIrpic, complex **5.3b** incorporates bipyridyl based ligands and as such is expected to exhibit significantly blueshifted emission compared to FIrpic, similar to that of **5.2b** and **5.2d**.

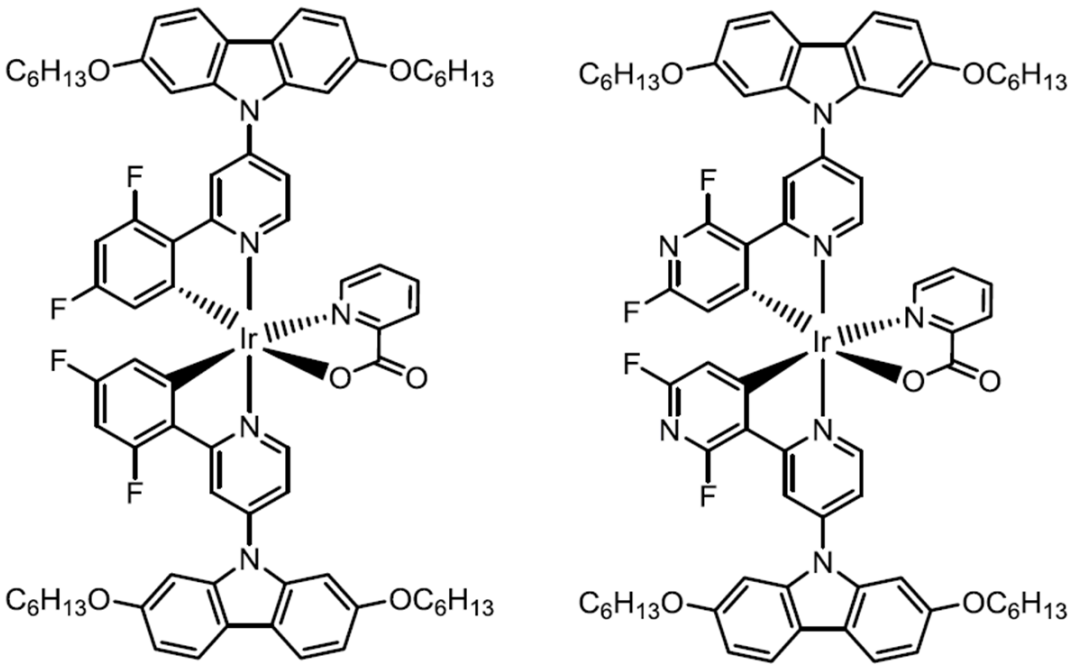

Figure 5.14: Chemical structures of the blue emitting iridium complexes characterised in section 5.4. These aim to improve the solubility of FIrpic by functionalisation of the ligands with carbazole based side groups, as well as blueshift the emission by use of a bipyridyl based ligand in the case of **5.3b**.

5.4.1 Absorption and photoluminescence spectra

The absorption spectra of **5.3a** and **5.3b**, shown in Figure 5.15, were measured in 10^{-5} M toluene solution. Strong absorption peaks are seen in the region of 295 - 305 nm for both materials, with broad secondary peaks observed between 350 and 420 nm, peaking at 364 nm for **5.3a** and 381 nm for **5.3b**.

Normalised photoluminescence spectra in toluene solution are shown in Figure 5.16, showing that the addition of 2,7-dihexyloxycarbazole redshifts the emission compared to the alkyl or mesityl substituted complexes already characterised. The excitation wavelength was 400 nm. The emission spectrum of **5.3a**, which peaks at 480 nm, is redshifted by 11 nm compared to that of FIrpic ($\lambda_{\mathrm{max,PL}}$ = 469 nm). This is a

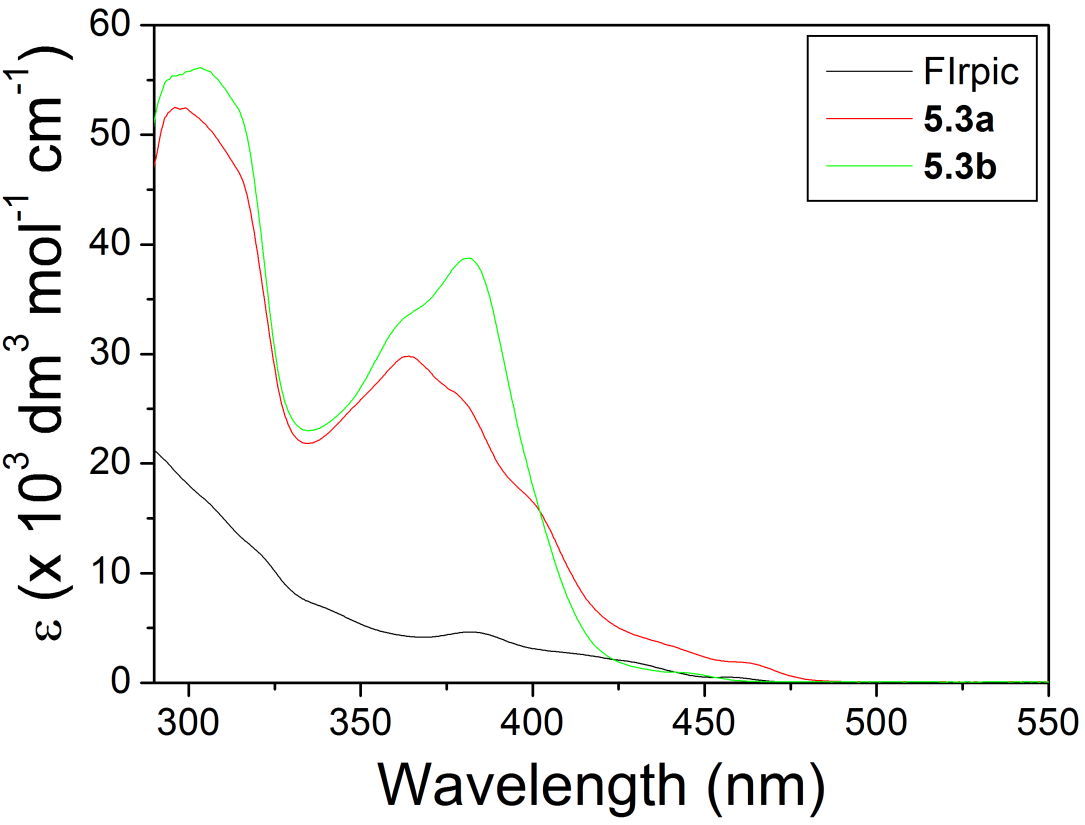

Figure 5.15: Extinction coefficient spectra of the carbazole-based iridium emitters **5.3a-b** and FIrpic in toluene solution.

larger shift than was observed for any of the complexes in section 5.2, and with CIE coordinates of (0.14, 0.39) is more blue-green in colour than sky blue.

The bipyridyl complex **5.3b** is blueshifted to $\lambda_{max,PL}$ = 459 nm, and with CIE coordinates of (0.16, 0.23) its photoluminescence emission is not as deep blue as the corresponding alkyl and mesityl substituted complexes **5.2b** and **5.2d**.

Further investigation of the photoluminescence spectra of **5.3b** in chlorobenzene and chloroform solution carried out by colleagues in the OEM group revealed broadening of the emission, which was not observed in toluene solution and is strongest in chloroform solution. This may be due to the presence of both the strongly donating carbazole and the strongly accepting difluoropyridine part of the ligand leading to an

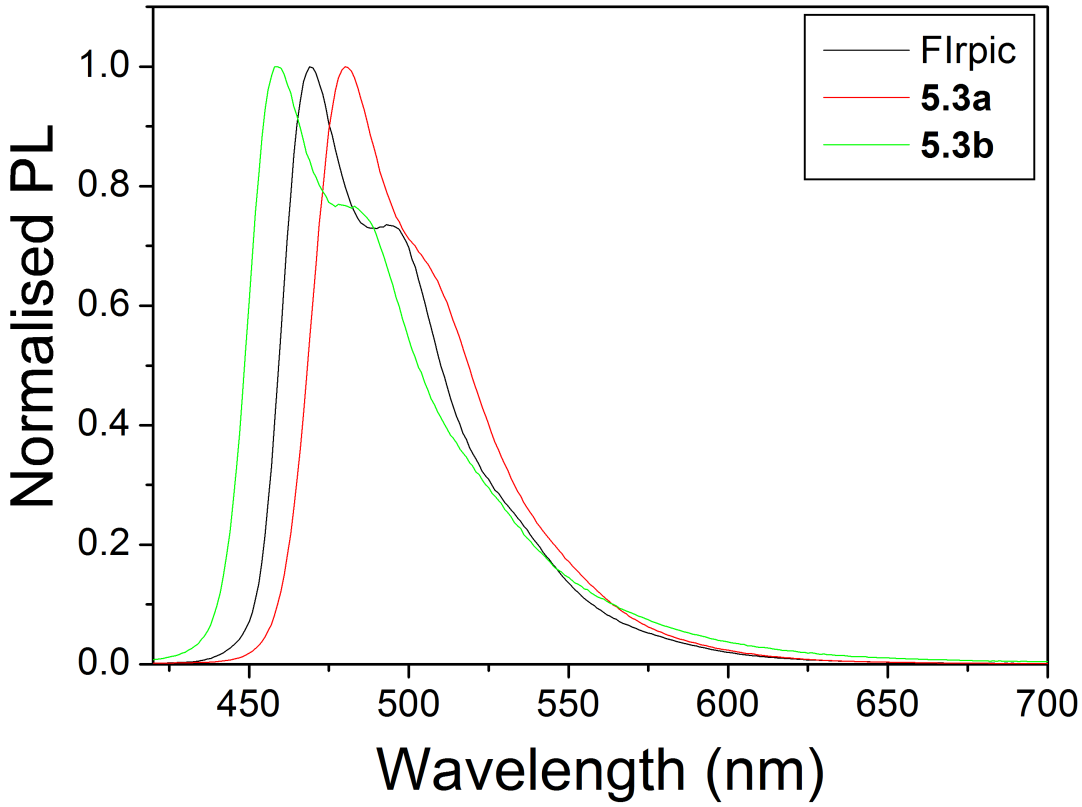

Figure 5.16: Normalised photoluminescence spectra of the carbazole-based iridium emitters **5.3a-b** and FIrpic in toluene solution. Excitation wavelength 400 nm.

ICT state. The dual emission is similar to that observed by Yeh *et al.* in tris-pyridyl azolate based complexes [19]. Investigation into the nature of this emission is ongoing.

5.4.2 Characterisation of electrophosphorescent devices

Again, the complexes were tested in both single layer and multilayer devices using PVK as the host and OXD-7 as the electron transport material, and TPBI as the evaporated electron transport layer for the multilayer devices.

The structure of single layer devices fabricated was ITO // PEDOT:PSS (HIL 1.5) // PVK:OXD-7:Ir (100:50:12, 78 nm) // Ba (4 nm) // Al (80 nm), while the structure of multilayer devices was ITO // PEDOT:PSS (HIL 1.5) // PVK:OXD-7:Ir (100:50:8)

Material	Structure [a]	Turn-on [b] voltage / V	E.Q.E. [c] / %	Device [c] efficiency / cd A^{-1}	Brightness [c] / cd m^{-2}	Power [c] efficiency / lm W^{-1}
FIrpic	S	8.0	1.9	4.1	720	1.4
5.3a	S	7.0	5.3	13.1	1909	4.5
5.3b	S	9.5	1.4	2.6	246	0.9
FIrpic	M	6.0	7.8	17.0	1266	7.4
5.3a	M	5.5	9.4	23.5	3998	10.4
5.3b	M	7.5	4.3	9.1	597	3.3

Table 5.5: Summary of the performance of single layer and multilayer devices comparing **5.3a-b** and FIrpic in single and bilayer devices.
[a]: Device structure: S (single layer), M (multilayer) incorporating a 30 nm evaporated layer of TPBI.
[b]: Voltage at which the device reaches a brightness of 10 cd m^{-2}.
[c]: Peak values for the device.

// TPBI (25 nm) // LiF (1 nm) // Al (100 nm). The device efficiency and brightness data are summarised in Table 5.5. Figure 5.17 shows the *J*-*V*, *L*-*V* and device efficiency data for both single and multilayer devices.

Single layer devices with **5.3a** as the emitter are significantly improved in both efficiency and brightness compared to FIrpic, which can again be attributed to reduced aggregation in film than FIrpic due to improved solubility. The maximum efficiency for **5.3a** devices was 13.1 cd A^{-1} and 5.3% E.Q.E. with a peak brightness of 1,909 cd m^{-2} compared to 4.1 cd A^{-1} and 1.9% E.Q.E. with a peak brightness of 720 cd m^{-2} for FIrpic. The bipyridyl complex, following the same pattern as the similar **5.2** series bipyridyl complexes, exhibits reduced efficiency and brightness at 2.6 cd A^{-1} and 1.4% E.Q.E. and a peak brightness of 246 cd m^{-2}.

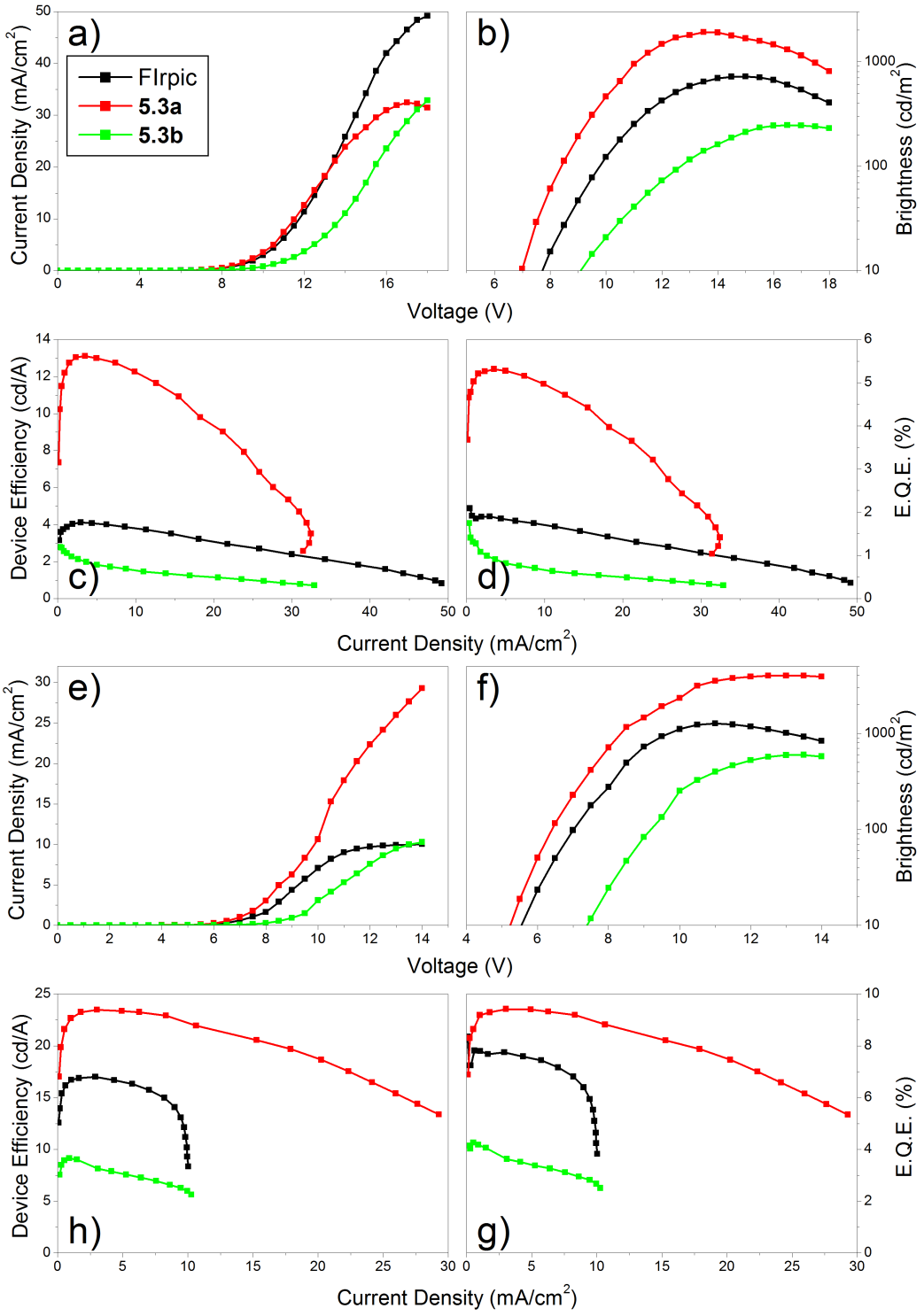

Figure 5.17: *J-V*, *L-V* and device efficiency data comparing **5.3a-b** and FIrpic for (panels a - d) single layer devices with structure ITO // PEDOT:PSS (HIL 1.5) // PVK:OXD-7:Ir (100:50:12, 78 nm) // Ba (4 nm) // Al (80 nm), and (panels e - h) bilayer devices with structure ITO // PEDOT:PSS (HIL 1.5) // PVK:OXD-7:Ir (100:50:8) // TPBI (25 nm) // LiF (1 nm) // Al (100 nm).

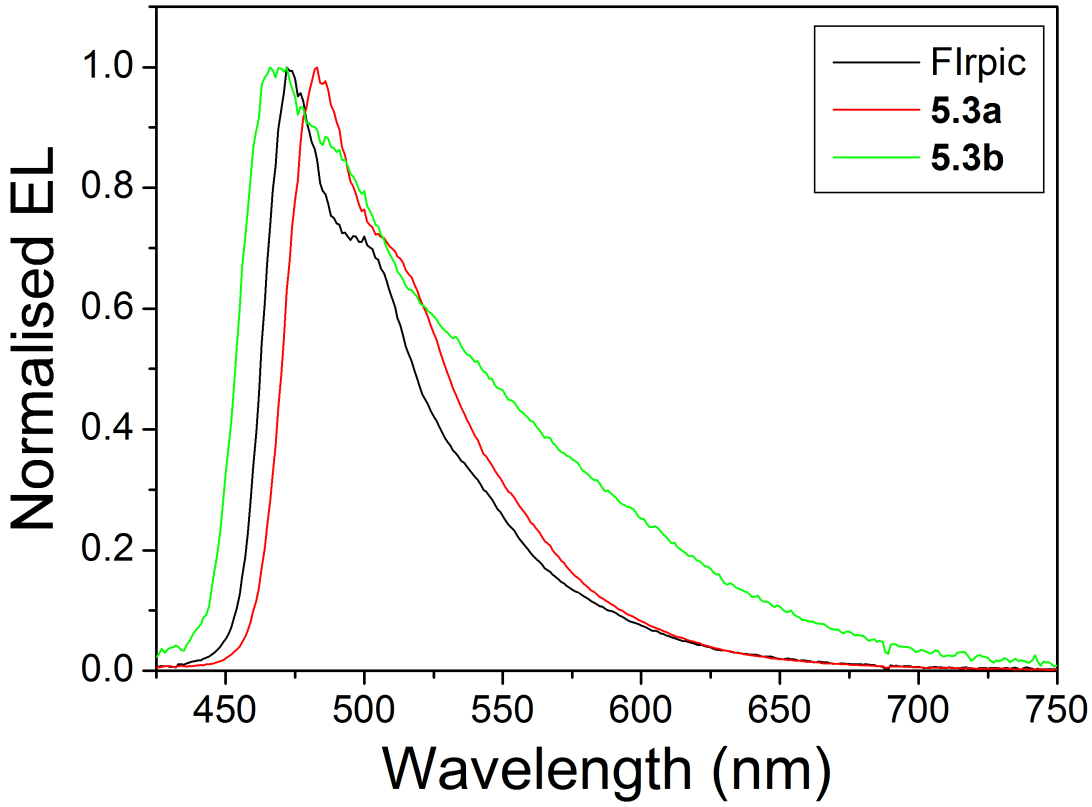

Figure 5.18: Normalised electroluminescence spectra of the carbazole-based iridium emitters **5.3a-b** compared with FIrpic and complex **4.2a**. Device structure ITO // PEDOT:PSS (HIL 1.5) // PVK:OXD-7:Ir (100:50:8) // TPBI (25 nm) // LiF (1 nm) // Al (100 nm)

The same trend is seen in the multilayer devices, except that higher brightnesses and efficiencies as well as lower turn on voltages were obtained. The best performing device was 23.5 cd A^{-1} and 9.4% E.Q.E. with a peak brightness of 3,998 cd m^{-2} obtained using **5.3a** as the emitter.

The electroluminescence spectra of complexes **5.3a-b** in multilayer devices are shown in Figure 5.18, along with that of FIrpic for comparison. The spectrum of **5.3a** is redshifted compared to FIrpic, with a peak in emission at 483 nm, an 11 nm shift from the emission peak of FIrpic which was seen at 472 nm in this set of devices. This is also a redshift of 6 nm compared to **4.2a**.

The bipyridyl complex **5.3b** is blueshifted compared to FIrpic with an emission peak around 469 nm. This is comparable to the emission peak of the cyano substituted complex **5.2c**, although the device performance for **5.3b** is not as good as that of **5.2c**. The emission spectrum of **5.3b** has a much more intense tailoff than expected between 500 nm and 700 nm, this is similar to the dual emission seen by colleagues in the photoluminescence spectrum of the complex in chlorobenzene solution. Investigations into the nature of this emission are ongoing.

Finally, a set of devices was fabricated comparing the two highest efficiency complexes tested in this chapter, **4.2a** with the mesityl group and **5.3a** with the carbazole based group. The PEDOT:PSS used in these devices is the higher conductivity Clevios HIL 1.1 instead of the HIL 1.5 used in previous devices. The device structure was ITO // PEDOT:PSS (HIL 1.1) // PVK:OXD-7:Ir (100:50:8) // TPBI (32 nm) // LiF (0.7 nm) // Al (100 nm). Figure 5.19 shows the *J-V*, *L-V* and device efficiency data for these devices.

Using the higher conductivity PEDOT:PSS significantly increases the current density of the device, but also increases the device efficiency and brightness due to improved charge carrier balance. A maximum efficiency of 28.8 cd A^{-1} and 11.4% E.Q.E. was achieved for **5.3a**, with a peak brightness of 13,350 cd m^{-2}. This compares favourably with **4.2a**, which reached a maximum efficiency of 22.5 cd A^{-1} and 9.7% E.Q.E. with a peak brightness of 11,090 cd m^{-2}. The better performance of **5.3a** compared to **4.2a** could be explained by the greener emission of **5.3a** however. The CIE coordinates of the **5.3a** emission were (0.18, 0.47) compared to (0.18, 0.40) for **4.2a** in this device.

The effect of the change in PEDOT:PSS on the hole injection can be investigated

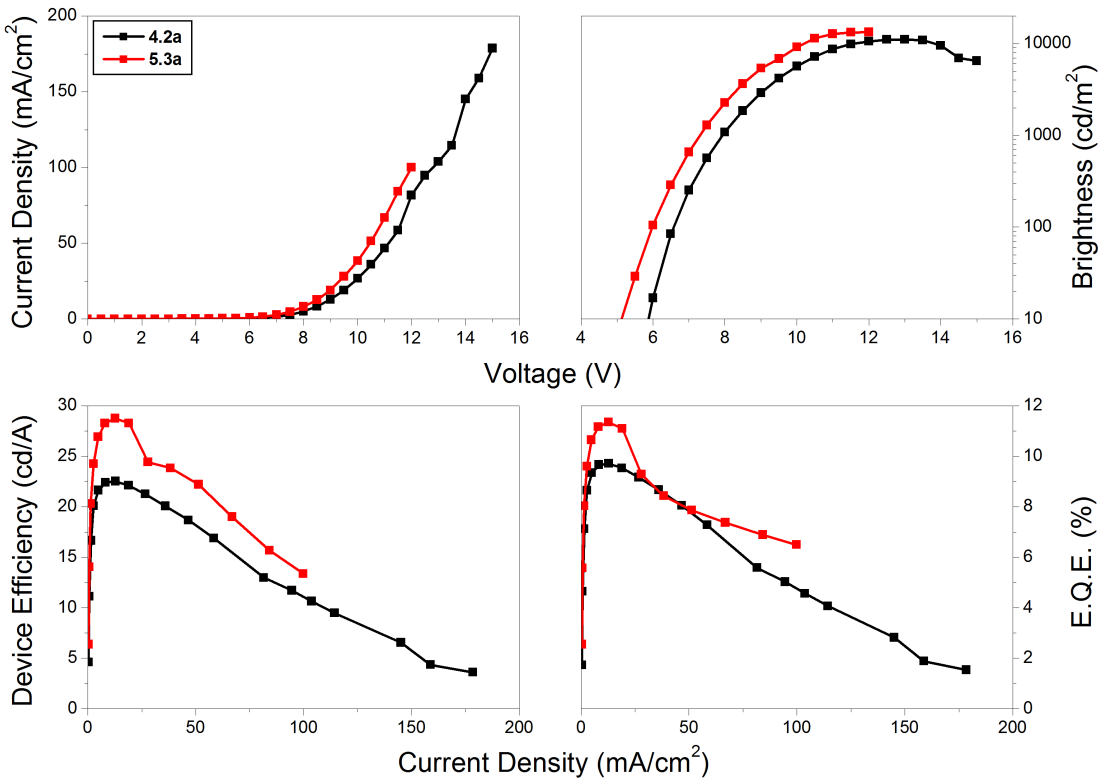

Figure 5.19: *J-V*, *L-V* and device efficiency data comparing **5.3a** with **4.2a** in bilayer devices with structure ITO // PEDOT:PSS (HIL 1.1) // PVK:OXD-7:Ir (100:50:8) // TPBI (32 nm) // LiF (0.7 nm) // Al (100 nm).

further by comparing the *J-V* data on a Fowler-Nordheim plot, as described in section 2.6.1. The structure of these devices, fabricated as part of the same batch, was ITO // PEDOT:PSS (HIL 1.1 or 1.5) // PVK:OXD-7:**4.2a** (100:50:8) // TPBI (32 nm) // LiF (0.7 nm) // Al (100 nm).

Plotting the *J-V* data on a log-log plot (Figure 5.20, left) shows three main regions to the *J-V* data: a small dark current at low voltage (1) which may be due to thermally generated free carriers or electron injection, a region dominated by hole injection (2) and finally a bulk conduction region (3) characterised by SCLC (section 2.6.2). Region 1 is not seen in the device using the high resistivity PEDOT 1.5 as a hole injection layer, where there is no current at all at low voltages.

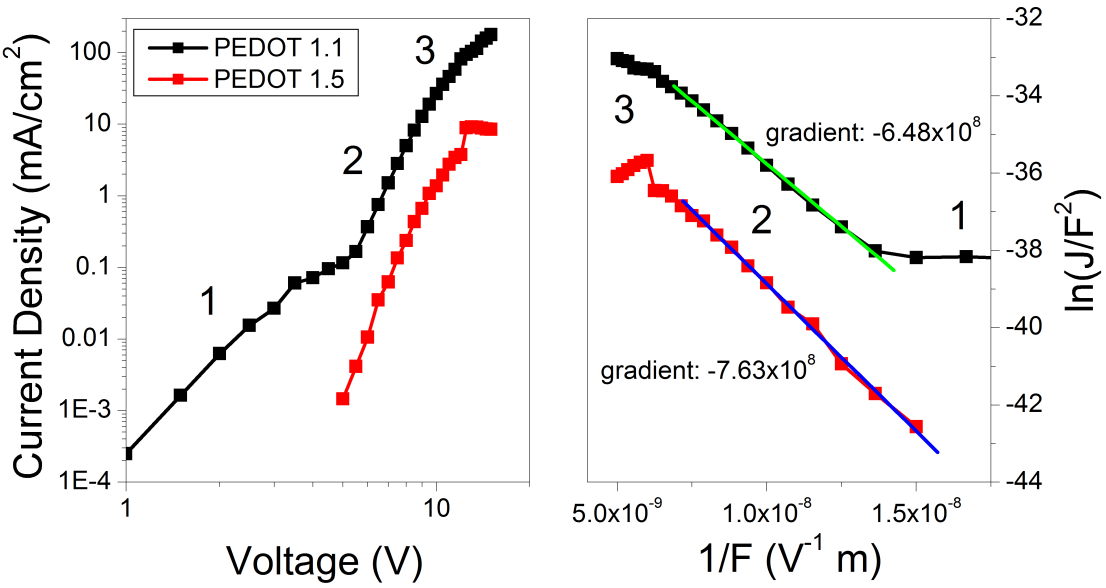

Figure 5.20: Left: log-log plot of the J-V data from devices with different PEDOT:PSS hole injection layer. Right: Fowler-Nordheim plot of the same data showing the gradient of the hole injection region.

It can be seen from the Fowler-Nordheim plot shown in the right hand panel of Figure 5.20 that the gradient of region 2 is slightly lower for the PEDOT 1.1 device than for PEDOT 1.5, which indicates that the barrier height for hole injection has been slightly lowered. A proper calculation of the barrier height (from equation 2.11) would require the charge carrier effective mass for PVK of which there are few, if any, reports in the literature. However by using the free electron mass as an approximate value for effective hole mass, an indication of the barrier heights can be calculated resulting in a barrier height of 0.21 eV for PEDOT 1.1 and 0.23 eV for PEDOT 1.5. This slight reduction in the barrier for hole injection may explain the increase in efficiency when PEDOT 1.5 is replaced by PEDOT 1.1 in these devices.

5.5 Conclusions

In this chapter a range of new sky blue and deep blue iridium(III) emitters have been characterised and tested in devices. The first series consisted of sky blue FIrpic derivatives incorporating solubilising alkyl (**5.1a-c**) or mesityl groups (**4.2a**, **5.1d**). All emitters in this series outperformed commercially available FIrpic in single layer devices, with **4.2a** the best performing at a maximum efficiency of 10.1 cd A^{-1} and 4.6% E.Q.E. and a peak brightness of 2,290 cd m^{-2}, retaining the sky blue emission of FIrpic. This was subsequently increased to 22.5 cd A^{-1} and 9.7% E.Q.E. with a peak brightness of 11,090 cd m^{-2} when a higher conductivity PEDOT:PSS was used in conjunction with a 32 nm evaporated layer of TPBI as an electron transport layer.

The better performance of **4.2a** over FIrpic is attributed to its improved solubility in organic solvents, which results in reduced aggregation in thin film and reduced concentration quenching in addition to its higher radiative yield.

The alkyl substituted complexes **5.1b-c** showed broadened green emission in single layer devices which was not observed in the solution or film photoluminescence spectra. The intensity of this broadening was dependent on the concentration of the dopant emitter and was originally attributed to an electroplex, but was not seen during subsequent investigation using a new batch of the material. This difference could therefore be due to differences in material purity between batches.

The second series of emitters studied consisted of derivatives of the mesityl- and *t*-butyl complexes **4.2a** and **5.1a** with cyano substituted or bipyridyl based ligands to progressively blueshift the emission. The blueshift in emission reduces the device

efficiency and brightness, but multilayer devices using cyano substituted **5.2c** reached a maximum efficiency of 13.0 cd A^{-1} and 7.3% E.Q.E. at a peak wavelength of 467 nm and CIE coordinates of (0.16, 0.28). Devices with the bipyridyl complex **5.2c** had lower efficiency and an emission spectrum distorted by a device microcavity effect.

The reduction in device efficiency as emission is blueshifted could be due to quenching by low energy dimer trap states in the PVK host, and further research into new hosts and their suitability for deep blue dopants is needed for a high efficiency deep blue OLED device.

Finally, the third series of emitters consisted of a sky blue FIrpic derivative and a blueshifted bipyridyl complex with 2,7-dihexyloxycarbazole solubilising units. The sky blue complex **5.3a** outperformed both FIrpic and complex **4.2a**, with the best device fabricated reaching a maximum efficiency of 28.8 cd A^{-1} and 11.4% E.Q.E. as well as a peak brightness of 13,350 cd m^{-2}, although the emission was slightly greener than that of **4.2a** and FIrpic. The blueshifted bipyridyl complex did not perform as well in devices, but investigation is ongoing into the dual emission observed by colleagues in its photoluminescence spectrum in more polar solvents.

References

[1] L. Xiao, Z. Chen, B. Qu, J. Luo, S. Kong, Q. Gong & J. Kido, *Advanced Materials* **23** (2010), 926 - 952

[2] K. S. Yook & J. Y. Lee, *Advanced Materials* **24** (2012), 3169 - 3190

[3] H. Xu, R. Chen, Q. Sun, W. Lai, Q. Su, W. Huang & X. Liu, *Chemical Society Reviews* **43** (2014), 3259 - 3302

[4] R. J. Holmes, B. W. D'Andrade, S. R. Forrest, X. Ren, J. Li & M. E. Thompson, *Applied Physics Letters* **83** (2003), 3818 - 3820

[5] J. Lee, J.-I. Lee, J.-W. Lee & H. Y. Chu, *Organic Electronics* **11** (2010), 1159 - 1164

[6] K. S. Yook & J. Y. Lee, *Organic Electronics* **12** (2011), 1711 - 1715

[7] V. Jankus & A. P. Monkman, *Advanced Functional Materials* **21** (2011), 3350 - 3356

[8] V. N. Kozhevnikov, Y. Zheng, M. Clough, H. A. Al-Attar, G. C. Griffiths, K. Abdullah, S. Raisys, V. Jankus, M. R. Bryce & A. P. Monkman, *Chemistry of Materials* **25** (2013), 2352 - 2358

[9] I. R. Laskar, S.-F. Hsu & T.-M. Chen, *Polyhedron* **25** (2006), 1167 - 1176

[10] K. A. King, P. J. Spellane & R. J. Watts, *Journal of the American Chemical Society* **107** (1985), 1431 - 1432

[11] C. Adachi, R. C. Kwong, P. Djurovich, V. Adamovich, M. A. Baldo, M. E. Thompson & S. R. Forrest, *Applied Physics Letters* **79** (2001), 2082 - 2084

[12] S. Tao, S. L. Lai, C. Wu, T. W. Ng, M. Y. Chan, W. Zhao & X. Zhang, *Organic Electronics* **12** (2011), 2061 - 2064

[13] E. Baranoff, B. F. E. Curchod, F. Monti, F. Steimer, G. Accorsi, I. Tavernelli, U. Rothlisberger, R. Scopelliti, M. Grätzel & Md. K. Nazeeruddin, *Inorganic Chemistry* **51** (2012), 799 - 811

[14] Y. Zhou, W. Li, Y. Liu, L. Zeng, W. Su & M. Zhou, *Dalton Transactions* **41** (2012), 9373 - 9381

[15] F. Kessler, Y. Watanabe, H. Sasabe, H. Katagiri, Md. K. Nazeeruddin, M. Grätzel & J. Kido, *Journal of Materials Chemistry C* **1** (2013), 1070 - 1075

[16] C.-H. Yang, M. Mauro, F. Polo, S. Watanabe, I. Muenster, R. Fröhlich & L. De Cola, *Chemistry of Materials* **24** (2012), 3684 - 3695

[17] H. R. Park, D. H. Lim, Y. K. Kim & Y. Ha, *Journal of Nanoscience and Nanotechnology* **12** (2012), 668 - 673

[18] Y. Zheng, M. A. Fox, G. C. Griffiths, F. B. Dias, H. A. Al-Attar, M. R. Bryce & A. P. Monkman, manuscript to be submitted.

[19] Y.-S. Yeh, Y.-M. Cheng, P.-T. Chou, G.-H. Lee, C.-H. Yang, Y. Chi, C.-F. Shu & C.-H. Wang, *ChemPhysChem* **7** (2006), 2294 - 2297

6 Characterisation of substituent effects on the molecular dipole moment and colour tuning of iridium(III) complexes with carbazole-based ligands.

This chapter describes the characterisation of a series of tris-cyclometalated iridium complexes in which the carbazole-based ligands have been systematically substituted with either an electron withdrawing trifluoromethyl group or an electron donating methoxy group. The work follows on from initial characterisation of these materials that was performed during the final year research project of my MPhys undergraduate degree [1].

Solution photoluminescence spectra show the effect that systematic chemical substitution has on the emission of the complexes, achieving colour tuning over a wide wavelength range from green to red ($\lambda_{\mathrm{max,PL}}$ from 505 nm to 630 nm). Additionally, measurements of the solvatochromic shift in solvents of different polarity, as well as the absorption strength of the metal to ligand charge transfer transition, correlate with TD-DFT computational values of the molecular dipole moment of the complexes. The molecular dipole moment affects the carrier mobility and therefore the device performance.

The work presented in this chapter has contributed to the following publications:

1. *Highly Efficient, Solution-Processed, Single-Layer, Electrophosphorescent Diodes and the Effect of Molecular Dipole Moment.* Hameed A. Al-Attar, Gareth C. Griffiths, Tom N. Moore, Mustafa Tavasli, Mark A. Fox, Martin R. Bryce &

Andrew P. Monkman, *Advanced Functional Materials* **21** (2011), 2376 - 2382

2. *Colour tuning from green to red by substituent effects in phosphorescent tris-cyclometalated iridium(III) complexes of carbazole-based ligands: synthetic, photophysical, computational and high efficiency OLED studies.* Mustafa Tavasli, Tom N. Moore, Yonghao Zheng, Martin R. Bryce, Mark A. Fox, Gareth C. Griffiths, Vygintas Jankus, Hameed A. Al-Attar & Andrew P. Monkman, *Journal of Materials Chemistry* **22** (2012), 6419 - 6428

6.1 Review

Substitution of functional groups onto the ligands of organometallic complexes is a well established method to achieve shifts in the colour of emission. A number of studies have been published investigating the effect of substitution with different electron donating or electron withdrawing groups on the emission colour of phosphorescent complexes, such as that of Grushin *et al.* who substituted fluorine, trifluorylmethyl or methoxy groups among others on aryl-pyridine based Ir complexes to achieve colour tuning from *ca.* 500 to 595 nm in devices [2]. Meanwhile, Zhou *et al.* used different electron-withdrawing main group (specifically Boron, Silicon, Germanium, Nitrogen, Phosphorus, Oxygen and Sulphur) containing moieties to achieve colour tuning from 505 - 609 nm [3].

Colour tuning of iridium complexes has also been achieved by varying the ancillary ligand of heteroleptic complexes. For example, You *et al.* [4] and Gu *et al.* [5] demonstrated colour tuning from sky blue to red in photoluminescence spectra simply

by changing the ancillary ligand. Chang *et al.* (Reference [6]) demonstrated a shift from deeper blue ($\lambda_{\mathrm{max,PL}}$ = 455 nm) to orange-red ($\lambda_{\mathrm{max,PL}}$ = 574 nm), again with ancillary ligand substitution, and further demonstrated thermally evaporated devices in the green ($\lambda_{\mathrm{max,EL}}$ = 526 nm) that reached a peak efficiency of 23.2 cd A^{-1} and 6.11% E.Q.E.

Few systematic studies of substituent effects on complexes with carbazole-pyridine based ligands have been published. Yang *et al.* [7], as well as Bettington *et al.* at the University of Durham [8], both reported large redshifts of 83 - 85 nm when the carbazole-based moiety was substituted at the 2-position compared to at the 3-position. The latter work describes the parent materials on which the materials investigated in this chapter are based. Colour tuning from green to red in similar carbazole-pyridine and carbazole-isoquinaline based complexes was also reported by Ho *et al.* [9] with green ($\lambda_{\mathrm{max,PL}}$ = 508 nm) thermally evaporated devices obtaining a peak efficiency of 43.4 cd A^{-1} and 12.9% E.Q.E.

An additional factor to consider is that the functionalisation of ligands with substituent groups also affects the dipole moment of the molecule. This could have further effects on the optical and electrical properties of an OLED device, such as the polarisation induced redshifts observed in electroluminescence with increasing dopant concentration [10, 11] as well as the charge transport properties of the material.

The solvatochromic shift, i.e. the degree of shift in emission as the solvent polarity is increased, is often used as a measure of the dipole moment of a chromophore. The solvent dipoles reorient on excitation, stabilising the excited state and lowering its energy [12]. This leads to a redshift in emission as solvent polarity is increased

(Negative solvatochromism can also be observed in some materials, where the emission and absorption are blueshifted with increasing solvent polarity, for example as seen in reference [13]).

The family of iridium complexes introduced in the following section have systematically substituted electron donating or withdrawing groups onto the ligands. As well as characterising the effect that this has on the colour tuning of these complexes, the effect of the change in molecular dipole moment was investigated.

6.2 Materials

The homoleptic tris-cyclometalated iridium complexes under investigation in this chapter were synthesised in the Department of Chemistry at the University of Durham via standard Suzuki-Miyaura cross-coupling reactions [16] and cyclometalation procedures as published elsewhere [14, 15]. The chemical structures of the complexes investigated as part of this work are shown in Figure 6.1.

The parent materials **6.1a** and **6.2a**, with the isomeric structures [2-(Cz-3'-yl)-Py]$_3$ and [2-(Cz-2'-yl)-Py]$_3$ respectively (where Cz denotes *N*-hexylcarbazole) have been reported previously [8], with similar complexes reported by Yang *et al.* [7]. The substitution of the pyridine unit onto the carbazole moiety at either the C-2 or C-3 position on the ligand resulted in substantial shifts in photoluminescence and electroluminescence characteristics, including a difference of 85 nm between phosphorescence emission maxima that was observed between the two complexes.

These two parent complexes were substituted systematically with either an electron withdrawing trifluoromethyl group or an electron donating methoxy group at two dif-

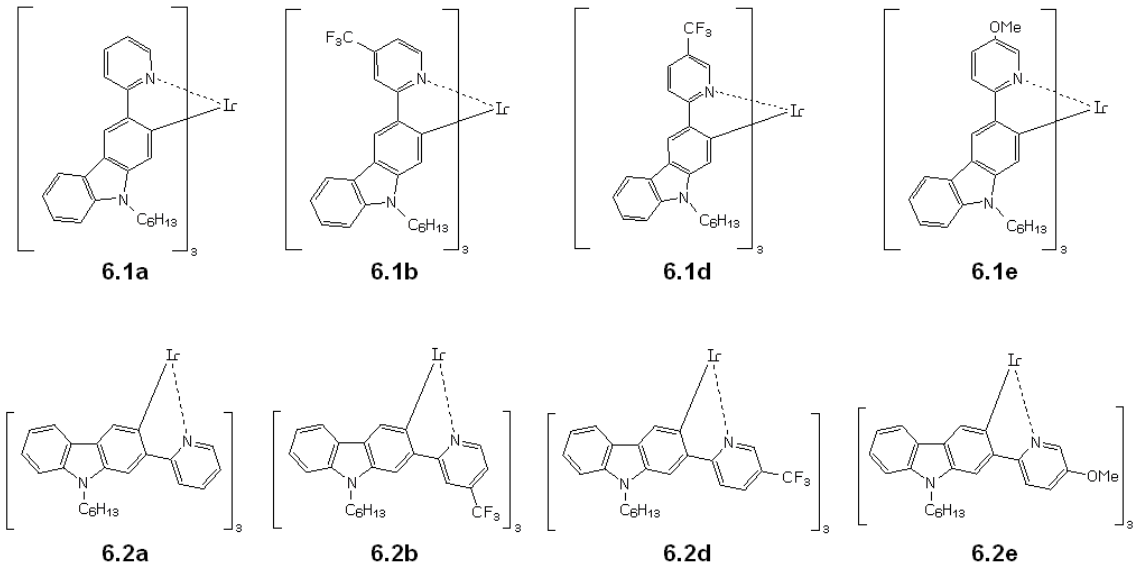

Figure 6.1: Chemical structures of the family of iridium complexes investigated in this chapter. Complexes **6.1c** and **6.2c** are not included as they were not investigated as part of this work.

ferent locations on the pyridine unit of the ligand to study the effect this would have on the fine tuning of their photophysical properties and their performance in OLED devices. Complexes **6.1b** and **6.2b** have an electron withdrawing CF_3 group substituted at the *para* position of the pyridine ring while **6.1d** and **6.2d** have the same unit substituted at the *meta* position. Complexes **6.1e** and **6.2e** have the electron donating OMe group substituted at the *meta* position of the pyridine ring.

Complex **6.1c**, with the electron donating OMe group substituted in the *para* position, was synthesised using a different procedure to the others [15] and was characterised separately. Due to the similarity in both photophysical properties and device performance between this material and the parent complex **6.1a**, the corresponding series **6.2** complex **6.2c** was not synthesised.

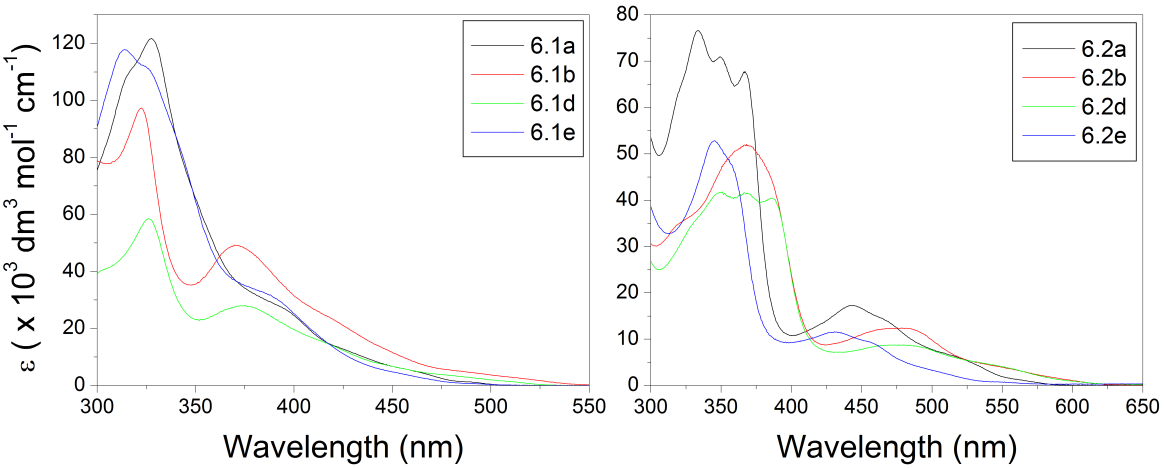

Figure 6.2: Absorption coefficient spectra of series **6.1** and **6.2** complexes measured in toluene solution.

6.3 Absorption and photoluminescence measurements

Initial photophysical characterisation of these materials were carried out previously [1, 14], and full characterisation of the parent materials **6.1a** and **6.1b** has also been reported [8]. Further photophysical measurements were carried out in order to calculate the photoluminescence quantum yields and absorption coefficients of the new materials, and to determine the solvatochromic shift of emission in solvents of differing polarities as an experimental measure of the molecular dipole moment.

Absorption coefficient spectra of series **6.1** and **6.2** iridium complexes as measured in dilute toluene solution are shown in Figure 6.2. Strong absorption bands attributed to $^1\pi - \pi^*$ transitions are seen in the 310 - 330 nm region for series **6.1** and 330 - 390 nm for series **6.2**. Strong bands observed between 360 - 400 nm for series **6.1** and 420 - 500 nm for series **6.2** are assigned to ^{1}MLCT transitions. These overlap with further weak bands related to ^{3}MLCT transitions and $^3\pi - \pi^*$ transitions at lower energies.

For series **6.1** materials, the relative strengths of the ^{1}MLCT absorption bands

correlate with the strength of the of the molecular dipole moment. Substitution of an electron donating MeO group in the *meta* position (complex **6.1e**) has little effect on the position or strength of the ^{1}MLCT band. Substitution of the electron withdrawing CF_3 group (complexes **6.1b** and **6.1d**) results in a blueshift of approximately 20 nm compared to the ^{1}MLCT band of the parent **6.1a** and an increase in strength of the ^{1}MLCT transition, with the strongest band observed when the substitution is in the *para* position (complex **6.1b**). The relative strengths of the ϵ values of the ^{1}MLCT band compared to the peak $^1\pi - \pi^*$ transition for series **6.1** increase in the order **6.1a** (0.21) < **6.1e** (0.29) < **6.1d** (0.45) < **6.1b** (0.49) and are summarised in Table 6.1. For comparison, the corresponding value for $Ir(ppy)_3$ in toluene solution was measured to be 0.17.

In contrast, for series **6.2** materials, substitution of electron withdrawing groups results in a ^{1}MLCT band redshift of approximately 20 nm compared to that of the parent complex **6.2a**, and there is no significant effect on the relative strength of the ^{1}MLCT absorption band. Computational studies of the molecular orbitals indicate that there is increased carbazole ligand character to the excited state in series **6.2** compared to series **6.1** [15], which may explain the reduced effect that substitution has on the dipole moment of the series **6.2** materials.

Normalised photoluminescence spectra of series **6.1** and **6.2** iridium complexes as measured in 10^{-5} M toluene solution are shown in Figure 6.3, with the emission maxima summarised in Table 6.1. The different chemical substituents and their position on each ligand result in colour tuning over a large wavelength range. The photoluminescence spectrum maxima in toluene solution range from 505 nm to 630 nm, a difference of 125

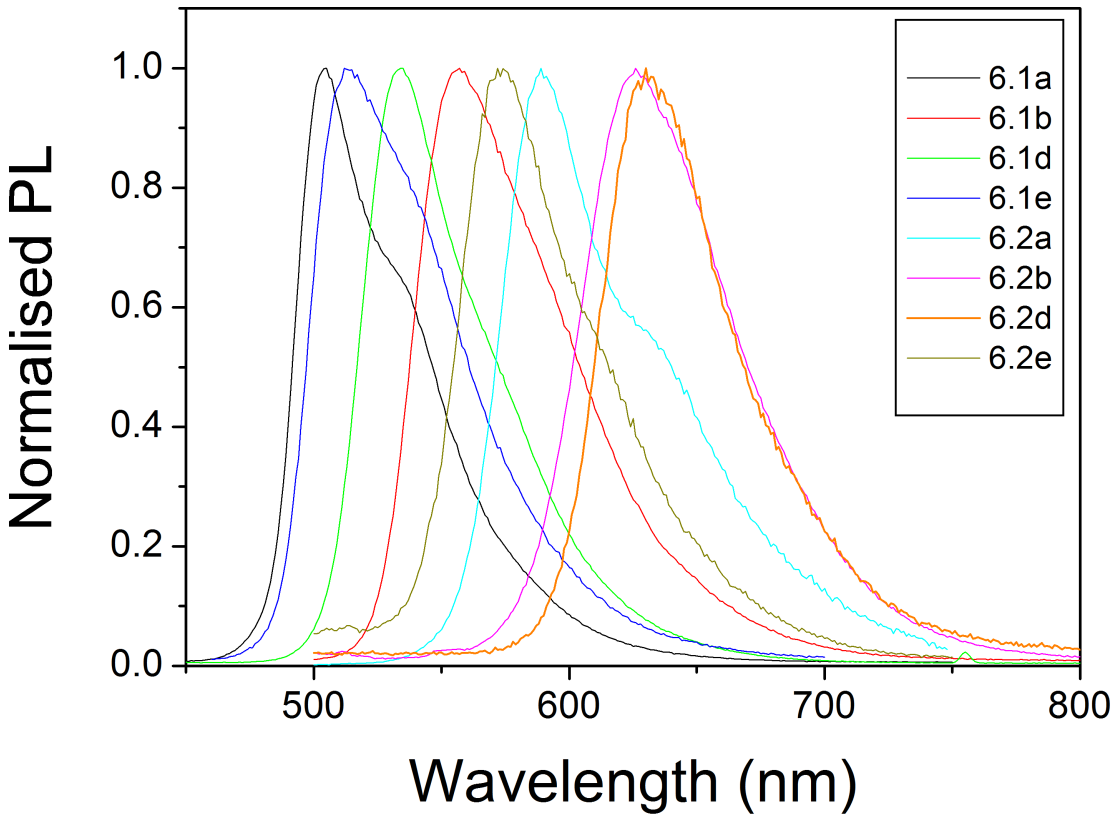

Figure 6.3: Normalised photoluminescence spectra of series **6.1** and **6.2** complexes measured in toluene solution.

nm.

Substitution of OMe at the *meta* position results in a redshift of 7 nm for **6.1e** compared to **6.1a**, while the same substitution for **6.2e** leads to a blueshift of 17 nm from **6.2a**. Substitution of CF_3 in series **6.1** redshifts emission substantially, by 30 nm for *meta*-substituted **6.1d** and 52 nm for *para*-substituted **6.1b**. The same substitutions in series **6.2** also lead to a substantial redshift in emission, but the location of the substitution makes little difference in this case with a redshift of 37 nm for *para*-substituted **6.2b** and 41 nm for *meta*-substituted **6.2d**. This also suggests that there is increased carbazole contribution to the excited state in series **6.2** materials.

The calculated Stokes shifts for these complexes are small, ranging from approxi-

Material	$\lambda_{max,PL}$ [a] / nm	ϕ_{PL} [b]	MLCT peak [c] strength	$\Delta\lambda$ [d] / nm	$\Delta T_1 - S_0$ [e] / Debye
$Ir(ppy)_3$	508	0.40	0.17	16	0.90
6.1a	505	0.54	0.21	19	1.22
6.1b	557	0.45	0.49	42	5.29
6.1d	535	0.63	0.45	34	3.74
6.1e	512	0.35	0.29	23	2.09
6.2a	589	0.11	-	-	-
6.2b	626	0.15	-	-	-
6.2d	630	0.10	-	-	-
6.2e	572	0.12	-	-	-

Table 6.1: Summary of photophysical data for series **6.1** and **6.2** complexes, with comparison of experimentally determined MLCT absorption strengths and solvatochromic shifts with computed transition dipole moments for series **6.1** complexes only.
[a]: Measured in toluene solution.
[b]: PLQY ± 5%, using $Ir(ppy)_3$ ($\phi = 0.40$) [18] as a reference. Measured in degassed toluene solution with an excitation wavelength of 340 nm.
[c]: Relative intensity of ^{1}MLCT band compared to peak $^1\pi - \pi^*$ transition.
[d]: Maximum peak shift in phosphorescence maximum in different polarity solvents.
[e]: Computed transition dipole moment as detailed in reference [17].

mately 0.11 to 0.20 eV, which indicates that there is a considerable iridium contribution to emission from MLCT transitions [15]. The weaker lower energy shoulders seen in the emission of CF_3 substituted materials show that there must be significant metal character in the molecular orbitals of these complexes in particular.

Photoluminescence quantum yield (PLQY) measurements in degassed toluene solution are shown in Table 6.1. PLQY values of series **6.1** complexes (0.35 to 0.63) are higher than those of series **6.2** (0.10 to 0.15), which could be attributed to the increased carbazole contribution to the excited state reducing the efficiency of radiative decay. Measurements on two similar complexes (2-pyridinyl-N-ethylcarbazole)$_2$Ir(acac) and (3-pyridinyl-N-ethylcarbazole)$_2$Ir(acac) followed the same pattern with PLQY values of 0.02 and 0.22 respectively [7].

6.4 Solvatochromic shifts of photoluminescence spectra

Photoluminescence spectra for complexes **6.1a**, **6.1b**, **6.1d** and **6.1e** were measured in six solvents of increasing polarity: cyclohexane (non-polar, 0 Debye), toluene (0.36 D), 1,4-dioxane (0.45 D), chlorobenzene (1.54 D), ethyl acetate (1.88 D) and acetonitrile (3.84 D) [17], shown in Figure 6.4. Significant redshifts of emission were observed for all four complexes as the solvent polarity increased. The peak shape becomes more Gaussian with increasing solvent polarity, indicating larger ICT character.

The maximum peak shift in the phosphorescence maximum $\Delta\lambda$, between the non-polar solvent cyclohexane and the most polar solvent acetonitrile, increases in the order **6.1a** ($\Delta\lambda$ = 19 nm, 0.09 eV) < **6.1e** ($\Delta\lambda$ = 23 nm, 0.11 eV) < **6.1d** ($\Delta\lambda$ = 34 nm, 0.14 eV) < **6.1b** ($\Delta\lambda$ = 42 nm, 0.17 eV). This pattern correlates with the order of the relative strengths of the ^{1}MLCT band compared to the $^1\pi - \pi^*$ band in the absorption spectra, and computed values for the transition dipole moments as detailed in reference [17].

Figure 6.5 shows the corresponding solvatochromic shift for series **6.2** complexes **6.2b**, **6.2d** and **6.2e** in five solvents of increasing polarity from toluene to acetonitrile. The same pattern is seen, with the complexes with electron-withdrawing substituents once again exhibiting the strongest shifts. The *para*-substituted complex **6.2b** shows the largest shift in emission peak of 16 nm as measured between toluene solution and acetonitrile solution. The overall shift is much weaker in series **6.2** when compared to that of series **6.1**, again suggesting that the increased carbazole contribution to the excited state in series **6.2** results in the substituent electron donating or withdrawing

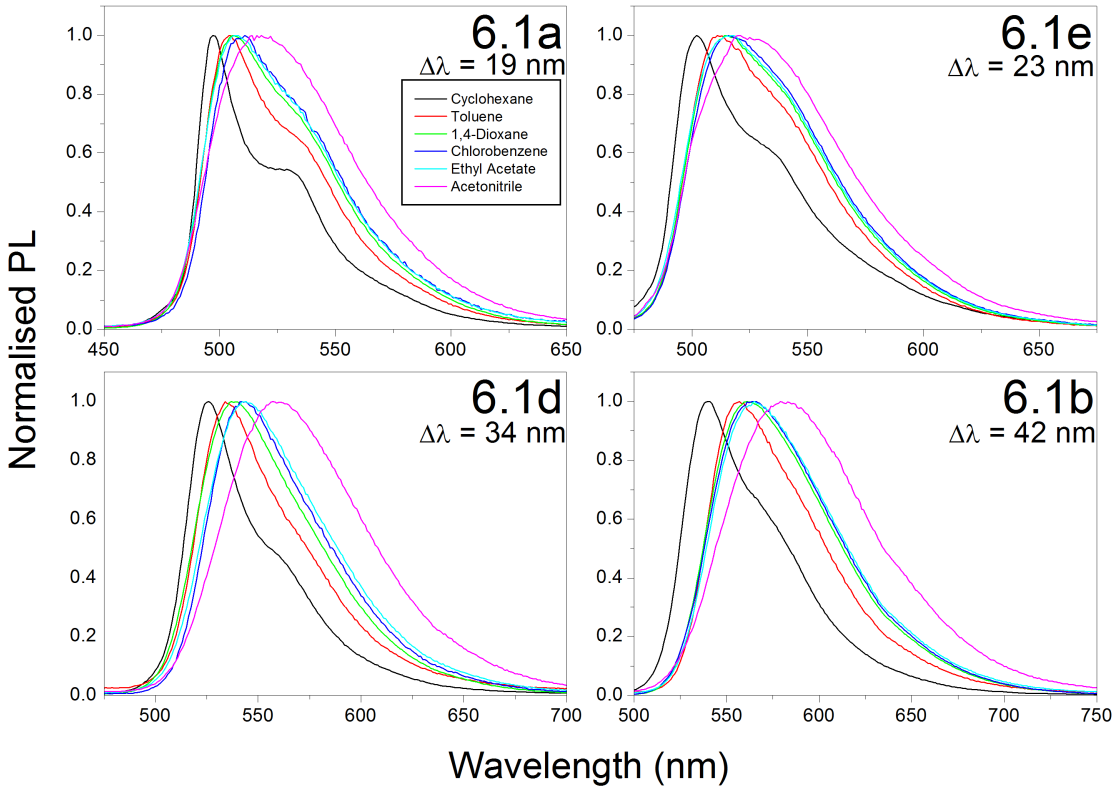

Figure 6.4: Photoluminescence emission spectra of complexes **6.1a**, **6.1b**, **6.1d** and **6.1e** in six solvents of increasing polarity: cyclohexane (non-polar), toluene (0.36 D), 1,4-dioxane (0.45 D), chlorobenzene (1.54 D), ethyl acetate (1.88 D) and acetonitrile (3.84 D) [17], demonstrating the increasing solvatochromic shift $\Delta\lambda$ observed as the molecular dipole moment of the complex increases.

groups having a reduced effect on the molecular dipole moment.

The corresponding solvatochromic shift data for $Ir(ppy)_3$ is shown in Figure 6.6 for comparison. The phosphorescence emission maximum shifts by 16 nm between non-polar cyclohexane solution and acetonitrile solution, which is slightly less than the 19 nm observed for the parent complex **6.1a**, indicating that the molecular dipole moment of $Ir(ppy)_3$ is weaker than **6.1a**.

The absorption coefficient data and the measurement of the solvatochromic shift for series **6.1** materials and the reference material $Ir(ppy)_3$ both correlate with calculated values of the transition dipole moments of these materials obtained from TD-DFT

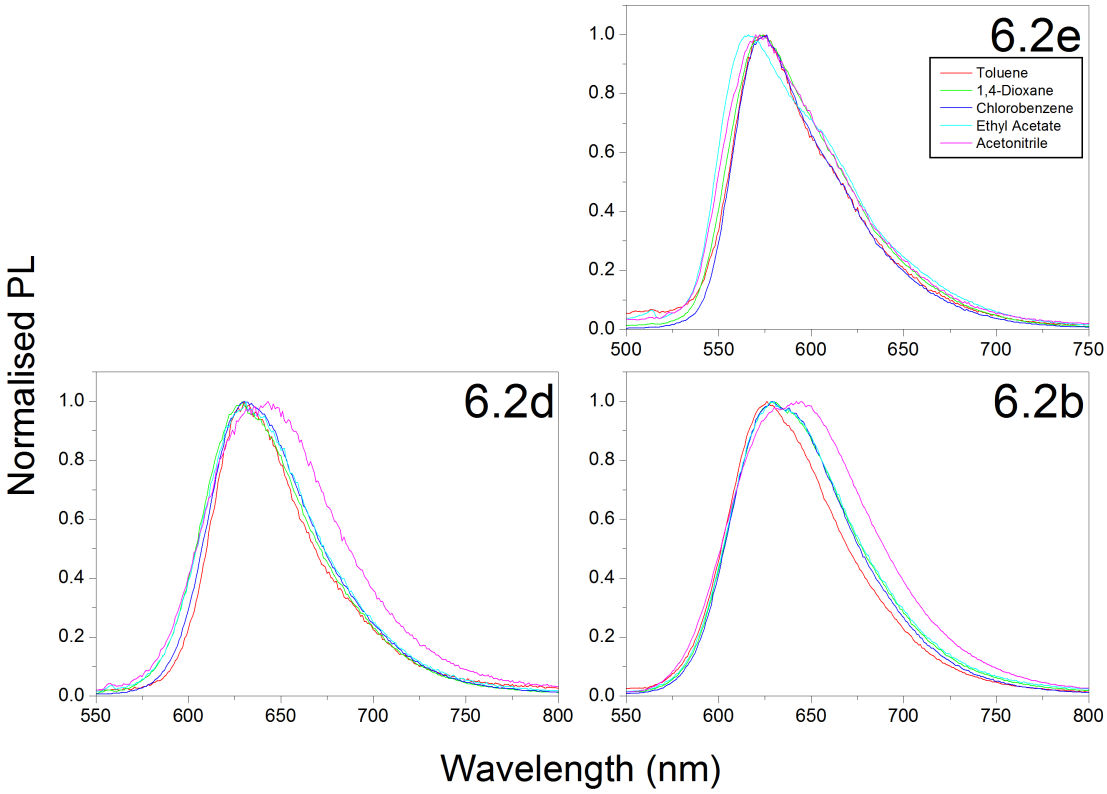

Figure 6.5: Photoluminescence emission spectra of complexes **6.2b**, **6.2d** and **6.2e** in five solvents of increasing polarity: toluene (0.36 D), 1,4-dioxane (0.45 D), chlorobenzene (1.54 D), ethyl acetate (1.88 D) and acetonitrile (3.84 D) [17], demonstrating the weaker solvatochromic effect exhibited by series **6.2** complexes.

computations carried out by Dr. Mark A. Fox of the Department of Chemistry at the University of Durham, using the B3LYP functional at the LANL2DZ:3-21G* basis set [17]. These transition dipole moment values are summarised in Table 6.1.

The dipole moments of the complexes can be calculated from the experimental data using the Lippert-Mataga equation [12]

$$\overline{\nu_A} - \overline{\nu_F} = \frac{2\left(\mu_E - \mu_G\right)^2}{hca^3}\left(\frac{\epsilon - 1}{2\epsilon + 1} - \frac{n^2 - 1}{2n^2 + 1}\right) + \text{const.} \tag{6.1}$$

where $\overline{\nu_A} - \overline{\nu_F}$ is the Stokes shift, μ_E and μ_G are the excited and ground state dipoles, ϵ and n are the solvent permittivity and refractive index and a is the radius of

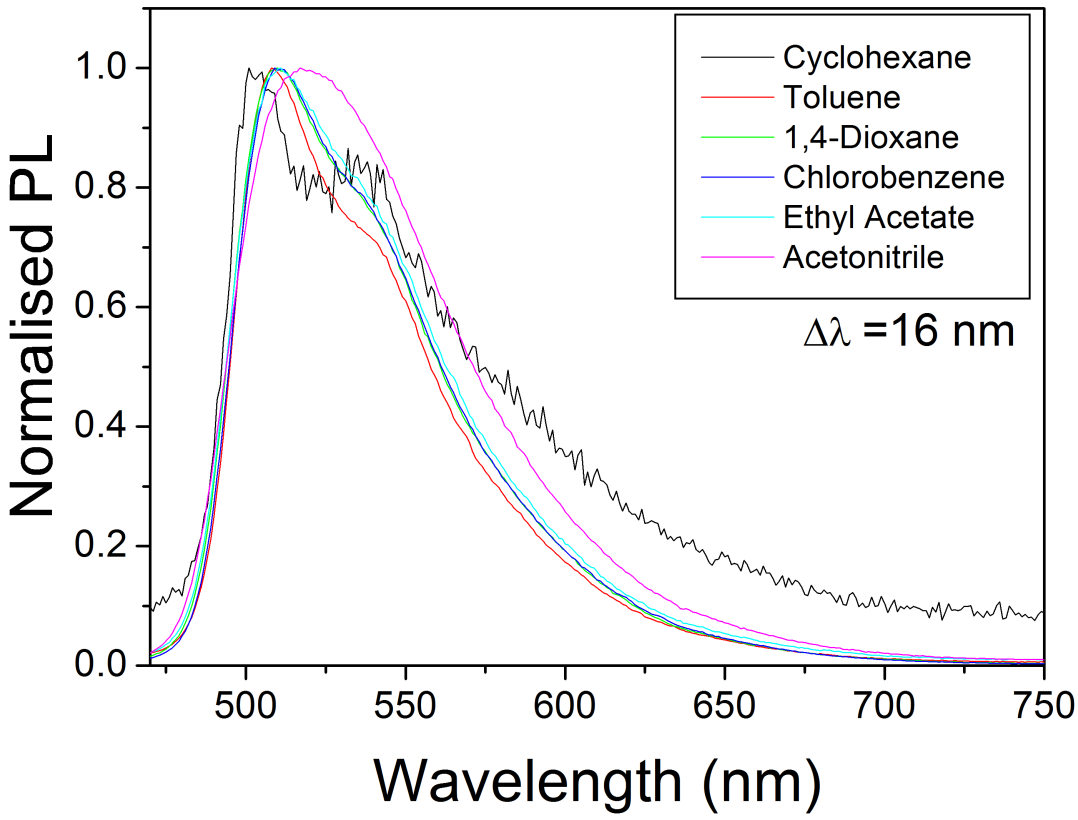

Figure 6.6: Solvatochromic shift in the emission spectrum of $Ir(ppy)_3$ in six solvents of increasing polarity, for comparison with series **6.1** complexes. A shift of 16 nm is observed, compared to 19 nm for the parent complex **6.1a**.

the solvent cavity occupied by the fluorophore.

Additionally, the solvent orientation polarisability Δf is defined as

$$\Delta f = \frac{\epsilon - 1}{2\epsilon + 1} - \frac{n^2 - 1}{2n^2 + 1}. \tag{6.2}$$

A plot of the wavenumber of the emission maximum against the solvent orientation polarisability Δf (as the effect of the solvent polarity only results in a comparatively small shift in absorption spectra compared to the shift in emission spectra for these materials) therefore results in a straight line with the gradient indicative of the strength of

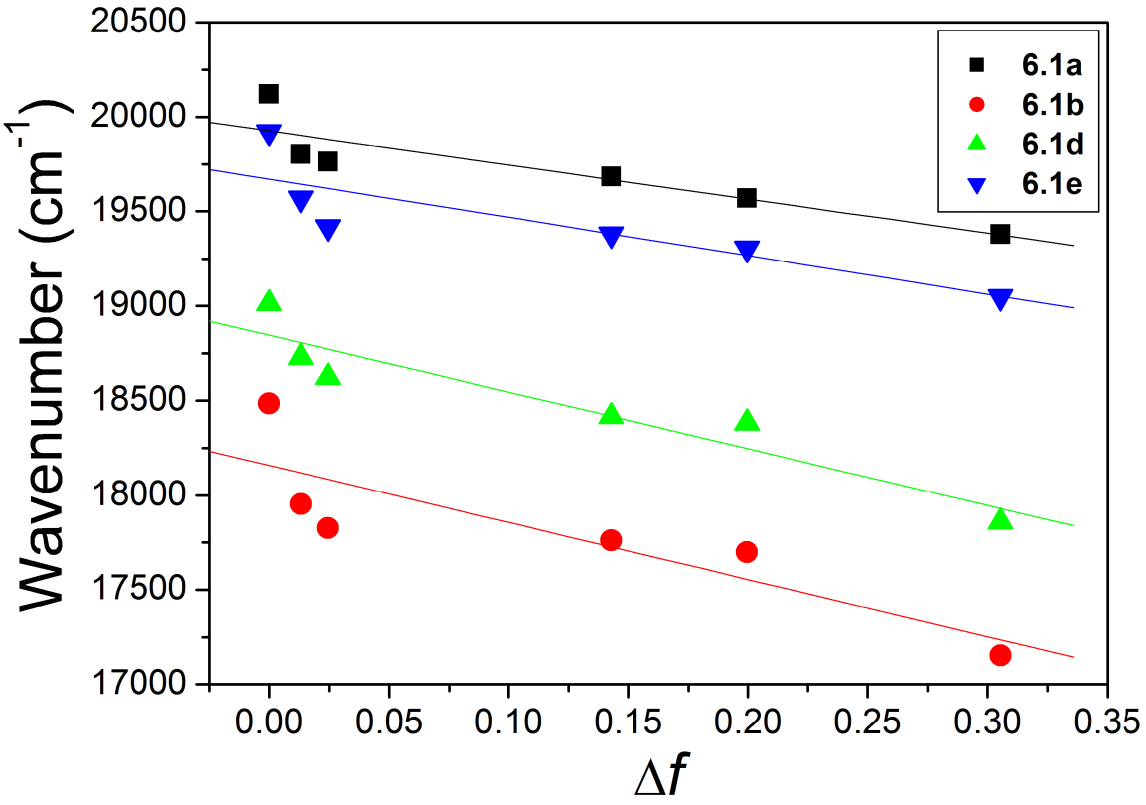

Figure 6.7: Lippert plot of the photoluminescence peak (in wavenumbers) in different solvents for **6.1** materials against the solvent orientation polarisability.

the transition dipole moment. This plot for the **6.1** series is shown in Figure 6.7, showing a broadly linear trend in emission maximum as the solvent orientation polarisability increases.

Assuming the cavity radii are similar for all complexes, the progressively steeper slopes of the plot show that the difference between excited and ground state dipole moments increase with **6.1a** having the smallest difference and **6.1b** having the largest difference.

This work shows that simple substitutions to the chemical structure of a phosphorescent dopant can have a major effect on both the colour of emitted light and on the strength of the molecular dipole moment. The increasing molecular dipole moment

Material	Turn-on [a] voltage / V	E.Q.E. [b] / %	Device [b] efficiency / cd A^{-1}	Brightness [b] / cd m^{-2}	Power [b] efficiency / lm W^{-1}
6.1a	10.0	12.0	40.0	3000	8.5
6.1b	7.0	7.9	23.3	2110	7.0
6.1c	12.0	9.2	30.5	2600	7.0
6.1d	7.5	10.2	36.5	2980	10.0
6.1e	10.5	11.5	36.6	2900	7.5
6.2a	13.0	5.6	10.3	120	2.0
6.2b	11.5	5.8	4.3	300	1.1
6.2d	14.0	4.0	2.4	110	0.6
6.2e	10.5	1.0	1.9	90	0.5

Table 6.2: Summary of the performance of single-layer electrophosphorescent devices made by Dr. Hameed Al-Attar containing series **6.1** and **6.2** complexes. Device structure: ITO // PEDOT:PSS (60 nm) // PVK:40% PBD:8% Ir (90 nm) // Ba (4 nm) // Al (100 nm).
[a]: Voltage at which the device reaches a brightness of 10 cd m^{-2}.
[b]: Peak values for the device.

strength of the dopant affects the carrier mobility in devices, which will be discussed further in the next section.

6.5 Electrophosphorescent device results

Initial characterisation of simple single emissive layer devices using these materials have been carried out previously [1]. Further devices were made by Dr. Hameed Al-Attar with the structure ITO // PEDOT:PSS (60 nm) // PVK:40% PBD:8% Ir (90 nm) // Ba (4 nm) // Al (100 nm). The efficiency and luminance data for these devices are summarised in Table 6.2 [15].

Devices containing complex **6.1a** reached a maximum efficiency of 40 cd A^{-1} and 12% E.Q.E., which is particularly high for single layer solution processed OLED devices [17]. Devices containing complex **6.2a** reached a maximum efficiency of 10.3 cd A^{-1}

and 5.6% E.Q.E.

The large differences in the current density observed for the series **6.1** devices suggest that the carrier mobility in these devices is being determined by the molecular dipoles of the dopant complexes, which can be considered as a quasi-permanent dipole as the lifetime of the transition dipole moment is on the order of microseconds for these complexes.

These randomly oriented dipole moments of the dopant molecules cause positional and energetic disorder, with larger transition dipole moments resulting in higher disorder. This can affect the electron and hole mobilities in different ways as described in reference [17], which perturbs the charge carrier balance in the devices. This leads to an increase in the dark current with lower exciton formation and a corresponding decrease in the device efficiency. This can be seen in the data shown in Table 6.2, where the efficiency of series **6.1** devices decreases according to the same trend as increasing molecular dipole moment of the dopant complex.

The wide range of colours emitted by this family of complexes and their high device efficiencies make them attractive for use in full colour displays and components of white light devices. A two-colour white device could be made by pairing an orange emitter with a blue emitter, or a three-colour white could be achieved with red, green and blue emitting components.

6.6 Conclusions

To conclude, colour tuning by the systematic substitution of electron donating or electron withdrawing groups has been demonstrated with a series of iridium complexes

incorporating carbazole-based ligands. The emission of this family of complexes spans a wide range of colours from green to red.

Measurements of the degree of the solvatochromic shift in photoluminescence emission with increasing solvent polarity, as well as the relative strength of the metal to ligand charge transfer transition in the absorption spectrum, correlate with values of the molecular dipole moment obtained by TD-DFT calculations for the series **6.1** materials. In contrast, a comparatively smaller shift was observed for the **6.2** materials which also exhibit lower quantum yields. This may be due to increased carbazole contribution to the excited state in the latter series.

Finally, highly efficient single layer solution processable devices have been demonstrated by colleagues that reach a current efficiency of 40 cd A^{-1} and an E.Q.E. of 12% for **6.1a**. The good colour tunability of these materials and their ease of processing in solution are promising for display applications, phosphorescent white light emission and large area devices.

These materials also demonstrate how systematic substitution can allow synthetic chemists great control over both the optical and electrical properties of phosphorescent complexes which will be useful in the design of new materials.

References

[1] G. C. Griffiths, *Characterisation and Optimisation of Electrophosphorescent OLED Devices*, MPhys thesis, Durham University (2009)

[2] V. V. Grushin, N. Herron, D. D. LeCloux, W. J. Marshall, V. A. Petrov & Y. Wang, *Chemical Communications* (2001), 1494 - 1495

[3] G. Zhou, C.-L. Ho, W.-Y. Wong, Q. Wang, D. Ma, L. Wang, Z. Lin, T. B. Marder & A. Beeby, *Advanced Functional Materials* **18** (2008), 499 - 511

[4] Y. You & S. Y. Park, *Journal of the American Chemical Society* **127** (2005), 12438 - 12439

[5] X. Gu, T. Fei, H. Zhang, H. Xu, B. Yang, Y. Ma & X. Liu, *European Journal of Inorganic Chemistry* (2009), 2407 - 2414

[6] C.-J. Chang, C.-H. Yang, K. Chen, Y. Chi, C.-F. Shu, M.-L. Ho, Y.-S. Yeh & P.-T. Chou, *Dalton Transactions* (2007), 1881 - 1890

[7] C. Yang, X. Zhang, H. You, L. Zhu, L. Chen, L. Zhu, Y. Tao, D. Ma, Z. Shuai & J. Qin, *Advanced Functional Materials* **17** (2007), 651 - 661

[8] S. Bettington, M. Tavasli, M. R. Bryce, A. Beeby, H. Al-Attar & A. P. Monkman, *Chemistry - A European Journal* **13** (2007), 1423 - 1431

[9] C.-L. Ho, Q. Wang, C.-S. Lam, W.-Y. Wong, D. Ma, L. Wang, Z.-Q. Gao, C.-H. Chen, K.-W. Cheah & Z. Lin, *Chemistry - An Asian Journal* **4** (2009), 89 - 103

[10] V. Bulović, A. Shoustikov, M. A. Baldo, E. Bose, V. G. Kozlov, M. E. Thompson & S. R. Forrest, *Chemical Physics Letters* **287** (1998), 455 - 460

[11] C.-L. Chiang, S.-M. Tseng, C.-T. Chen, C.-P. Hsu & C.-F. Shu, *Advanced Functional Materials* **18** (2008), 248 - 257

[12] J. R. Lakowicz, *Principles of Fluorescence Spectroscopy* Third Edition (2006), Springer

[13] W. Leslie, R. A. Poole, P. R. Murray, L. J. Yellowlees, A. Beeby & J. A. G. Williams, *Polyhedron* **23** (2004), 2769 - 2777

[14] T. Moore, *Cyclometallated Iridium-Carbazole Complexes for OLED Applications*, MSci thesis, Durham University (2008)

[15] M. Tavasli, T. N. Moore, Y. Zheng, M. R. Bryce, M. A. Fox, G. C. Griffiths, V. Jankus, H. A. Al-Attar & A. P. Monkman, *Journal of Materials Chemistry* **22** (2012), 6419 - 6428

[16] N. Miyaura & A. Suzuki, *Chemical Reviews* **95** (1995), 2457 2483

[17] H. A. Al-Attar, G. C. Griffiths, T. N. Moore, M. Tavasli, M. A. Fox, M. R. Bryce & A. P. Monkman, *Advanced Functional Materials* **21** (2011), 2376 - 2382

[18] K. A. King, P. J. Spellane & R. J. Watts, *Journal of the American Chemical Society* **107** (1985), 1431 - 1432

7 White electroluminescence from single polymers exhibiting broadened blue intramolecular charge transfer emission

This chapter describes work carried out on a series of novel white-emitting single copolymers incorporating fluorene (F) and dibenzothiophene-S,S-dioxide (S) units synthesised by Dr. Katy Moss in the Department of Chemistry at the University of Durham [1]. The F/S system exhibits broad, efficient blue intramolecular charge transfer emission, and red-emitting 4,7-bis(2-thienyl)-2,1,3-benzothiadiazole (TBT) and green-emitting 2,1,3-benzothiadiazole (BT) units were added to the copolymer to achieve white light emission.

Firstly, literature reports of single-polymer white light OLED devices are reviewed as well as previous work carried out in Durham on the properties of the F/S system. Absorption and photoluminescence emission characterisation of the materials in thin film are then presented. The photoluminescence emission spectra of polymers incorporating all three red, green and blue emitter units show good spectral coverage throughout the visible spectrum, with the CIE coordinates of the PL emission indicating the potential applications these materials have for white light OLED devices.

Multilayer solution processable devices incorporating two of the most promising materials were fabricated with varying emissive layer thicknesses, with the colour of light emitted varying considerably as a function of emissive layer thickness. A comparison of the two materials (with one incorporating the S unit and the other without) in

single layer and multilayer devices indicated that the S unit was necessary for broad, efficient emission in the blue region of the spectrum, although the overall efficiency was higher without the S unit. It is concluded that the materials are promising for applications in white light OLED devices with more optimisation needed, for example optimisation of the balance of charge carrier units in the copolymer.

7.1 Review

White light emission from single polymer systems offers an alternative approach towards white OLED fabrication, where all the chromophores needed for white light emission are components of one single copolymer. This approach has several advantages over polymer blend or multilayer device structures, such as ease of processing and reduced phase separation that may have an effect on device stability and change the colour of light emitted over time [2, 3].

A number of reviews of the history and current state of research into single polymer white OLED devices have been published [3–5]. There are two main ways in which white emission can be achieved. The chromophores can either be incorporated into the main chain of the polymer, or they can be attached to the backbone as side chains.

Some examples of copolymers where the chromophores are incorporated into the main polymer chain follow. Efficient two-colour single polymer devices were reported by Liu *et al.* with polyfluorene as the blue emitting polymer backbone and TPABT as an orange emitting dopant [6]. Devices with the structure ITO // PEDOT:PSS (40 nm) // polymer (70 nm) // Ca (10 nm) // Al (100 nm) reached device efficiencies of 8.99 cd A^{-1}, 5.75 lm W^{-1} and 3.8% E.Q.E. and CIE coordinates of (0.35, 0.34) with

no reported voltage dependence of the emission.

A single copolymer reported by Luo *et al.* consisted of a polyfluorene backbone as blue emitter doped with BT as a green emitter and TBT as a red emitter [7]. The best devices, with the structure ITO // PEDOT (50 nm) // PVK (40 nm) // polymer (75 nm) // Ba (3-4 nm) // Al (200 nm), achieved an efficiency of 6.20 cd A^{-1} and 3.84% E.Q.E. when tested in a nitrogen-filled drybox. Additionally, promising CIE coordinates of (0.35, 0.34) were reportedly stable over a range of device operating voltages.

Chuang *et al.* extended this approach by incorporating oxadiazole and triarylamine groups as charge transporting side chains attached to the polyfluorene backbone [8]. Also incorporating a thermally evaporated electron transport layer of TPBI for an overall device architecture of ITO // PEDOT:PSS (35 nm) // polymer (50 - 70 nm) // TPBI (30 nm) // Mg:Ag (100 nm) // Ag (100 nm), devices with a maximum efficiency of 4.87 cd A^{-1} and 2.22% E.Q.E. were reported with CIE coordinates of (0.37, 0.36).

A number of polymers where chromophores are incorporated as side chains attached to the polymer backbone have also been reported. Liu *et al.* reported a three colour fluorescent polymer with devices that obtained CIE coordinates of (0.33, 0.36) at an efficiency of 8.6 cd A^{-1} and 5.4 lm W^{-1} with a structure of ITO // PEDOT:PSS (40 nm) // polymer (90 nm) // Ca (10 nm) // Al (100 nm) [9]. Subsequent optimisation of a solution processable electron injection/transport layer consisting of phosphonate-functionalised polyfluorene [10] increased the device performance to 15.4 cd A^{-1}, 11.4 lm W^{-1} and 6.7% E.Q.E. but also had the effect of shifting the CIE coordinates to (0.37, 0.42).

Side chain chromophores can also be phosphorescent iridium emitters, for example the polymer reported by Shao *et al.* consists of blue and yellow iridium phosphors attached to a fluorinated poly(arylene ether phosphine oxide) backbone [11]. Devices with structure ITO // PEDOT:PSS (40 nm) // polymer (40 nm) // SPOO13 (50 nm) // LiF (1 nm) // Al (100 nm) achieved a maximum efficiency of 18.4 cd A^{-1}, 8.5 lm W^{-1} and 7.1% E.Q.E. although a colour shift from (0.31, 0.42) to (0.28, 0.40) was observed as the voltage was increased from 7 to 10 V. This was attributed to increased charge trapping on the orange emitter at lower voltages.

At the University of Durham, dual fluorescence from copolymers containing (9,9-dioctylfluorene) (F) and dibenzothiophene-S,S-dioxide (S) units have been investigated. For simple F/S copolymers, the photoluminescence emission was observed to broaden and redshift with increasing S unit content as the intramolecular charge transfer state (ICT) is stabilised and the proportion of emission from locally excited states is reduced [12]. Devices containing polymers with increasing S unit content showed increasing efficiency as well as emission broadened towards green-white emission [13]. A maximum E.Q.E. of 1.3% was obtained at CIE coordinates of (0.24, 0.41) for the polymer with highest S unit content. The S unit was also credited with improving electron injection and electron transport in the device. Addition of the red-emitting TBT unit to this polymer in increasing amounts shows progressively stronger red emission in the photoluminescence spectrum [14], tuning the emission towards coordinates promising for lighting applications from (0.38, 0.38) to (0.31, 0.32) [13].

These results form a promising basis for the development of white light emitting devices. New materials building on this work have been synthesised incorporating

green-emitting BT units as well as red-emitting TBT units so that three colour emission with good spectral coverage can be achieved. These materials will be introduced in the next section.

7.2 Materials

Two series of copolymers were synthesised in Dr. Katy Moss at the Department of Chemistry, University of Durham [1]. In addition to the F and S units already described, the polymers incorporate either a carbazole-based or arylamine-based hole transport unit. As the S unit is a good electron transporter, the ratio of the two charge transport units can be easily tuned to optimise charge carrier mobility through a device layer.

With the addition of 4,7-bis(2-thienyl)-2,1,3-benzothiadiazole (TBT) as a red emitter and 2,1,3-benzothiadiazole (BT) as a green emitter in small concentrations, white light emitting single polymers with balanced charge transport properties can be obtained.

Figure 7.1 shows the structure of the carbazole-based polymers **7.1** and **7.2**. The percentage composition of each polymer is summarised in Table 7.1. These two polymers both contain the red emitting TBT unit at different concentrations to determine how much red emitter is needed for a two-colour white emitter with good spectral coverage.

Figure 7.2 shows the structure of the arylamine-based polymers **7.3**, **7.4**, **7.5** and **7.6**. The percentage composition of each polymer is summarised in Table 7.2. Polymer **7.3** is the parent polymer of this series and only contains F, S and hole transport units

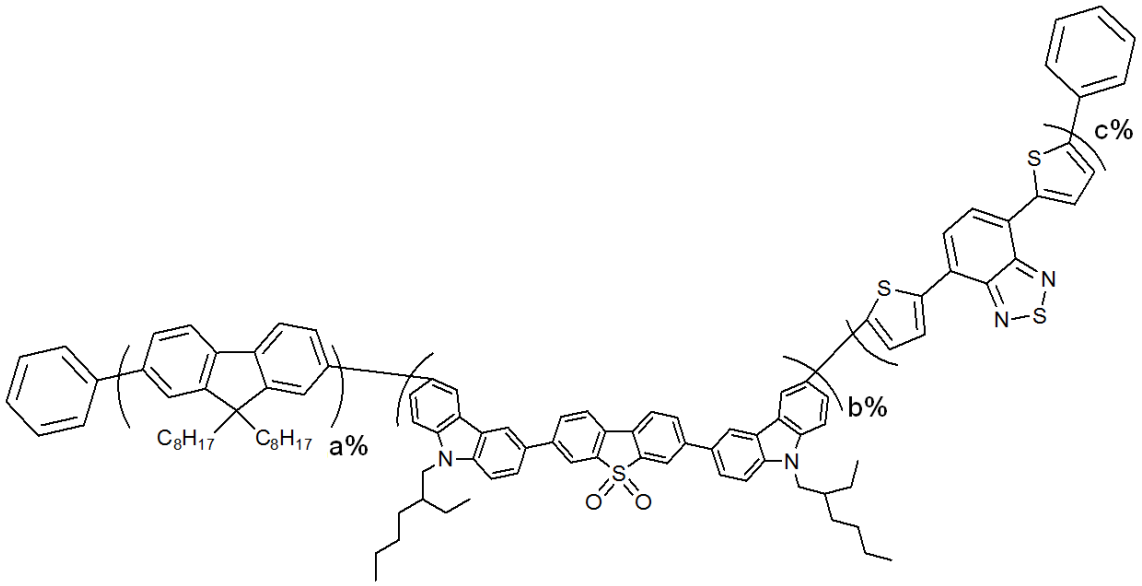

Figure 7.1: Chemical structure of the carbazole-based white-emitting copolymers **7.1** and **7.2**. For **7.1** the relative composition of the three components is a=69.95%, b=30% and c=0.05%. For **7.2** the red emitter component is increased so that a=69.925%, b=30% and c=0.075%.

Polymer	a (%)	b (%)	c (%)
7.1	69.95	30	0.05
7.2	69.925	30	0.075

Table 7.1: Composition of carbazole-based polymers **7.1** and **7.2**. The percentages of components in the polymer are given by a, b and c, where a is the percentage of F in the polymer, b the amount of the carbazole/S unit and c the amount of the TBT red emitter [1].

without any red or green emitter. Polymer **7.4** contains the red emitting TBT unit for a two-colour white emitting polymer, while **7.5** has both red TBT and green BT emitters incorporated to provide good overall spectral coverage throughout the visible region.

In order to investigate the role of the S unit on the emission of the polymer and the performance of devices, polymer **7.6** was synthesised which is analogous to **7.5**, but without any S unit incorporated.

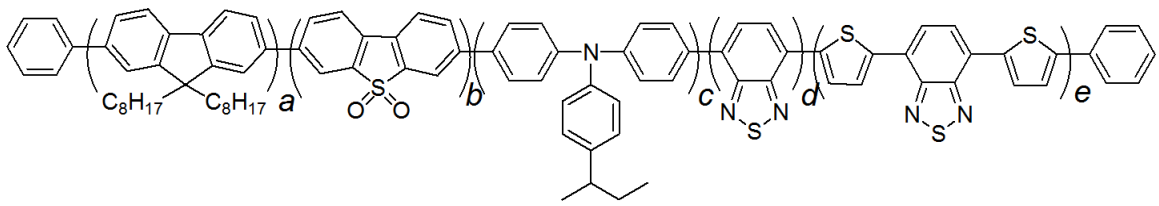

Figure 7.2: Chemical structure of the arylamine-based copolymers **7.3** to **7.6**. Polymer **7.3** is the parent polymer with the composition a=85%, b=5% and c=10%, without any green or red emitter d or e. Polymer **7.4** is a two colour white-emitting polymer with an added TBT red emitter in the ratio a=84.925%, b=5%, c=10%, d=0% and e=0.075%, whereas a green emitting BT component is added to **7.5** for a composition of a=84.825%, b=5%, c=10%, d=0.1% and e=0.075%. Polymer **7.6** is analogous to **7.5** except without the S unit and has the composition a=89.825%, b=0%, c=10%, d=0.1% and e=0.075%

Polymer	a (%)	b (%)	c (%)	d (%)	e (%)
7.3	85	5	10	0	0
7.4	84.925	5	10	0	0.075
7.5	84.825	5	10	0.1	0.075
7.6	89.825	0	10	0.1	0.075

Table 7.2: Composition of arylamine-based polymers **7.3** to **7.6**. The percentages of components in the polymer are given by a, b, c, d and e, where a is the percentage of F in the polymer, b the amount of the S unit, c the amount of the arylamine unit, d the amount of green emitter and e the amount of red emitter [1].

7.3 Absorption and photoluminescence emission spectra

Absorption and photoluminescence emission spectra of all copolymers were measured in thin film. All films were spin coated from 10 mg/ml toluene solution onto 1 cm diameter quartz substrates at 2500 rpm for 60 seconds and baked on a hotplate at 120° C for 10 minutes, resulting in *ca.* 70 - 90 nm thick films.

Figure 7.3 shows normalised absorption and photoluminescence spectra of the two carbazole-based white-emitting copolymers **7.1** and **7.2**. Increasing the percentage of the red emitting TBT segment from 0.05% to 0.075% has little effect on the absorption spectrum, with both copolymers showing a single absorption peak at *ca.* 375 nm.

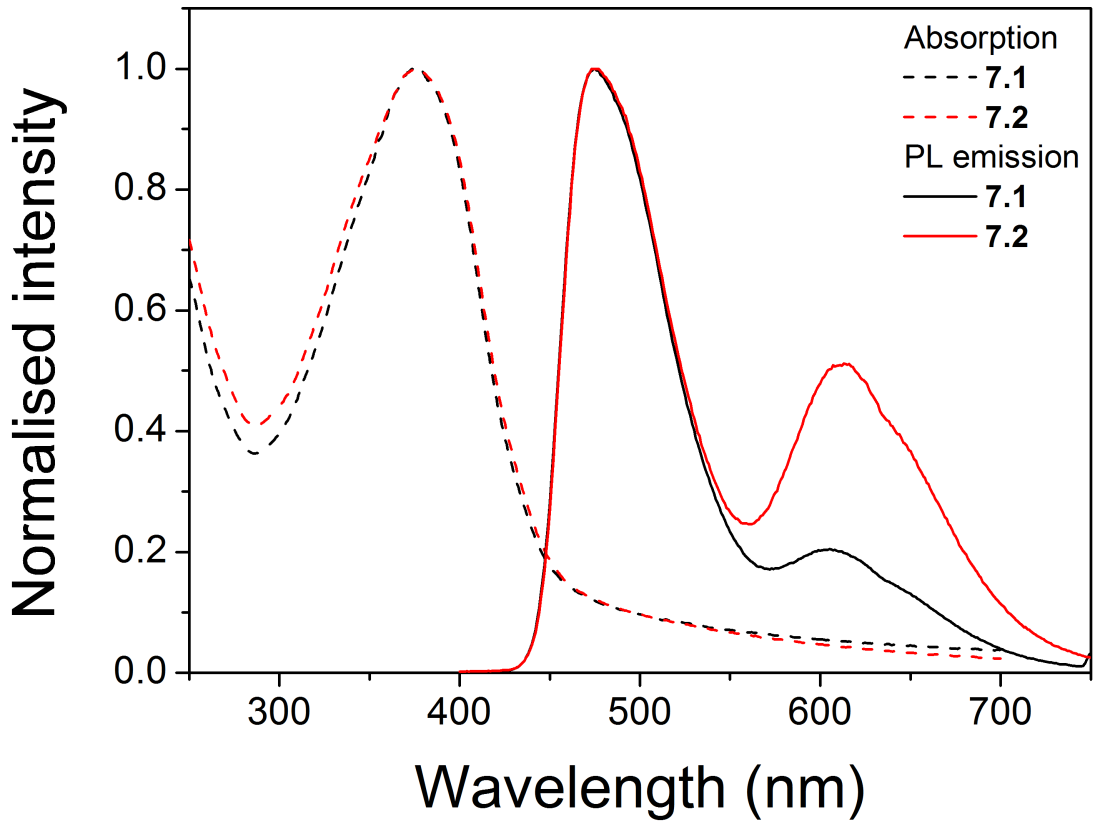

Figure 7.3: Normalised absorption and photoluminescence emission spectra of the two carbazole-based white-emitting copolymers **7.1** and **7.2** in film. The excitation wavelength for the PL emission measurement was 375 nm.

The intensity of the red peak of the emission spectrum is increased considerably, from 0.20 times to 0.51 times the intensity of the blue emission peak. Both polymers have emission peaks in the blue region of the spectrum at 475 nm, while the red peak is observed at 605 nm for **7.1** and 613 nm for **7.2**. The CIE coordinates of the PL emission of these two copolymers are (0.23, 0.32) for **7.1** and (0.31, 0.34) for **7.2**. These are plotted in Figure 7.6. The increased red emission results in better spectral coverage and shifts the overall photoluminescence emission of the polymer closer towards the white area of the CIE diagram.

Figure 7.4 shows normalised absorption and photoluminescence spectra of the three

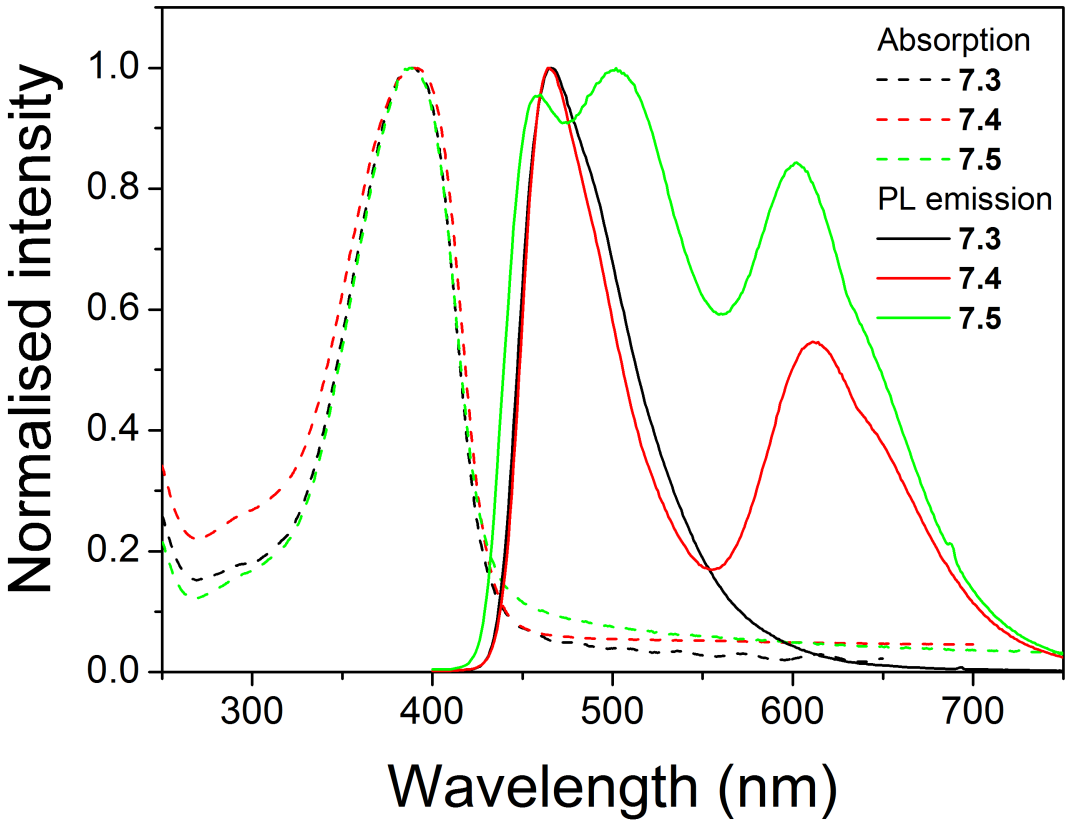

Figure 7.4: Normalised absorption and photoluminescence emission spectra of the three arylamine-based copolymers **7.3**, **7.4** and **7.5** in film. The excitation wavelength for the PL emission measurement was 390 nm.

arylamine-based copolymers **7.3**, **7.4** and **7.5**. The parent polymer **7.3**, without any green or red emitter, exhibits an absorption peak at *ca.* 389 nm and a blue emission peak at 466 nm. With the addition of 0.075% red-emitting TBT (copolymer **7.4**), emission in the red region of the spectrum peaking at 611 nm is observed. Incorporation of 0.1% green-emitting BT (copolymer **7.5**) results in three broad emission peaks at 465 nm (blue), 507 nm (green) and 607 nm (red), covering a wide range of the visible spectrum with CIE coordinates of (0.33, 0.37). The proximity of this broad photoluminescence emission to the white point makes this polymer particularly promising for white OLED applications. The CIE coordinates for **7.3** and **7.4** are (0.16, 0.25) and

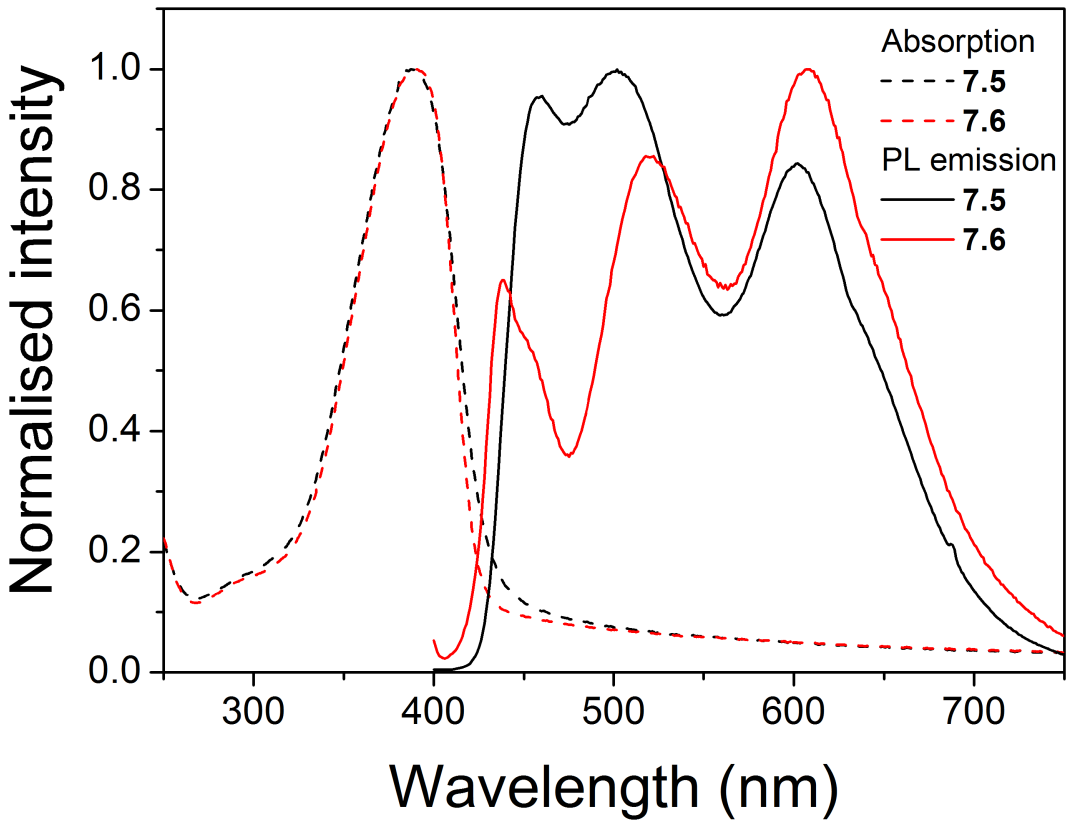

Figure 7.5: Comparison of the normalised absorption and photoluminescence emission spectra of copolymer **7.6**, not containing the S unit, with the S-containing copolymer **7.5** in film. The excitation wavelength for the PL emission measurement was 390 nm.

(0.31, 0.28) respectively. Again, there is little change in the absorption spectra of the copolymers when green and red emitting dopants are added.

Figure 7.5 compares the absorption and photoluminescence emission spectra of polymers **7.5** and **7.6**, showing how the inclusion of the S unit in polymer **7.5** affects the emission of the film. Polymer **7.6**, without the S unit, has an unchanged absorption spectrum compared to **7.5**, but has reduced emission in the blue region at 438 nm due to the absence of the charge transfer interaction between F and S that leads to a broadened blue-green emission in polymer **7.5**. Peaks in the photoluminescence emission spectrum of **7.6** are also observed at 520 nm (green) and 607 nm (red), and

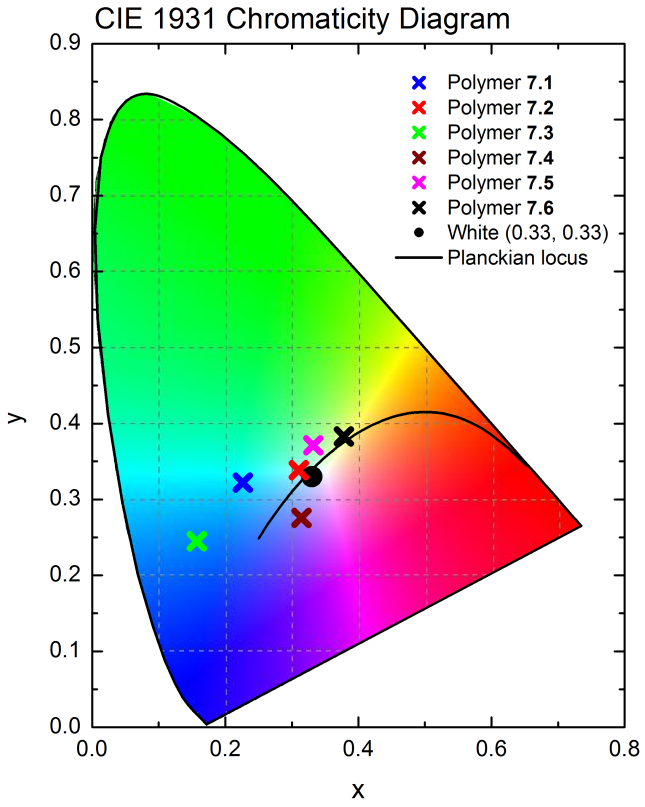

Figure 7.6: CIE chromaticity diagram showing the coordinates of photoluminescence emission for polymers **7.1** to **7.6**. Polymers **7.2** (0.31, 0.34), **7.5** (0.33, 0.37) and **7.6** (0.38, 0.38) in particular show promising emission for white OLED devices.

Polymer	PLQY (%)
7.5	39 ± 3
7.6	29 ± 3

Table 7.3: Photoluminescence quantum yields of unencapsulated films of **7.5** and **7.6**, excitation wavelength 395 nm.

the CIE coordinates of the photoluminescence emission of this polymer is shifted away from the white point to (0.38, 0.38) as shown in Figure 7.6.

Photoluminescence quantum yields of (39 ± 3)% and (29 ± 3)% were measured for unencapsulated films of **7.5** and **7.6** respectively, fabricated in the same manner as those for absorption and emission measurements. The measured PLQY values are summarised in Table 7.3. The photoluminescence spectra of **7.5** and **7.6** and their proximity to the desired white coordinates on the CIE chromaticity diagram make these materials particularly promising for white OLED applications.

7.4 Characterisation and optimisation of single polymer white OLEDs

The two white-emitting polymers **7.5** and **7.6** were chosen for the initial device characterisation due to their promising photoluminescence CIE coordinates, and to determine the role of the S unit in the copolymer. Multilayer devices with a *ca.* 30 nm thick layer of high molecular weight PVK (Aldrich, average M_W 1,100,000) as a solution processable hole transport/electron blocking layer were fabricated for both polymers, with optimisation of the thickness of the emissive polymer layer. Subsequent sets of devices were made to compare the two polymers in both single layer and multilayer device architectures to determine what role the S unit plays in the polymer system.

7.4.1 Thickness optimisation of 7.5 multilayer devices

Table 7.4 summarises the performance and efficiency of multilayer devices with different emissive layer thicknesses of polymer **7.5**, while Figure 7.7 shows their full *J*-*V*, *L*-*V* and device efficiency data. The thickness of the emissive layer was varied by spin coating the polymer from 5, 8, 10 and 12 mg/ml toluene solution. This resulted in layer thicknesses of 34.1, 53.5, 67.2 and 81.8 nm respectively measured by ellipsometry. PVK layers were spin coated from a 7 mg/ml chlorobenzene solution, resulting in a layer thickness of 30 nm. The overall device architecture was ITO // PEDOT:PSS (HIL 1.1) // PVK (30 nm) // **7.5** (x nm) // Ba (4 nm) // Al (125 nm).

As the emissive layer thickness increases, the turn-on voltage of the device increases from 6 V to 9.5 V. The highest efficiencies of 0.81% E.Q.E. and 1.37 cd A^{-1} were

Device	Thickness [a] / nm	Turn-on [b] voltage / V	E.Q.E. [c] / %	Device [c] efficiency / cd A^{-1}	Brightness [c] / cd m^{-2}	Power [c] efficiency / lm W^{-1}
1	34.1	6.0	0.42	0.78	2386	0.36
2	53.5	7.0	0.61	1.17	2846	0.38
3	67.2	7.5	0.53	1.02	2037	0.22
4	81.8	9.5	0.81	1.37	716	0.32

Table 7.4: Summary of the performance of multilayer devices with varying thicknesses of **7.5**. Device structure ITO // PEDOT:PSS (HIL 1.1) // PVK (30 nm) // **7.5** (x nm) // Ba (4 nm) // Al (125 nm).
[a]: Device thicknesses obtained by spin coating from concentrations of 5, 8, 10 and 12 mg/ml toluene solution.
[b]: Voltage at which the device reaches a brightness of 10 cd m^{-2}.
[c]: Peak values for the device.

obtained for the thickest emissive layer of 81.8 nm, although that device was also the least bright at 716 cd m^{-2}. An emissive layer of 53.5 nm produced reasonable efficiencies of 0.61% E.Q.E. and 1.17 cd A^{-1} at a much higher brightness of 2,846 cd m^{-2}. However the major effect of varying the thickness of the emissive layer was on the colour of light emitted by the device.

The electroluminescence spectra of these devices are shown in Figure 7.8. The spectra vary considerably as the thickness of the emissive layer is changed. The green-blue component of emission is weakened significantly as the emissive layer thickness increases, while the red emission grows stronger. At a layer thickness of 34.1 nm the blue peak is twice the intensity of the red peak, but at a thickness of 81.8 nm the blue peak is barely visible and the predominant emission of the device is red. This may be due to a significant device microcavity effect, or by increased trapping at the BT and TBT units in the thicker emissive layers.

A similar electroluminescence spectrum to that of the 81.8 nm device was reported

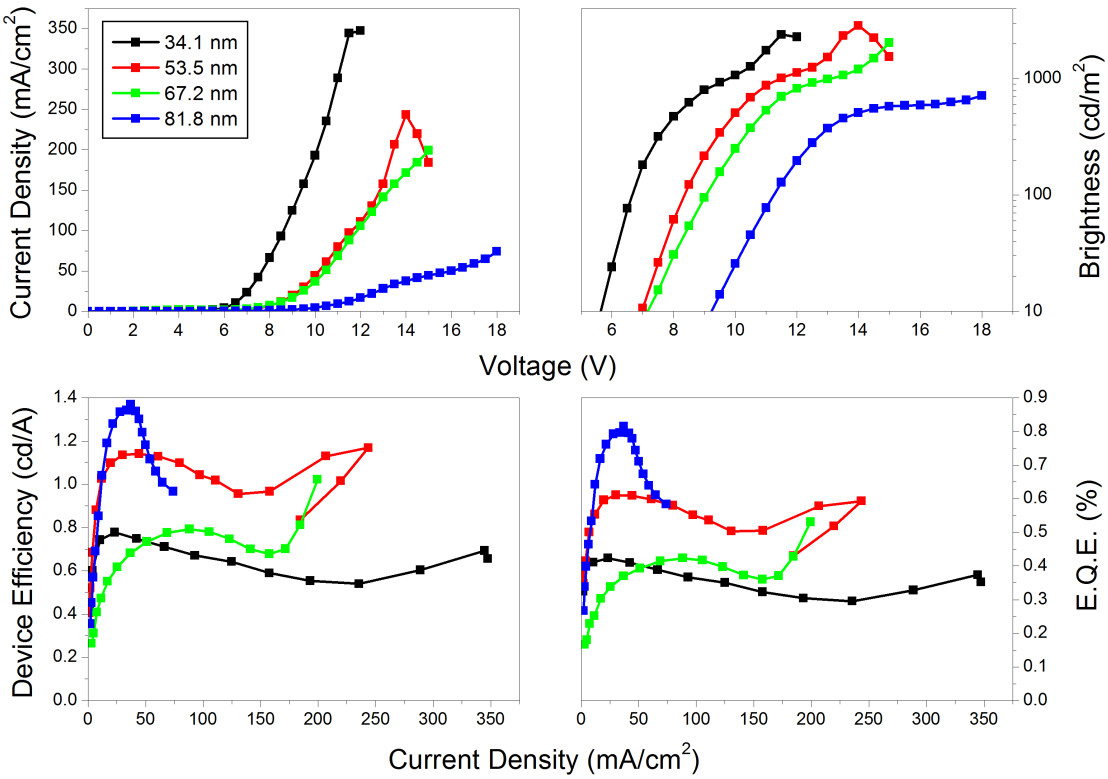

Figure 7.7: *J-V*, *L-V* and device efficiency data for multilayer devices with varying thicknesses of **7.5**. Device structure ITO // PEDOT:PSS (HIL 1.1) // PVK (30 nm) // **7.5** (x nm) // Ba (4 nm) // Al (125 nm). Increasing the layer thickness both increases the turn-on voltage and decreases the current flow through the device. The peak brightness of 2846 cd m^{-2} was obtained at a thickness of 53.5 nm while a peak efficiency of 1.37 cd A^{-1} and 0.81% E.Q.E. was obtained at 81.8 nm, the thickest layer measured.

for a device based on a comparable single polymer by Chuang *et al.* [8] with the structure ITO // PEDOT:PSS (35 nm) // polymer // TPBI (30 nm) // Mg:Ag (100 nm) // Ag (100 nm). The emissive layer thickness was between 50 and 70 nm for a range of polymers. Only one device was presented for each polymer and no variation of emissive layer thickness was reported for any one polymer. The difference between EL and PL spectra in this case was attributed to the BT and TBT units acting as charge trapping sites.

Figure 7.9 shows the CIE coordinates of these devices. Dots denote the CIE co-

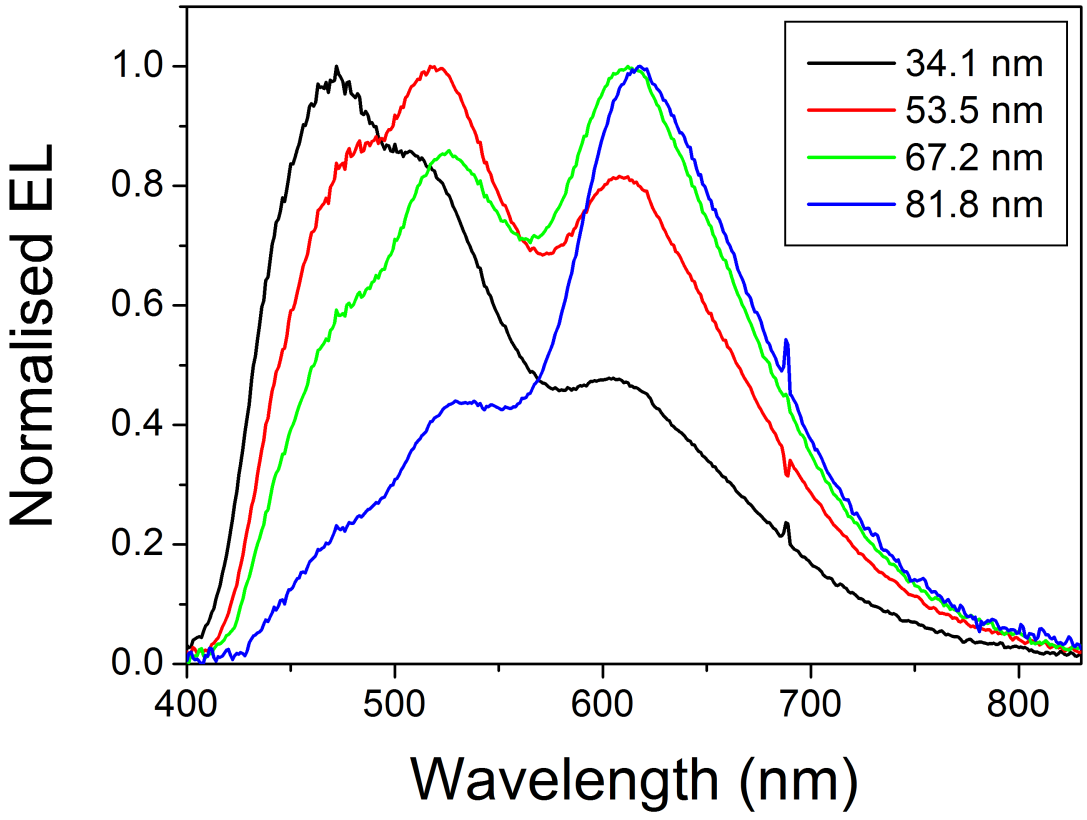

Figure 7.8: Normalised electroluminescence spectra of multilayer devices with varying thicknesses of **7.5**. Device structure ITO // PEDOT:PSS (HIL 1.1) // PVK (30 nm) // **7.5** (x nm) // Ba (4 nm) // Al (125 nm). The spectrum varies considerably as the thickness of the emissive layer is changed, with progressively weaker blue/green emission as the layer thickness increases.

ordinates at peak brightness, while lines and arrows indicate the extent and direction of the drift in CIE coordinates with increasing voltages for brightnesses above 100 cd m^{-2}. For the thinnest emissive layer the emission is on the blue side of the white point at (0.28, 0.32), and as the layer thickness is increased the emission progressively shifts away from the white point towards the red with the thickest emissive layer resulting in emission at (0.48, 0.42).

The colour stability of devices with increasing voltage is also shown in Figure 7.9 for brightnesses above 100 cd m^{-2}. The CIE coordinates are highly stable for the thicker

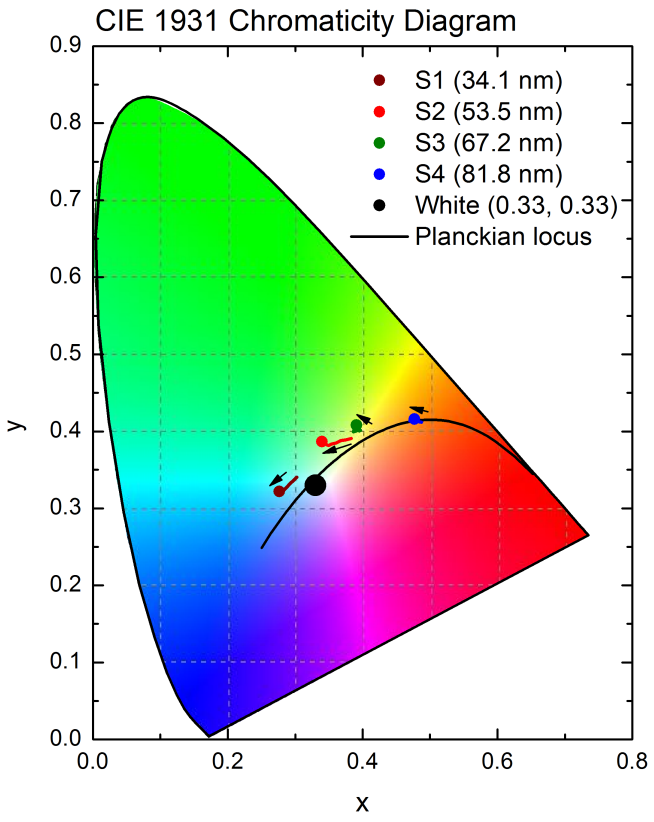

Figure 7.9: CIE chromaticity diagram showing coordinates of the electroluminescence of polymer **7.5** at different thicknesses, also indicating the extent and direction of the colour shift with increasing voltage. Device structure ITO // PEDOT:PSS (HIL 1.1) // PVK (30 nm) // **7.5** (x nm) // Ba (4 nm) // Al (125 nm). The emission shifts progressively away from the white point with increasing thickness. Coordinates:
34.1 nm: (0.28, 0.32)
53.5 nm: (0.34, 0.39)
67.2 nm: (0.39, 0.41)
81.8 nm: (0.48, 0.42)

emissive layers, where the colour of emission is predominantly red. A change of (-0.006, +0.007) was observed for the 67.2 nm emissive layer and (-0.010, +0.004) for the 81.8 nm layer. However there is a more substantial drift observed for the thinner emissive layers, with a change of (-0.026, -0.015) for the 34.1 nm emissive layer and (-0.043, -0.003) for the 53.5 nm layer.

It has been shown by Gather *et al.* that in white emitting single copolymer systems similar to this that the colour shift is due to field-dependent trapping on the red chromophore rather than saturation of the red chromophore or movement of the emission zone away from the anode [15]. In that case, the colour shift was due to the decrease in the relative contribution of emission from the red chromophore only, with the relative contribution from the green increasing slightly with increasing voltage. Devices with

7.5 (and **7.6**) both show the colour shift originating from a decrease in both red and green emission relative to the blue, which would be consistent with the green emitting BT unit also acting as a trapping site in these devices.

7.4.2 Thickness optimisation of 7.6 multilayer devices

Table 7.5 summarises the performance and efficiency of multilayer devices with different emissive layer thicknesses of polymer **7.6**, while Figure 7.10 shows their full *J-V*, *L-V* and device efficiency data. As before, the polymer was spin coated from 5, 8, 10 and 12 mg/ml toluene solution, resulting in layer thicknesses of 33.8, 55.1, 84.8 and 96.4 nm respectively. The PVK layer was spin coated from a 7 mg/ml chlorobenzene solution as before. The overall device architecture was ITO // PEDOT:PSS (HIL 1.3) // PVK (30 nm) // **7.6** (x nm) // Ba (4 nm) // Al (62 nm).

Increasing the emissive layer thickness has a similar effect on device turn-on voltage, efficiency and brightness as before. The turn-on voltage increases from 6.5 V to over

Device	Thickness [a] / nm	Turn-on [b] voltage / V	E.Q.E. [c] / %	Device [c] efficiency / cd A^{-1}	Brightness [c] / cd m^{-2}	Power [c] efficiency / lm W^{-1}
1	33.8	6.5	0.89	2.05	903	0.92
2	55.1	8.0	1.39	3.09	759	1.14
3	84.8	11.0	1.37	2.22	187	0.60
4	96.4	10.5	1.89	3.33	265	0.89

Table 7.5: Summary of the performance of multilayer devices with varying thicknesses of **7.6**. Device structure ITO // PEDOT:PSS (HIL 1.3) // PVK (30 nm) // **7.6** (x nm) // Ba (4 nm) // Al (62 nm).
[a]: Device thicknesses obtained by spin coating from concentrations of 5, 8, 10 and 12 mg/ml toluene solution.
[b]: Voltage at which the device reaches a brightness of 10 cd m^{-2}.
[c]: Peak values for the device.

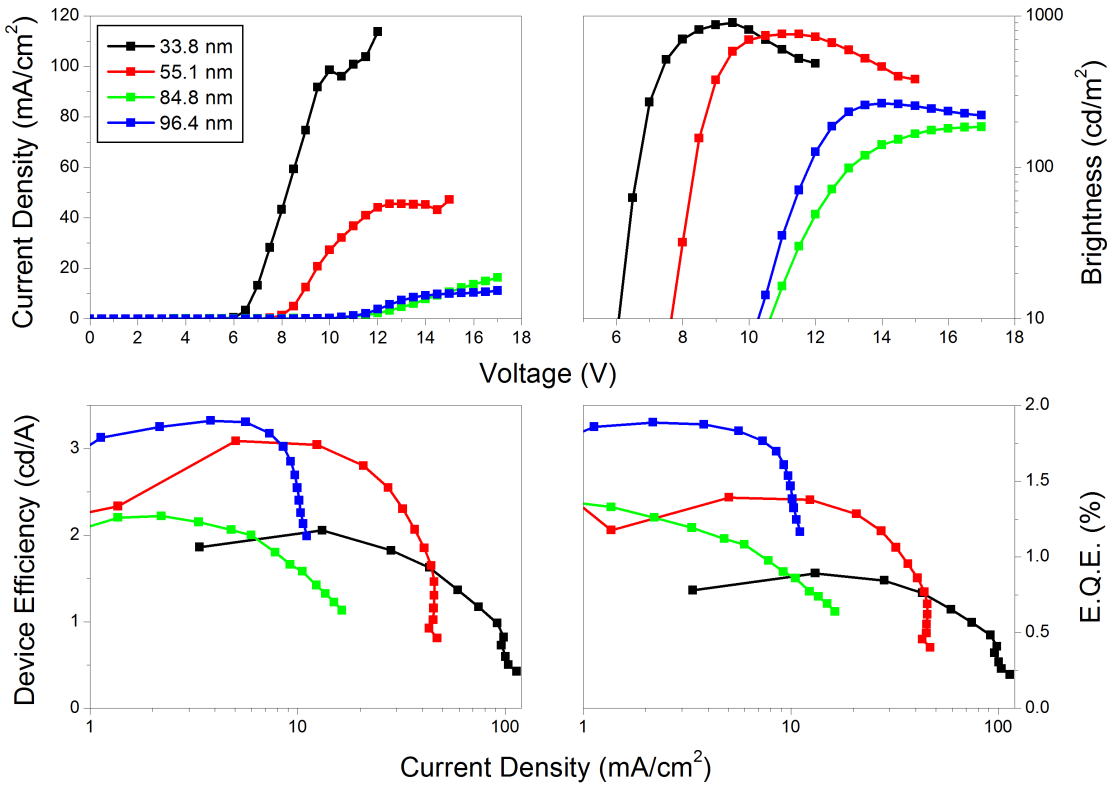

Figure 7.10: *J-V*, *L-V* and device efficiency data for multilayer devices with varying thicknesses of **7.6**. Device structure ITO // PEDOT:PSS (HIL 1.3) // PVK (30 nm) // **7.6** (x nm) // Ba (4 nm) // Al (62 nm). Increasing the layer thickness both increases the turn-on voltage and decreases the current flow through the device. Peak brightness of 903 cd m^{-2} was obtained at a thickness of 33.8 nm while a peak efficiency of 3.33 cd A^{-1} and 1.89% E.Q.E. was obtained at 96.4 nm, the thickest layer measured.

10 V as the device thickness increases. The highest device efficiency (1.89% E.Q.E. and 3.33 cd A^{-1}) was achieved at a thickness of 96.4 nm, while thinner emissive layers resulted in higher brightnesses (903 cd m^{-2} at 33.8 nm).

The electroluminescence spectra of the devices, shown here in Figure 7.11, were again strongly dependent on the thickness of the emissive layer with weaker blue/green emission and stronger red emission as the thickness increases. Comparing the blue emission of **7.5** seen in Figure 7.8 with that of **7.6** in Figure 7.11 shows the effect the S unit has on the electroluminescence of the polymer. For **7.5** the blue emission is

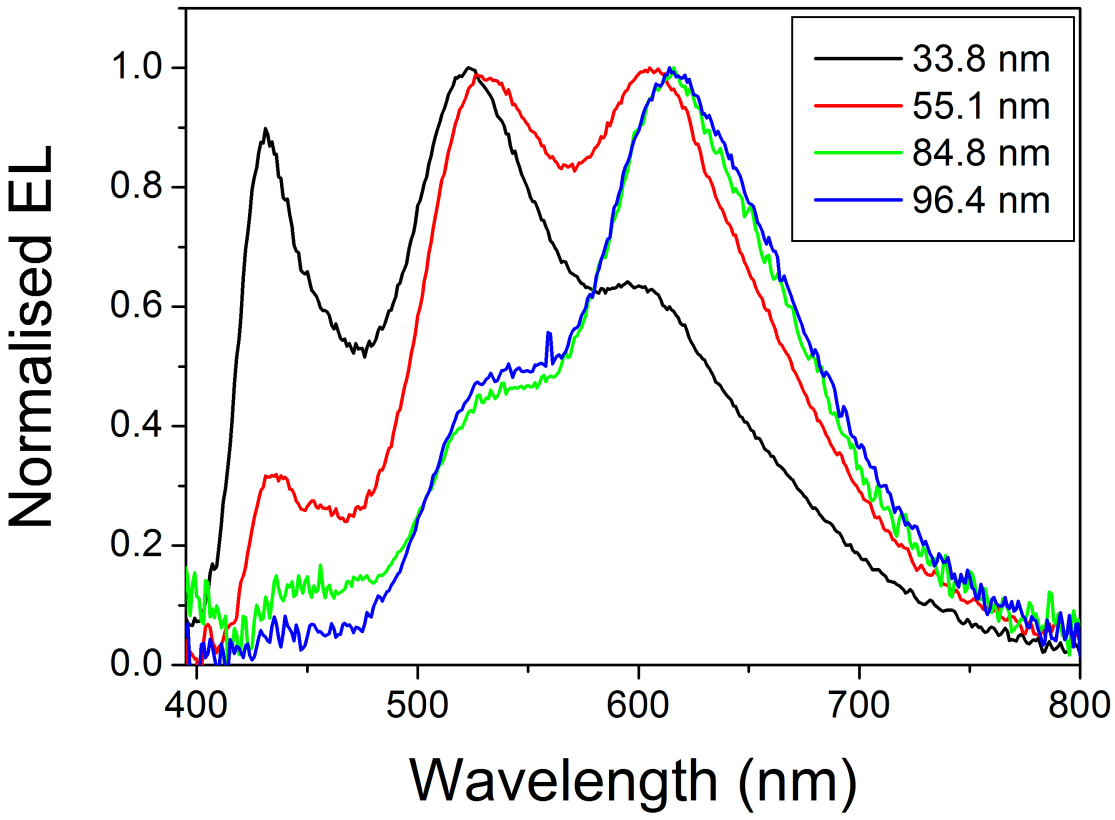

Figure 7.11: Normalised electroluminescence spectra of multilayer devices with varying thicknesses of **7.6**. Device structure ITO // PEDOT:PSS (HIL 1.3) // PVK (30 nm) // **7.6** (x nm) // Ba (4 nm) // Al (62 nm). Again, there is considerable variation in the emission spectrum as the thickness of the emissive layer is changed, with progressively weaker blue/green emission as the layer thickness increases.

broader and redshifted, peaking at 471 nm, while for **7.6** the blue emission is narrower and peaks at 431 nm. This is expected based on both the photoluminescence spectra of the polymers and the already established effect that the S unit has in previously reported materials.

Figure 7.12 shows the CIE coordinates of these devices. For the thinnest emissive layer the emission lies at (0.31, 0.36) at peak brightness, close to the white point. As the layer thickness is increased the emission again progressively shifts away from the white point towards the red, with the thickest emissive layer resulting in emission at

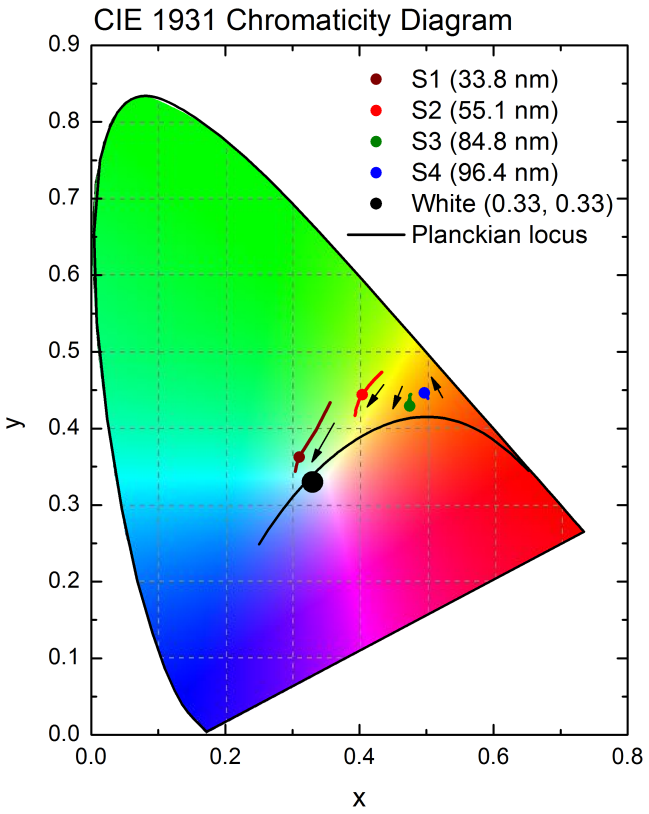

Figure 7.12: CIE chromaticity diagram showing coordinates of the electroluminescence of polymer **7.6** at different thicknesses, also indicating the extent and direction of the colour shift with increasing voltage. Device structure ITO // PEDOT:PSS (HIL 1.3) // PVK (30 nm) // **7.6** (x nm) // Ba (4 nm) // Al (62 nm). The emission shifts progressively away from the white point with increasing thickness. Coordinates:
33.8 nm: (0.31, 0.36)
55.1 nm: (0.40, 0.44)
84.8 nm: (0.48, 0.43)
96.4 nm: (0.49, 0.45)

(0.49, 0.45).

Figure 7.12 also shows the colour stability of devices with increasing voltage for brightnesses above 100 cd m^{-2}. Again, the CIE coordinates are highly stable for the thicker emissive layers where the red emission dominates. A change of (+0.001, -0.012) is observed for the 84.8 nm emissive layer and (+0.006, -0.005) for the 96.4 nm layer. However a greater drift at thinner emissive layers is seen compared to **7.5**, with a change of (-0.052, -0.089) for the 33.8 nm emissive layer and (-0.041, -0.057) for the 55.1 nm layer.

7.4.3 Comparison of 7.5 and 7.6 single layer and multilayer devices

After the thickness characterisation of the emissive layer of multilayer **7.5** and **7.6** devices, the two polymers were compared in both single layer and multilayer devices, with

a final set of devices adding a layer of 1,3,5-tris(1-phenyl-1H-benzimidazol-2-yl)benzene (TPBI), deposited by thermal evaporation, to the device structure as an electron transport layer.

Table 7.6 summarises the performance and efficiency of single layer and multilayer devices comparing both polymers **7.5** and **7.6**, while Figure 7.13 shows their full *J-V*, *L-V* and device efficiency data (data for devices incorporating TPBI are shown in Figure 7.17). The emissive layer in single layer devices was spin coated from 10 mg/ml toluene solution, resulting in layer thicknesses of 64.6 nm and 71.8 nm for **7.5** and **7.6** respectively.

For multilayer devices, the PVK layer was spin coated from a 7 mg/ml chlorobenzene solution as before while the emissive layers were spin coated from 8 mg/ml toluene solutions. The emissive layer thicknesses were measured as 54.9 nm for **7.5** and 61.7 nm for **7.6**. The overall device architecture was ITO // PEDOT:PSS (HIL 1.3) // PVK (30 nm) (multilayer devices only) // **7.5** or **7.6** // Ba (4 nm) // Al (100 nm).

Material	Structure [a]	Turn-on [b] voltage / V	E.Q.E. [c] / %	Device [c] efficiency / cd A^{-1}	Brightness [c] / cd m^{-2}	Power [c] efficiency / lm W^{-1}
7.5	S	5.0	0.41	0.81	2241	0.42
7.6	S	4.5	0.90	1.96	5967	1.12
7.5	M	8.5	1.34	2.42	1940	0.80
7.6	M	8.0	1.66	3.62	931	1.27
7.5	M + TPBI	5.5	3.79	6.18	943	3.11
7.6	M + TPBI	5.5	4.34	8.16	1451	4.57

Table 7.6: Summary of the performance of single layer and multilayer devices comparing **7.5** and **7.6**.
[a]: Device structure: S (single layer), M (multilayer) incorporating a *ca* 30 nm layer of PVK, or multilayer incorporating both PVK and a 30 nm layer of TPBI.
[b]: Voltage at which the device reaches a brightness of 10 cd m^{-2}.
[c]: Peak values for the device.

Devices containing an electron transport layer of TPBI had a device architecture of ITO // PEDOT:PSS (HIL 1.5) // PVK (30 nm) // **7.5** or **7.6** // TPBI (30 nm) // LiF (1 nm) // Al (100 nm). Full *J*-*V*, *L*-*V* and device efficiency data for these devices are shown in Figure 7.17.

Single layer devices have low efficiency, with devices containing **7.5** having an efficiency of 0.81 cd A^{-1} and 0.41% E.Q.E. Devices with a single layer of **7.6** are slightly more efficient at 1.96 cd A^{-1} and 0.90% E.Q.E. Single layer devices also exhibit extremely high current flow through the device, reaching a peak current density of the order of 800 mA cm^{-2}. This may imply that the charge transport properties of the polymers are not balanced and that further optimisation of the chemical structure of the polymer is needed.

The addition of a PVK layer between the emissive layer and the anode to form multilayer devices results in an increase in efficiency attributable to the PVK acting as a hole transport and electron blocking layer. The device efficiencies are increased to 2.42 cd A^{-1} and 1.34% E.Q.E. for **7.5** and 3.62 cd A^{-1} and 1.66% E.Q.E. for **7.6**. However these devices exhibit reduced brightness, and the turn on voltage is increased from 4.5 - 5.0 V to 8.0 - 8.5 V.

The electroluminescence spectra of these devices are shown in Figure 7.14. The **7.5** devices exhibit good spectral coverage in both single layer and multilayer devices due to the broadened blue-green emission of the F/S system, while for **7.6** the blue emission is reduced by the thickness of the emissive layer, resulting in an orange-red emission shifted away from the white.

The CIE coordinates of these devices at peak brightness are shown in Figure 7.15,

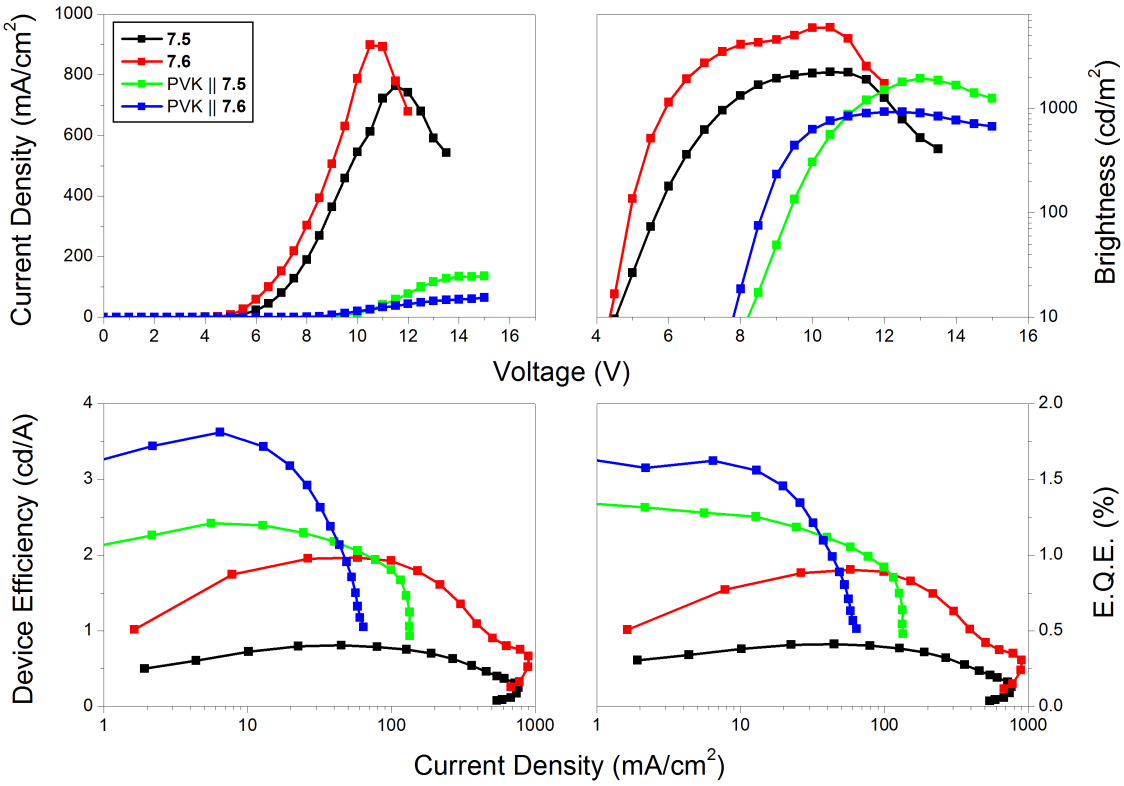

Figure 7.13: *J-V*, *L-V* and device efficiency data for single layer and multilayer devices comparing **7.5** and **7.6**. Device structure ITO // PEDOT:PSS (HIL 1.3) // PVK (30 nm) (multilayer devices only) // **7.5** or **7.6** // Ba (4 nm) // Al (100 nm).

also indicating the extent and direction of the colour shift with increasing brightness. The CIE coordinates of **7.5** devices are close to the white point at (0.31, 0.35) for single layer devices and (0.35, 0.39) for multilayer devices. Those of the **7.6** devices are shifted away from the white point due to the reduced contribution from the blue emitter, at (0.39, 0.44) for both single layer and multilayer devices.

All these devices however exhibit substantial changes in CIE coordinates as the brightness of the device increases, as shown in Figure 7.15. For the single layer devices the changes are (-0.053, -0.052) for **7.5** and (-0.053, -0.019) for **7.6**, while for the multilayer devices the changes are (-0.038, -0.038) and (-0.031, -0.046) respectively.

Figure 7.16 shows photographs of (left) the emission of **7.5** in a multilayer device

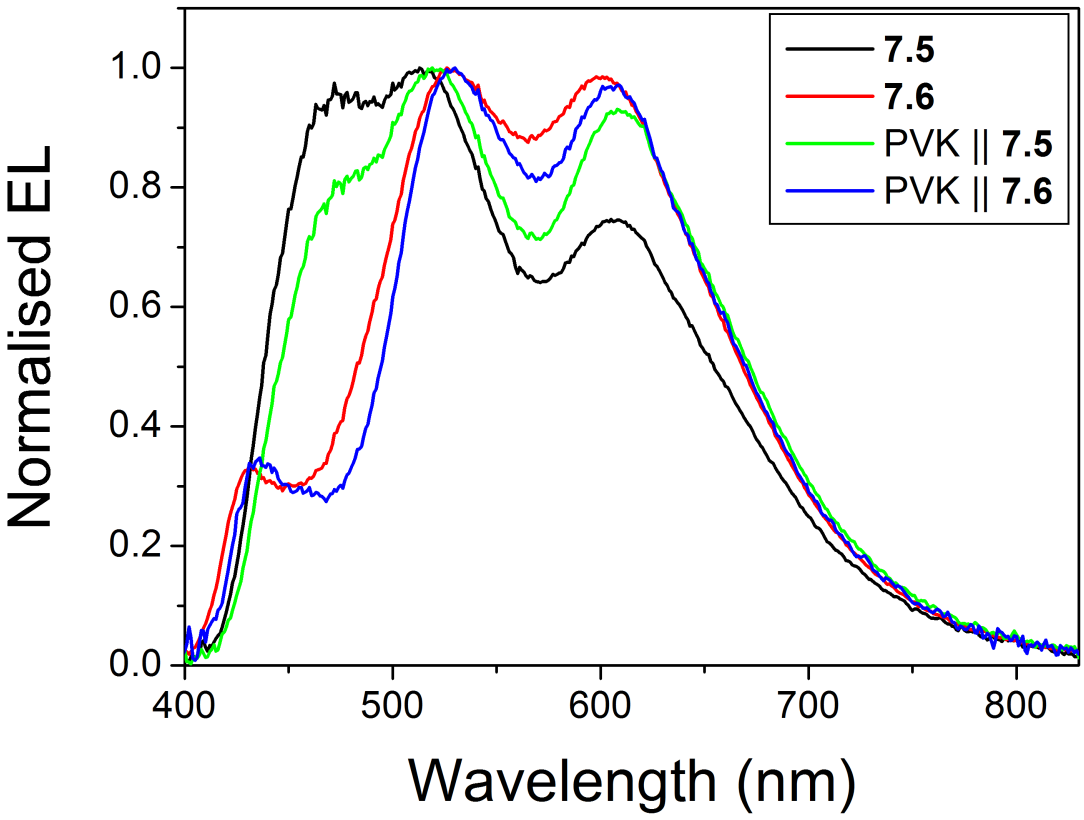

Figure 7.14: Normalised electroluminescence spectra of single layer and multilayer devices comparing **7.5** and **7.6**. Device structure ITO // PEDOT:PSS (HIL 1.3) // PVK (30 nm) (multilayer devices only) // **7.5** or **7.6** // Ba (4 nm) // Al (100 nm).

operating at a bias of 16 V and (right) the emission of the same polymer in a single layer device operating at a bias of 10 V. The single layer devices exhibit a much higher brightness at lower voltage, but also at a lower device efficiency.

The effect of adding a 30 nm layer of TPBI as an electron transporting layer (and also changing the cathode from barium to lithium fluoride) on the device performance is shown in Figure 7.17. The efficiency of **7.5** devices is increased from 2.42 cd A^{-1} and 1.34% E.Q.E. to 6.18 cd A^{-1} and 3.79% E.Q.E. due to the improved electron injection into the polymer layer and better charge balance. Similarly, the efficiency of **7.6** devices is increased from 3.62 cd A^{-1} and 1.66% E.Q.E. to 8.16 cd A^{-1} and 4.34%

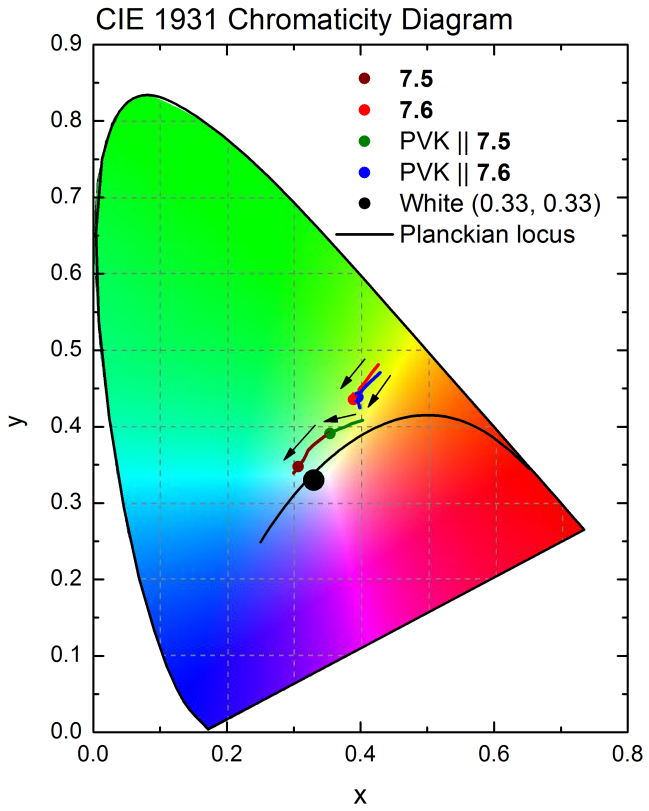

Figure 7.15: CIE chromaticity diagram showing coordinates of the electroluminescence of polymers **7.5** and **7.6** in single layer and multilayer devices, also indicating the extent and direction of the colour shift with increasing voltage. Device structure ITO // PEDOT:PSS (HIL 1.3) // PVK (30 nm) (multilayer devices only) // **7.5** or **7.6** // Ba (4 nm) // Al (100 nm). Polymer **7.5** exhibits better white emission in both single layer and multilayer devices due to the broadened blue emission from the interaction between F and S units.
Coordinates:
7.5: (0.31, 0.35)
7.6: (0.39, 0.44)
PVK // **7.5**: (0.35, 0.39)
PVK // **7.6**: (0.39, 0.44)

E.Q.E. Additionally, the turn-on voltage is reduced to 5.5 V.

Electroluminescence spectra of the hybrid devices are shown on the left hand panel of Figure 7.18. The spectra again show the broadened blue-green emission of **7.5** compared to the sharper blue peak observed with **7.6** when no S unit is present. The emission of both devices is more intense in the red than that of the comparable bilayer devices with the same emissive layer thickness and no TPBI layer. The addition of the 30 nm layer of TPBI to the device structure results in a shift in CIE coordinates from (0.35, 0.39) to (0.41, 0.39) for **7.5** and from (0.39, 0.44) to (0.42, 0.40) for **7.6**. The CIE coordinates of the hybrid devices are shown on the right hand panel of Figure 7.18. It is anticipated that a slightly thinner emissive layer may result in more balanced emission across the three component colours.

The CIE coordinates of these devices are more stable with increasing voltage than

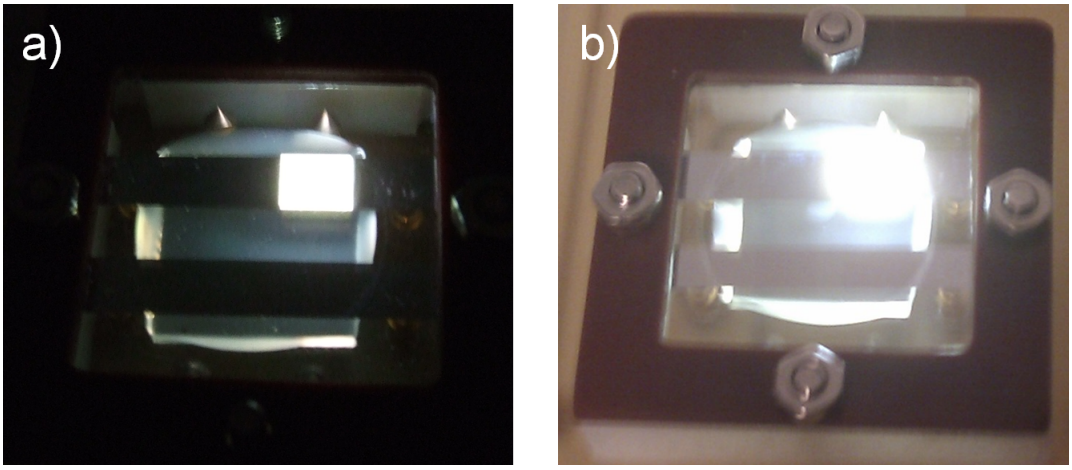

Figure 7.16: Photograph of a) emission of **7.5** in a multilayer device operating at 16 V and b) emission of **7.5** in a single layer device operating at 10 V.

those of the devices without TPBI. The coordinates of the **7.5** devices shift by a maximum of (-0.034, -0.012) while those of the **7.6** devices shift by a maximum of (-0.026, -0.017).

7.5 Conclusions

In conclusion, white electroluminescence has been demonstrated from two single copolymers **7.5** and **7.6** containing red, green and blue chromophores in the polymer backbone. Broadened intramolecular charge transfer emission due to the interaction of the fluorene (F) and dibenzothiophene-S,S-dioxide (S) units in the molecular structure of copolymer **7.5** resulted in improved spectral coverage in the blue-green region of the spectrum compared to that of **7.6**, which did not incorporate the S unit.

Multilayer devices based on polymer **7.5** reached a maximum efficiency of 2.42 cd A^{-1} and 1.34% E.Q.E. and a peak brightness of 1,940 cd m^{-2}, although devices based on **7.6** without the S unit achieved higher efficiencies of 3.62 cd A^{-1} and 1.66% E.Q.E. The emission is highly dependent on the thickness of the emissive layer due

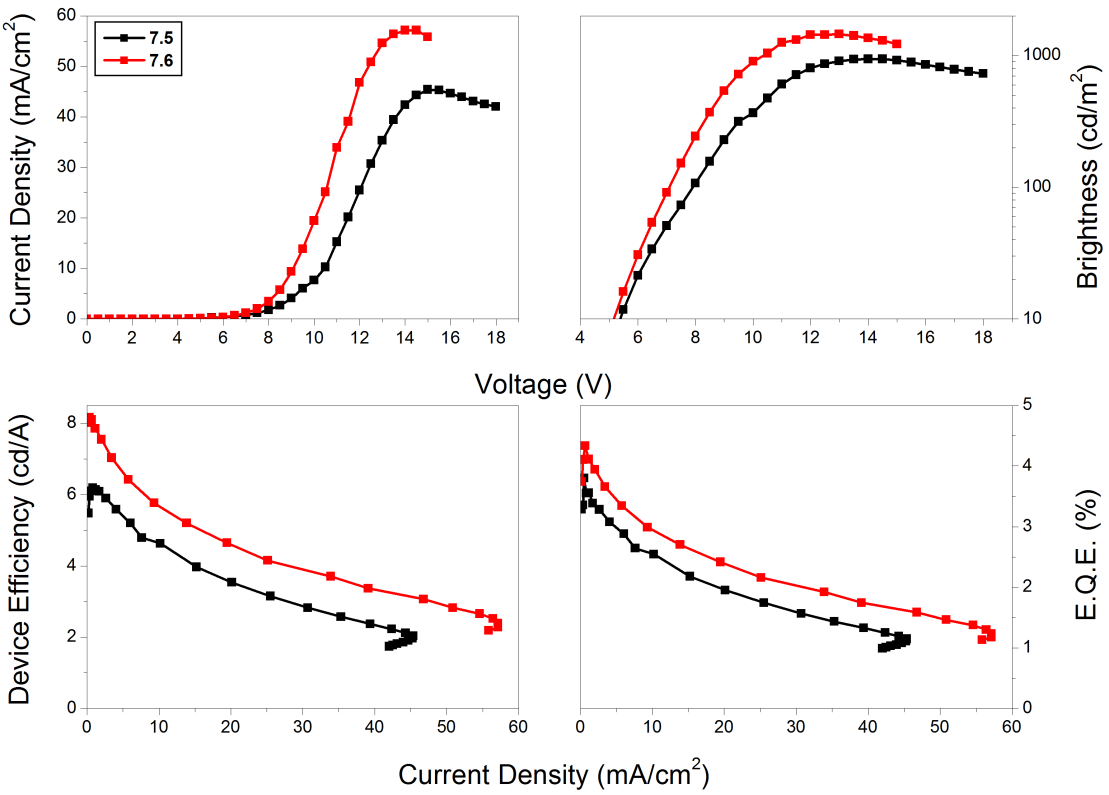

Figure 7.17: *J-V*, *L-V* and device efficiency data for multilayer devices comparing **7.5** and **7.6** incorporating an electron transporting layer of TPBI. Device structure ITO // PEDOT:PSS (HIL 1.5) // PVK (30 nm) // **7.5** or **7.6** // TPBI (30 nm) // LiF (1 nm) // Al (100 nm).

to the device microcavity effect, but CIE coordinates of (0.34, 0.39) were obtained for multilayer **7.5** devices, which compares favourably to coordinates of (0.40, 0.44) obtained for a multilayer **7.6** device with a similar emissive layer thickness.

However, a significant brightness dependent colour shift was observed in single layer and multilayer devices, especially at lower emissive layer thicknesses in multilayer devices, due to field dependent trapping at both the BT and TBT chromophores.

Both device efficiency and colour stability were improved by addition of a thermally evaporated electron transporting layer of TPBI, with **7.5** devices reaching an efficiency of 6.18 cd A^{-1} and 3.79% E.Q.E. and **7.6** devices reaching 8.16 cd A^{-1} and 4.34%

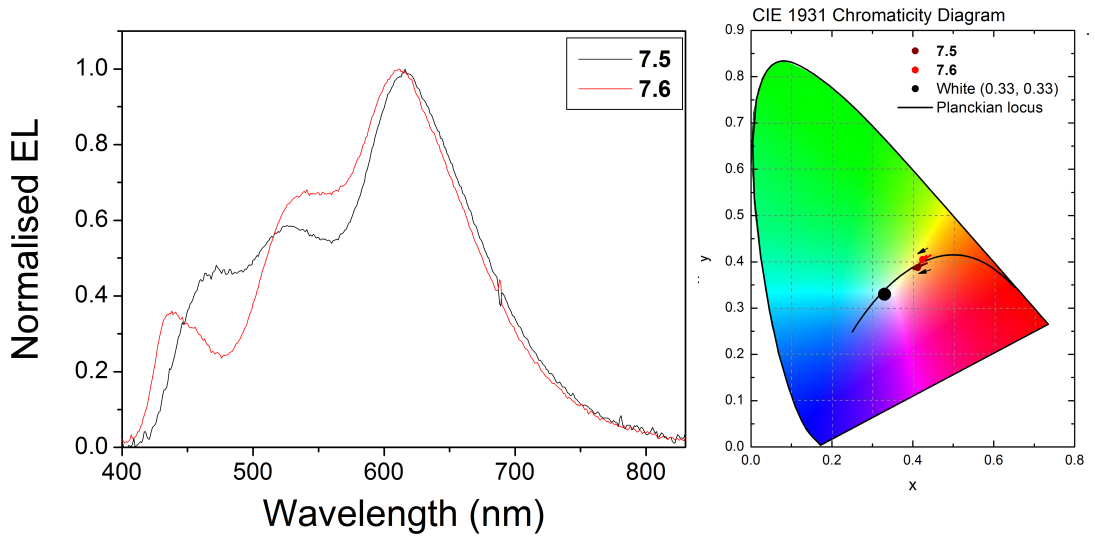

Figure 7.18: Left: Normalised electroluminescence spectra of multilayer devices comparing **7.5** and **7.6** incorporating an electron transporting layer of TPBI. Device structure ITO // PEDOT:PSS (HIL 1.5) // PVK (30 nm) // **7.5** or **7.6** // TPBI (30 nm) // LiF (1 nm) // Al (100 nm). Right: CIE chromaticity diagram showing the CIE coordinates of the devices, also indicating the extent and direction of the colour shift with increasing voltage.

E.Q.E. This however had the added effect of shifting the emission towards the red, to (0.41, 0.39) for **7.5** and to (0.42, 0.40) for **7.6**.

These materials are therefore promising for applications in white light OLED devices although more optimisation is needed in both device architecture and polymer structure, for example working to reduce the magnitude of the colour shift when the emission is closer to the white, as well as optimisation of the balance of charge carrier units in the copolymer.

References

[1] K. C. Moss, *Novel Intramolecular Charge Transfer Materials and their Optoelectronic Properties*, PhD thesis, Durham University (2012)

[2] M. C. Gather, A. Köhnen & K. Meerholz, *Advanced Materials* **23** (2011), 233 - 248

[3] S. Reineke, M. Thomschke, B. Lüssem & K. Leo, *Reviews of Modern Physics* **85** (2013), 1245 - 1293

[4] K. T. Kamtekar, A. P. Monkman & M. R. Bryce, *Advanced Materials* **22** (2010), 572 - 582

[5] I. ul Haq Raja, J. Y. Lee, I. T. Kim & S. H. Lee, *Monatshefte für Chemie - Chemical Monthly* **139** (2008), 725 - 737

[6] J. Liu, Q. Zhou, Y. Cheng, Y. Geng, L. Wang, D. Ma, X. Jing & F. Wang, *Advanced Functional Materials* **16** (2006), 957 - 965

[7] J. Luo, X. Li, Q. Hou, J. Peng, W. Yang & Y. Cao, *Advanced Materials* **19** (2007), 1113 - 1117

[8] C.-Y. Chuang, P.-I. Shih, C.-H. Chien, F.-I. Wu & C.-F. Shu, *Macromolecules* **40** (2007), 247 - 252

[9] J. Liu, L. Chen, S. Shao, Z. Xie, Y. Cheng, Y. Geng, L. Wang, X. Jing & F. Wang, *Advanced Materials* **19** (2007), 4224 - 4228

[10] B. Zhang, C. Qin, J. Ding, L. Chen, Z. Xie, Y. Cheng & L. Wang, *Advanced Functional Materials* **20** (2010), 2951 - 2957

[11] S. Shao, J. Ding, L. Wang, X. Jing & F. Wang, *Journal of the American Chemical Society* **134** (2012), 20290 - 20293

[12] F. B. Dias, S. King, A. P. Monkman, I. I. Perepichka, M. A. Kryuchkov, I. F. Perepichka & M. R. Bryce, *Journal of Physical Chemistry B* **112** (2008), 6557 - 6566

[13] S. M. King, I. I. Perepichka, F. B. Dias, M. R. Bryce & A. P. Monkman, *Advanced Functional Materials* **19** (2009), 586 - 591

[14] F. B. Dias, K. T. Kamtekar, T. Cazati, G. Williams, M. R. Bryce & A. P. Monkman, *ChemPhysChem* **10** (2009), 2096 - 2014

[15] M. C. Gather, R. Alle, H. Becker & K. Meerholz, *Advanced Materials* **19** (2007), 4460 - 4465

8 Conclusions

This thesis has presented the characterisation and testing in OLED devices of a wide range of new materials for solution processable organic light emitting diodes synthesised by researchers in the Department of Chemistry at the University of Durham. In this chapter, the main conclusions of the work are summarised.

In chapter 4, a series of three new high triplet energy electron transport materials were tested. Due to the twisted chemical structure, these materials were expected to have a higher triplet energy than the commercially available analogue, OXD-7. In multilayer devices with the sky blue emitter FIrpic as a dopant, all devices had a comparable efficiency regardless of which OXD material was used, but the turn on voltage required to attain a brightness of 10 cd m^{-2} increased as the LUMO of the electron transporting material increased.

The exciplex emission of PVK:electron transport devices without a phosphorescent dopant emitter also followed this trend, confirming previous theoretical studies that OXD-7 has the lowest LUMO level of the materials tested. The results indicate that the LUMO level of material **4.1a** may be higher than that of PVK, and as such there is no energy lost to PVK:electron transport exciplexes using this material.

Although the performance of devices incorporating FIrpic were similar regardless of which electron transporting materials was used, the development of high triplet energy electron transport materials will serve to reduce quenching if deeper blue emitters are to be used in devices.

Secondly, single layer solution processable OLED devices were optimised for emis-

sive layer thickness, iridium dopant concentration and OXD-7 concentration. The iridium dopant used was one of a new series of sky blue FIrpic derivatives with branched aryl ring dendrimer side chains to improve solubility and shield the iridium core. The maximum efficiency obtained with these devices was not as high as single layer devices using FIrpic reported in the literature, reflecting the need to further optimise, for example, the PEDOT:PSS layer and the cathode.

The emitters with the bulky dendrimer side chains were no better performing than complex **4.2a**, a FIrpic derivative with a simple twisted mesityl side group which is easier and cheaper to synthesise. Therefore the emitters characterised in chapter 5 investigated this further, using the optimised device architecture to characterise a series of emitters with simpler alkyl and mesityl solubilising groups.

All new sky blue emitters tested outperformed FIrpic, with multilayer devices incorporating an evaporated electron transport layer and **4.2a** as the emitter reaching 22.5 cd A^{-1} and 9.7% E.Q.E. with a peak brightness of 11,090 cd m^{-2}. The better device performance of **4.2a** over the other emitters tested was attributed to reduced aggregation in thin film due to better solubility, as well as reduced concentration quenching and the higher radiative yield of **4.2a**.

Adding cyano substituents or using a bipyridyl based ligand to blueshift emission reduced the device efficiency due to low energy triplet trap states in the PVK host. Devices doped with the cyano substituted complex **5.2c** reached a maximum efficiency of 13.0 cd A^{-1} and 7.3% E.Q.E. at a peak wavelength of 467 nm and CIE coordinates of (0.16, 0.28).

Replacing the mesityl substituent with a 2,7-dihexyloxycarbazole unit further in-

creased device efficiency for the sky blue emitting FIrpic derivative (complex **5.3a**) to 28.8 cd A^{-1} and 11.4% E.Q.E. as well as a peak brightness of 13,350 cd m^{-2}, although the emission was slightly greener than that of **4.2a**. The corresponding blueshifted bipyridyl (complex **5.3b**) did not perform as well in devices, but investigation is ongoing into the dual emission observed by colleagues in its photoluminescence spectrum in more polar solvents.

In Chapter 6 a range of complexes were investigated which incorporated systematically substituted electron withdrawing or donating groups to tune the colour of emission from green to red. The magnitude of the solvatochromic shift of the **6.1** series emitters as well as the relative strength of the MLCT band in the absorption spectra, correlate with calculated values of the molecular dipole moment for these complexes.

With the pyridine unit on the ligand linked to the carbazole unit at the C-2 position (series **6.2**) as opposed to the C-3 position (series **6.1**), carbazole contribution to the excited state is increased. This resulted in a reduction in both the radiative yield of the complexes and the observed solvatochromic shift.

Finally, in chapter 7 solution processable devices demonstrating white electroluminescence from single copolymers were fabricated and optimised for emissive layer thickness. The copolymers exploited broadened blue-green intramolecular charge transfer emission due to the interaction of fluorene (F) and dibenzothiophene-S,S-dioxide (S) units that had previously been demonstrated in Durham, and with the addition of red and green chromophore units to the copolymer structure, white emission with good spectral coverage was obtained.

Multilayer solution processable devices with polymer **7.5** reached a maximum ef-

ficiency of 2.42 cd A^{-1} and 1.34% E.Q.E. and a peak brightness of 1,940 cd m^{-2} at CIE coordinates of (0.35, 0.39). This compares to a higher efficiency of 3.62 cd A^{-1} and 1.66% E.Q.E. obtained for comparable devices using copolymer **7.6** without the S unit, but at CIE coordinates of (0.40, 0.44).

The emission spectrum of both polymers was strongly dependent on the emissive layer thickness, possibly due to a device microcavity effect, and additionally a brightness dependent colour shift was observed that can be attributed to trapping at the green BT and red TBT chromophores.

Colour stability was improved however by addition of an evaporated TPBI electron transport layer, which also increased the maximum device efficiency to 6.18 cd A^{-1} and 3.79% E.Q.E. for **7.5** and 8.16 cd A^{-1} and 4.34% E.Q.E. for **7.6**. The emission of the multilayer hybrid devices was shifted to the red at (0.41, 0.39) for **7.5** and to (0.42, 0.40) for **7.6**. This could be improved further by optimisation of the emissive layer thickness for the multilayer hybrid devices.